Universitat Autònoma de Barcelona

Tesi Doctoral

Millora del tractament de les imatges captades pels satèl·lits Landsat-8 i Sentinel-2 mitjançant espectroradiometria de camp i sensors embarcats en Vehicles Aeris no Tripulats (UAV)

Autor: *Joan-Cristian Padró Garcia*
Director: *Xavier Pons Fernández*

Programa de Doctorat en Geografia
Departament de Geografia

Universitat Autònoma de Barcelona
Bellaterra, gener 2019

PRÒLEG

Aquesta Tesi doctoral ha estat realitzada entre l'1 de març de 2016 i el 31 de desembre de 2018. En aquest temps he iniciat, desenvolupat i completat una recerca que considero digna de ser presentada i interessant per a la comunitat científica.

No ha estat fàcil, però si he pogut fer-la en tan poc temps és perquè hi ha hagut una motivació personal que m'ha empès a dedicar-hi cada minut de què he disposat. És per això que escric aquest pròleg, per explicar en quatre línies el perquè de dedicar una part de la meva vida a una Tesi titulada "*Millora del tractament de les imatges captades pels satèl·lits Landsat-8 i Sentinel-2 mitjançant espectroradiometria de camp i sensors embarcats en Vehicles Aeris no Tripulats (UAV)*", així com el perquè de la meva total implicació:

Sóc graduat en Geografia per la Universitat Autònoma de Barcelona (UAB) i he fet un Màster en Teledetecció i Sistemes d'Informació Geogràfica, però prèviament vaig fer dos anys del Grau en Filosofia, també a la UAB. Encara que laboralment estudiar filosofia és una decisió que podria ser considerada poc prometedora, sí que m'ha estat útil per la vida. En concret, per preguntar-me què és cert i com puc arribar a certeses. La certesa és una qüestió que a vegades no ens aturem a discutir: simplement acceptem els fets com a certs en tant que fets, i les dades certes en tant que dades.

Quan vaig estudiar Teledetecció, va haver-hi un moment en què em vaig qüestionar si les propietats físiques de la superfície terrestre que es mesuren des d'un satèl·lit situat a uns 800 km de distància, s'ajusten a la realitat. No podia creure'm una cosa així sense contrastar-la empíricament, així que em vaig introduir en el món de l'espectroradiometria de camp i la validació de les dades de satèl·lit. Quan vaig tenir la possibilitat de fer el doctorat, vaig decidir arribar fins al fons de la qüestió i contribuir en la millora de les tècniques de validació convencionals, introduint noves tecnologies com són els drons.

El resultat ha estat que no només he resolt la meva inquietud inicial (la contrastació empírica que les dades de satèl·lit s'ajusten a la realitat), sinó que també he pogut aportar una nova metodologia per corregir les dades satèl·lit de manera que s'ajustin més encara a les dades de veritat terreny.

Índex

ÍNDEX

Agraïments

Agraïments

En primer lloc, vull donar les gràcies al Grup de Recerca Mètodes i Aplicacions en Teledetecció i Sistemes d'Informació Geogràfica (GRUMETS) per donar-me l'oportunitat de realitzar la Tesi Doctoral dins d'aquest equip de magnífics i magnífiques professionals, posant a la meva disposició els materials necessaris per dur a terme la recerca planejada. En tant que director de GRUMETS i d'aquesta Tesi, vull agrair al Dr. Xavier Pons les incomptables hores que ha dedicat en el disseny, construcció, execució i revisió la meva (nostra) recerca, unes hores que hem gaudit colze a colze i que han derivat en el que em permeto dir que és una bona amistat. Espero haver retornat la confiança que des d'un inici es va dipositar en mi, i que la inversió de temps i de recursos s'hagi vist compensada amb un increment del prestigi del grup gràcies als resultats de la meva feina. Sense la contribució de tots i cadascun dels membres del grup de recerca GRUMETS la realització de la meva Tesi no hagués estat possible i, per tant, cada membre de GRUMETS se la pot sentir seva en una petita però indispensable part.

La consecució d'aquesta Tesi no hagués estat possible sense la col·laboració de la Generalitat de Catalunya, que ha finançat la meva recerca amb una beca pre-doctoral de formació d'investigadors (FI-DGR 2016B_00410) durant els darrers tres anys. Alhora, agreixo a la Unió Europea el finançament del projecte ECOPOTENTIAL (H2020 641762-2 EC), una part del qual fou concedit al Departament de Geografia (GRUMETS) per via del Dr. Pere Serra, i que ha permès la difusió de la recerca d'aquesta Tesi en prestigioses revistes científiques i congressos internacionals. En la mateixa línia, agraeixo al Ministerio de Economía y Competitividad el finançament del projecte ACAPI (CGL2015-69888-P (MINECO/FEDER-ERDF, EU)) concedit a GRUMETS, ja que també ha permès el finançament de la meva participació en congressos nacionals. S'agraeix a les agències espacials estatunidenca (National Aeronautics and Space Administration, NASA) i europea (European Space Agency, ESA) que posin a disposició de qualsevol investigador i gratuïtament les dades satel·litàries que s'han utilitzat en aquesta Tesi.

Vull manifestar la meva profunda gratitud al Departament de Geografia (DdG) de la Universitat Autònoma de Barcelona (UAB) per haver posat a la meva disposició les instal·lacions i els espais dels que he estat fent ús. També vull remarcar la professionalitat de tots els seus integrants, des del personal administratiu fins als catedràtics, passant pels tècnics, professors i estudiants, tots ells i elles sempre contribuint al bon funcionament del departament i disposats i disposades a compartir els seus coneixements amb els companys i companyes. Voldria destacar el suport professional i personal que m'han donat la Dra. Carme Miralles, la Dra. Anna Badia i la Dra. Meritxell Gisbert, així com el suport logístic i operatiu rebut per part del Dr. Joan-Carles Llurdés i el Sr. Roger Milego.

A un nivell més proper i de recerca diària, però alhora imprescindible per a la realització de la meva Tesi, vull agrair l'enorme col·laboració de les meves companyes de despatx, la Dra. Alaitz Zabala i la Sra. Cristina Cea, que han creat un clima de treball i serenor imprescindible per créixer cada dia amb fermesa, a més d'estar sempre disposades a aturar les seves tasques per solucionar els problemes que em sorgien. Als companys del despatx del costat, el Sr. Òscar González, el Sr. Guillem Closa, el Sr. Mario Padial, la Dra. Maria Mira i el Dr. Juanjo Vidal-Macua, també sempre disposats a donar un cop de mà a la meva Tesi i a fer-la avançar amb els seus sempre assenyats consells. A la resta de companys i companyes de GRUMETS, que més enllà de la seva feina diària i indispensable, han aconseguit que fos divertit venir a treballar amb elles i ells, la Sra. Ivette Serral, el Dr. Joan Masó, la Sra. Ester Prat, la Dra. Cristina Domingo, el Dr. Miquel Ninyerola, el Dr. Pere Serra, el Dr. Jordi Cristóbal i el Dr. Ricardo Díaz-Delgado. Menció especial mereix l'equip tècnic i programador de GRUMETS, format pel Sr. Abel Pau, la Sra. Núria Julià, el Dr. Lluís Pesquer, el Sr. Xavier Calaf i el Dr. Xavier Pons, que han desenvolupat i posat a la meva disposició eines informàtiques fetes a mida de la meva recerca.

Estic especialment agraït al Sr. David Aragonés i al Dr. Ricardo Díaz-Delgado, així com al Dr. Javier Bustamante, el Sr. Diego García, i la resta d'integrants de la Estación Biológica de Doñana (EBD), pel seu suport tècnic i humà en la col·laboració que va conduir a l'elaboració dels primers

resultats de la meva Tesi. Sense la seva excel·lent feina no hagués iniciat amb èxit aquest camí. També vull agrair al Dr. Daniel Doktor i al Sr. Maximilian Lange la seva col·laboració des del Helmholtz Centre for Environmental Research (UFZ).

Vull agrair a l'empresa HEMAV S.L., i en especial al seu cap d'operacions, el Sr. Francisco-Javier Muñoz, que hagi posat a disposició de la meva recerca diverses plataformes dron i sensors multiespectrals punters tecnològicament, a més de pilots professionals per la realització de vols amb la màxima qualitat. El seu suport ha estat clau per la realització de gran part de la meva Tesi. De la mateixa manera ha estat clau la participació del Sr. Jordi Planas, l'alumne de Màster en Teledetecció (TD) i Sistemes d'Informació Geogràfica (SIG) que va engegar la recerca relacionada amb determinats capítols de la Tesi i amb qui, juntament amb el Sr. Raül Filter, sempre ha estat un plaer treballar donada la seva exigència. El Sr. Luis Angel Ávila, alumne que va col·laborar molt entusiasmadament amb l'anàlisi de dades en el capítol central de la Tesi, també és mereixedor del meu profund respecte i agraïment.

Vull agrair la col·laboració del Centre Tecnològic i Forestal de Catalunya (CTFC), en especial del Dr. Lluís Brotons, de la Sra. Magda Pla i del Sr. Jaume Balagué (NordDron). Han posat a disposició de la meva recerca diversos recursos materials i humans per l'adquisició d'imatges de dron cabdals en la consecució de la Tesi. També hi han participat de manera molt rellevant el Sr. Vicenç Carabassa i el Dr. Josep Maria Alcañiz, del Grup de Recerca Consolidat en Protecció de Sòls (PROTECSOLS) del Centre de Recerca en Ecologia i Aplicacions Forestals (CREAF), impulsors d'una part important de la recerca i connectors amb els usuaris finals de la investigació que conjuntament hem portat a terme. Del CREAF, també vull agrair al Dr. Jordi Sardans el seu suport logístic i els seus assenyats consells.

Agrair als vuit alumnes del Màster en TD i SIG a qui he dirigit o co-dirigit tesines de final de màster, ja que m'han donat l'oportunitat de créixer com a docent i d'avançar en la meva recerca: la Sra. Renata Vidal, el Sr. Llorenç Anfruns, la Sra. Evangelina Avogadro, el Sr. Jordi Planas, el Sr. Xavier Cabré, el Sr. Damián Sabater, la Sra. Alba Moya i el Sr. Luís Angel Avila. Moltes gràcies companys i companyes.

Encara que repeteixi alguns noms, vull agrair als companys i companyes que hem fet pinya l'hora de dinar, compartint paelles, xoricets, cerveses, vi, rovellons, ratafia,... la sempre espectacular estrella de la faràndula Sra. Ivette Serral, el magnífic Sr. Guillem Closa, l'elegant Sr. Òscar González, el poeta i rondallaire Sr. Eduard Pla, el mestre cerveser Sr. Roger Milego, la mestra ratafiaire Sra. Sandra Saura, la parella de papes Sr. Carles Batlle i Sra. Ingrid Regalado, la bagenca i per això excelsa Sra. Ester Prat, el director d'obres mestres Sr. Abel Pau, el genial trompetista Sr. Xavi Calaf, la doctora en rialles Dra. Cristina Domingo i el meu programador de capçalera durant uns mesos, Sr. Dani Díaz. També a la colla del vint-i-u, Ruyé McLego, Williams McLosa, Michael Borland, Xavi Abdul-Khalaf, Oscar Smith i Jorge Arlauckas. Addicionalment, i amb menys temps esmerçat, a la colla del frontó, Xavier Pons, Mike Ninyerola i Gorka Muñoa.

Finalment vull agrair l'incondicional suport i afecte que sempre he rebut de la meva família. Molt especialment vull agrair a la Sra. Marta Garcia i al Sr. Josep-Ignasi Padró que sempre m'hagin tingut un plat a taula mentre jo em centrava en realitzar la Tesi, ja que sense ells ni hauria pogut fer el Grau en Geografia, ni el Màster en TD i SIG ni el Doctorat en Geografia; vosaltres vau confiar en mi en les èpoques més fosques de la meva vida i vau fer de mi algú de profit, així que us estaré eternament agraït i espero compensar algun dia tot el que heu fet per mi. A la Sra. Marta Padró i al Sr. Francesc-Josep Padró, per haver estat pacients en els meus canvis d'ànim i haver-me aferrat al dia a dia, sabent que sempre podria comptar amb vosaltres per qualsevol imprevist. Gràcies a la iaia Matilde per donar-me l'alternativa al Bingo i distreure'm cada diumenge, i també als avis que ja no hi són, la iaia Maruja, l'avi Paco i l'avi Joan per l'educació que em vau donar. Al meu tiet i la meva tieta, el Sr. Francesc Garcia i la Sra. Mercedes Rivera per tot el seu suport i savis consells. Al Sr. Fernando Elboj, pel seu desinteressat suport logístic i gastronòmic. A la Sra. Miriam Corrius Mujal, que m'ha donat tot l'amor del món per estimar la vida amb alegria, i que m'ha permès destinar el temps necessari a la realització de la Tesi sense deixar de ser feliç.

Gràcies a totes i tots per haver contribuït a la realització d'aquesta Tesi doctoral.

Millora del tractament de les imatges captades pels satèl·lits Landsat-8 i Sentinel-2 mitjançant espectroradiometria de camp i sensors embarcats en Vehicles Aeris no Tripulats (UAV)

Resum / Resumen / Abstract

Resum (català)

La irrupció tecnològica dels Vehicles Aeris no Tripulats (UAV o drons) com a noves plataformes de teledetecció, està fent evolucionar la Geografia cap a una nova escala d'observació de la Terra. Mitjançant diferents instruments de captació de dades (e.g. satèl·lits, aeronaus), actualment es poden monitoritzar i analitzar quantitativament diversos fenòmens que afecten la superfície terrestre a diferents escales, així com els seus canvis. Convencionalment, la validesa de les mesures de teledetecció satel·litària es comprova mitjançant el seu ajust respecte de mesures *in-situ* captades amb espectroradiòmetres de camp o mitjançant la inter-comparació entre sensors satel·litaris. De fet, és necessari corregir radiomètricament les imatges de satèl·lit per obtenir dades el més similars possible a les que s'obtindrien a nivell de superfície terrestre i que siguin coherents entre diferents sensors.

No obstant, encara hi ha un salt d'escala molt gran entre l'adquisició de dades de camp i les dades satel·litàries o aèries convencionals, fet que en complica la validació *in-situ*. La principal hipòtesi d'aquesta recerca és que els UAV poden omplir el buit d'escala entre imatges de satèl·lit i mesures *in-situ* convencionals, millorant així la correcció radiomètrica d'imatges satel·litàries. L'objectiu d'aquesta recerca és introduir l'ús de dades captades amb UAV, en sinergia amb dades espectroradiomètriques de camp, per complementar i millorar el tractament radiomètric de les imatges captades pels satèl·lits Landsat-8 i Sentinel-2, vinculant així observacions sobre el terreny (espectroradiometria de camp), observacions a escala local (UAV) i observacions a escala global (satèl·lits), obtenint més solidesa, continuïtat i coherència en les dades d'observació de la Terra a totes les escales.

A diferència dels satèl·lits, els drons tenen la característica de volar a molt baixa altura (e.g. menys de 120 m, segons la llei espanyola actual), de manera que les imatges captades pels seus sensors tenen molt més detall espacial (e.g. 10 cm per píxel) i pràcticament no estan influenciades per l'atmosfera. D'altra banda, les tècniques convencionals d'espectroradiometria de camp presenten dificultats operatives vinculades a la georeferenciació i remostreig espacial de les dades, la lentitud en la captura de mesures o la dificultat d'accedir a determinades cobertes del sòl. Així, la hipòtesi d'aquesta recerca contempla que l'ús de drons permet mostrejar una àrea molt més gran, de manera molt més ràpida, més sistemàtica, amb més detall i amb una més acurada georeferenciació que l'espectroradiometria de camp convencional, però amb una exactitud radiomètrica útil per als nostres propòsits de fer de pont entre les dades dels

espectroradiòmetres de mà i les dades de satèl·lit. Per aconseguir-ho, a partir d'imatges captades amb sensors a bord d'UAV i calibrades al seu torn mitjançant dades de reflectància mesurades *in-situ*, s'obtenen referències radiomètriques per validar i/o corregir imatges de satèl·lit, contribuint així a introduir una nova capa de dades entre l'escala *in-situ* i l'escala satel·litària.

En el primer capítol de l'apartat dels continguts (2.1) s'analitzen i es validen diferents mètodes de correcció radiomètrica utilitzats per imatges de satèl·lits Landsat-7, Landsat-8 i Sentinel-2, mitjançant mesures espectroradiomètriques de camp captades al moment de pas quasi-simultani de dos dels satèl·lits. La mètrica principal és el càlcul de l'arrel de la mitjana del quadrat dels errors (RMSE) entre les dades de reflectància espectral en les mesures *in-situ* i les imatges de satèl·lit corregides radiomètricament amb diferents mètodes, però també s'utilitza el càlcul de coeficients de determinació (R^2) per avaluar la coherència entre parelles d'imatges de satèl·lit captades amb pocs minuts de diferència en la mateixa àrea geogràfica. Aquesta validació és molt rellevant per a quantificar la consistència de dades captades per diferents sensors i millorar el processat de sèries temporals d'imatges. En el segon capítol de l'apartat dels continguts (2.2) s'analitzen quatre mètodes de georeferenciació d'imatges de dron. Per cada mètode s'avalua l'exactitud geomètrica quantificant les diferències amb precisió centimètrica entre el posicionament de punts de coordenades conegudes mesurades amb sistemes globals de navegació per satèl·lit (GNSS) d'alta exactitud i la seva corresponent posició en la imatge de dron, utilitzant com a indicadors d'exactitud l'RMSE planimètric (radial) (RMSEr) i l'RMSE altimètric (RMSEz). Aquest estudi contextualitza l'ús combinat d'imatges de dron i d'imatges obtingudes amb sensors aeroportats o satel·litaris des d'un punt de vista geomètric, alhora que proporciona dades precises dels límits de cada mètode de georeferenciació. En el tercer capítol de l'apartat dels continguts (2.3) es presenta el procés mitjançant el qual s'utilitzen dades de radiometria de camp per corregir radiomètricament imatges captades amb drons, per posteriorment utilitzar-les com a referències per validar diferents mètodes de correcció radiomètrica d'imatges Landsat-8 i Sentinel-2. També s'utilitzen les dades de dron com a referència radiomètrica per corregir radiomètricament les imatges de satèl·lit, objectiu principal de la tesi. En el quart capítol de l'apartat dels continguts (2.4) s'aplica l'ús d'imatges de dron, corregides mitjançant dades d'espectroradiometria de camp, en la generació de cartografia temàtica de cobertes del sòl. L'aplicació dóna suport al monitoratge de la restauració en explotacions mineres a cel obert, una important tasca per a la recuperació ambiental d'aquests espais.

En els resultats del capítol 2.1, les diferències entre les dades de reflectància espectral *in-situ* i les imatges de satèl·lit corregides radiomètricament amb el mètode que obté millors resultats, ofereixen un RMSE mitjà considerant totes les bandes espectrals del 3.486 % (en reflectància); en tots els mètodes provats hi ha un R^2>0.929 entre parelles d'imatges de satèl·lit captades amb pocs minuts de diferència en la mateixa àrea geogràfica, també considerant totes les bandes. Els resultats del capítol 2.2 mostren les diferents exactituds de cadascun dels mètodes provats per a la georeferenciació d'imatges de dron, a més d'una avaluació dels recursos econòmics, de temps i de personal que requereix cada mètode, obtenint en el millor dels casos (mitjançant georeferenciació indirecta) un RMSEr≤0.023 m i un RMSEz≤0.030 m. Els resultats del capítol 2.3 mostren l'ajust de les dades de radiometria de camp amb les dades de dron (R^2>0.946) i d'aquestes amb les dades de satèl·lit. Posteriorment s'avalua l'ajust (en reflectància) entre àrees de test i la correcció radiomètrica d'imatges de satèl·lit utilitzant dades del dron com a referència radiomètrica (RMSEvis≤2.018 %), així com la coherència de les imatges del Landsat-8 i del Sentinel-2 corregides amb aquest mètode (RMSEvis≤1.147 %). Els resultats relatius al capítol 2.4 no només proporcionen la representació cartogràfica de la restauració en l'explotació minera, sinó que també forneixen dades estadístiques sobre l'extensió relativa de cada tipus de coberta, i han permès d'elaborar un protocol pensat per ser útil a l'administració, als propietaris d'explotacions mineres i, en general, a la recuperació mediambiental d'espais altament degradats.

En conclusió, en aquesta Tesi es fa una anàlisi de diversos mètodes de correcció radiomètrica d'imatges de satèl·lit i es validen mitjançant dades espectroradiomètriques de camp, però, addicionalment, es millora el tractament radiomètric de les dades satel·litàries mitjançant la introducció de dades captades amb drons. El mètode innova amb l'establiment de sinergies entre dades de radiometria de camp, dades de dron i dades satel·litàries, vinculant diferents escales de treball d'una manera eficient i millorada respecte els antecedents. En futures recerques, es preveu aplicar el mètode desenvolupat però utilitzant sensors per drons amb una configuració espectral més ajustada a la configuració dels sensors satel·litaris, i també fent vols coordinats de diversos drons al moment de pas dels satèl·lits. S'albira que aquesta recerca contribuirà a obtenir sèries temporals d'imatges molt més coherents que les obtingudes fins ara, assolint una informació més acurada de l'estat i l'evolució d'àrees protegides d'alt interès ecosistèmic local i global en tot el planeta.

Resumen (castellano)

La irrupción tecnológica de los Vehículos Aéreos no Tripulados (UAV o drones) como nuevas plataformas de teledetección, está haciendo evolucionar la Geografía hacia una nueva escala de observación de la Tierra. Mediante diferentes instrumentos de captación de datos (p. ej. satélites, aeronaves), actualmente se pueden monitorizar y analizar cuantitativamente varios fenómenos que afectan la superficie terrestre a diferentes escalas, así como sus cambios. Convencionalmente, la validez de las medidas de teledetección satelital se comprueba mediante su ajuste respecto de medidas *in-situ* captadas con espectrorradiómetros de campo o mediante la inter-comparación entre sensores satelitales. De hecho, es necesario corregir radiométricamente las imágenes de satélite para obtener datos lo más similares posible a los que se obtendrían a nivel de superficie terrestre y que sean coherentes entre diferentes sensores.

Sin embargo, todavía hay un salto de escala muy grande entre la adquisición de datos de campo y los datos satelitales o los datos aéreos convencionales, lo que complica la validación *in-situ*. La principal hipótesis de esta investigación es que los UAV pueden llenar el hueco de escala existente entre las imágenes de satélite y las medidas *in-situ* convencionales, mejorando así la corrección radiométrica de imágenes satelitales. El objetivo de esta investigación es introducir el uso de datos captados con UAV, en sinergia con datos espectroradiométricos de campo, para complementar y mejorar el tratamiento radiométrico de las imágenes captadas por los satélites Landsat-8 y Sentinel-2, vinculando así observaciones sobre el terreno (espectrorradiometría de campo), observaciones a escala local (UAV) y observaciones a escala global (satélites), obteniendo más solidez, continuidad y coherencia en los datos de observación de la Tierra en todas las escalas.

A diferencia de los satélites, los drones tienen la característica de volar a muy baja altura (p. ej. menos de 120 m, según la ley española actual), de modo que las imágenes captadas por sus sensores tienen mucho más detalle espacial (p. ej. 10 cm por píxel) y prácticamente no están influenciadas por la atmósfera. Por otra parte, las técnicas convencionales de espectrorradiometría de campo presentan dificultades operativas vinculadas a la georreferenciación y remuestreo espacial de los datos, la lentitud en la toma de medidas o la dificultad de acceder a determinadas cubiertas del suelo. Así, la hipótesis de esta investigación contempla que el uso de drones permite muestrear un área mucho mayor, de manera mucho más rápida, más sistemática, con más detalle y con una más cuidadosa georreferenciación que la espectrorradiometría de campo convencional, pero con una exactitud radiométrica útil para nuestros propósitos de hacer de puente

entre los datos de los espectrorradiómetros de mano y lo datos satelitales. Para ello, a partir de imágenes captadas con sensores a bordo de UAV y calibradas a su vez mediante datos de reflectancia medidos *in-situ*, se obtienen referencias radiométricas para validar y/o corregir imágenes de satélite, contribuyendo así a introducir una nueva capa de datos entre la escala *in-situ* y la escala satelital.

En el primer capítulo del apartado de los contenidos (2.1) se analizan y se validan diferentes métodos de corrección radiométrica utilizados para imágenes de satélites Landsat-7, Landsat-8 y Sentinel-2, mediante medidas espectrorradiométricas de campo captadas al momento de paso casi-simultáneo de dos de los satélites. La métrica principal es el cálculo de la raíz de la media del cuadrado de los errores (RMSE) entre los datos de reflectancia espectral *in-situ* y las imágenes de satélite corregidas radiométricamente con diferentes métodos, pero también se utiliza el cálculo de coeficientes de determinación (R^2) para evaluar la coherencia entre parejas de imágenes de satélite captadas con pocos minutos de diferencia en la misma área geográfica. Esta validación es muy relevante para cuantificar la consistencia de datos captados por diferentes sensores y mejorar el procesado de series temporales de imágenes. En el segundo capítulo del apartado de los contenidos (2.2) se analizan cuatro métodos de georreferenciación de imágenes de dron. Por cada método se evalúa la exactitud geométrica cuantificando las diferencias con precisión centimétrica entre el posicionamiento de puntos de coordenadas conocidas medidas con sistemas globales de navegación por satélite (GNSS) de alta exactitud y su correspondiente posición en la imagen de dron, con indicadores de exactitud como el RMSE planimétrico (radial) (RMSEr) y RMSE altimétrico (RMSEz). Este estudio contextualiza el uso combinado de imágenes de dron e imágenes obtenidas con sensores aeroportados o satelitales desde un punto de vista geométrico, a la vez que proporciona datos precisos de los límites de cada método de georreferenciación. En el tercer capítulo del apartado de los contenidos (2.3) se presenta el proceso mediante el que se utilizan datos de radiometría de campo para corregir radiométricamente imágenes captadas con drones, para posteriormente utilizarlas como referencias para validar diferentes métodos de corrección radiométrica de imágenes Landsat-8 y Sentinel-2. También se utilizan los datos de dron como referencia radiométrica para corregir radiométricamente las imágenes de satélite, objetivo principal de la tesis. En el cuarto capítulo del apartado de los contenidos (2.4) se aplica el uso de imágenes de dron, corregidas mediante datos de espectrorradiometría de campo, en la generación de cartografía temática de cubiertas del suelo. La aplicación apoya el monitoreo de restauraciones en explotaciones mineras a cielo abierto, una importante tarea para la recuperación ambiental de estos espacios.

En los resultados del capítulo 2.1, las diferencias entre los datos de reflectancia espectral *in-situ* y las imágenes de satélite corregidas radiométricamente con el método que obtiene mejores resultados, ofrecen un RMSE medio considerando todas las bandas espectrales del 3.486 % (en reflectancia); en todos los métodos probados hay un R^2>0.929 entre parejas de imágenes de satélite captadas con pocos minutos de diferencia en la misma área geográfica, también considerando todas las bandas. Los resultados del capítulo 2.2 muestran las diferentes exactitudes de cada uno de los métodos probados para la georreferenciación de imágenes de dron, además de una evaluación de los recursos económicos, de tiempo y de personal que requiere cada método, obteniendo en el mejor de los casos (mediante georreferenciación indirecta) un RMSEr≤0.023 m y un RMSEz≤0.030 m. Los resultados del capítulo 2.3 muestran el ajuste de los datos de radiometría de campo con los datos de dron (R^2>0.946) y de éstas con los datos de satélite. Posteriormente se evalúa el ajuste (en reflectancia) entre áreas de test y la corrección radiométrica de imágenes de satélite utilizando datos del dron como referencia radiométrica (RMSEvis≤2.018 %), así como la coherencia de las imágenes del Landsat-8 y del Sentinel-2 corregidas con este método (RMSEvis≤1.147 %). Los resultados relativos al capítulo 2.4 no sólo proporcionan la representación cartográfica de la restauración en la explotación minera, sino que también proveen datos estadísticos sobre la extensión relativa de cada tipo de cubierta, y han permitido elaborar de un protocolo pensado para ser útil a la administración, a los propietarios de explotaciones mineras y, en general, a la recuperación medioambiental de espacios altamente degradados.

En conclusión, en esta Tesis se hace un análisis de diversos métodos de corrección radiométrica de imágenes de satélite y se validan mediante datos espectroradiométricos de campo, pero, adicionalmente, se mejora el tratamiento radiométrico de los datos satelitales mediante la introducción de datos captados con drones. El método innova con el establecimiento de sinergias entre datos de radiometría de campo, datos de dron y datos satelitales, vinculando diferentes escalas de trabajo de una manera eficiente y mejorada respecto a los antecedentes. En futuras investigaciones, se prevé aplicar el método desarrollado pero utilizando sensores para drones con una configuración espectral más ajustada a la configuración de los sensores satelitales, y también haciendo vuelos coordinados de varios drones al momento de paso de los satélites. Se vislumbra que esta investigación contribuirá a obtener series temporales de imágenes mucho más coherentes que las obtenidas hasta ahora, logrando una información más detallada del estado y la evolución de áreas protegidas de alto interés ecosistémico local y global en todo el planeta.

Abstract (English)

The technological breakthrough of Unmanned Aerial Vehicles (UAV or drones) as new remote sensing platforms is making Geography evolve towards a new scale of Earth observation. By using different data capture instruments (e.g. satellites, aircrafts), several phenomena that affect the Earth's surface as well as its changes, can currently be monitored and analyzed quantitatively at different scales. Conventionally, the validity of the satellite remote sensing measures is checked by the fitting to *in-situ* measurements captured with field spectrometers or by inter-comparison between satellite sensors. In fact, it is necessary to radiometrically correct the satellite images to obtain the most similar data to those that would be obtained at ground level and, moreover, to obtain coherent data between different satellite sensors.

However, there is still a very large-scale gap between the acquisition of field data and satellite data or manned airborne data, which complicates the *in-situ* validation. The main hypothesis of this research is that the UAV can fill the gap between satellite images and conventional *in-situ* measurements, thus improving the radiometric correction of satellite imagery. The aim of this research is to introduce the use of data captured with UAV, in synergy with field spectroradiometric data, to complement and improve the radiometric treatment of the images captured by the Landsat-8 and Sentinel-2 satellites, linking field observations (field spectroradiometry), observations at the local scale (UAV) and observations at the global scale (satellites), obtaining more solidity, continuity and coherence in the Earth observation data at all scales.

Unlike satellites, drones have the characteristic of flying at a very low altitude (e.g. less than 120 m, in compliance with current drone regulations in Spain), so that the images captured by their sensors have much more spatial detail (e.g. 10 cm per pixel) and are practically not influenced by the atmosphere. On the other hand, the conventional techniques of field spectroradiometry present operational difficulties linked to data georeferencing and spatial resampling, the slowness on the capture of measures or the difficulty of accessing certain land covers. Thus, the hypothesis of this research considers that the use of drones allows sampling a much larger area, much faster, more systematically, in more detail and with a more accurate georeferencing than conventional field spectroradiometry, but with a radiometric accuracy useful for our purposes of filling the gap between the field spectroradiometric data and the satellite data. To achieve this goal, from images captured with sensors on board of UAV and calibrated in turn by means of *in-situ* measured reflectance data, radiometric references are obtained to validate

and/or correct satellite images, contributing towards introducing a new data layer between the *in-situ* scale and the satellite scale.

In the first chapter of the contents section (2.1), different radiometric correction methods for images of Landsat-7, Landsat-8 and Sentinel-2 satellites are analyzed and validated by means of spectroradiometric field measurements captured at almost simultaneously overpass of two of the satellites. The main metric is the calculation of the root mean square error (RMSE) between the *in-situ* spectral reflectance and satellite images radiometrically corrected with different methods; the calculation of the coefficient of determination (R^2) is also used to evaluate the coherence between pairs of satellite images captured with a few minutes of difference in the same geographical area. This validation is crucial for quantifying the consistency of data captured by different sensors and improving the processing of satellite image time series. In the second chapter of the contents section (2.2), four drone imagery georeferencing methods are analyzed. For each method, the geometric accuracy is evaluated by quantifying the centimetric differences between the positioning of point coordinates measured with high accuracy Global Navigation Satellite System (GNSS) receivers and its corresponding position in the drone image with accuracy indicators, such as the planimetry (radial) RMSE (RMSEr) and the altimetry RMSE (RMSEz). This study contextualizes the combined use of drone images and images obtained with airborne or satellite sensors from a geometric point of view, while providing accurate data on the limits of each georeferencing method. The third chapter of the contents section (2.3) focuses on the process by which field radiometry data is used to radiometrically correct images captured with drones, so that said data can be later used as references to validate different radiometric correction methods of Landsat-8 and Sentinel-2 imagery. The drone data is also used as radiometric reference to radiometrically correct the satellite images, which is the main objective of the PhD thesis. In the fourth chapter of the contents section (2.4), drone images corrected with *in-situ* field spectroradiometric data are applied to generate land cover thematic maps. The application supports the monitoring of restorations undertaken in open-pit mining excavations, which represents an important task in the environmental recovery and conservation of these spaces.

In the results of chapter 2.1, the differences between the *in-situ* spectral reflectance data and the radiometrically corrected satellite images with the method that obtains the best results offer an average RMSE, considering all the spectral bands, of 3.486 % (in reflectance); in all tested methods, there is an R^2>0.929 between pairs of satellite images

captured with a few minutes difference in the same geographical area, which also consider all the bands. The results of chapter 2.2 show the different accuracies of each of the tested methods for drone imagery georeferencing as well as an evaluation of the economic, time and personnel resources required for each method, thereby obtaining, in the best case, (through indirect georeferencing) an RMSEr≤0.023 m and a RMSEz≤0.030 m. The results of chapter 2.3 show the fitting of the field radiometry data with the drone data (R^2>0.946) and these with the satellite data. Subsequently, it is evaluated the fitting (in reflectance) between test areas and the radiometric correction of satellite images using drone data as a radiometric reference (RMSEvis≤2.018 %), as well as the coherence of the Landsat-8 and Sentinel-2 images corrected with this method (RMSEvis≤1.147 %). The results related to chapter 2.4 provide not only the cartographic representation of the open-cast mine restoration, but also the statistical data on the relative extension of each land cover, and involved developing a protocol that could be useful for legislators, owners of mining operations and, generally, the environmental recovery of highly degraded spaces.

In conclusion, this PhD thesis not only analyzes several radiometric correction methods of satellite images that are validated using field spectroradiometric data but also it supports measures for improving radiometric treatment of satellite data by introducing data captured with drones. The method innovates by establishing synergies between field spectroradiometric data, drone data and satellite data, linking different geographical scales in an efficient and improved way with respect to the antecedents. Future research will focus on applying the developed method by using drone-embedded sensors with spectral settings that better fits the satellite sensors features, and planning coordinated flights of several drones at the satellite overpass. This research will contribute towards obtaining more coherent image time series than in previous works, by achieving more accurate information on the state and the evolution of protected areas of high local and global ecosystem interest throughout the planet.

Capítol 1: Introducció i objectius

1.1. Introducció

L'observació de la Terra mitjançant teledetecció és una font de dades fonamental per monitoritzar i analitzar quantitativament diversos fenòmens que afecten a la superfície terrestre [Díaz-Delgado et al., 2018]. Així, la teledetecció contribueix a la conservació del medi ambient i l'assoliment de l'objectiu d'un desenvolupament sostenible de la societat [Nacions Unides, 2018]. Per definició, la teledetecció és una ciència que es basa en l'obtenció de dades d'un objecte d'estudi sense entrar en contacte directe amb ell [Pons i Arcalís, 2012], és a dir, utilitza tècniques no invasives. Per aconseguir-ho, habitualment s'utilitzen sensors que capten radiació electromagnètica, malgrat que també n'hi ha des sensibles a ones sonores o gravitacionals. Existeixen sensors actius i sensors passius [Lillesand et al., 2008]: els sensors actius emeten la seva pròpia energia i en mesuren la intensitat reflectida per la superfície, com és el cas del sonar, el radar o el lidar; els sensors passius en canvi, mesuren l'energia emesa pel propi objecte d'estudi en qüestió, com en el cas de la mesura de la temperatura de la superfície terrestre, o l'energia emesa per una font externa (típicament la solar) i que és reflectida per la superfície terrestre, com en el cas de la reflectància de la superfície terrestre [Chuvieco, 2008]. Aquesta Tesi s'emmarca en el tractament de dades captades per sensors passius sensibles a l'energia solar reflectida per la superfície terrestre.

La radiació electromagnètica és l'emissió i propagació d'energia sense necessitat d'un suport material. Segons la teoria ondulatòria, l'energia electromagnètica es propaga a la velocitat de la llum en forma d'ones electromagnètiques. Les ones es caracteritzen per la seva freqüència (Hz) i la seva longitud d'ona (m), que determinen l'energia que poden transportar. Fonamentalment, com més alta és la freqüència més curta és la longitud d'ona i més energia és capaç de transportar la radiació, i a la inversa. L'espectre electromagnètic és el conjunt de totes les radiacions electromagnètiques, des dels raigs gamma (longitud d'ona més curta) fins a les ones de radio i televisió (longitud d'ona més llarga). Convencionalment, l'espectre electromagnètic es divideix en diferents regions en funció de la longitud d'ona (o de la freqüència). En teledetecció ambiental se sol treballar amb dades captades en les regions espectrals ubicades entre la regió espectral de l'ultraviolat (UV) i la regió espectral de les microones (MW), longituds d'ona compreses entre 10 nm i 1 m, aproximadament. En aquesta Tesi es fan servir dades captades per sensors passius sensibles a longituds d'ona entre els 0.4 μm i els 2.5 μm, una part de l'espectre electromagnètic coneguda com a regió de l'espectre solar (Figura 1), essent les longituds d'ona en què es concentra gran part de l'energia que arriba a la Terra procedent del Sol.

Figura 1: Esquema de l'espectre electromagnètic, ampliant la regió de l'espectre solar, ja que és d'on provenen les dades de teledetecció utilitzades en aquesta Tesi. Adaptació del lloc web educacional de l'Agència Europea de l'Espai (http://sci.esa.int/education/50368-the-electromagnetic-spectrum/).

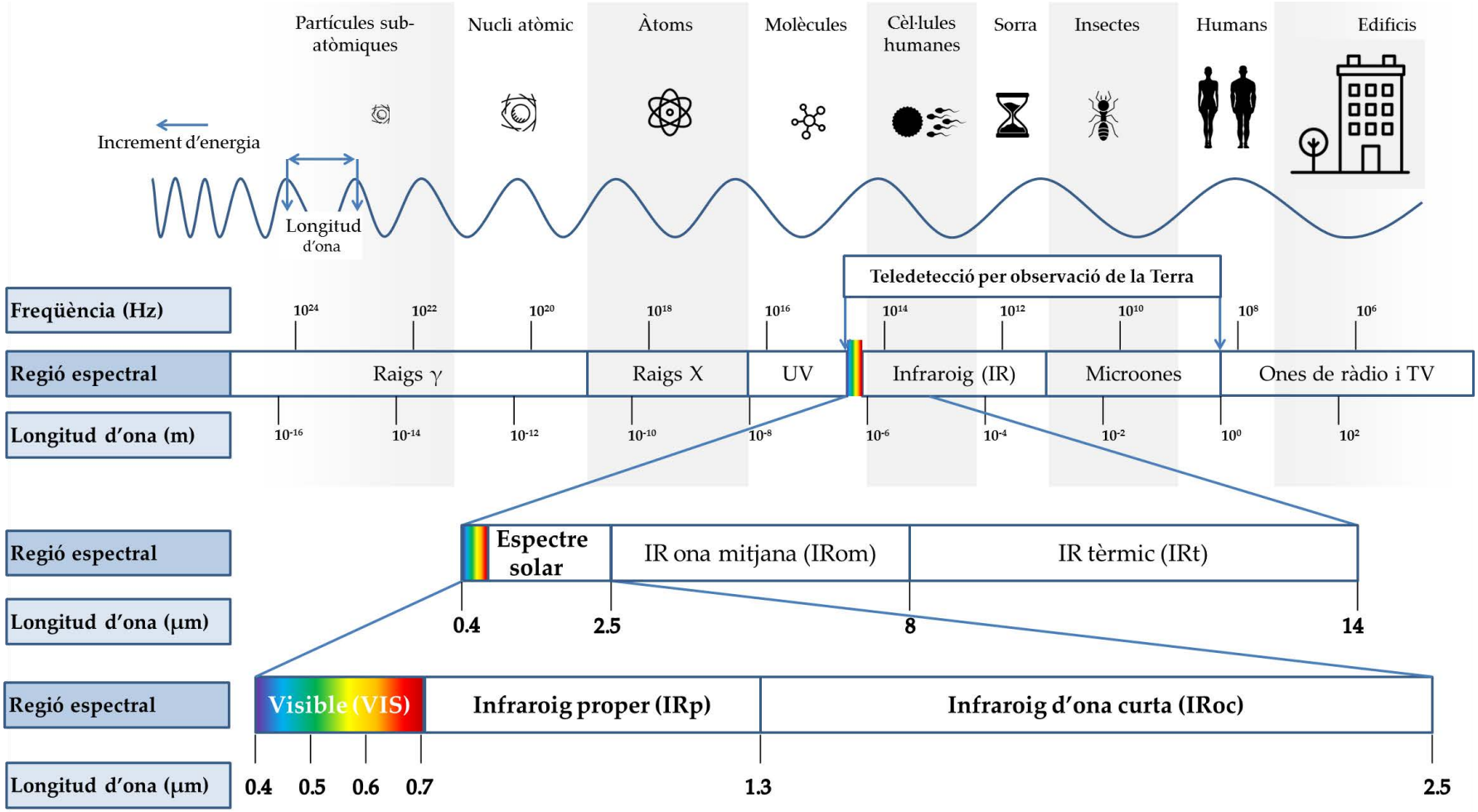

Les lleis físiques fonamentals que relacionen l'energia i la longitud d'ona són la Llei de desplaçament Wien i la Llei de Planck, crucials per a establir la configuració espectral dels sensors utilitzats en teledetecció. Segons la Llei de desplaçament de Wien, hi ha una relació inversa entre la temperatura absoluta d'un cos negre i la longitud d'ona on es troba la màxima energia radiativa que emet. Seguint la llei de Wien, un cos a la temperatura aproximada del Sol (5900 K) emet el màxim de radiació a una longitud d'ona entre els 0.4 μm i els 0.7 μm aproximadament, regió espectral coneguda com a visible (VIS); en canvi, emet progressivament menys energia en longituds d'ona més curtes, com l'UV entre 0.01 μm i 0.4 μm, i més llargues, com a infraroig proper (IRp) entre els 0.7 μm i els 1.3 μm o l'infraroig d'ona curta (IRoc) entre els 1.3 μm i els 2.5 μm. En l'infraroig d'ona mitjana (IRom), entre els 2.5 μm i els 8 μm, l'energia solar ja és molt més feble i es confon amb l'emesa per la pròpia Terra, ja que un cos a la temperatura mitjana aproximada de la Terra (300 K) emet el màxim de radiació en una longitud d'ona més llarga (entre els 8 μm i els 14 μm aproximadament), regió espectral coneguda com a infraroig tèrmic (IRt). Segons la Llei de Planck, l'energia radiativa emesa per un cos negre augmenta amb la temperatura de manera que, a una certa temperatura, el cos té el punt de màxima radiació a longituds d'ona més curtes com més alta és la temperatura fixada. Aleshores, per un cos negre a la temperatura del Sol és possible calcular l'energia teòrica que arriba a la part superior de l'atmosfera terrestre (Top Of Atmosphere (TOA) en anglès). Addicionalment, hi ha estudis que han permès mesurar empíricament la irradiància que arriba a la part superior de l'atmosfera [Chance i Kurucz, 2010]. Cal tenir en compte que l'energia solar que arriba a la part superior de l'atmosfera no és la que acaba arribant a la superfície (Bottom Of Atmosphere (BOA)), ja que diversos gasos, partícules, etc, de l'atmosfera interfereixen l'energia en determinades longituds d'ona (e.g. ozó (O_3) en l'UV) i a més l'atmosfera és més densa a nivell de mar que a més altitud. Actualment es disposa de models de transferència radiativa, com el MODerate resolution atmospheric TRANsmission (MODTRAN 5) [Berk et al., 2014] que permeten calcular la transmitància atmosfèrica en condicions típiques a diferents altituds.

En el marc de la teledetecció ambiental s'utilitzen diverses magnituds físiques relacionades amb l'energia electromagnètica (Taula 1). Específicament, dins la teledetecció que utilitza sensors passius en la regió de l'espectre solar, possiblement una de les magnituds físiques més interessant és la reflectància superficial espectral (ρs_λ), que es pot definir com la proporció de flux radiant reflectit per una superfície respecte del flux radiant incident, en una determinada longitud d'ona [Nicodemus et al., 1977]. De fet, la reflectància de la superfície és una variable essencial per caracteritzar els tipus principals

de cobertes terrestres amb la màxima exactitud [Milton et al., 2009]. La informació espectral permet cartografiar superfícies, la salut dels conreus, la salut dels boscos, la contaminació de les aigües o els canvis en les cobertes del sòl, entre moltes altres aplicacions.

Taula 1: Magnituds físiques de base vinculades a la teledetecció mitjançant sensors passius sensibles a l'espectre solar.

Magnitud física	Descripció	Unitat	Símbol
Energia radiant espectral	Energia transportada per la radiació electromagnètica per longitud d'ona.	$J \cdot \mu m^{-1}$	Q_λ o E_λ
Flux radiant espectral	Energia radiada, transportada o rebuda en la unitat de temps i per longitud d'ona.	$W \cdot \mu m^{-1}$	Φ_λ o F_λ
Intensitat radiant espectral	Flux energètic emès per una font puntual per unitat d'angle sòlid en una direcció donada i per longitud d'ona.	$W \cdot sr^{-1} \cdot \mu m^{-1}$	I_λ
Radiància espectral	Flux energètic per unitat d'angle sòlid que es radia des d'una font superficial en una direcció donada, per unitat de superfície aparent de la font en aquella direcció i per longitud d'ona.	$W \cdot m^{-2} \cdot sr^{-1} \cdot \mu m^{-1}$	L_λ
Irradiància espectral	Flux radiant rebut per unitat de superfície d'un receptor i per longitud d'ona.	$W \cdot m^{-2} \cdot \mu m^{-1}$	S_λ o E_λ
Reflectància espectral	Quocient entre el flux radiant reflectit per una superfície i el flux radiant incident, per longitud d'ona.	Adimensional (típicament entre 0 i 1, o en %)	R_λ o ρ_λ
Transmitància espectral	Quocient entre el flux energètic transmès per un material o una superfície plana oposats a la radiació incident i el flux energètic incident, per longitud d'ona.	Adimensional (típicament entre 0 i 1, o en %)	τ_λ

Font: Diccionari terminològic de teledetecció [Pons i Arcalís, 2012].

En base als principis físics descrits, l'energia emesa pel Sol i que arriba a la superfície de Terra i és posteriorment reflectida per la seva superfície, és una font de dades per la teledetecció orientada a l'observació terrestre. Però hi ha unes longituds d'ona concretes on la radiació solar penetra més fàcilment l'atmosfera, conegudes com a finestres atmosfèriques, i longituds d'ona on la radiació solar no la penetra amb la mateixa facilitat, conegudes com a parets atmosfèriques. La configuració espectral dels sensors satel·litaris està fortament condicionada per aquestes regions espectrals, de tal manera que per captar radiació solar reflectida per la superfície terrestre es construeixen sensors sensibles en les bandes espectrals on hi ha finestres atmosfèriques (Figura 2).

Figura 2: Irradiància solar teòrica d'un cos negre a 5900 K (línia taronja), irradiància solar proporcionada per Chance i Kurucz al sostre de l'atmosfera (línia groga), transmitància atmosfèrica calculada amb MODTRAN 5 considerant una atmosfera estàndard continental a latituds mitjanes i a nivell de mar (línia blava) i resultat d'aplicar la transmitància a la irradiància de Chance i Kurucz, és a dir, irradiància solar estimada a nivell de mar (línia blanca).

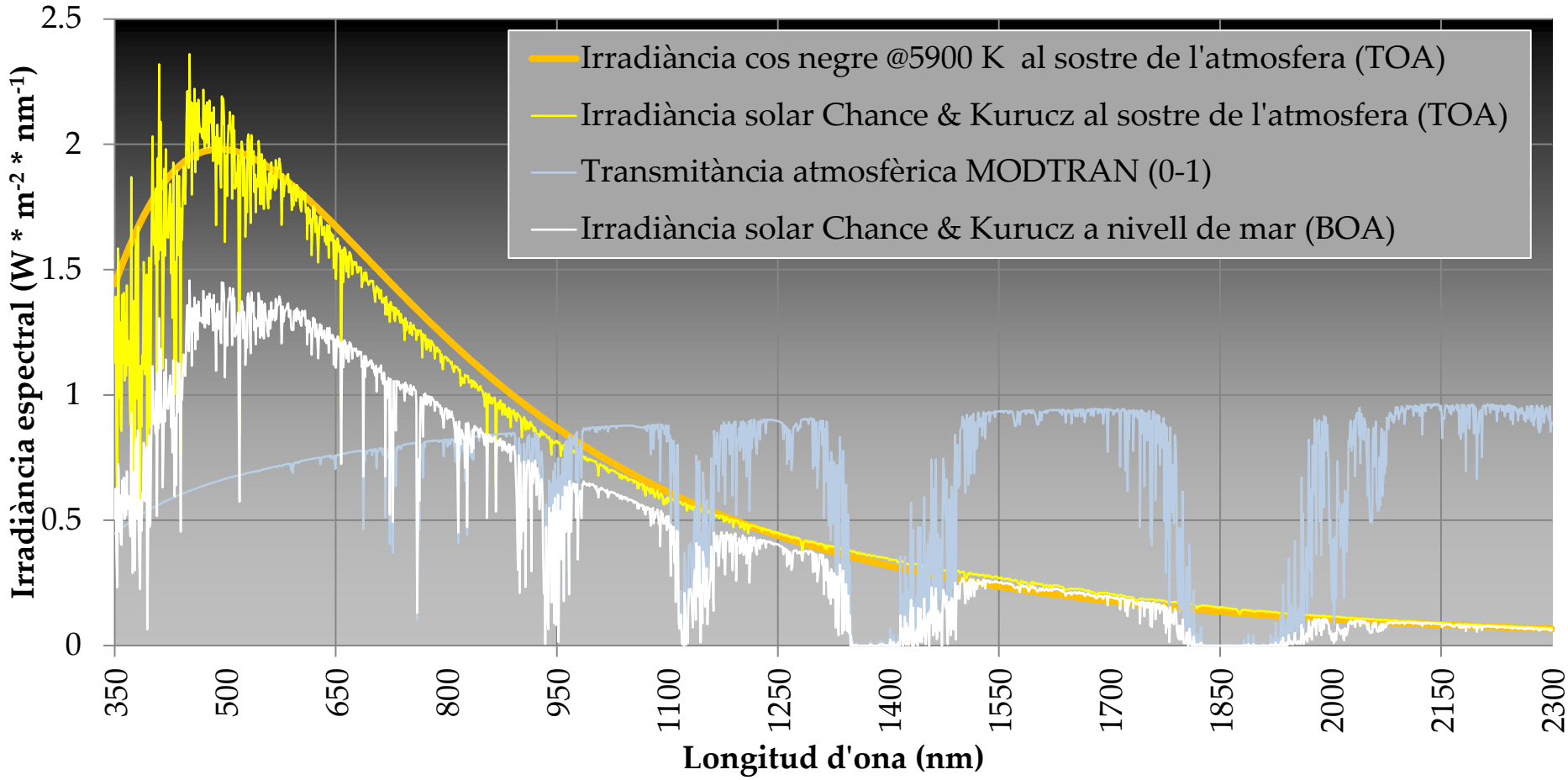

Els sensors de teledetecció poden estar ubicats en molts tipus de plataformes (satèl·lits, globus, aeronaus, vaixells, portats per humans,...), que abasten diverses escales de treball. En aquesta Tesi s'utilitzen dades d'instruments satel·litaris a bord dels satèl·lits Landsat-8 i Sentinel-2 (escala global), Vehicles Aeris no Tripulats (UAV) (escala local) i espectroradiòmetres de camp (escala *in-situ*). Amb la finalitat de millorar la radiometria de les dades satel·litàries mitjançant la correcció dels efectes atmosfèrics, s'introdueixen dades captades amb sensors portats en UAV i calibrats mitjançant dades espectroradiomètriques de camp, de tal manera que les dades satel·litàries s'ajustin millor a les dades captades a escala local i *in-situ*. És per això que a continuació es presenta una visió sinòptica dels mitjans de teledetecció en aquestes tres escales.

1.2. Imatges procedents de satèl·lit (Landsat-8 i Sentinel-2)

La teledetecció mitjançant satèl·lits n'inclou de situats en diverses òrbites terrestres. Els geostacionaris, com per exemple els satèl·lits meteorològics Meteosat (Meteorological Satellite) [EUMETSAT, 2018], estan en òrbites terrestres altes, a uns 35786 km de la superfície de la Terra, ja que a aquella distància es pot orbitar a la mateixa velocitat angular que la Terra en el pla equatorial i es pot observar una part del planeta constantment des del mateix punt de vista. Els situats en òrbites terrestres mitjanes, com els satèl·lits de sistemes de posicionament i navegació globals (GNSS) com el GPS o el GALILEO [GPS, 2018; ESAa, 2018], orbiten en diferents plans orbitals entre els 5000 km i els 25000 km. Els satèl·lits d'observació de recursos naturals estan situats en òrbites baixes, entre els 160 km i els 1000 km. Els satèl·lits d'òrbita baixa tenen un període orbital d'uns 90 minuts, i els que porten instruments òptics segueixen una òrbita polar heliosíncrona entre 600 km i 1000 km, com els de les missions Landsat [NASAa, 2018] i Sentinel-2 [ESAb, 2018], comportant que el satèl·lit passa per cada latitud aproximadament a la mateixa hora solar i, per tant, la il·luminació és similar, facilitant la interpretació de les imatges. La cobertura global que ofereixen les plataformes satel·litàries les fa inigualables respecte altres tipus de plataformes, tant en termes de resolució temporal com de productivitat, ja que malgrat ser molt cares, el preu per hectàrea mostrejada és molt baix. Un altre dels avantatges de la teledetecció orbital és la multitemporalitat, molt important tant des del punt de vista de seguiment diari (per exemple, de freqüència cada 15 minuts en imatges meteorològiques), setmanal o mensual (aplicat a cultius), com des del punt de vista interanual (registre històric coherent al llarg de desenes d'anys), clau per a la comprensió de fenòmens naturals o antropogènics [Pons i Arcalís, 2012] (Figura 3).

Figura 3: Òrbites habituals dels satèl·lits d'Observació de la Terra. Noti's que els satèl·lits Landsat-8 i Sentinel-2 orbiten en òrbita baixa, polar i heliosíncrona.

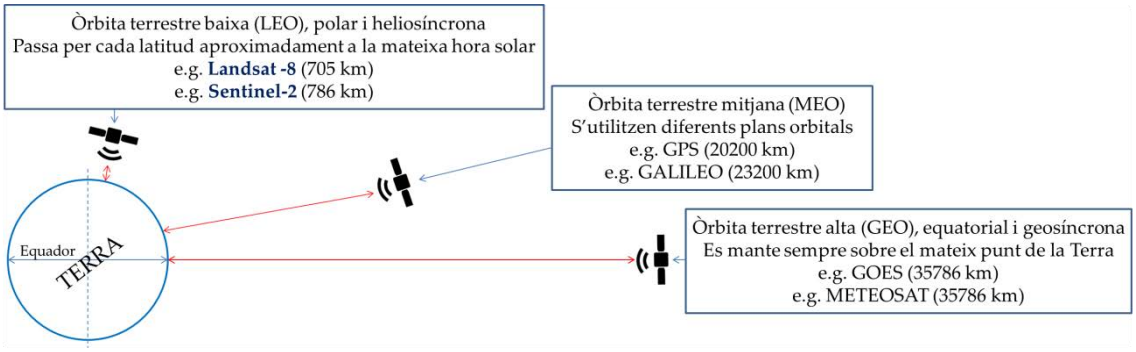

Per tal maximitzar beneficis científics, socials i econòmics, les diverses agències espacials d'arreu del món col·laboren a través d'iniciatives com el Sistema Global de Sistemes d'Observació de la Terra (Global Earth Observation System of Systems, GEOSS)) [GEOSS, 2018]. A GEOSS hi participen, entre altres, la National Aeronautics and Space Administration (NASA) i l'Agència Europea de l'Espai (ESA), aportant imatges multiespectrals d'alta resolució espacial en el marc dels programes Landsat Data Continuity Mission (LDCM) [NASAa, 2018] i Copernicus Sentinel-2 (S2) [Copernicus, 2018], respectivament (Figura 4). Un dels conjunts d'imatges satel·litàries d'alta resolució espacial més longeus és el programa Landsat. A través de la LDCM s'han adquirit imatges des de l'any 1972. La continuïtat de les dades adquirides durant aquests més de 40 anys, implica l'ús de diferents sensors (Multispectral Scanner System (MSS), Thematic Mapper (TM), Enhanced Thematic Mapper Plus (ETM+) i Operational Land Imager (OLI)), tots ells sensibles a la regió solar de l'espectre electromagnètic. La LDCM també inclou la càmera Return Beam Vidicon (RBV), bandes tèrmiques (a l'MSS del Landsat-3 i als TM/ETM+), i sensors tèrmics (Thermal Infrared Sensor, TIRS al Landsat-8), que estan fora de focus d'aquesta Tesi. Actualment s'adquireixen imatges a partir de l'ETM+, a bord del Landsat-7, que disposa de 6 bandes òptiques, i de l'OLI, a bord del Landsat-8, que disposa de 9 bandes òptiques amb una funció de resposta espectral relativa (RSRF) més optimitzada que els sensors LDCM previs (Figura 5). El programa europeu Copernicus complementa el programa Landsat i dóna continuïtat al programa francès SPOT [ESAc, 2018]. El sensor Multispectral Imager (MSI) (Figura 6), amb 13 bandes òptiques, a bord dels dos satèl·lits Sentinel-2, proporciona imatges des de 2015 (Sentinel-2A) i 2017 (Sentinel-2B) [ESAb, 2018], amb característiques espectrals, temporals i espacials millorades respecte de la sèrie LDCM, però específicament dissenyades per donar suport i continuïtat al programa Landsat [ESAc, 2018; Drusch et al., 2012].

Figura 4: Característiques bàsiques dels sensors de l'espectre solar de les missions Landsat i de la missió Sentinel-2. MSS: Multispectral Scanner System; TM: Thematic Mapper; ETM+: Enhanced Thematic Mapper Plus; OLI: Operatinal Land Imager; MSI: Multispectral Imager; RBV: Return Beam Vidicon; TIRS: Thermal Infrared Sensor; WRS: Worldwide Reference System; MGRS: Military Grid REference System; NASA: National Aeronautics and Space Administration; NOAA: National Oceanic and Atmospheric Administration; USGS: United States Geologial Survey; ESA: European Space Agency.

	Landsat-1	Landsat-2	Landsat-3	Landsat-4	Landsat-5	Landsat-6	Landsat-7	Landsat-8	Sentinel-2A	Sentinel-2B
Llançament Decomissió	23/07/1972 06/01/1978	22/01/1975 27/07/1983	05/03/1978 07/11/1983	16/07/1982 01/06/2001	01/03/1984 15/01/2013	05/10/1993 05/10/1993	15/04/1999	11/02/2013	23/06/2015	07/03/2017
Nom sensor espectre solar	MSS	MSS	MSS	TM	TM	ETM	ETM+	OLI	MSI	MSI
Altres sensors de TD	RBV (vídeo)	RBV (vídeo)	RBV (vídeo)	MSS	MSS		ETM+ (IRt)	TIRS (IRt)		
Resolució temporal (dies)	18	18	18	16	16		16	16	10	10
Alçada òrbita (km)	907	908	915	705	705		705	705	786	786
Nombre d'òrbites Sistema de tesselat	251 WRS-1	251 WRS-1	251 WRS-1	233 WRS-2	233 WRS-2		233 WRS-2	233 WRS-2	143 MGRS	143 WRS-2
Operador	NASA	NASA	NASA	NOAA	NOAA	NOAA	NOAA	NASA | USGS	ESA	ESA

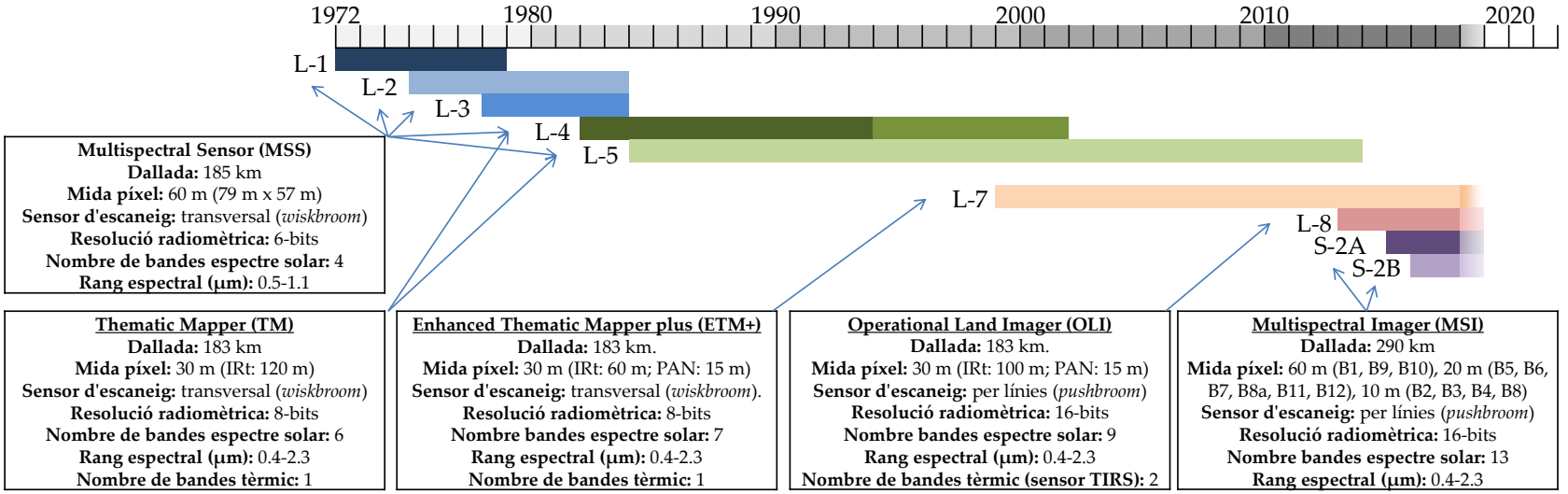

Figura 5: Configuració espectral i funció de resposta espectral relativa (RSRF) del sensor Operational Land Imager (OLI) a bord del satèl·lit Landsat-8.

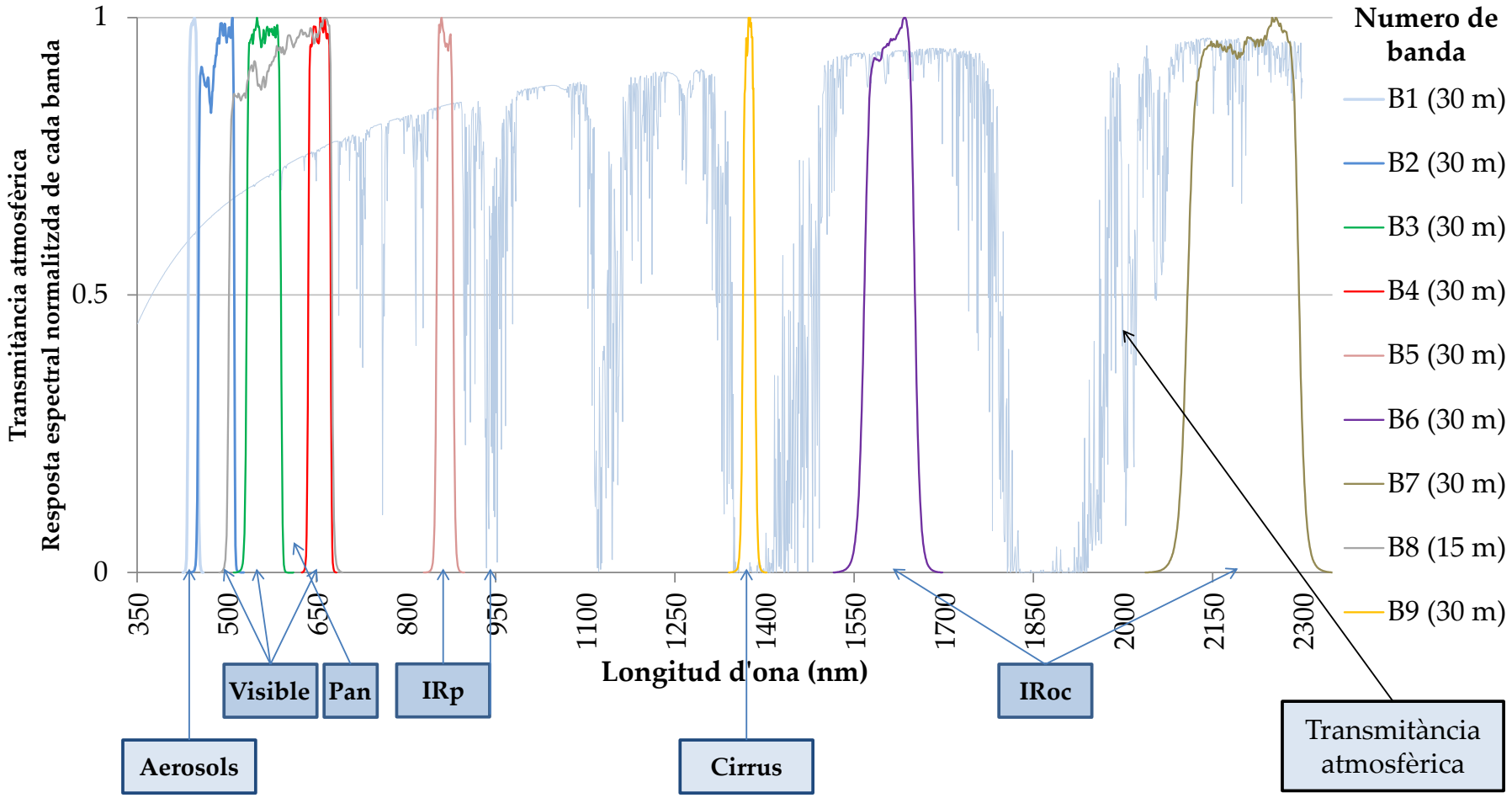

Figura 6: Configuració espectral i funció de resposta espectral relativa (RSRF) del sensor Multispectral Imager (MSI) a bord del satèl·lit Sentinel-2A.

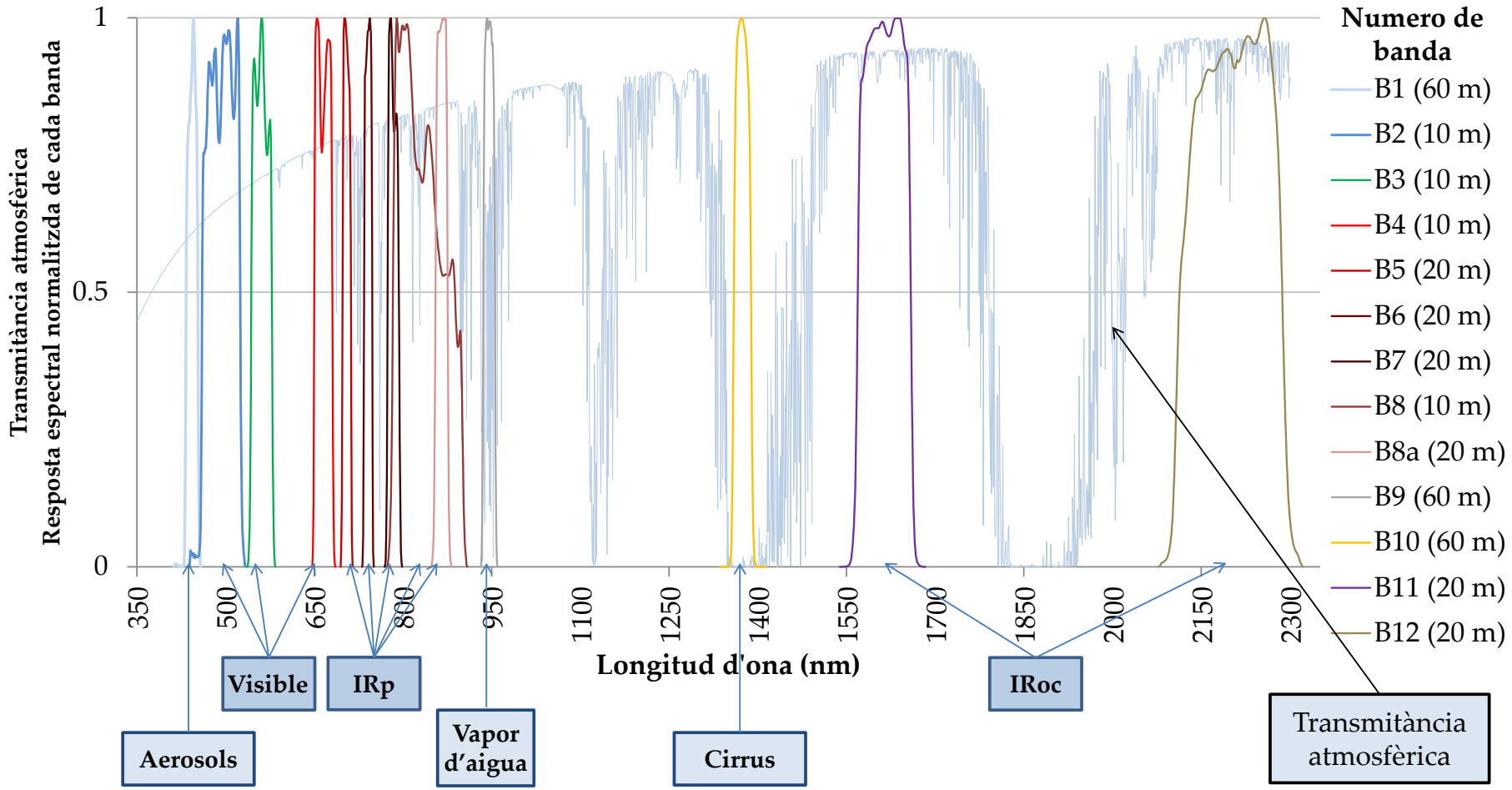

Per ser completament comparables, les imatges adquirides en diferents dates i per diferents sensors han de ser convertides a productes de reflectància mitjançant correccions radiomètriques (atmosfèriques i, idealment, també incloent correccions topogràfiques) [Pons i Solé-Sugrañes, 1994; Liou, 2002; Hadjimitsis et al., 2009; Kaufman i Sendra, 1988; Chavez, 1988; Vermote et al., 2016].

Històricament s'han fet diversos esforços per revisar la coherència radiomètrica dels sensors de la sèrie Landsat, comparant-los entre ells o amb altres sensors de característiques espectrals similars [Chander et al., 2009; Barsi et al., 2014]. Per exemple, a Mishra et al. [2016] s'utilitzen àrees de calibratge pseudoinvariants (Pseudoinvariant Calibration Sites, PICS), que són extensions espacialment uniformes i espectralment estables al llarg del temps emprades per la calibració en òrbita des del Landsat-5 fins al Landsat-8. Un altre exemple el trobem a Czapla-Myers et al. [2015], on s'utilitzen àrees de test de calibració radiomètrica (Radiometric Calibration Test Sites), extensions permanentment monitoritzades utilitzades per calibrar els sensors del Landsat-8. El 2016, l'ESA va completar el reprocessat del Nivell 1 del seu arxiu històric d'imatges captades amb els sensors MSS, TM, ETM+ i OLI, i va utilitzar PICS per validar la coherència entre sensors entre OLI i MSI [Saunier et al., 2017]. A Gascon et al. [2017] es descriuen en profunditat les prestacions del sensor MSI a bord del Sentinel-2A, validant-lo amb PICS i dades de reflectància *in-situ*. Les mesures radiomètriques *in-situ*, combinades amb dades de sensors satel·litaris de resolució espacial més grollera, com el Moderate Resolution Imaging Spectroradiometer (MODIS), també són àmpliament utilitzades per validar les dades procedents dels sensors dels Landsat (o similars) [Zhang et al., 2010; Markham et al., 2014]. Recentment, la NASA [Claverie i Masek, 2017] va presentar un producte harmonitzat conjunt del Landsat-8 i del Sentinel-2 (Harmonized Landsat and Sentinel Product (HLS)). Es tracta d'un producte molt interessant que adopta el sistema de tessel·lat de dades del Sentinel-2 (Military Grid Reference System, MGRS) i remostreja les dades MSI (10 m o 20 m) a la resolució espacial d'OLI (30 m). A partir del 2016, una iniciativa de col·laboració internacional de calibració i validació del comitè d'observació de la Terra (Committee on Earth Observation Satellites—Working Group on Calibration and Validation CEOS-WGCV) [ACIX, 2018; CEOS-WGCV, 2018] ha avaluat els resultats de diversos mètodes de correcció atmosfèrica que s'apliquen a les imatges d'OLI i MSI. Es validen els resultats de reflectància obtinguts amb els diferents mètodes comparant-los amb producte diari de 500 m de reflectància de MODIS (MOD09GA), i amb mesures de referència *in-situ* [ACIX, 2018]. A part, també es validen els valors de profunditat òptica atmosfèrica (Total Optical Depth, TOD) i contingut de vapor d'aigua estimats en les

correccions, comparant-los amb les mesures de la xarxa robotitzada de monitorització d'aerosols (Aerosol Robotic Network, AERONET) [Holben et al., 1998].

Amb aquestes correccions, la radiancia espectral en el sensor (Ls_λ) ($W \cdot m^{-2} \cdot sr^{-2} \cdot \mu m^{-1}$) es converteix en reflectància superficial espectral (ρs_λ) (adimensional), eliminant els efectes atmosfèrics i tenint en compte els efectes d'il·luminació derivats de la posició solar (θs, ϕs), la morfologia del terreny i la posició del sensor (θv, ϕv), on θ és l'angle zenital i ϕ és l'angle azimutal. La majoria dels gasos atmosfèrics i els aerosols produeixen efectes com ara la dispersió, l'absorció i la polarització de la radiació solar, que condueixen a canvis en la irradiància incident en la superfície terrestre [Liou, 2002]. De fet, a través del seu trajecte des de la part superior de l'atmosfera fins a la superfície terrestre (trajecte descendent), i de tornada al sensor una vegada reflectit (trajecte ascendent), l'energia es dispersa i s'absorbeix provocant l'extinció del flux d'energia inicial (irradiància exoatmosfèrica espectral ($E_{SUN\lambda}$) ($W \cdot m^{-2} \cdot \mu m^{-1}$)). Aquest fenomen d'extinció de la llum es quantifica amb la magnitud espectral coneguda com transmitància atmosfèrica espectral (τ_λ) (adimensional). La transmitància depèn de la profunditat òptica atmosfèrica total espectral (Total Optical Depth, TOD) ($\tau_{0\lambda}$), on una major TOD implica transmitàncies menors. La transmitància també depèn de l'angle zenital del vector d'il·luminació (com més gran sigui l'angle més petita és transmitància). Simultàniament, la dispersió atmosfèrica comporta que part d'aquest flux d'energia es redistribueixi en forma de radiació difusa (radiància atmosfèrica espectral, $Latm_\lambda$ ($W \cdot m^{-2} \cdot sr^{-2} \cdot \mu m^{-1}$)), contribuint a la radiació rebuda tant per la superfície de la Terra com pel sensor. Per tant, en termes generals, les correccions atmosfèriques del senyal reflectit per la superfície terrestre tenen dues incògnites principals (dependents de la longitud d'ona) [Turner et al., 1971]: la profunditat òptica atmosfèrica total que debilita el senyal, i la radiància atmosfèrica que contribueix al senyal reflectit per la superfície terrestre.

D'acord amb aquest context teòric, s'han desenvolupat molts enfocs teòrics per obtenir dades de reflectància corregides radiomètricament a partir d'imatges satel·litàries multiespectrals en l'espectre solar. Aquests plantejaments es poden resumir en tres grups principals: les aproximacions basades en principis físics, les aproximacions basades en les propietats de les imatges, i les aproximacions basades en referències radiomètriques.

Aproximacions basades en principis físics: La tècnica més complexa és l'ús d'un Model de Transferència Radiativa (Radiative Transfer Model, RTM), que analitza el fenomen físic de transferència d'energia en forma de radiació electromagnètica a través de l'atmosfera. La propagació de la radiació a través d'un medi és afectada per processos d'absorció,

emissió i dispersió. Una equació de transferència radiativa descriu aquestes interaccions matemàticament i té aplicació en les correccions atmosfèriques. La seva implementació pràctica porta a models molt diferents, des d'aproximacions simplificades fins a aproximacions enormement complexes. Entre els més de vint models que han estat o són utilitzats per a la transferència radiativa en l'atmosfera terrestre o d'altres planetes cal esmentar, pel seu ús en l'observació de la Terra, el MODTRAN [Berk et al., 2014] i el 6S [Vermote et al., 1997, Kotchenova et al., 2006; Kotchenova i Vermote, 2007]. A partir d'aquest darrer RTM, es genera el producte oficial de reflectància proporcionat per l'United States Geological Survey (USGS) [Vermote et al., 2016], anomenat Landsat Surface Reflectance Code (6S-LaSRC) en la seva versió específica per imatges del Landsat-8.

Aproximacions basades en les propietats de les imatges: Tot i que els enfocs físics solen obtenir un millor just, la falta de disponibilitat de les dades necessàries per executar aquests models, especialment dades coincidents en el temps i/o l'espai, de la imatge a corregir, ha donat lloc a l'ús d'altres tècniques que eviten la utilització de dades atmosfèriques accessòries. Aquests enfocs es basen en el mètode de la resta de l'objecte fosc (Dark Object Subtraction, DOS) [Chavez, 1988] que assumeix l'existència de píxels en la imatge que han de proporcionar una reflectància propera a zero (objectes foscos), on es pot estimar la contribució radiativa de l'atmosfera ($Latm_\lambda$) a la radiància rebuda pel sensor (Ls_λ). Les àrees preferides per a l'obtenció de la constant de luminància (Kl) són àrees a l'ombra, ja sigui per ombreig topogràfic (cas en el qual les ombres es localitzen gràcies a un Model Digital d'Ombres projectades (MDO)) o per autoombreig topogràfic (cas en el qual les autoombres es localitzen gràcies a un Model Digital d'Il·luminacions (MDI)). Quan no es produeixen ombres (perquè el relleu és massa pla en relació amb la posició de la font d'il·luminació) es pot recórrer, per exemple, a zones d'aigua força pura, que en l'IRoc pràcticament donen una constant de luminància correcta, però que en regions espectrals en què l'aigua presenta una certa reflexió cal considerar-la adequadament. Diverses versions del mètode DOS fan diferents suposicions sobre el llindar de la determinació de la radiància atmosfèrica (propietats de l'histograma, valor mínim, aigua pura, vegetació densa (DDV) [Pflug, 2016], etc.), com és el cas de l'ATCOR [Richter i Schläpfer, 2016]. A partir d'aquest darrer mètode, millorat amb dades atmosfèriques accessòries si estan disponibles, es genera el producte oficial de reflectància proporcionat per l'ESA [Mueller-Wilm, 2017] en la seva versió específica per a imatges del Sentinel-2. La tècnica de la resta de l'objecte fosc es pot aplicar en moltes imatges, essent una aproximació molt utilitzada, tot i que no corregeix efectes d'adjacència i proporciona resultats menys ajustats en la proporció que el píxel corregit tingui una reflectància molt

diferent de la que tenia el píxel on s'ha determinat la constant de luminància (sobreestimació o subestimació de la contribució de l'atmosfera).

Aproximacions basades en referències radiomètriques: Aquests enfocs utilitzen valors de referència radiomètrica (ja sigui a partir d'objectes invariants o de mesures de dades de camp preses simultàniament a pas de satèl·lit) per obtenir les incògnites del model físic (principalment les atmosfèriques). En el cas del mètode d'objecte invariant, s'assumeix que una imatge conté àrees amb una reflectància acuradament coneguda i estable. La correcció es realitza ajustant els valors de la imatge en aquestes àrees als seus valors de referència radiomètrica. A Hall et al. [1991] es va proposar la tècnica d'objectes invariants per obtenir una resposta radiomètrica comuna en imatges adquirides per diferents sensors en diferents dates. A Hadjimitsis et al. [2009] es van utilitzar àrees anomenades pseudoinvariants per la correcció radiomètrica de sèries temporals d'imatges, obtenint resultats d'alta qualitat. A Pons et al. [2014] es va presentar una tècnica híbrida entre la resta de l'objecte fosc i l'ús Àrees Pseudoinvariants (PIA), que consisteix a determinar la TOD espectral ($\tau_{0\lambda}$) i a la radiancia atmosfèrica espectral ($Latm_{\lambda}$) tot ajustant el resultat del model amb els valors de referència de les àrees radiomètricament estables (PIA). Les PIA foren extretes prèviament de la sèrie diària de més de 10 anys de productes de reflectància obtinguts del sensor TERRA-MODIS (MOD09GA). El mètode va permetre generar automàticament productes de reflectància d'imatges MSS, TM i ETM+. L'avaluació de la robustesa de la sèrie temporal del mètode PIA i la coherència de signatures en diverses cobertes del sòl (àrees urbanitzades, boscos de pi blanc, boscos de pi roig, alzinar) va ser molt positiva, així com també va obtenir bons resultats en la classificació de la cobertura terrestre de la Península Ibèrica (1980-2015) [Vidal-Macua et al., 2016] a partir de dades procedents de diversos sensors de la sèrie Landsat fins al Landsat-7. En el cas de l'ús de dades radiomètriques de camp com a referència, les mesures s'utilitzen de manera similar a les del cas anterior, però aquestes mesures només es poden utilitzar com a referència per corregir la imatge adquirida simultàniament a la captura de dades *in-situ* (Figura 7).

En els tres tipus d'aproximacions, algunes sofisticacions fan ús dels Models Digitals d'Elevació (MDE) o dels Models Digitals de Superfície (MDS) per considerar els efectes del terreny en l'angle d'il·luminació i, per tant, millorar l'exactitud en quantificar la quantitat d'energia que es rep per unitat de superfície [Pons i Solé-Sugrañes, 1994; Richter i Schläpfer, 2016] o per modelitzar l'augment de la transmitància atmosfèrica en funció de l'augment d'altitud del terreny [Pons et al., 2014; Vermote et al., 2016].

Figura 7: Esquema fonamental del components que formen l'algorisme bàsic de correcció radiomètrica descrit a Pons i Solé-Sugrañes [1994] i a Pons et al. [2014]. Aquest algorisme, implementat en el programari MiraMon, rep el nom de CorRad-MiraMon i la seva aplicació en imatges de satèl·lit resulta en l'obtenció d'imatges en reflectància superficial espectral, obtenint els paràmetres atmosfèrics mitjançant la tècnica de la resta de l'objecte fosc [Pons i Solé-Sugrañes, 1994] o, alternativament, mitjançant Àrees Pseudoinvariants (PIA) o mesures in-situ [Pons et al., 2014].

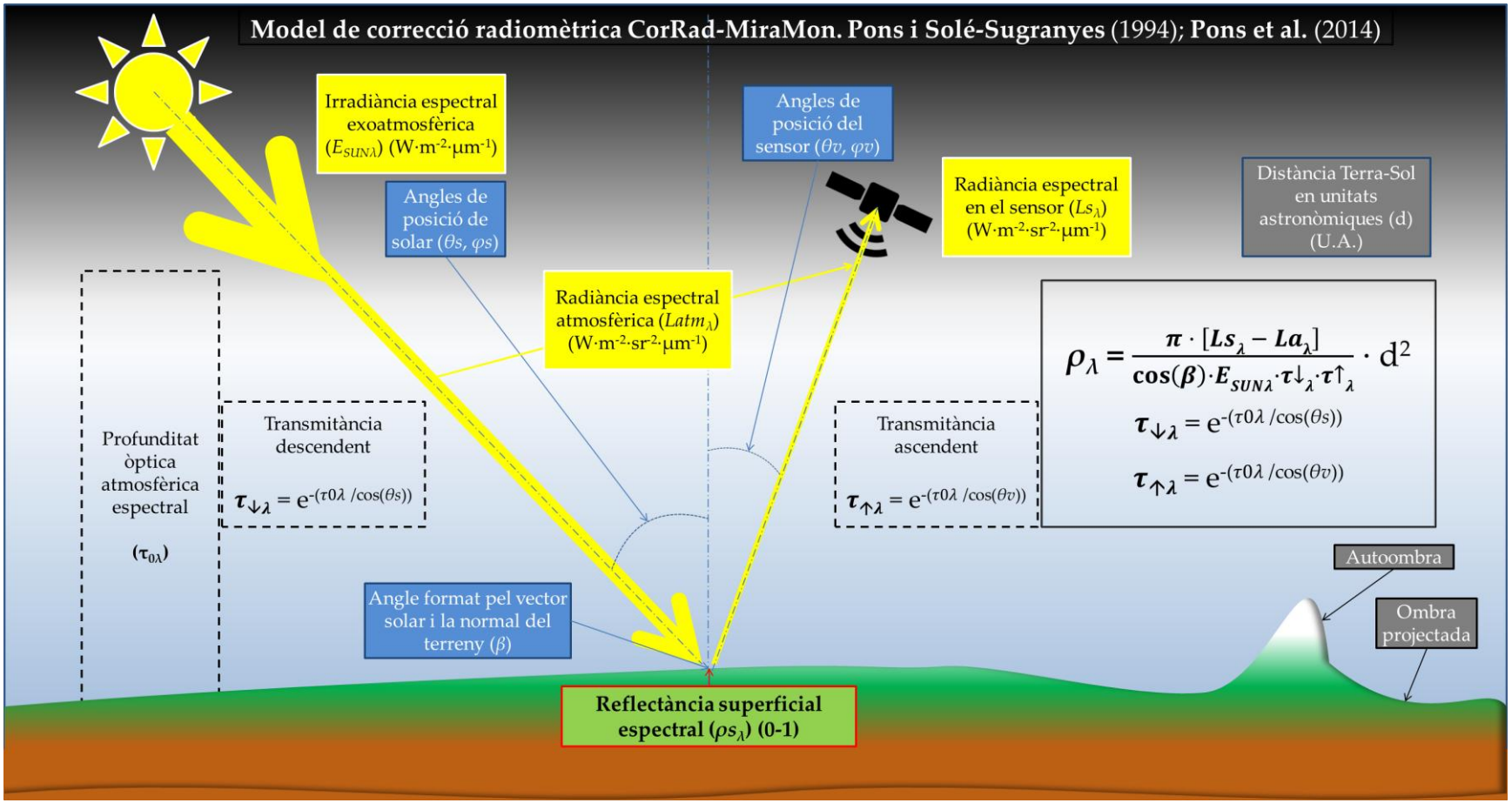

Com a alternativa a aquestes tres aproximacions, també és possible utilitzar simplement un ajust lineal empíric (*Empirical Line*). Aquest enfoc requereix mesures espectroradiomètriques *in-situ* de reflectància superficial espectral (ρs_λ), captades simultàniament al pas del satèl·lit. Aquest senzill mètode consisteix a corregir tota la imatge de radiància ajustant cada banda a valors de reflectància *in-situ*, mitjançant regressió lineal [Smith i Milton, 1999; Xu i Huang, 2007], en comptes d'utilitzar les dades per obtenir les incògnites atmosfèriques d'un model físic [Pons et al., 2014]. Tanmateix, aquesta tècnica no és operativa per a corregir imatges captades amb anterioritat a una campanya de mesura espectroradiomètrica de camp o per una gran àrea, motiu pel qual alguns autors van proposar ajustos lineals utilitzant referències pseudoinvariants (Pseudoinvariant Features, PIF) [Song et al., 2001].

1.3. Imatges procedents de Vehicles Aeris no Tripulats (UAV)

La teledetecció (admetent com a tal la interpretació visual d'imatges captades remotament) mitjançant sensors embarcats en vehicles aeris ha estat utilitzada des de l'inici de l'aeronàutica al segle XIX, i va agafar molta importància amb el desenvolupament de l'aviació durant el segle XX, especialment utilitzant càmeres fotogràfiques. Els sensors fotogramètrics a bord d'aeronaus tripulades, que habitualment volen entre els 1000 m i els 10000 m d'altura, són una font d'informació geogràfica molt valuosa que permet obtenir imatges amb resolucions espacials típicament entre els 10 cm i els 100 cm depenent de l'altura i velocitat de vol, i de l'estructura de la càmera (bàsicament de la longitud focal, les lents, l'angle de visió instantani [i el gra de l'emulsió en sensors fotogràfics] i la mida del sensor). Una aeronau tripulada és capaç de transportar sensors relativament pesats i complexos, com sensors passius multiespectrals [PNOA, 2018a; ICGC, 2018a], hiperespectrals [de Miguel et al., 2014] o sensors actius com els lidar [PNOA, 2018b; ICGC, 2018b). Per contra, el cost de les operacions amb aquests ginys tripulats és força elevat i requereix una operativa complexa. Durant els inicis del segle XXI s'ha popularitzat la teledetecció mitjançant Vehicles Aeris no Tripulats (UAV) degut al seu baix cost i a la seva versatilitat. Els UAV, altrament anomenats Sistemes Aeris no Tripulats (UAS) quan es considera el sistema conjunt de sensors i plataforma, o anomenats popularment drons [Pons i Arcalís, 2012], es caracteritzen per tenir un sistema de posicionament i una controladora del sistema de propulsió que permeten un pilotatge programat. Aquest fet és el que els diferencia dels tradicionals aparells de radiocontrol, ja que en els UAV no és necessari dirigir l'aeronau manualment per mitjà d'una emissora,

sinó que es pot definir un pla de vol sobre un mapa (típicament digital), introduir-lo a la controladora perquè el realitzi autònomament, i determinar la cadència amb la qual s'hauran d'adquirir les imatges. Hi ha UAV de diverses dimensions, pesos i capacitats, des dels militars d'ala fixa de més de 150 kg, fins als microdrons multicòpters de pocs centenars de grams [Salamí et al., 2014]. La legislació espanyola actual [BOE, 2017] no permet el vol d'UAV a una altura superior als 120 m d'altura, així com també limita l'activitat de drons amb un pes superior als 25 kg. No obstant, drons lleugers d'entre 15 kg i 1.5 kg són aptes per portar sensors òptics útils per a teledetecció mediambiental [Manfreda et al., 2018] i ser operats en ús civil. Els sensors òptics que ofereix el mercat i que són prou lleugers com per ésser embarcats en drons de baix pes (e.g. Parrot Sequoia [Parrot, 2018] o MicaSense RedEdge [MicaSense, 2015]) cobreixen les regions espectrals del visible i l'IRp, sense arribar a l'IRoc degut l'augment de pes que suposa el sistema d'estabilització tèrmica que requereixen els sensors a l'IRoc (tal com succeeix en els espectroradiòmetres de camp que són sensibles a aquestes regions espectrals (e.g ASD FieldSpec 3 [Hatchell, 1999])). Els sensors comercials de baix pes específicament dissenyats per a UAV són capaços d'oferir unes resolucions espacials molt elevades, habitualment properes o inferiors als 10 cm per píxel tenint en compte el màxim d'altura de vol que permet la llei. El llegat científic i tècnic procedent de la fotogrametria aèria convencional, combinat amb les noves tècniques de fotogrametria digital i de visió per computació, permet tractar fotogramètricament les imatges captades amb sensors portats en UAV per tal de generar ortomosaics i/o models tridimensionals de la superfície. Si ens centrem en la georeferenciació de fotogrames, se sol obtenir de les dades dels sensors de posicionament de bord [Colomina i Molina, 2014], i principalment s'opta entre dos mètodes de georeferenciació: georeferenciació directa i georeferenciació indirecta. La georeferenciació directa es basa en sistemes de navegació integrats, que utilitzen dades del receptor GNSS (e.g. GPS) per determinar la posició en l'espai (XYZ), i de la Unitat de Mesura Inercial (IMU) per calcular els paràmetres d'orientació externa del sensor en el moment de l'adquisició de la imatge [Skaloud et al., 2014; Rehak i Skaloud, 2017]. L'exactitud de les dades obtingudes a partir del GNSS a bord és un factor clau per a una correcta georeferenciació directa i, per tant, també ho són la qualitat dels receptors i la tècnica utilitzada per determinar-ne la posició. Amb tècniques diferencials, basades en el senyal portador (l'L1 (1575 MHz) o l'L2 (1227 MHz)), es determina el nombre de cicles de fase (ambigüitat) més la part de longitud d'ona que ha transcorregut entre el satèl·lit emissor i l'antena del receptor, obtenint més precisió que amb el senyal pseudo-aleatori codificat (el codi C/A (1.023 MHz) o el codi P (10.23 MHz)) transmès per la pròpia ona portadora. A

més, i donat que en la majoria d'aplicacions de la teledetecció ambiental no sol ser necessari un coneixement en temps real de la posició (Real-Time Kinematic, RTK), les dades del GNSS es poden millorar post-processant-les. Amb el post-processat de dades cinemàtiques (Post-Processed Kinematic, PPK) se sol determinar amb millor exactitud i precisió la posició d'un giny en moviment (com un UAV), considerant factors externs al segment usuari, com la posició corregida de cada satèl·lit de la constel·lació en el moment d'emissió del senyal, o el retard del senyal degut al seu pas a través l'atmosfera. Les dades necessàries per realitzar les correccions relacionades amb les òrbites i els rellotges dels satèl·lits les proporciona el segment de control global del sistema, mentre que a nivell regional s'obtenen dades per corregir errors de propagació del senyal tenint en compte una (o més) posició de referència estàtica, coneguda amb molta exactitud. Coneixent els errors que dóna el senyal GNSS en la posició de referència, es determinen les correccions necessàries i es poden aplicar a les dades de posicionament registrades pel receptor de l'UAV si s'han utilitzat els mateixos satèl·lits que per a la referència. En el post-processat també es consideren factors relacionats amb el giny, com la distància entre el centre de l'òptica del sensor i la base de l'antena del GNSS (distància anomenada *lever-arm*), o la posició de l'UAV entre successives mesures del receptor per determinar amb exactitud la coordenada del centre del fotograma en el moment de disparament (Figura 8).

Figura 8: Tècniques de mesura de pseudodistàncies entre els satèl·lits GNSS i els receptors (basades en codi o en la seva fase portadora), i mètode de posicionament diferencial cinemàtic post-processat.

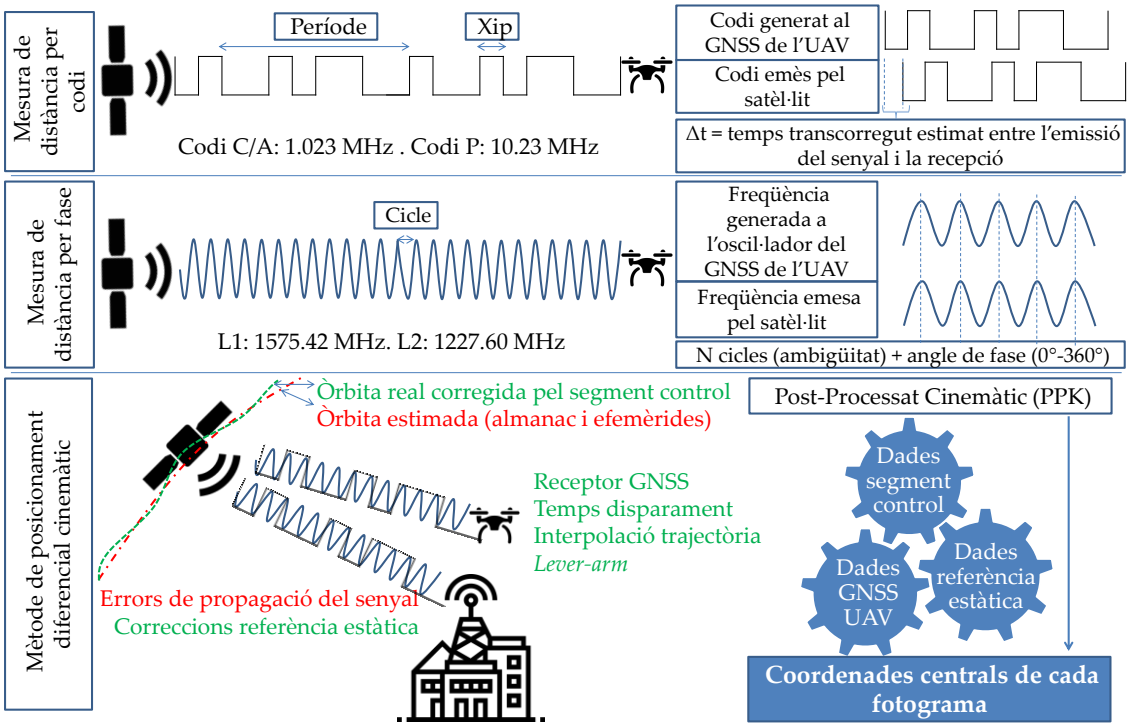

En canvi, la georeferenciació indirecta de les imatges d'UAV es basa en punts de control geomètric sobre el terreny (GCP), ubicacions amb coordenades conegudes que normalment es mesuren amb receptors GNSS estàtics d'alta qualitat (i.e. GPS-Diferencial) i s'envolten d'un fons característic (típicament arlequinat) per ser visible a les imatges captades per l'UAV [Rumpler et al., 2014] (Figura 9). Aquests punts de control actuen com a "xinxetes" que posicionen els fotogrames en coordenades molt fiables, i el bloc d'ajust de tots els fotogrames es realitza respectant al màxim aquestes posicions. La georeferenciació indirecta implica més temps de treball de camp i de processat que la georeferenciació directa; la seva exactitud depèn de la correcta mesura i distribució de les posicions dels GCP [Martínez-Carricondo et al., 2018], de l'habilitat del tècnic en localitzar les referències a les imatges i de la quantitat de GCP, però habitualment té l'avantatge d'arribar a exactituds similars de mida de píxel [Turner et al., 2014].

Pel fet de volar a tan baixa altura, les imatges captades mitjançant sensors a bord de drons tenen la peculiaritat, respecte de les captades per aeronaus tripulades o per satèl·lits, de no estar tan afectades pels efectes de la interacció entre la llum solar i l'atmosfera en el seu trajecte ascendent entre la superfície i el sensor. Així, l'obtenció de reflectància superficial espectral a partir d'imatges de dron requereix una aproximació diferent a la que s'ha descrit per a les imatges de satèl·lit, ja que la radiància espectral es pot obtenir quasi empíricament per la proximitat de l'UAV amb la superfície d'estudi, amb una de les aproximacions següents:

Aproximacions basades en sensors d'irradiància: La irradiància espectral que arriba a la superfície a ser observada es pot estimar a nivell de sensor utilitzant un sensor d'irradiància (Downwelling Light Sensor, DLS), que se situa a la part superior del dron i mesura la irradiància en el moment del disparament, desant la dada en el fitxer de metadades (Exchangeable Image File, EXIF, de fet inclòs en el propi format de la imatge, no com un fitxer a part) que va associat a cada imatge. La dada del DLS, és doncs utilitzada per obtenir imatges en reflectància a nivell del sensor [Hakala et al., 2018].

Aproximacions basades en un panell de calibratge: Una altra aproximació consisteix a realitzar fotografies d'un panell de calibratge (amb una reflectància coneguda), abans d'enlairar-se, amb la mateixa càmera amb què es volarà. A partir d'aquestes fotografies prèvies es pot obtenir la irradiància en el moment d'inici del vol, i assumint que s'ha mantingut constant durant tota l'operació, es poden corregir totes les imatges posteriors obtenint valors de reflectància a nivell de superfície [MicaSense, 2015]. Sovint, es realitzen

fotografies dels panells de calibratge abans i també després del vol, per tal de captar possibles canvis en la irradiància durant la captura de les imatges.

Aproximacions basades en diversos panells de calibratge: Una tercera aproximació consisteix a utilitzar referències radiomètriques visibles des de la imatge de dron i caracteritzades mitjançant mesures espectroradiomètriques de camp per tal de realitzar una correcció empírica lineal ajustant els valors del dron als valors de reflectància *in-situ*, obtenint imatges en reflectància a nivell de superfície [Iqbal et al., 2018]. Les mesures *in-situ*, que solen ser fetes amb instruments hiperespectrals, s'han de remostrejar espectralment per fer-les correspondre a les bandes del sensor multiespectral de UAV. Cal tenir en compte que en el moment de realització d'aquesta Tesi pocs fabricants de sensors comercials per UAV ofereixen informació tècnica sobre la funció de resposta espectral relativa (RSRF) de cada banda del sensor [Ciesielski, 2016] (Figura 8), una informació molt necessària en treballs radiomètrics acurats. En absència de la difusió pública de la RSRF del sensor, se sol utilitzar la informació relativa a l'amplada de banda definida pel fabricant i normalment associada a l'amplada a mitja alçària (FWHM) de cada banda del sensor [Parrot, 2018].

En aquest context, l'ús de dades de adquirides amb UAV per a propòsits espectroradiomètrics ha evolucionat molt en els darrers cinc anys [Aasen et al., 2018]. Diversos autors han comparat imatges adquirides amb sensors òptics hiperespectrals o multiespectrals a bord d'UAV amb dades captades per satèl·lits GEOSS [Zabala, 2017; Matese et al., 2015], o amb dades d'espectroradiometria de camp [Markelin, 2013; Honkavaara et al., 2012]. Recents iniciatives internacionals [OPTIMISE, 2018] exploren les noves oportunitats que les plataformes i sensors UAV podrien aportar a l'observació de la Terra. MacArthur i Robinson [2015] van presentar una revisió de l'estat de l'art en l'espectroradiometria de camp i van avançar l'impacte de les noves tecnologies basades en UAV, especialment pel que fa al suport a la calibració empírica i la validació d'observacions de satèl·lits. Al mateix temps, destacaren la importància de processar acuradament imatges d'UAV per garantir la seva fiabilitat.

Figura 9: Els sensors embarcats en Vehicles Aeris no Tripulats (UAV) de menys de 25 kg ofereixen una molt alta resolució espacial degut a la seva baixa altura de vol sobre el terreny. En aquesta figura es mostra l'exemple pel cas d'un sensor multiespectral típic per a UAV, amb una mida de píxel al sensor de 3.75 µm i una longitud focal de 3.98 mm, resultant en una mida de píxel nadiral d'uns 10 cm volant a 100 m d'altura. La georeferenciació indirecta mitjançant punts de control requereix la mesura de punts amb coordenades molt ben conegudes (e.g. GPS diferencial) i clarament visibles des de la imatge de l'UAV. La configuració espectral dels sensors multiespectrals d'UAV sol restringir-se a bandes del visible i l'infraroig proper (e.g. MicaSense RedEdge).

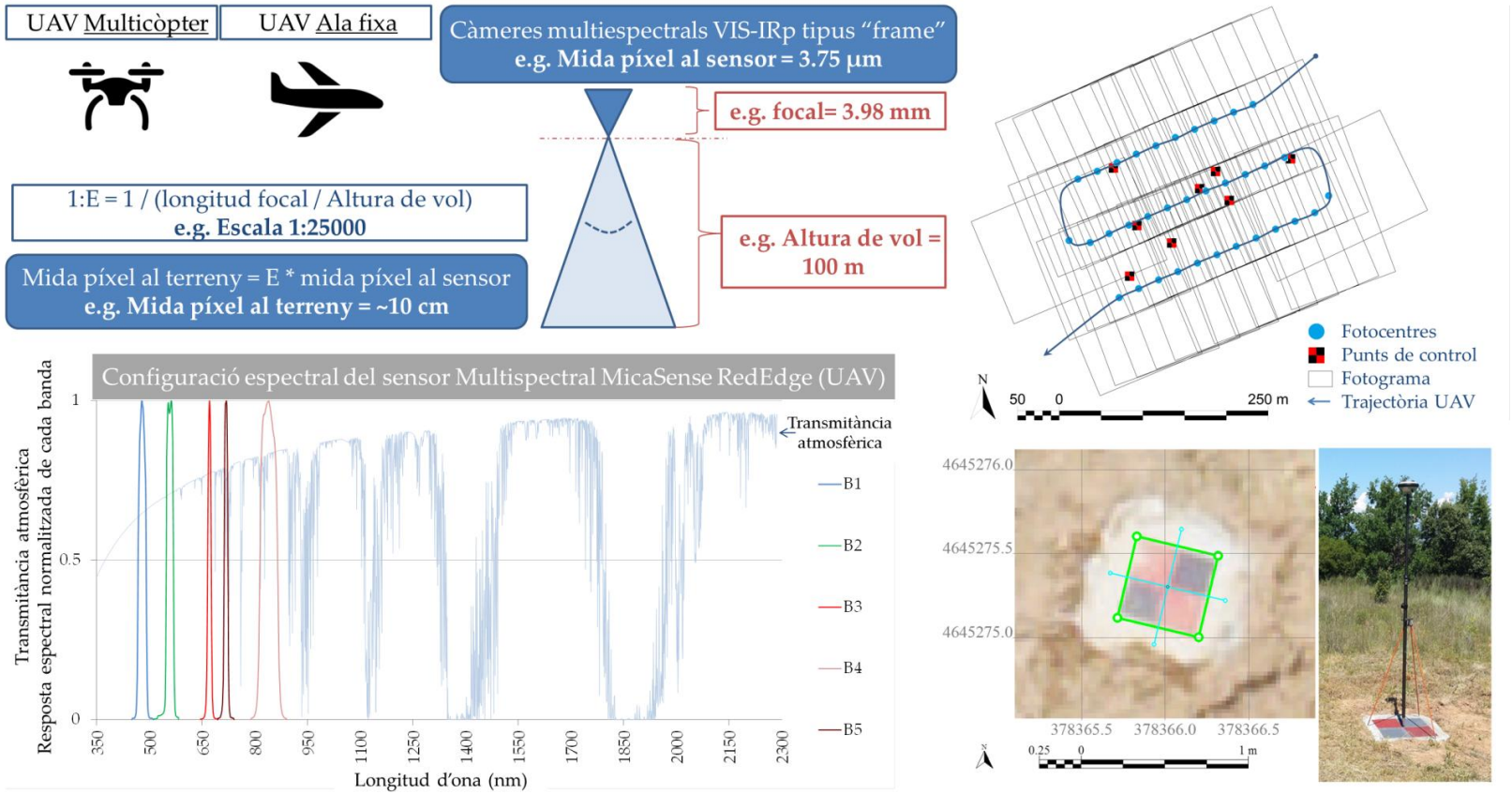

1.4. Espectroradiometria de camp

La teledetecció mitjançant espectroradiòmetres de camp permet mesurar *in-situ* la reflectància d'una superfície, a nivell quasi-puntual i amb la resolució espectral molt elevada. Les mesures espectroradiomètriques de camp tenen l'avantatge d'haver estat realitzades molt a prop de l'objecte d'estudi, típicament a menys de 2 m, raó per la qual s'assumeix que no hi ha pràcticament cap distorsió en la mesura que sigui deguda a la interacció entre la reflexió de la llum solar i l'atmosfera en el curt espai que hi ha entre el sensor i la superfície mostrejada. L'espectroradiometria de camp, realitzada amb radiòmetres de mà, és una ciència que proporciona dades molt valuoses per a la validació de dades de teledetecció captades per sensors ubicats en plataformes situades a molta més distància de la superfície, com els satèl·lits o les aeronaus tripulades, però també de dades captades més a prop, com des de drons.

Durant anys, en la teledetecció s'ha intentat relacionar les dades d'espectroradiometria de camp amb les imatges de satèl·lit [McCoy, 2005]. La mesura espectroradiomètrica de la reflectància, efectuada simultàniament al pas del satèl·lit, és una font d'informació per avaluar i reforçar l'exactitud de la correcció radiomètrica [Milton et al., 2009; Smith i Milton, 1999]. Per contra, les dades espectroradiomètriques tenen l'inconvenient de tenir molt poc abast espacial, ja que durant un temps acceptable de 20 minuts abans i després del pas del satèl·lit, un operari especialitzat pot mostrejar raonablement a una superfície equivalent a 20 píxels de l'OLI 30 m, 45 píxels de l'MSI 20 m, o 180 píxels de l'MSI 10 m. El mostreig ha de ser molt acurat, precís, ràpid i representatiu per poder ésser comparat fidelment amb les imatges que es pretenen validar. A més, el remostreig espacial de les dades puntuals captades amb radiòmetres de mà no és un procés trivial, donat que la georeferenciació de les mesures no sempre té l'exactitud que es requereix, especialment en zones boscoses [Sanchez Alberola et al., 2018], i el mostreig realitzat *in-situ* no és fàcilment adaptable a la malla de dades provinents d'altres plataformes. Encara que el mostreig en zones planes i homogènies sigui relativament senzill, un dels principals problemes de la radiometria de camp és la dificultat d'accedir a determinats tipus de superfícies que són molt rellevants en el medi natural, com masses d'aigua o masses forestals [Peña-Martinez et al., 2003; Mueller et al., 2000], i presenta dificultats en mostrejar àrees heterogènies com camps de fruiters, tot i que per superar aquests reptes a vegades s'han utilitzat dispositius elevadors [Colwell et al., 1983].

Els protocols habituals de captura de dades espectroradiomètriques *in-situ* [Jiménez i Díaz-Delgado, 2015; Mira et al., 2015; Meroni i Colombo, 2009], orientades a ser

comparades amb imatges aèries o satel·litàries captades simultàniament [de Miguel, 2014; Jiménez et al., 2007], consisteixen, en primer lloc, a dissenyar unes àrees de mostreig que siguin homogènies quant al tipus de superfície. Aquestes àrees convé que siguin espacialment representatives de la mida de píxel de les imatges remotes a comparar, tenint en compte que idealment un mínim de dos píxels en totes direccions respecte l'àrea de mostreig central han de ser igualment homogènies i representatives per no introduir efectes d'adjacència. Posteriorment, s'ha de definir el patró de mostreig dins de l'àrea d'interès, generalment a l'interior de l'àrea que correspon a un píxel de les imatges de satèl·lit que es pretén corregir/validar. Aquest patró pot ser en creu, en ziga-zaga o aleatori, però sempre en una posició respecte del Sol que eviti que l'operari faci ombra.

Els espectroradiòmetres de camp (e.g. ASD FieldSpec 3 [Hatchell, 1999] o OceanOptics USB2000+ [OceanOptics, 2006]) habitualment compten amb un cable de fibra òptica que permet apuntar cap a la superfície de mostreig, de manera que el punter habitualment se situa en posició nadiral per evitar distorsions en la mesura derivades de la direccionalitat de la reflectància, especialment en superfícies poc lambertianes com l'aigua. Prèviament a la mesura de la reflectància, es procedeix a mesurar el corrent fosc de l'instrument per evitar biaixos en les mesures. Després se sol mesurar la irradiància espectral que incideix a la superfície mitjançant un panell de referència que s'assumeix que reflecteix la totalitat de l'energia que hi incideix en totes les longituds d'ona en què es treballa (e.g. Spectralon®). Aleshores és quan es mostreja la reflectància de la superfície d'interès, realitzant diverses lectures seqüencials, habitualment en un nombre entre 10 i 100. Un cop mostrejada l'àrea, les lectures són tractades estadísticament per avaluar-ne la dispersió i la centralitat, que determinaran la validesa de la mitjana de les diferents lectures i permetran obtenir la signatura espectral de la superfície mesurada espectroradiomètricament (Figura 10). Finalment, és convenient integrar la signatura espectral considerant les diferents RSRF (o el FWHM en la seva absència) de cada banda del sensor aeroportat o satel·litari amb el qual es volen comparar les dades de camp.

Finalment, un cop s'han caracteritzat espectralment les superfícies d'interès, cal fer el tractament geomètric adient per comparar els valors dels píxels de les imatges amb els corresponents valors mesurats *in-situ*. Aquest procés no és trivial perquè no sempre es té el posicionament exacte de cadascuna de les mesures, tot i haver seguit un patró de mostreig i sovint tenir un GNSS en l'equipament. Aleshores, és habitual fer un tractament geoestadístic per fer equiparables les dades espectrals mesurades en una àrea de terreny concreta a l'àrea que correspon als píxels de la imatge a validar/corregir.

Figura 10: Exemple de dades captades amb un espectroradiòmetre de camp (ASD FieldSpec 3) en diferents tipus de cobertes (falguerar, matollar, duna i aigua), en un mostreig circular dissenyat perquè correspongui amb píxels del sensor OLI del Landsat-8 i MSI del Sentinel-2. Fotografies gentilesa de David Aragonés.

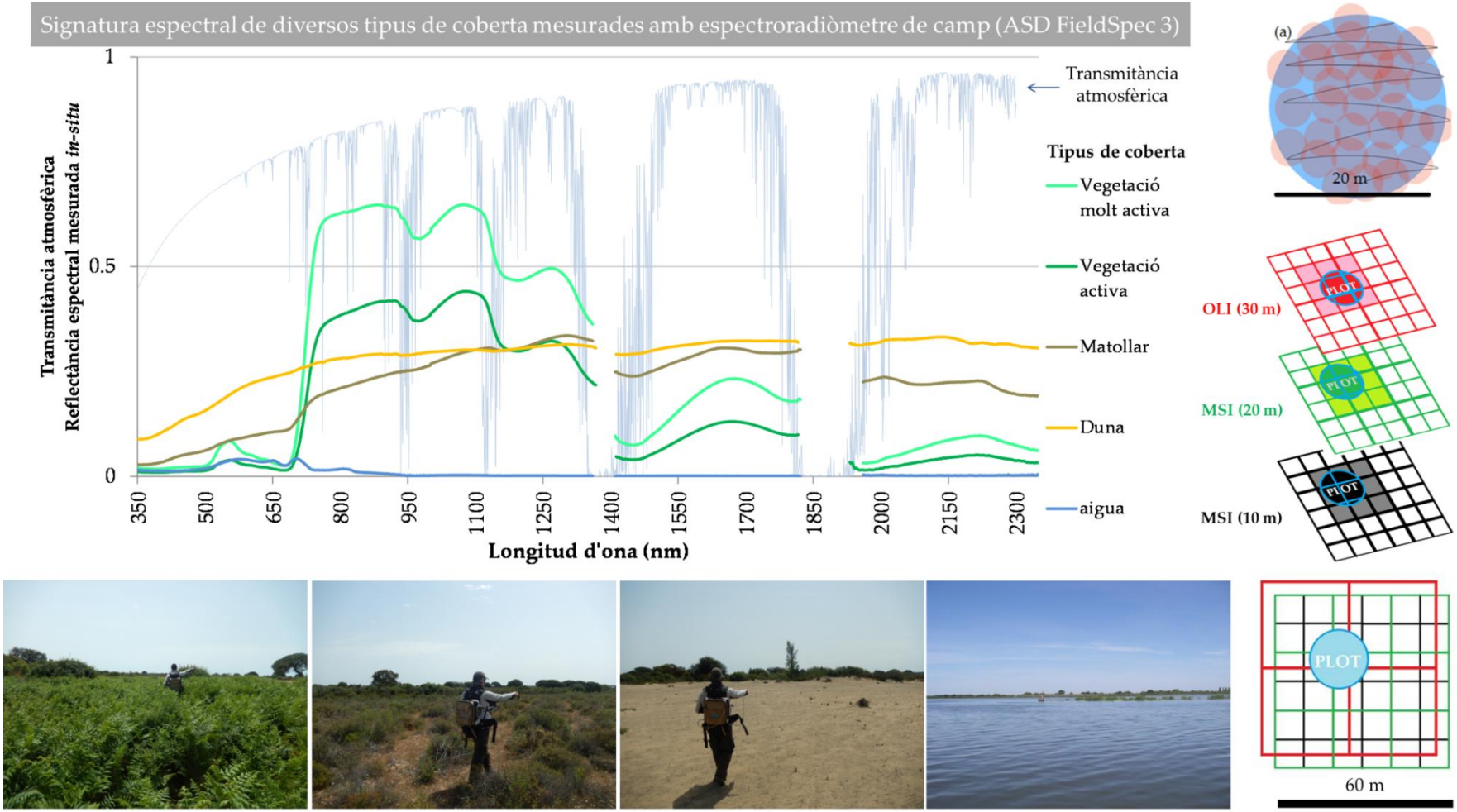

1.5. Objectius i estructura dels continguts

L'objectiu principal de la recerca realitzada en el marc d'aquesta Tesi ha estat, des del seu plantejament inicial, aprofundir en les creixents possibilitats que ofereixen els UAV per a recollir dades *in-situ* amb la finalitat de millorar el processament i/o la interpretació de les dades de satèl·lits que formen part de GEOSS [GEOSS, 2018], fent especial èmfasi en els satèl·lits Landsat-8, del programa LDCM [NASAa, 2018], i Sentinel-2 (A i B) del programa Copernicus [Copernicus, 2018]. En base als antecedents descrits en la introducció, l'actual revolució que estan representant els UAV permet pensar en la necessitat d'investigar en la utilitat que pot tenir el seu ús com a noves fonts de dades, en sinergia amb l'explotació de dades espectroradiomètriques *in-situ* convencionals. La novetat d'aquesta Tesi rau en el fet d'utilitzar dades d'UAV amb l'objectiu principal de perfeccionar la correcció radiomètrica dels sensors satel·litaris i millorar així la cartografia de cobertes del sòl. D'acord amb les idees exposades, es plantegen els següents objectius generals i específics:

Objectiu general (OG) 1: Millora del tractament de les dades captades per sensors del GEOSS, com el Landsat-8 i Sentinel-2.

- Objectiu específic (OE) 1.1: Obtenir una correcció radiomètrica acurada i regular de dades en l'espectre visible i infraroig no tèrmic dels sensors embarcats en satèl·lits del GEOSS com el Landsat-8 i el Sentinel-2, en les seves observacions sobre zones ibèriques.
- Objectiu específic (OE) 1.2: Establir un protocol geoestadístic que permeti definir les amplades espectrals, la grandària sobre el terreny i la intensitat de mostreig dels sensors *in-situ* (radiòmetre de mà i dron) per tal de poder assolir l'objectiu 1. En aquest objectiu es defineix el sistema de mostreig, el qual inclourà diverses classes de cobertes del sòl, podent fer una comparació a nivell d'objecte.
- Tasca específica: Recollir dades *in-situ* amb radiòmetres de mà (o espectroradiòmetre de camp) i sensors multiespectrals embarcats en drons per establir el protocol apuntat als objectius específics anteriors.

Objectiu general (OG) 2: Millora del tractament de dades captades amb UAV en relació amb les imatges procedents d'altres plataformes de teledetecció (i.e. Landsat-8 i Sentinel-2), i millora de la cartografia de cobertes del sòl a partir de dades captades per sensors embarcats en UAV.

- Objectiu específic (OE) 2.1: Investigar l'exactitud posicional de mètodes de correcció geomètrica d'imatges d'UAV, focalitzada en la combinació de dades d'UAV i imatges dels satèl·lits Landsat-8 i Sentinel-2.
- Objectiu específic (OE) 2.2: Investigar els mètodes de correcció radiomètrica de dades multiespectrals d'UAV i el seu ajust amb dades recollides *in-situ* a fi d'obtenir informació útil per al coneixement de serveis ecosistèmics.
- Objectiu específic (OE) 2.3: Generar cartografia temàtica utilitzant dades d'UAV i mètodes de classificació digital, aplicable a la millora de la conservació mediambiental a escala local i global.
- Tasca específica: Recollir dades temàtiques de cobertes del sòl *in-situ* amb una molt alta resolució espacial mitjançant drons.

La hipòtesi principal és: Els UAV poden omplir el buit d'escala entre imatges de satèl·lit i mesures *in-situ* convencionals millorant així la correcció radiomètrica d'imatges satel·litàries amb la introducció de veritat terreny obtinguda de la sinergia entre la radiometria de camp convencional i sensors embarcats en drons.

La hipòtesi es basa en el fet que la captació de la dada des d'un dron pot ser més representativa que la del mostreig puntual i pot permetre realitzar un mostreig molt més dens i extens que el convencional. Tanmateix, l'espectroradiometria de camp proporciona l'exactitud radiomètrica necessària per calibrar les dades adquirides amb el sensor de l'UAV. Així, el raonament es fonamenta en:

(i) La major àrea sobre el terreny que pot observar un sensor elevat amb un UAV a la vertical del terreny permet captar tots els elements que s'inclouen en el píxel d'una imatge de satèl·lit, 30 metres de costat en el sensor OLI del Landsat-8, i 20 o 10 metres de costat (segons la banda espectral) en el sensor MSI del Sentinel-2, de forma georeferenciada i amb un mostreig regular (ràster).

(ii) La major versatilitat del dron permet desplaçar el sensor a la mateixa coordenada i repetir el mostreig amb un esforç logístic menor, més ràpidament i a menor cost que un avió o un helicòpter.

(iii) Les mesures radiomètriques de camp en punts identificables en la imatge del dron poden ser utilitzades per a calibrar les dades del dron i obtenir així, amb l'UAV, més extensió de dades però alhora ajustades a les mesures radiomètriques que es farien amb un radiòmetre de mà *in-situ* (Figura 11).

Figura 11: Esquema del raonament d'escalat des del mostreig en el terreny mitjançant mesures espectroradiomètriques, ascendint a la correcció radiomètrica d'imatges d'UAV, a la seva adaptació a les malles de píxels de les imatges de satèl·lit i a la correcció radiomètrica d'aquestes a partir de les imatges d'UAV.

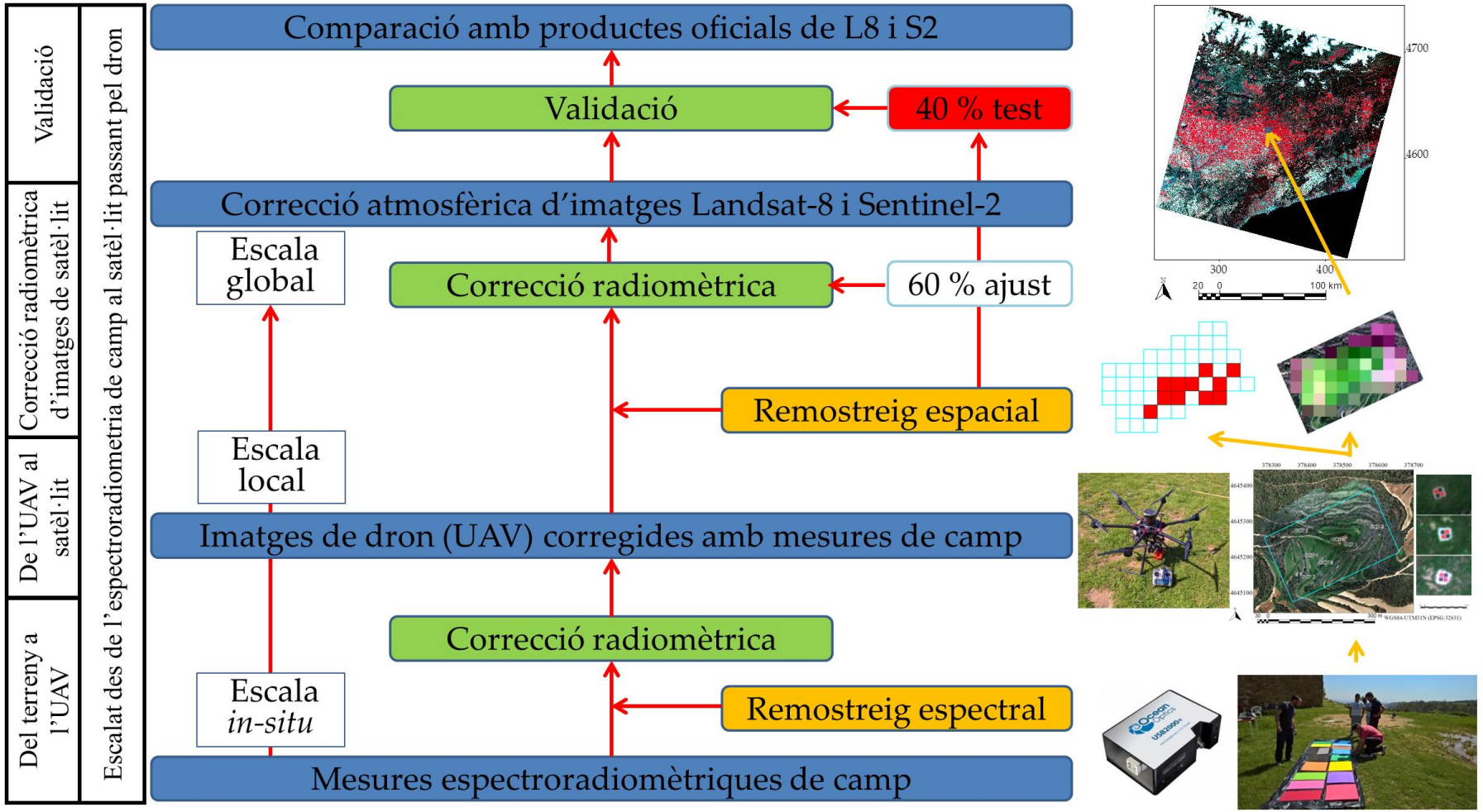

El mètode principal de treball consisteix en la captura *in-situ* de dades hiperespectrals amb radiòmetres de camp alhora que es capten imatges mitjançant un sensor multiespectral embarcat en un UAV i al pas quasi-simultani dels satèl·lits Landsat-8 i Sentinel-2 per la seva posterior comparació. Les dades espectroradiomètriques de camp tenen la funció de calibrar les dades del dron, que un cop corregides geomètricament i radiomètricament s'usen com a referència per corregir radiomètricament les imatges de satèl·lit. Per tal que sigui operativa aquesta metodologia, es realitzen mesures de camp en el moment de vol de l'UAV i de pas dels satèl·lits, essent la metodologia òptima una de les principals tasques investigades. La metodologia emprada està enfocada a poder corregir les imatges de satèl·lit amb una referència empírica consistent en un volum de mostra extraordinàriament millor que el que hom pot obtenir a mà amb tècniques convencionals. Les imatges d'UAV es correlacionen amb mesures espectroradiomètriques puntuals en panells de diverses respostes espectrals per tal de comprovar-ne la validesa i corregir possibles biaixos. Dins de l'àmbit d'estudi es delimiten unes àrees d'ajust on es realitzen els experiments de correcció radiomètrica de satèl·lit mitjançant imatges d'UAV, i la validació dels resultats obtinguts es duu a terme en àrees de test, metodologia típicament emprada en teledetecció [Colwell et al., 1983; Diaz-Delgado et al., 2017; Vidal-Macua, 2017]. Addicionalment, es realitzen estudis aplicats mitjançant imatges d'UAV de molt alta resolució espacial (<10 cm), aplicant tècniques de correcció geomètrica, correcció radiomètrica i mètodes de classificació digital, per tal de generar productes cartogràfics d'alta qualitat i resolució espacial.

Pel que fa a l'estructura dels continguts de la tesi, hi ha quatre capítols on es descriuen detalladament la metodologia i els resultats que satisfan els objectius proposats.

En el primer capítol de l'apartat dels continguts (2.1) s'analitza l'estat de l'art i diversos mètodes de correcció radiomètrica (6S-LaSRC, 6S-LEDAPS, Sen2Cor-SNAP, ATCOR-3, SAC-QGIS, PIA-MiraMon) utilitzats per obtenir reflectàncies a nivell de superfície a partir d'imatges dels Landsat-7, Landsat-8 i Sentinel-2. El repte rau a validar, mitjançant dades espectroradiomètriques captades al moment de pas quasi-simultani de dos dels satèl·lits, la informació espectral que s'obté en les imatges corregides per cada mètode. Aquesta validació és molt rellevant per comprovar la consistència de dades captades per diferents sensors, però també perquè ho siguin al llarg del temps i millorar el processat de sèries temporals d'imatges. En aquest capítol es col·labora principalment amb la Estación Biológica de Doñana (EBD-CSIC) en la captura i tractament de dades espectroradiomètriques de camp, tasca directament relacionada amb l'OG1.

En el segon capítol de l'apartat dels continguts (2.2) s'analitzen quatre mètodes de georeferenciació d'imatges de dron, tres dels quals són mètodes de georeferenciació directa i el restant consisteix en la georeferenciació indirecta. Per cada mètode s'avalua l'exactitud geomètrica quantificant les diferències centimètriques entre el posicionament de referències establertes amb GNSS diferencial d'alta precisió i la seva corresponent posició en la imatge de dron. Aquesta anàlisi es contextualitza amb l'ús combinat d'imatges de dron i imatges obtingudes amb sensors aeroportats o satel·litaris, els seus costos en termes de personal involucrat, temps de processat o necessitat de suport sobre el terreny. En aquest capítol es col·labora amb l'empesa HEMAV en la captura i tractament de dades d'UAV, tasca directament relacionada amb l'OG2.

En el tercer capítol de l'apartat dels continguts (2.3) es descriu detalladament el procés mitjançant el qual s'utilitzen dades d'espectroradiometria de camp per corregir radiomètricament imatges captades amb drons, i un cop corregides s'utilitzen com a referències per validar els mètodes de correcció radiomètrica oficials per les imatges del Landsat-8 (6S-LaSRC) i del Sentinel-2 (Sen2Cor-SNAP). Addicionalment, s'utilitzen les dades de dron com a referència radiomètrica per corregir radiomètricament les imatges de satèl·lit mitjançant l'algorisme CorRad-MiraMon. El disseny experimental consisteix a realitzar mesures radiomètriques de camp i vols de dron en el moment de pas quasi-simultani dels dos satèl·lits objectes d'estudi, fet que permet comparar les reflectàncies a nivell de superfície de les imatges dels dos satèl·lits corregides amb diferents mètodes. En aquest capítol també es col·labora amb l'empesa HEMAV en la captura i tractament de dades d'UAV, tasca directament relacionada amb l'OG1 i l'OG2, esdevenint el capítol central de la Tesi.

En el quart capítol de l'apartat dels continguts (2.4) s'aplica l'ús d'imatges de dron, corregides mitjançant dades d'espectroradiometria de camp, per la generació de cartografia temàtica de cobertes del sòl. L'aplicació dóna suport al monitoratge de la restauració en explotacions mineres a cel obert, amb l'elaboració d'un protocol integrat amb la cartografia oficial i pensat per ser útil per l'administració, pels propietaris d'explotacions mineres, i per la recuperació mediambiental d'espais altament degradats. En aquest capítol també es col·labora amb Centre de Recerca Ecològica i Aplicacions Forestal (CREAF) i el Centre Tecnològic Forestal de Catalunya (CTFC) en la captura i tractament de dades d'UAV, tasca directament relacionada amb l'OG2.

Per una millor comprensió de la relació dels objectius de la Tesi i la seva relació amb els capítols de continguts on es desenvolupen, vegeu el resum gràfic (Figura 12).

Figura 12: Resum gràfic dels objectius de la Tesi i la seva implementació en els diferents capítols de continguts que la conformen.

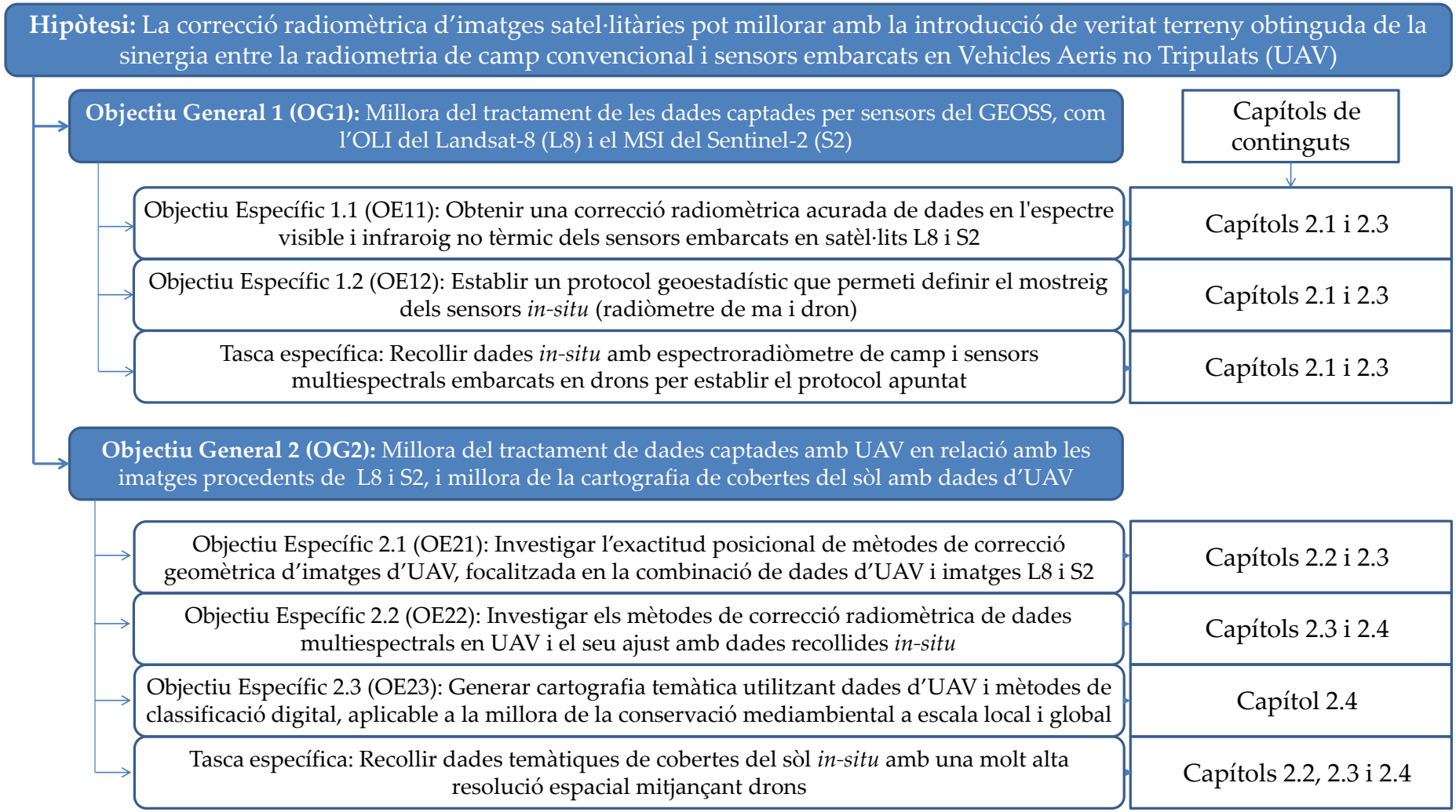

Capítol 2: Continguts

2.1: Ús d'Àrees Pseudoinvariants (PIA) en la correcció radiomètrica d'imatges Landsat-7/8 i Sentinel-2 adquirides simultàniament: Contribució al llegat de la sèrie temporal del Landsat.

2.2: Comparació de quatre mètodes de georeferenciació d'UAV per propòsits de monitoratge ambiental focalitzats en l'ús combinat amb plataformes aèries i satel·litàries.

2.3: Correcció radiomètrica d'escenes Landsat-8 i Sentinel-2A utilitzant imatges de dron en sinergia amb espectroradiometria de camp.

2.4: Monitoratge de restauracions en mines a cel obert utilitzant Sistemes Aeris no Tripulats (UAS).

2.1. Ús d'Àrees Pseudoinvariants (PIA) en la correcció radiomètrica d'imatges Landsat-7/8 i Sentinel-2 adquirides simultàniament: Contribució al llegat de la sèrie temporal del Landsat

Padró J.C., Pons X., Aragonés D., Díaz-Delgado R., García D., Bustamante J., Pesquer L., Domingo-Marimon C., González-Guerrero O., Cristóbal J., Doktor D., Lange M. (2017). Radiometric Correction of Simultaneously Acquired Landsat-7/Landsat-8 and Sentinel-2A Imagery Using Pseudoinvariant Areas (PIA): Contributing to the Landsat Time Series Legacy. *Remote Sensing, 9 (12), 1319-1345*. DOI: 10.3390/rs9121319. http://dx.doi.org/10.3390/rs9121319. (IF: 3.406, Q2: 8/30 (2017) [Remote Sensing]).

Resum: L'ús d'Àrees Pseudoinvariants (PIA) permet realitzar una correcció radiomètrica raonablement robusta i automàtica de sèries temporals d'imatges de teledetecció, tal com es mostra en estudis previs en què s'utilitzen PIA per corregir grans conjunts de dades d'imatges Landsat captades amb els sensors MSS, TM i ETM+. Una de les principals virtuts de les PIA és que contribueixen a obtenir més coherència entre les dades de teledetecció captades amb diferents sensors. El present treball valida l'ús del mètode PIA en la correcció radiomètrica de parells d'imatges (Landsat-7 (ETM+) o Landsat-8 (OLI) i Sentinel-2A (MSI)) adquirides gairebé simultàniament, fent especial èmfasi en els sensors OLI i MSI, pels quals encara no s'havia validat l'ús del mètode basat en PIA. S'han utilitzat quatre parells d'imatges d'una regió del sud-oest de la Península Ibèrica, corresponents a quatre dates diferents, juntament amb mesures d'espectroradiometria de camp recollides en el moment de pas dels satèl·lits, per avaluar una correcció radiomètrica basada en PIA. Els resultats de la implementació del MiraMon (PIA-MiraMon) mostren una gran coherència entre els sensors (R^2>0.964) i excel·lents correlacions amb les dades *in-situ* (R^2>0.9). També s'han avaluat altres alternatives metodològiques, ATCOR3 (ETM+, OLI, MSI), SAC-QGIS (ETM+, OLI, MSI), 6S-LEDAPS (ETM+), 6S-LaSRC (OLI) i Sen2Cor-SNAP (MSI). Gairebé totes les alternatives metodològiques, en especial els mètodes oficials de cada sensor, 6S-LEDAPS per a l'ETM+, 6S-LaSRC per a l'OLI i Sen2Cor-SNAP per a l'MSI, han proporcionat resultats similars als obtinguts amb el mètode PIA. No obstat, la coherència entre les imatges del Landsat i del Sentinel-2 corregides amb els mètodes oficials és superada pel mètode PIA-MiraMon. L'enfoc basat en el PIA es pot aplicar a gairebé qualsevol imatge (fins i tot a imatges que no tenen informació atmosfèrica addicional, o amb nuvolositat) i es pot utilitzar per integrar dades procedents de noves plataformes com Landsat-8 o Sentinel-2, estenent les dades globals adquirides des de 1972 en el marc del programa Landsat. Aquesta recerca contribueix així a la seva continuïtat amb la incorporació radiomètricament consistent de dades captades pel Landsat-8 i el Sentinel-2, un objectiu de gran interès per a la comunitat ambiental, científica i tècnica.

Paraules clau: correcció radiomètrica; Landsat-7; Landsat-8; Sentinel-2A; llegat Landsat; espectroradiometria de camp; Àrees Pseudoinvariants (PIA).

remote sensing

MDPI

Article

Radiometric Correction of Simultaneously Acquired Landsat-7/Landsat-8 and Sentinel-2A Imagery Using Pseudoinvariant Areas (PIA): Contributing to the Landsat Time Series Legacy

Joan-Cristian Padró [1,*], Xavier Pons [1], David Aragonés [2], Ricardo Díaz-Delgado [2], Diego García [2], Javier Bustamante [2], Lluís Pesquer [3], Cristina Domingo-Marimon [3], Òscar González-Guerrero [1], Jordi Cristóbal [4,5], Daniel Doktor [6] and Maximilian Lange [6]

1 Grumets Research Group, Departament de Geografia, Edifici B, Universitat Autònoma de Barcelona, 08193 Bellaterra, Spain; Xavier.Pons@uab.cat (X.P.); Oscar.gonzalez.guerrero@uab.cat (Ò.G.-G.)
2 Remote Sensing and GIS Laboratory (LAST-EBD), Estación Biológica de Doñana (CSIC), C/Américo Vespucio 26, Isla de la Cartuja, 41092 Sevilla, Spain; daragones@ebd.csic.es (D.A.); rdiaz@ebd.csic.es (R.D.-D.); diegogarcia@ebd.csic.es (D.G.); jbustamante@ebd.csic.es (J.B.)
3 Grumets Research Group, CREAF, Edifici C, Universitat Autònoma de Barcelona, 08193 Bellaterra, Spain; l.pesquer@creaf.uab.cat (L.P.); Cristina.Domingo@uab.cat (C.D.-M.)
4 Asiaq-Greenland Survey, P.O. Box 1003-3900 Nuuk, Greenland, Denmark; jcr@asiaq.gl
5 Geophysical Institute and Institute of Northern Engineering, University of Alaska Fairbanks, 903 Koyukuk Dr, Fairbanks, AK 99709, USA
6 Department of Computational Landscape Ecology, Helmholtz Centre for Environmental Research—UFZ Permoserstr, 15, 04318 Leipzig, Germany; daniel.doktor@ufz.de (D.D.); maximilian.lange@ufz.de (M.L.)
* Correspondence: joancristian.padro@uab.cat; Tel.: +34-935-814-343

Received: 7 November 2017; Accepted: 12 December 2017; Published: 15 December 2017

Abstract: The use of Pseudoinvariant Areas (PIA) makes it possible to carry out a reasonably robust and automatic radiometric correction for long time series of remote sensing imagery, as shown in previous studies for large data sets of Landsat MSS, TM, and ETM+ imagery. In addition, they can be employed to obtain more coherence among remote sensing data from different sensors. The present work validates the use of PIA for the radiometric correction of pairs of images acquired almost simultaneously (Landsat-7 (ETM+) or Landsat-8 (OLI) and Sentinel-2A (MSI)). Four pairs of images from a region in SW Spain, corresponding to four different dates, together with field spectroradiometry measurements collected at the time of satellite overpass were used to evaluate a PIA-based radiometric correction. The results show a high coherence between sensors (r^2 = 0.964) and excellent correlations to in-situ data for the MiraMon implementation ($r^2 > 0.9$). Other methodological alternatives, ATCOR3 (ETM+, OLI, MSI), SAC-QGIS (ETM+, OLI, MSI), 6S-LEDAPS (ETM+), 6S-LaSRC (OLI), and Sen2Cor-SNAP (MSI), were also evaluated. Almost all of them, except for SAC-QGIS, provided similar results to the proposed PIA-based approach. Moreover, as the PIA-based approach can be applied to almost any image (even to images lacking of extra atmospheric information), it can also be used to solve the robust integration of data from new platforms, such as Landsat-8 or Sentinel-2, to enrich global data acquired since 1972 in the Landsat program. It thus contributes to the program's continuity, a goal of great interest for the environmental, scientific, and technical community.

Keywords: radiometric correction; Landsat-7; Landsat-8; Sentinel-2A; Landsat Legacy; field spectroradiometry; pseudoinvariant areas (PIA)

1. Introduction and Objective

Long time series of remotely sensed images are necessary for a large variety of applications that are related to Earth Observation (e.g., monitoring land cover change, studying surface temperature dynamics, etc.). One of the longest medium spatial resolution data sets is the Landsat Program. Images have been acquired in this program since 1972, and it is supervised by the National Aeronautics and Space Administration (NASA) and the United States Geological Survey (USGS). The Landsat Data Continuity Mission (LDCM) involves the use of different sensors (Multispectral Scanner System (MSS), Thematic Mapper (TM), Enhanced Thematic Mapper Plus (ETM+), and Operational Land Imager (OLI)), having in common to be sensitive in the region of the electromagnetic spectrum comprised between visible and short wave infrared regions (about 400 nm and 2350 nm) [1]. The LDCM also includes the Return Beam Vidicon (RBV) camera, thermal bands (in the MSS of Landsat-3 and TM/ETM+), and thermal sensors (Thermal Infrared Sensor, TIRS in Landsat-8), which are out of the focus of this paper. Currently, images are still acquired from ETM+, on board Landsat-7, and from OLI, on board Landsat-8. Recently, new sensors with similar spectral characteristics are complementing the Landsat program within the Global Earth Observation System of Systems (GEOSS) [2]. Among them, the Multispectral Imager (MSI) sensor on board the two Sentinel-2 satellites (European Space Agency, ESA) is especially relevant, providing imagery since 2015 (Sentinel-2A) and 2017 (Sentinel-2B) [3], with improved characteristics that are specifically designed to support the Landsat Program [4,5]. Several efforts have been made to review the Landsat Legacy inter-sensor comparison, or to even compare them to other sensors, such as ALI (EO-1) [6,7]. For instance, Mishra et al. [8] used Pseudo Invariant Calibration Sites (PICS), which are spatially uniform sites spectrally stable over time, for on-orbit calibration of Landsat-5 through Landsat-8, and Czapla-Myers et al. [9] used Radiometric Calibration Test Sites that are permanently monitored for Landsat-8. In 2016, ESA completed the processing of its MSS, TM, ETM+, and OLI Level 1 historical archive, and used PICS to validate the inter-sensor coherence between OLI and MSI [10]. Gascon et al. [11] describes Sentinel-2A performance in depth and validates it using PICS and in-situ surface reflectance data. In-situ radiometric measurements, together with sensors with higher spectral but coarser spatial resolution, such as MODIS, are also widely used to validate Landsat and Landsat-like sensors by the Committee on Earth Observation Satellites—Working Group on Calibration and Validation (CEOS-WGCV) [12]—and others [13,14]. Recently, NASA [15] presented a Harmonized Landsat-8 and Sentinel-2 (HLS) product. This is a very interesting product that adopts the tiling system of Sentinel-2 data (Military Grid Reference System, MGRS) and resamples MSI data (10 m or 20 m) to the spatial resolution of OLI (30 m). However, this product does not fit the purpose of this paper due to the unavailability of HLS imagery in some areas that are used in our study and the absence of ETM+ images, as well as the pixel upscaling of MSI imagery. Since 2016, an international collaborative initiative called CEOS-WGCV Atmospheric Correction Inter-comparison Exercise (ACIX) [16] has focused on the results of several atmospheric correction processors that are applied to OLI and MSI imagery from global test sites. Methods are compared by validating the aerosol optical depth and the water vapor content output products with the Aerosol Robotic Network (AERONET) [17] measurements and by validating the surface reflectance results from different approaches with their output time series (one year) with the MODIS (MOD09GA) daily surface reflectance 500 m product, and with fiducial reference measurements [16].

In order to be fully comparable, imagery that were acquired on different dates and by different sensors has to be converted to surface reflectance products through radiometric corrections (atmospheric, and, ideally, also including topographic corrections) [18–24]. With these corrections, at-sensor spectral radiance (Ls_λ) ($W \cdot m^{-2} \cdot sr^{-2} \cdot \mu m^{-1}$) is converted to surface spectral reflectance (ρs_λ) (dimensionless), removing atmospheric effects and accounting for the illumination effects derived from the Sun position (θs, ϕs), the terrain morphology, and the sensor position (θv, ϕv), where θ is the zenith angle and ϕ is the azimuth angle. Most atmospheric gases and aerosols cause effects like scattering, absorption, and polarization of solar radiation, which lead to changes in the incoming irradiance [19,20].

Indeed, through its path from the Top of Atmosphere (TOA) to the Bottom of Atmosphere (BOA) (downwelling path), and back to the sensor once reflected (upwelling path), the energy is scattered and absorbed causing the extinction of the initial energy flux (exoatmospheric spectral irradiance ($E_{SUN\lambda}$) ($W \cdot m^{-2} \cdot \mu m^{-1}$)). This phenomenon of light extinction is quantified with the spectral magnitude known as atmospheric transmittance (τ_λ) (dimensionless). Transmittance is dependent on spectral atmospheric Total Optical Depth (TOD) ($\tau_{0\lambda}$), as greater TOD implies lower transmittances. Transmittance is also dependent on the zenith angle of the illumination vector (the greater the angle the smaller the transmittance). Simultaneously, scattering leads to energy redistribution, and, a part of this energy flux contributes, as diffuse radiance (atmospheric spectral radiance, $Latm_\lambda$ ($W \cdot m^{-2} \cdot sr^{-2} \cdot \mu m^{-1}$)), to the radiance received both at the Earth's surface and at the sensor. Therefore, in general terms, atmospheric corrections of the signal reflected from the Earth's surface have two main unknowns (wavelength dependent) [25]: the Total Optical Depth that weakens the signal, and the atmospheric radiance that contributes to the signal in addition to the reflected beam.

According to this theoretical context, many approaches have been developed to obtain atmospherically corrected surface reflectance data from multispectral imagery in the solar spectrum. These approaches can be summarized into three main groups: the physically based approaches, the image based approaches, and the radiometric reference approaches.

Physical approaches: The most tuned technique is the use of a Radiative Transfer Model (RTM), which accurately calculates the physical effects of the atmosphere over the entire light path, and for which several approaches exist (SCIATRAN [26,27], 6SV1 [28,29], DISORT [30,31], ARTS [32], 4A/OP [33], MODTRAN [34], or libRadtran [35]). Sophisticated physical RTM account for polarization effects, which involve complex calculations due to the dependency of the resulting phase function on the shape of the particle that interacts with the energy (further information on the inclusion of polarization in RTM can be found in the work of Kokhanovsky [19,36–38]). All of these physical RTM are usually very time consuming and need to be fed with accurate atmospheric composition data (e.g., water vapor content, ozone content, aerosol size, and distribution, etc.), which are sometimes obtained from other satellite sensors (MODIS [13] or SCIAMACHY [39]) or from auxiliary information, but ideally from in-situ atmospheric measurements. Although it is currently possible to obtain local atmospheric information from all over the world through global initiatives, such as AERONET (1379 sites on July 2017, some of them currently unavailable [40]), the spatial and temporal coverage of these measurements are scarce when going backwards, especially before 2000 (in 1997 nearly 60 locations contributed to the database) [17].

Image based approaches: Although physical approaches usually obtain better agreement, the unavailability of the data needed to run these models, especially data close in time and/or space to the target image, has led to the wide use of other techniques that avoid using remote or in-situ atmospheric measurements. These approaches are based on the Dark Object Subtraction method (DOS) [23] that assumes the existence of image pixels that should provide a close to zero radiance (dark objects), and assigns, at each band, their value to the atmospheric signal. The at-sensor digital numbers (DN) are converted to spectral radiances using calibration coefficients (gain and bias) that are provided in the image metadata or in specific calibration review works, to later subtract the atmospheric radiance value from every pixel in the atmospheric correction. Several versions of the DOS method make different assumptions about the threshold of the atmospheric radiance determination (histogram properties, minimum value, dense dark vegetation (DDV), etc.). The most basic version assumes total transmittance ($\tau = 1$), and does not account for the diffuse radiance contribution to the target irradiance. The COST version [41] models the downwelling transmittance as a function of the cosine of the Sun zenith angle (θs). Further approaches incorporate upwelling transmittance as a function of the cosine of the view zenith angle (θv), and account for the diffuse radiance that is affecting the target [13].

Radiometric reference approaches: These approaches use radiometric reference values (either from invariant objects or from field data measurements taken simultaneously at satellite pass) to obtain

the unknowns of the physical model (mainly atmospheric ones). In the case of the invariant object method, it is assumed that an image contains target areas with well-known and stable reflectance; the correction is carried out to fit the reflectance of these target areas to their radiometric reference values. A general approach to the invariant object technique was proposed by Hall et al. [42], who intended to obtain a common radiometric response for corrected images that were acquired by different sensors on different dates through "radiometric control sets", which are nonvegetated extremes of the Kauth–Thomas brightness-greenness scattergram; note that these authors point out that "the members of the radiometric control sets may not be the same pixels from image to image". Hadjimitsis et al. [21] used pseudoinvariant targets to atmospherically correct time series with high quality results. Pons et al. [43] presented a hybrid technique between DOS and pseudoinvariant areas (PIA), fitting spectral TOD ($\tau_{0\lambda}$), and spectral atmospheric radiance ($Latm_{\lambda}$) unknowns to match reference values of radiometrically stable areas, which were extracted from existing 10-year surface reflectance TERRA-MODIS products (MOD09GA). The method was able to automatically generate surface reflectance products from MSS, TM, and ETM+ imagery, being validated throughout spectral signature comparisons with Landsat and MODIS official surface reflectance products to evaluate the signature coherence in several land covers (built-up areas, Aleppo pine forests, Scots pine forests, holm oak forests), while the time-series robustness was evaluated with testing PIA not used the radiometric correction procedure (σ_{blue} = 0.54%; σ_{green} = 0.68%; σ_{red} = 0.69%; σ_{NIR} = 1.81%; σ_{SWIR1} = 1.56%; and, σ_{SWIR2} = 0.96%). PIA-based method also yielded good results for land cover classification of multisensory data from the Iberian Peninsula (1980–2015) [44]. In the case of radiometric field data acquired simultaneously to the capture of the image, the measurements are used in a similar way as in the previous case, but these measurements can only be used as a reference to correct the image acquired simultaneously.

In all three approaches, some sophistications make use of Digital Elevation Models (DEM) to consider the terrain effects on the illumination angle, and therefore, improve the accuracy by accounting for the amount of energy the surface receives per unit surface [18].

Alternatively to these three approaches, it is also possible to simply use a purely empirical line fitting. The empirical line fitting approach needs in-situ spectroradiometric measurements at satellite overpass to correct the whole radiance image by adjusting each band to at-surface reflectance measured values through linear regression [45,46], instead of using the data to obtain the unknowns of a physical model. However, this technique is not operational for backdated images or when a complete spatio-temporal field spectroradiometric measurements campaign is needed for a large area, and for that reason, some authors proposed linear fittings using pseudoinvariant features (PIF) [47].

The objective of this paper is to validate the performance of the PIA-based radiometric correction for the current ETM+, OLI, and MSI imagery (since for MSS-TM-ETM+ has already been validated in Pons et al. [43]).

The hypothesis of the present study is that surface reflectance retrieved from ETM+, OLI, and MSI imagery by the PIA-based approach is at least as good as that of other analyzed methods when compared to field data, and, because it has the advantage of allowing backdate radiometric image correction, this approach can contribute to complementing the Landsat time series legacy by adding Landsat-like sensors.

An experiment was designed to compare surface reflectances obtained through a PIA methodology (on ETM+, OLI, and MSI, MiraMon implementation) with field spectroradiometric data acquired at satellite overpass. Moreover, this field data was also compared with the results of commonly used atmospheric correction algorithms, such as ATmospheric CORrection (ATCOR3) [48] on ETM+, OLI, and MSI imagery, Semi-Automatic Classification plug-in implemented in QGIS (SAC-QGIS) [49] on ETM+, OLI, and MSI imagery, Second Simulation of a Satellite Signal in the Solar Spectrum—Landsat Ecosystem Disturbance Adaptive Processing System (6S-LEDAPS) [50] on ETM+ imagery, Landsat Surface Reflectance Code (6S-LaSRC) [51] on OLI imagery, and Sen2Cor implemented in SeNtinel's Application Platform (Sen2Cor-SNAP) [52] on MSI imagery. Finally, the inter-sensor coherence of

each radiometric correction method was evaluated by comparing the results of Landsat and Sentinel simultaneous acquisitions in the sampled pixels.

2. Study Area, Materials and Methods

2.1. Study Area

The study area is located in the region of the Doñana National Park (DNP), SW Spain, and also in SW Europe (Figure 1). Field spectroradiometry and model evaluation was performed in two different sub-areas, "Villanueva de los Castillejos" in the surroundings of the DNP under the scenes R037-29SPB (Sentinel-2 MGRS orbit and tile system [53]) and 203-034 (Landsat World Reference System-2 (WRS-2) path and row system [54]), and "Laguna de Santa Olalla" sub-area inside the DNP under the scenes R137-29SQB and 202-034. Besides the great ecological interest of the study area, it is a flat region and is at sea level. These characteristics mean that methods that do not account for relief illumination effects (such as SAC-QGIS, 6S-LEDAPS, or 6S-LaSRC) can be fairly compared to those that do account for relief illumination effects (such as ATCOR3, Sen2Cor-SNAP, or PTA-MiraMon). However, a method that includes a rigorous topographic correction would need to be considered in other regions with a rugged terrain.

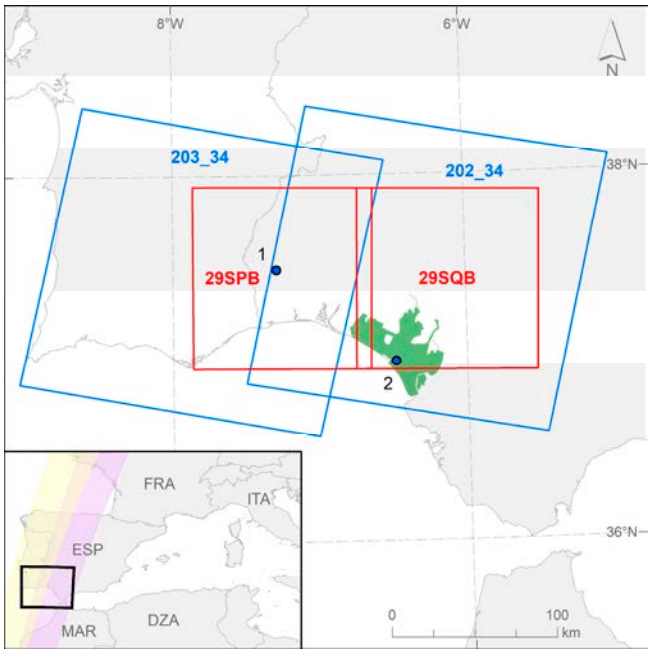

Figure 1. Study area: Doñana National Park in green (Spain, EU), Villanueva de los Castillejos sub-area (1), and Laguna de Santa Olalla sub-area (2). Also shown, Landsat (blue outline) [53] and Sentinel (red outline) scenes [54]. Location map in SW Europe with Sentinel-2 R037 orbit (yellow) and R137 orbit (purple).

2.2. Materials

2.2.1. Satellite Data: Landsat-7 ETM+, Landsat-8 OLI and Sentinel-2A MSI

Landsat-7 and Landsat-8 L1T (Level 1 T: precision terrain-corrected to UTM 29N, WGS84, TOA radiances products) images and the L2A (Level 2 A: geometry as L1T and surface reflectances corrected for atmospheric effects with a cloud mask, a cloud shadow mask, and a water and snow mask) official products were obtained from the USGS website through the EarthExplorer tool [55] (Figure 2). Sentinel-2A L1C (Level 1 C: product results from using a Digital Elevation Model to project the image in cartographic geometry (UTM 29N, WGS84); per-pixel radiometric measurements are provided in TOA reflectances) images and the L2A (Level 2 A: BOA reflectances in cartographic geometry (as L1C)) official products were obtained from the website of the European Space Agency (ESA)—Copernicus through the Scientific Data Hub tool [56] (Figure 2). The time and date of imagery acquisition are shown in Table 1.

Table 1. Features of Landsat-7, Landsat-8 and Sentinel-2A imagery used in the study.

Path/Orbit	Row/Granule	Date of Acquisition	Sun Elevation (Plot Area)	Sun Azimuth (Plot Area)	View Zenith Angle (Plot Area)	Start Time (UTC)	Source	Sensor
203	034	20 May 2016	65.72°	130.47°	3.16°	11:08:03	USGS	OLI
R037	T29SPB		68.70°	140.77°	8.72°	11:29:04	ESA	MSI
202	034	4 October 2016	45.12°	153.91°	0.90°	11:02:33	USGS	OLI
R137	T29SQB		45.72°	156.32°	2.73°	11:09:12	ESA	MSI
202	034	22 April 2017	59.59°	139.03°	0.61°	11:04:57	USGS	ETM+
R137	T29SQB		59.90°	140.01°	2.49°	11:06:51	ESA	MSI
202	034	1 June 2017	66.68°	124.59°	0.89°	11:02:05	USGS	OLI
R137	T29SQB		67.77°	126.71°	2.50°	11:06:51	ESA	MSI

TOA reflectances) images and the L2A (Level-2 A: BOA reflectances in cartographic geometry (as LTC)) official products were obtained from the website of the European Space Agency (ESA)—Copernicus through the Scientific Data Hub tool [56] (Figure 2). The time and date of imagery acquisition are shown in Table 1.

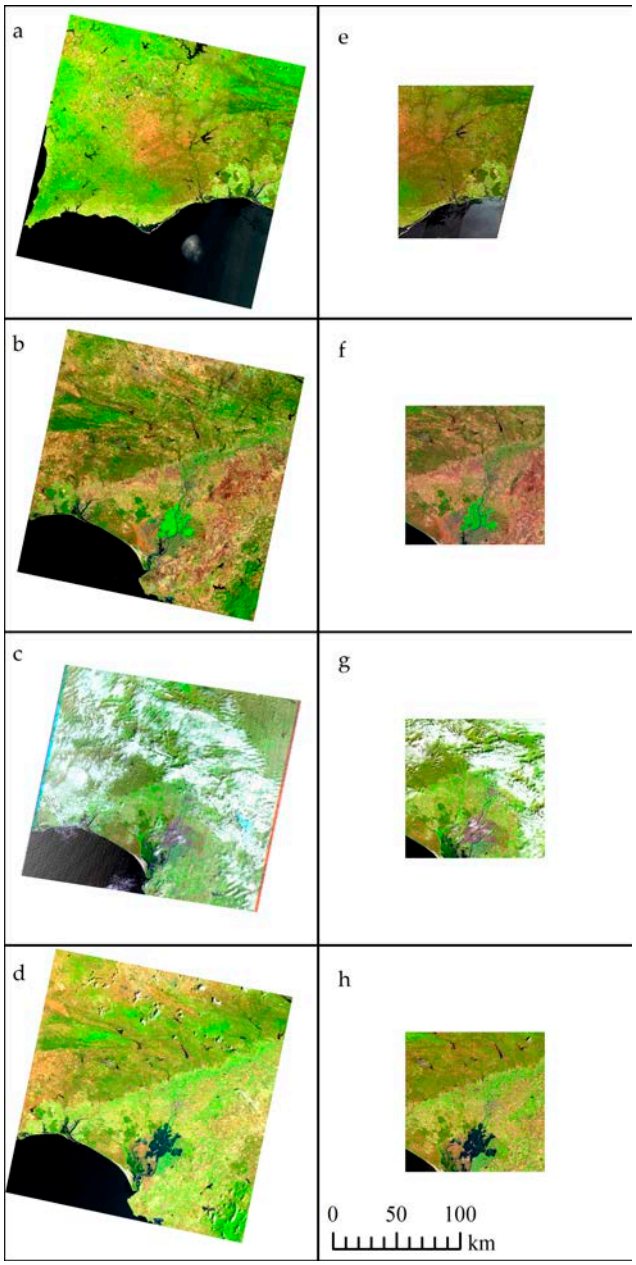

Figure 2. (**Left**) Landsat L1T images used. False color composite image (L7 RGB 543, L8 RGB 654); (**a**) 20 May 2016 (OLI) 203034; (**b**) 4 October 2016 (OLI) 202034; (**c**) 22 April 2017 (ETM+) 202034; (**d**) 1 June 2017 (OLI) 202034. (**Right**) Sentinel-2A L1C images used. False color composite image (S2 RGB 11-8-4); (**e**) 20 May 2016 T29SPB; (**f**) 4 October 2016 T29SQB; and, (**g**) 22 April 2017 T29SQB. (**h**) 1 June 2017 T29SQB.

Figure 2. (**Left**) Landsat L1T images used. False color composite image (L7 RGB 543, L8 RGB 654); (**a**) 20 May 2016 (OLI) 203034; (**b**) 4 October 2016 (OLI) 202034; (**c**) 22 April 2017 (ETM+) 202034; (**d**) 1 June 2017 (OLI) 202034. (**Right**) Sentinel-2A L1C images used. False color composite image (S2 RGB 11-8-4); (**e**) 20 May 2016 T29SPB; (**f**) 4 October 2016 T29SQB; and, (**g**) 22 April 2017 T29SQB. (**h**) 1 June 2017 T29SQB.

Table 1. Features of Landsat-7, Landsat-8 and Sentinel-2A imagery used in the study.

Path/Orbit	Row/Granule	Date of Acquisition	Sun Elevation (Plot Area)	Sun Azimuth (Plot Area)	View Zenith Angle (Plot Area)	Start Time (UTC)	Source	Sensor
203 R037	034 T29SPB	20 May 2016	65.72° 68.70°	130.47° 140.77°	3.16° 8.72°	11:08:03 11:29:04	USGS ESA	OLI MSI
202 R137	034 T29SQB	4 October 2016	45.12° 45.72°	153.91° 156.32°	0.90° 2.73°	11:02:33 11:09:12	USGS ESA	OLI MSI
202 R137	034 T29SQB	22 April 2017	59.59° 59.90°	139.03° 140.01°	0.61° 2.49°	11:04:57 11:06:51	USGS ESA	ETM+ MSI
202 R137	034 T29SQB	1 June 2017	66.60° 67.77°	124.39° 126.71°	0.89° 2.50°	11:02:09 11:06:51	USGS ESA	OLI MSI

The Sentinel-2 and Landsat sensors studied in this paper have six bands that correspond to each other. The spectral configuration of the ETM+ [57], OLI [58], and MSI [59] sensors has common matching bands in the blue, green, red, and short wave infrared (SWIR) regions (Table 2). Nevertheless, in the near infrared (NIR) region, the ETM+ NIR band is wider than the OLI NIR band, corresponding to MSI band 8 and band 8a, respectively. OLI bands are located in the same spectral regions as previous Landsat sensors to ensure spectral continuity [60], and MSI bands are located in the same regions to fit the heritage of Landsat and SPOT Copernicus Service Elements [61]. In other words, the bands that have the longest continuity in the LDCM are those that are located in the visible (VIS) and NIR since the Multispectral Scanner System (MSS) sensor [62], while since the Thematic Mapper (TM) [62], there is continuity in the two SWIR bands, as shown in Table 2. Besides, the Sentinel-2A MSI instrument has three channels in the red edge region (697.5 nm–793 nm) [59] that do not match the ETM+ or OLI sensors, and, for this reason, they are out of the scope of this work.

Table 2. Band correspondence between Multispectral Scanner System (MSS) (example for Landsat-1), Thematic Mapper (TM) (example for Landsat-5), Enhanced Thematic Mapper Plus (ETM+), Landsat-8 (OLI) and Sentinel-2A (MSI) (example for Sentinel-2A), fitting the continuity of the Landsat Program.

	Bandwidths (nm) (#: *Band Number*)					
Sensor	**Blue**	**Green**	**Red**	**NIR**	**SWIR1**	**SWIR2**
MSS [1]		504–602 (#4)	605–701 (#5)	811–990 (#7)		
TM [2]	452–518 (#1)	528–626 (#2)	626–710 (#3)	776–904 (#4)	1567–1785 (#5)	2096–2350 (#7)
ETM+ [3]	441–514 (#1)	519–611 (#2)	631–692 (#3)	772–898 (#4)	1547–1748 (#5)	2064–2346 (#7)
OLI [4]	452–512 (#2)	533–590 (#3)	636–673 (#4)	851–879 (#5)	1567–1651 (#6)	2107–2294 (#7)
MSI [5]	470–524 (#2)	543–578 (#3)	649–680 (#4)	782–898 (#8) 855–875 (#8a)	1569–1658 (#11)	2113–2286 (#12)

[1] Full Width Half Maximum (FWHM) of MSS in Landsat-1 [62]; [2] FWHM of TM in Landsat-5 [63]; [3] FWHM of ETM+ [57]; [4] FWHM of OLI [58]; [5] FWHM of MSI in Sentinel-2A [59].

2.2.2. Field Data: Instrument, Protocol and Sample Data

Field spectroradiometric measurements were acquired by the Remote Sensing and GIS Laboratory Doñana Biological station, Spanish Council for Scientific Research (LAST-EBD (CSIC)), following the Jiménez and Díaz-Delgado [64] methodology, which has been widely used in previous airborne and field campaigns [65,66]. The spectroradiometer used was an ASD FieldSpec3 (Analytical Spectral Devices, Boulder, CO, USA). The spectral range covers the VIS, NIR, and SWIR regions (350 nm–2500 nm), with a spectral resolution (Full Width Half Maximum, FWHM) of 3 nm for the VNIR region (350 nm–1000 nm) and 10 nm for the SWIR region (1000 nm–2500 nm), even though the sampling intervals are 1.4 nm and 2 nm, respectively [67]. Field spectroradiometry sampling areas were designed with a circular shape with a diameter of 20 m. Measurements were taken facing the Sun (to avoid self-shadows) and were collected by sweeping the circle in a zigzag pattern advancing towards the Sun; in the case of water, we made punctual measurements, while remaining as fixed

as possible in the selected water area, following the protocols stated in Peña-Martinez et al. [68] and Mueller et al. [69]. The pointer was located in zenithal position at 150 cm above the ground (nadir view), resulting in a footprint of 65–70 cm (Figure 3a). 20 to 40 measurements were made at each sampling plot and its arithmetic mean, median, and standard deviation was calculated. The reflectance of each land cover was obtained by dividing the average target radiance by the average (10 scans) of a white (Spectralon) reference panel radiance [70]. The two measurements were acquired alternatively and the instrument dark current was measured before each sampling [71,72]. Together with the radiometric measurements, its metadata was taken on the field with a Trimble PDA NOMAD with GPS and Cybertracker software, storing the time, date, location, etc. The accuracy of the GPS is about 5 m, but the areas where the sampling points were made are large and homogeneous enough to be sure that there was no problem correlating with the appropriate pixels. In the present work, the sampling area was previously identified as a homogeneous and flat land cover, including shallow lake water with presence of filamentous algae (*Cladophora fracta*) (Figure 3b), sand of dune (Figure 3c), senescent wheat crops, *albero* (organic ochre sandy clay (Figure 3d)), loamy sand of the dry shallow lake littoral zone, open grasslands (mainly *Vulpia membranacea* and *Malcolmia triloba*), shrubs (*Halimium halimifolium* and *Lavandula stoechas* (Figure 3f)), grasslands (mainly *Poa bulbosa* and *Trifolium subterraneum* (Figure 3e)), or active fern vegetation. Regarding the sampling points within the National Park near Laguna Santa Olalla, they have been used previously by our team in studies with airborne hyperspectral sensors since 2008. It is a well-known area of easy access and with a diverse land cover, of an adequate size, and where the different covers are very close to each other, being able to go from a lake of permanent waters to a dune with very reflective sand in a few minutes (a key characteristic for radiometric studies), and all of this in a protected area with different kinds of natural vegetation. Regarding those located in Villanueva de los Castillejos, they were selected in order to also test over a different satellite orbit and covers (water bodies used for irrigation and to water cattle, large extensions of homogeneous grasslands, etc.). On the outskirts of the town, there is a soccer field covered of *albero* that was also considered potentially interesting, as well as diverse crop fields of easy access.

Remote Sens. **2017**, *9*, 1319 8 of 26

with the appropriate pixels. In the present work, the sampling area was previously identified as a homogeneous and flat land cover, including shallow lake water with presence of filamentous algae (*Cladophora fracta*) (Figure 3b), sand of dune (Figure 3c), senescent wheat crops, *albero* (organic ochre sandy clay (Figure 3d)), loamy sand of the dry shallow lake littoral zone, open grasslands (mainly *Vulpia membranacea* and *Malcolmia triloba*), shrubs (*Halimium halimifolium* and *Lavandula stoechas* (Figure 3f)), grasslands (mainly *Poa bulbosa* and *Trifolium subterraneum* (Figure 3e)), or active fern vegetation. Regarding the sampling points within the National Park near Laguna Santa Olalla, they have been used previously by our team in studies with airborne hyperspectral sensors since 2008. It is a well-known area of easy access and with a diverse land cover, of an adequate size, and where the different covers are very close to each other, being able to go from a lake of permanent waters to a dune with very reflective sand in a few minutes (a key characteristic for radiometric studies), and all of this in a protected area with different kinds of natural vegetation. Regarding those located in Villanueva de los Castillejos, they were selected in order to also test over a different satellite orbit and covers (water bodies used for irrigation and to water cattle, large extensions of homogeneous grasslands, etc.). On the outskirts of the town, there is a soccer field covered of *albero* that was also considered potentially interesting, as well as diverse crop fields of easy access.

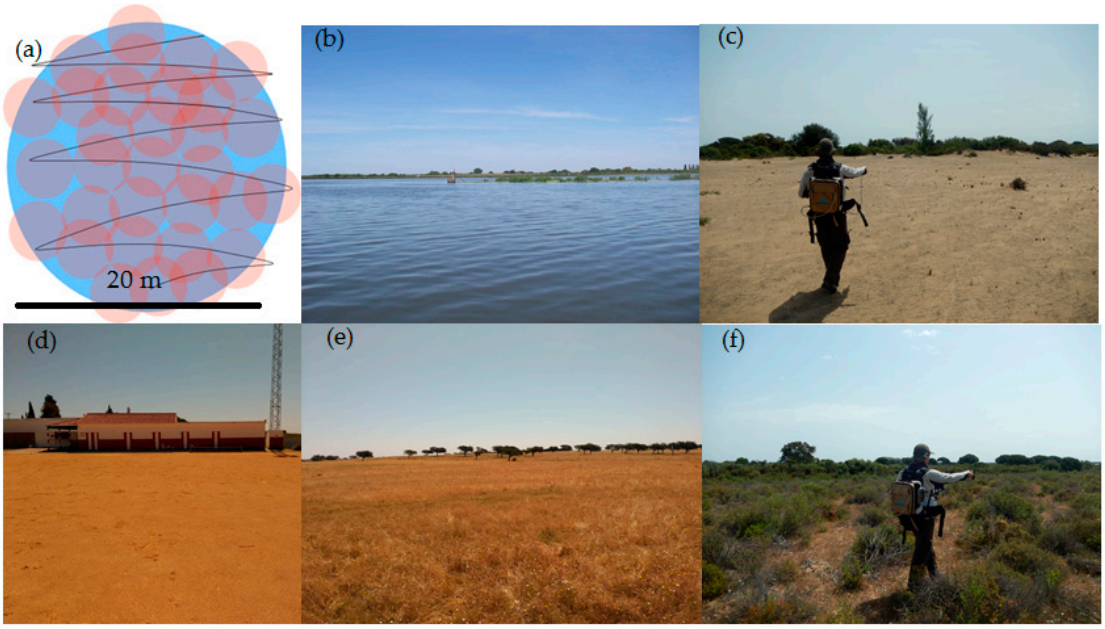

Figure 3. (**a**) Sampling footprint; (**b**) Shallow lake water (DG, 1 June 2017); (**c**) Sand dune (DG, 1 June 2017); (**d**) *Albero* (DA, 20 May 2016); (**e**) Grassland (DA, 20 May 2016); and, (**f**) Shrub (DG, 1 June 2017).

2.2.3. Field Data: Campaigns

On 20 May 2016, concurrently at Landsat-8 and Sentinel-2A overpass, five spectral measurements were collected at five locations in Villanueva de los Castillejos, Huelva (Spain). This zone is close to, but not inside the DNP. The interest of this experimental zone resided in the presence of senescent wheat crops, *albero* (x2) and meadow (x2) samples (Figure 4a,b). The meteorological conditions were good, but not optimum due to some cirrus coming from the south of the scene (Figure 2a,e). A measurement was made in water but it has been discarded of the study

area that was sampled in October 2016. In this campaign, samples of shallow lake water (x2), sand-dunes (x2), open grassland, and shrub vegetation were taken (Figure 4c). The meteorological conditions were good over this site, but the full satellite scene includes heavy clouded areas that are surrounding DNP (54% cloud cover in the ETM+ image and 11% in the MSI image) (Figure 2c,g). Note that this area is located at the central strip of the ETM+ scene, and therefore was not affected by the Scan-Line Corrector failure (SLC-off) gaps (SLC compensates for the forward motion of the satellite, and failed on 2003, causing images having wedge-shaped gaps that range from a single pixel in width near the image-nadir, to about 12 pixels towards the edges of the scene; geostatistical methods [73] and neighbor interpolation methods [74] are commonly used to fill these gaps when needed).

2.2.3. Field Data: Campaigns

On 20 May 2016, concurrently at Landsat-8 and Sentinel-2A overpass, five spectral measurements were collected at five locations in Villanueva de los Castillejos, Huelva (Spain). This zone is close to, but not inside the DNP. The interest of this experimental zone resided in the presence of senescent wheat crops, *albero* (x2), and meadow (x2) samples (Figure 4a,b). The meteorological conditions were good, but not optimum due to some cirrus coming from the south of the scene (Figure 2a,e). A measurement was made in water but it has been discarded of the study due to a sunglint in the Sentinel-2A image (Figure 4b).

On 1 June 2017, concurrently at Landsat-8 and Sentinel-2A overpass, nine spectral measurements were collected at nine locations in the same area of Laguna de Santa Olalla. In this campaign, samples of shallow lake water (x3), sand-dunes (x2), shrubs (x2), open grassland, and bracken were acquired (Figure 4c). The meteorological conditions were excellent (Figures 2d and 3h).

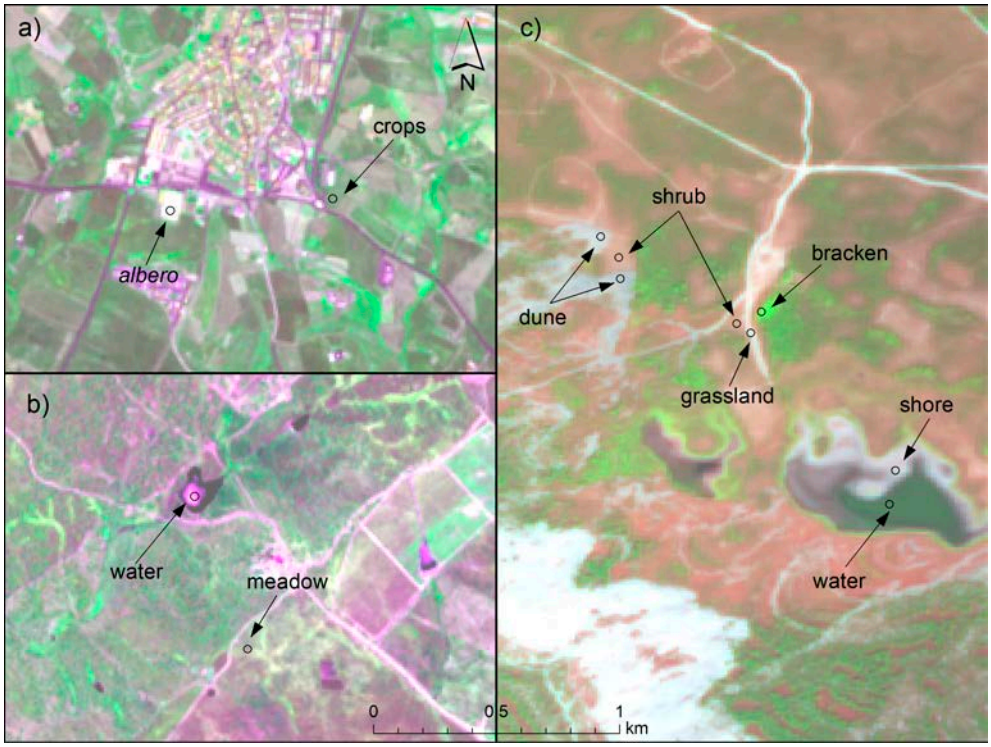

Figure 4. (**a**,**b**) Sampling points near Villanueva de los Castillejos; (**c**) Sampling points near Laguna Santa Olalla.

Figure 4. (**a**,**b**) Sampling points near Villanueva de los Castillejos; (**c**) Sampling points near Laguna Santa Olalla.

2.3. Methods

On 4 October 2016, concurrently at Landsat-8 and Sentinel-2A overpass, six spectral measurements were collected at six locations near Laguna de Santa Olalla, previously used for remote sensing airborne campaigns [65,66], inside the DNP. This zone allows for the rapid acquisition of spectral measurements of shallow lake water, sand-dune (x2), dry shallow lake littoral zone (loamy sand) (x2), and bracken (active fern vegetation) (Figure 4c). The meteorological conditions were good (Figure 2b,f).

On 22 April 2017, concurrently at Landsat-7 and Sentinel-2A overpass, six spectral measurements were collected at six locations in the same area around Laguna de Santa Olalla as the area that was sampled in October 2016. In this campaign, samples of shallow lake water (x2), sand-dunes (x2), open grassland, and shrub vegetation were taken (Figure 4c). The meteorological conditions were good over this site, but the full satellite scene includes heavy clouded areas that are surrounding DNP (54% cloud cover in the ETM+ image and 11% in the MSI image) (Figure 2c,g). Note that this area is located at the central strip of the ETM+ scene, and therefore was not affected by the Scan-Line Corrector failure (SLC-off) gaps (SLC compensates for the forward motion of the satellite, and failed on 2003, causing images having wedge-shaped gaps that range from a single pixel in width near the image-nadir, to about 12 pixels towards the edges of the scene; geostatistical methods [73] and neighbor interpolation methods [74] are commonly used to fill these gaps when needed).

2.3.1. Method 1: ATCOR Based Radiometric Corrections (ATCOR3 and Sen2Cor-SNAP)

In this study, we used the ATCOR3 software for ETM+/OLI/MSI corrections, while the Sen2Cor-SNAP software was used for MSI corrections. The code used in ATCOR3 [48] is also embedded in Sen2Cor-SNAP [75], performing atmospheric and topographic corrections [48]. The atmospheric radiance is obtained through DDV pixels, identified in an initial TOA pre-classification [48] (p. 220). DDV pixels are used as a reference assuming a known reflectance and adjusting the model to the TOD and atmospheric radiance stored in a Look-Up Table (LUT), pre-calculated with MODerate resolution atmospheric TRANsmission (MODTRAN 5). This fitting serves to define the

On 1 June 2017, concurrently at Landsat-8 and Sentinel-2A overpass, nine spectral measurements were collected at nine locations in the same area of Laguna de Santa Olalla. In this campaign, samples of shallow lake water (x3), sand-dunes (x2), shrubs (x2), open grassland, and bracken were acquired (Figure 4c). The meteorological conditions were excellent (Figures 2d and 3h).

2.3. Methods

2.3.1. Method 1: ATCOR Based Radiometric Corrections (ATCOR3 and Sen2Cor-SNAP)

In this study, we used the ATCOR3 software for ETM+/OLI/MSI corrections, while the Sen2Cor-SNAP software was used for MSI corrections. The code used in ATCOR3 [48] is also embedded in Sen2Cor-SNAP [75], performing atmospheric and topographic corrections [48]. The atmospheric radiance is obtained through DDV pixels, identified in an initial TOA pre-classification [48] (p. 220). DDV pixels are used as a reference assuming a known reflectance and adjusting the model to the TOD and atmospheric radiance stored in a Look-Up Table (LUT), pre-calculated with MODerate resolution atmospheric TRANsmission (MODTRAN 5). This fitting serves to define the MODTRAN 5 aerosol model that best fits the image. Once the aerosol type is chosen, transmittance is provided by a LUT, accounting for solar position, path length, and the physical components of TOD (τ_0): Rayleigh scattering, molecular absorption (O_3, H_2O, CO_2), and aerosol scattering. Sen2Cor-SNAP provides additional features described by Pflug [76]. As noted in the Sen2Cor Algorithm Theoretical Basis Document (ATBD), LUTs for ATCOR3 are based on MODTRAN 5, while Sen2Cor LUTs are based on the Library for Radiative Transfer (libRadtran) [75] (p. 6). Another difference between Sen2Cor and ATCOR3 is the use of the European Center for Medium-Range Weather Forecast (ECMWF) aerosol database when DDV are missing within the scene [76]. If a DEM is used for topographic correction, then the illumination effects are corrected (from local zenith angle, slope, and aspect), and the percentage of the sky viewed for every pixel and their adjacency effects are taken into account [75]. We used "Aerosol Type = Rural" and "Water Vapor Category = Mid-latitude summer (water vapor column: 2.92 cm for sea level)" for Landsat ATCOR3 atmospheric corrections of all of the months except for 4 October 2016 images, where was used Water "Vapor Category = Fall/Spring (water vapor column: 1.14 cm for sea level)". For Sentinel-2A imagery ATCOR-based algorithms presented best results with "Aerosol Type = Rural" and automatically detecting WV LUT category using band #9 and in Sen2Cor specific case using the standard Atmospheric Precorrected Differential Absorption (APDA) model. The same DEM was used in ATCOR3 and PIA-MiraMon Landsat and Sentinel imagery for topographic corrections and for the estimation of atmospheric parameters as function of height, a very detailed 5 m DEM from Plan Nacional de Ortofotografía Aérea (PNOA) [77], resampled and aligned by bilinear interpolation at 10 m, 20 m and 30 m to fit the different spatial resolutions involved. The Sen2Cor official products used the Shuttle Radar Topographic Mission (SRTM) 90 m DEM [78] default option for the same previous purposes.

2.3.2. Method 2: Semi-Automatic Classification (SAC-QGIS)

Semi-Automatic Classification (SAC) is a plug-in implemented in QGIS, which is designed to perform a land cover classification quickly, but an atmospheric correction is carried out in the pre-processing step [49]. This atmospheric correction is based on the basic DOS technique, inspired by Chavez [41] and Moran et al. [79], which approximates the path radiance value of a given band from the minimum value of the histogram (dark object), assuming an intrinsic reflectance of this object. This approximation assumes that the darkest object of the scene must have a reflectance (1%), but the rest of the radiance that is received by the satellite sensor proceeds from the atmospheric path, and must be then subtracted from every pixel before dividing the at-sensor spectral radiance by the irradiance. The model assumes that the transmittance is 1 [49], considering total atmospheric transparency in all of the images, which simplifies the model, but at the same time could act as a source of error. The SAC-QGIS method is quick and simple, fully image-based, avoiding the need

for atmospheric auxiliary data to perform the correction. Nevertheless, it does not approximate the TOD and does not account for topographic effects, a characteristic that is not relevant in the present study due to the flat morphology of the study area, but it is highly relevant in mountainous areas [80], although there are studies suggesting that topographic correction may not be justified in change detection routines computing spectral trends from pixel-based composites [81].

2.3.3. Method 3: 6S Based Radiometric Corrections (Landsat Surface Reflectance Code (LaSRC) and Landsat Ecosystem Disturbance Adaptive Processing System (LEDAPS) Atmospheric Correction)

The Landsat Surface Reflectance Code (LaSRC) [24,51] is a code that is designed to obtain Level 2A products, that is, to transform TOA radiance to surface reflectance. This code is based on the Second Simulation of the Satellite Signal in the Solar Spectrum (6S) [28,29] radiative transfer code. 6S uses a sophisticated procedure [82] that has been successfully validated and implemented for previous Landsat solar-reflective bands in the Landsat Ecosystem Disturbance Adaptive Processing System (LEDAPS) project [50,83,84]. LaSRC is thus an improved development that takes advantages of the better radiometric and spectral features of OLI, plus the better ancillary data sets [24]. LaSRC and LEDAPS are part of the USGS Climate Data Record (CDR) long-term consistently-processed data sets that are derived from Landsat data, having the purpose to deliver an atmospherically-corrected high level product that is useful for obtaining essential biophysical variables, such as NDVI, or for land cover mapping. For further information, see Vermote et al. [24,82,85], Kotchenova et al. [28,29], Masek et al. [50] and Feng et al. [83,84]. The 6S-based official products use Global Climate Model DEM for the estimation of atmospheric parameters as function of height, but not for topographic correction [50,51].

2.3.4. Method 4: Pseudoinvariant Area Radiometric Correction (PIA-MiraMon)

Pseudoinvariant Area (PIA) radiometric correction method [43] is a 2014 improvement of a simpler model that is published in Pons and Solé-Sugrañes [18] and implemented in the MiraMon software [86] from 1994 to retrieve surface reflectance from TOA radiance, accounting for TOD, atmospheric radiance, and topography (including self and cast-shadows, TOD dependency on height, etc.). The method consists of fitting the model on the basis of reference reflectance values that are saved in PIAs. In this case, PIAs are extracted from robustly filtered Terra-MODIS reflectance product (MOD09GA) imagery (500 m cell size) on the base of the high agreement between MODIS data and Landsat imagery [83,84]. The entire time series of the MODIS mid-resolution reflectance product images is rigorously filtered, removing cloud covered pixels, and those pixels with a zenithal view angle wider than 35°, because marginal pixels are seriously resampled due to the MODIS field of view geometry. A geostatistical analysis [87] is applied to detect spatial anomalies that complement the quality assessment of the official products. Selection of high quality MOD09GA imagery leads to a selection of pixels with lower standard deviation (around $\sigma < 2\%$, depending on the band) along the MODIS time series. Finally, a PIA polygon databank is then built for all of the time series to be corrected in the region of interest, becoming a reflectance reference to fit the model unknowns: Total Optical Depth ($\tau_{0\lambda}$) and atmospheric radiance ($Latm_\lambda$). Before running the model fully in a given band, each PIA is checked and its value is compared to the values of the image to be corrected in a previous loop simulation model to discard areas that cannot be assumed as invariant (e.g., clouds or their shadows, land cover change, snow, etc.). This ensures reliable PIAs. Note that a PIA can be spectrally heterogeneous while it is radiometrically stable, that is, even if there are different land covers inside the area, it is invariant if its global reflectance does not change over time. Thus, a PIA cannot be considered to be a typical pseudoinvariant feature [47], Pseudoinvariant Calibration Site [8], or Radiometric Calibration Test Site [9]. PIA-MM is not constricted with atmospheric models, since by PIA it is fitted the best combination of TOD and path radiance. The DEM that is used is the same as for ATCOR3, as previously described (Section 2.3.1).

2.3.5. Field Spectroradiometry as a Reference to Compare Radiometric Correction Results

Remote Sens. **2017**, *9*, 1319 12 of 26

The Relative Spectral Response Function (RSRF) of the ETM+ [57], OLI [58], and MSI [59] instruments was used to integrate in-situ reflectance measurements (Figure 5). Although it is possible to obtain a synthetic value by computing a simple mean from the nominal FWHM bandwidth, it is worth using the available RSRF and accounting for the sensitivity of every band of the satellite sensor [88,89]. After resampling field spectroradiometry data to the satellite sensor sensitivity, spectral field measurements were taken as the reference for the comparison of the accuracies of the radiometric correction methods. The comparison was made according to the sensor (ETM+, OLI or MSI) and acquisition date (May, October, April, June).

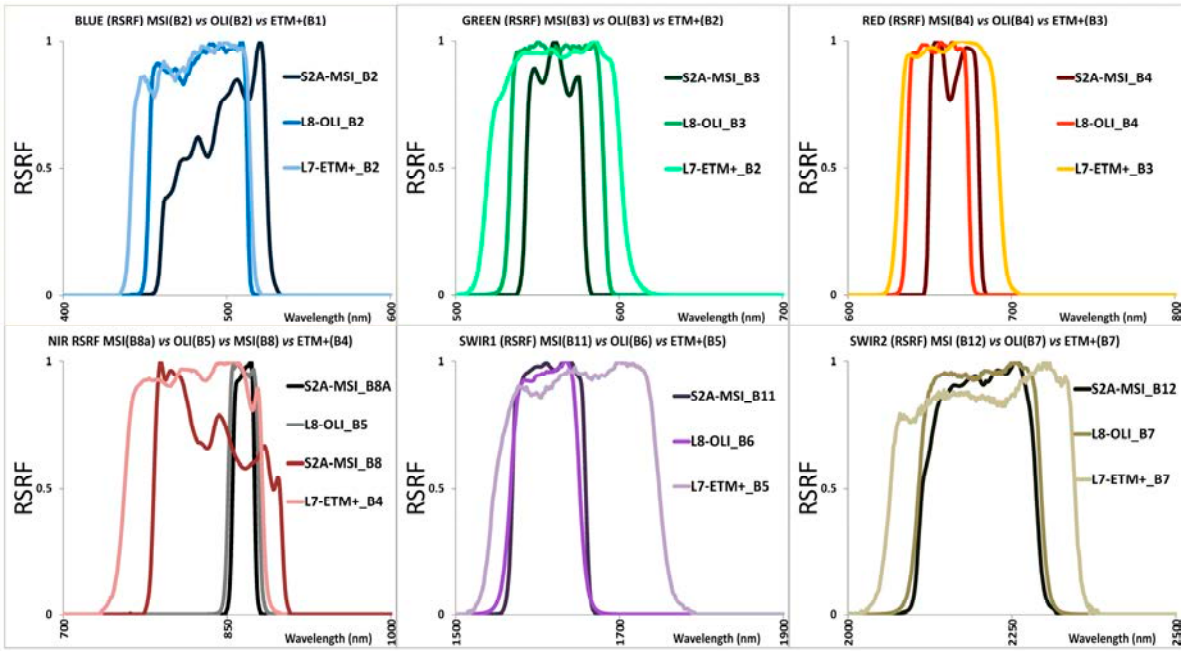

Figure 5. Relative Spectral Response Function (RSRF) of blue, green, red, NIR, SWIR1, and SWIR2 matching bands on MSI instrument in Sentinel-2A, OLI instrument in Landsat-8 and ETM+ instrument in Landsat-7.

Figure 5. Relative Spectral Response Function (RSRF) of blue, green, red, NIR, SWIR1, and SWIR2 matching bands on MSI instrument in Sentinel-2A, OLI instrument in Landsat-8 and ETM+ instrument in Landsat-7.

30 m and 20 m imagery was resampled to 10 m pixels to manage geometric issues (misalignment and different spatial resolutions). Then, a 10 m buffer from the center of field radiometry plot was done. This buffer is selecting a maximum of nine pixels of 10 m. The area intersected by the circle and each affected pixel is used to compute its contribution (weight) to the final reflectance value to be compared to the field radiometry. It is crucial that sites are uniform and homogeneous to have a minimal scale effect (Figure 6).

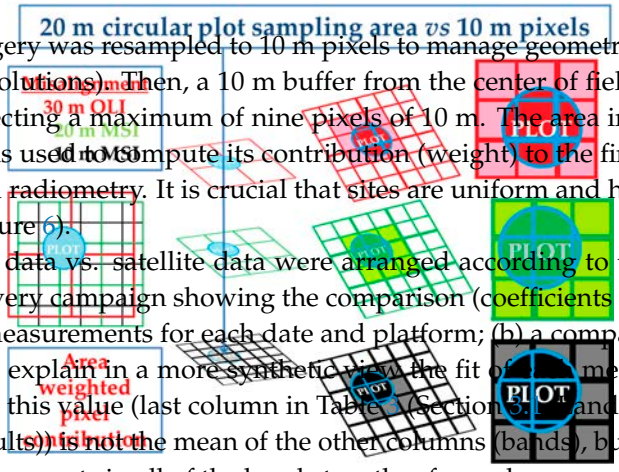

Figure 6. Geometric procedure used to compare pixels of Landsat-8 OLI (30 m) and Sentinel-2A MSI (20 m and 10 m) with field data plots of 20 m of diameter: 30 m and 20 m pixels are resampled to 10 m and the 20 m of diameter of plot area covers up to 9 pixels. The area that is intersected by the circle in each affected pixel is used to compute its contribution (weight) to the final reflectance value to be compared to the field radiometry.

The results of field data vs. satellite data were arranged according to three types of analysis: (a) detailed results for every campaign showing the comparison (coefficients of determination, r^2) of single, band-by-band, measurements for each date and platform; (b) a comparison (r^2) grouping all of the bands together to explain in a more synthetic view the fit of each method for each platform and each date (note that this value (last column in Table 4 (Section 3.1, Landsat results) and Table 5 (Section 3.2, Sentinel results)) is not the mean of the other columns (bands), but rather the r^2 obtained by comparing the measurements in all of the bands together for each sensor and date); and, (c) as an overall accuracy indicator, an additional summary information was provided, in reflectance units (%), by grouping all of the dates for each platform together to obtain the root mean square error (RMSE) of each spectral region and its mean value.

Summarizing the four field campaigns, there were 26 field reflectance measurements spectrally resampled to six bands, resulting in 156 band samples for evaluating the performance of each radiometric correction method of the corresponding satellite sensor. The coherence of each method

Figure 5. Relative Spectral Response Function (RSRF) of blue, green, red, NIR, SWIR1, and SWIR2 matching bands on MSI instrument in Sentinel-2A, OLI instrument in Landsat-8 and ETM+ instrument in Landsat-7.

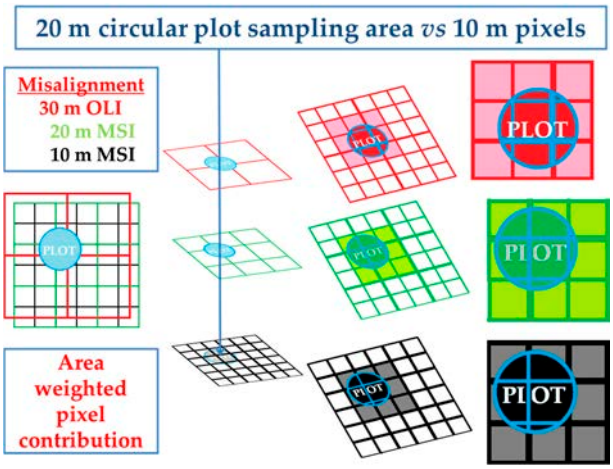

Figure 6. Geometric procedure used to compare pixels of Landsat-8 OLI (30 m) and Sentinel-2A MSI (20 m and 10 m) with field data plots of 20 m of diameter: 30 m and 20 m pixels are resampled to 10 m and the 20 m of diameter of plot area covers up to 9 pixels. The area that is intersected by the circle in each affected pixel is used to compute its contribution (weight) to the final reflectance value to be compared to the field radiometry.

Figure 6. Geometric procedure used to compare pixels of Landsat-8 OLI (30 m) and Sentinel-2A MSI (20 m and 10 m) with field data plots of 20 m of diameter: 30 m and 20 m pixels are resampled to 10 m and the 20 m of diameter of plot area covers up to 9 pixels. The area that is intersected by the circle in each affected pixel is used to compute its contribution (weight) to the final reflectance value to be compared to the field radiometry.

Summarizing the four field campaigns, there were 26 field reflectance measurements spectrally resampled to six bands, resulting in 156 band samples for evaluating the performance of each radiometric correction method of the corresponding satellite sensor. The coherence of each method

Table 3. Band-by-band coefficient of determination (r^2) between field spectroradiometry values and atmospheric corrections for Landsat-7 (ETM+) and Landsat-8 (OLI) imagery. Best values in bold.

Field vs. Landsat		Blue r^2	Green r^2	Red r^2	NIR r^2	SWIR1 r^2	SWIR2 r^2	All Bands r^2
May 2016	ATCOR3	0.998	**0.998**	**0.999**	0.993	**0.997**	**0.992**	0.987
	SAC-QGIS	0.996	**0.998**	0.998	**0.995**	0.996	0.991	0.961
	6S-LaSRC	**0.999**	**0.998**	**0.999**	**0.995**	0.996	**0.992**	0.982
	PIA-MM	0.996	**0.998**	0.998	**0.995**	0.996	0.991	**0.989**
October 2016	ATCOR3	0.950	0.916	0.940	0.902	0.954	0.967	0.918
	SAC-QGIS	0.940	0.909	0.936	0.902	**0.956**	**0.968**	0.862
	6S-LaSRC	**0.992**	**0.942**	**0.948**	**0.906**	0.955	**0.968**	0.892
	PIA-MM	0.939	0.907	0.935	0.895	0.953	**0.968**	**0.922**
April 2017	ATCOR3	0.956	**0.941**	**0.950**	0.972	**0.979**	**0.964**	0.908
	SAC-QGIS	**0.958**	0.936	0.949	**0.973**	**0.979**	0.962	0.871
	6S-LEADAPS	**0.958**	0.936	0.949	**0.973**	**0.979**	0.962	**0.919**
	PIA-MM	**0.958**	0.937	**0.950**	**0.973**	**0.979**	0.962	0.918
June 2017	ATCOR3	0.935	0.934	0.916	0.989	0.959	0.929	0.948
	SAC-QGIS	0.933	0.934	0.917	0.989	0.959	0.929	0.907
	6S-LaSRC	**0.939**	**0.939**	**0.919**	0.989	0.959	0.929	0.941
	PIA-MM	0.933	0.935	0.918	**0.990**	**0.962**	**0.931**	**0.954**

Summarizing the four field campaigns, there were 26 field reflectance measurements spectrally resampled to six bands, resulting in 156 band samples for evaluating the performance of each radiometric correction method of the corresponding satellite sensor. The coherence of each method is evaluated by correlating the 156 samples of the Landsat and the Sentinel pairs of radiometrically corrected images, which were acquired almost simultaneously (+21 min. on May images, +6 min. on October images, +2 min. on April images, and +5 min on June images), and assuming that the results should ideally be highly similar. It is important to note that, as seen in the previous section, the Landsat official products and the Sentinel-2A official products do not use the same radiometric correction method, but many final users work with these products and so it was interesting to also add this comparison.

The overall workflow of the comparison between field spectroradiometry data and the radiometrically corrected data is summarized in Figure 7. The results are first given for Landsat platforms and then for Sentinel-2A.

Landsat official products and the Sentinel-2A official products do not use the same radiometric correction method, but many final users work with these products and so it was interesting to also add this comparison.

The overall workflow of the comparison between field spectroradiometry data and the radiometrically corrected data is summarized in Figure 7. The results are first given for Landsat platforms and then for Sentinel-2A.

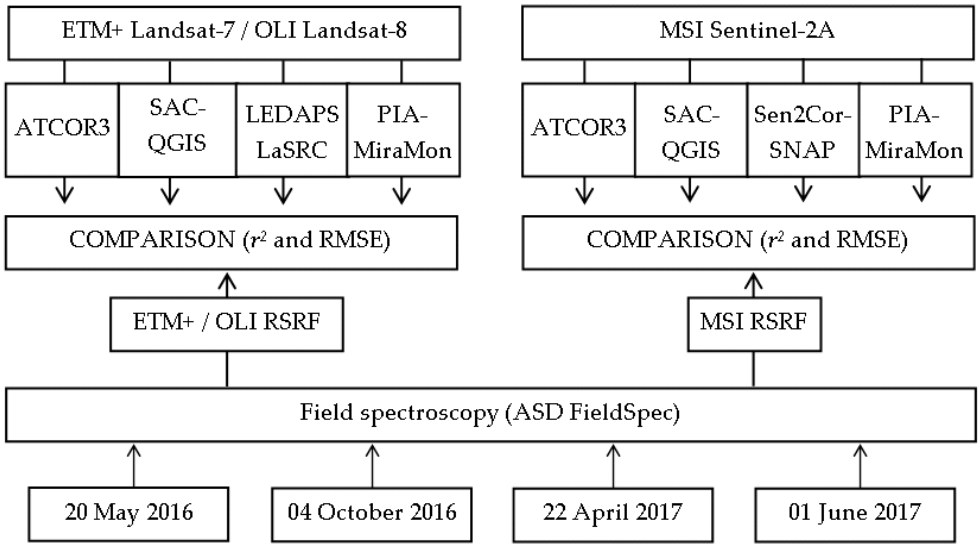

Figure 7. General workflow, for a given date, of radiometric correction methods and their comparison with field spectroradiometry data.

3. Results

3.1. Results for Landsat Platforms

Landsat-8 imagery acquired on 20 May 2016 yielded an excellent fit with in-situ measurements. 6S-LaSRC had the highest r^2 for blue band (0.999), ATCOR3 for SWIR1 bands (0.997) and both tie in the red and SWIR2 bands (0.999, 0.992). PIA-MiraMon, 6S-LaSRC and SAC-QGIS had the best agreement for the NIR bands (0.995) and tie with ATCOR in green band (0.998). When all band samples were grouped together (Table 3), PIA-MiraMon had a superior r^2 agreement (0.989), followed by ATCOR3 (0.987), 6S-LaSRC (0.982) and SAC-QGIS (0.961).

For Landsat-8 imagery that was acquired on 4 October 2016, 6S-LaSRC had better agreement with the blue, green, red and NIR bands (0.992, 0.942, 0.948, 0.906), SAC-QGIS for SWIR1 (0.956) and SAC-QGIS, 6S-LaSRC and PIA-MiraMon tie in the SWIR2 band (0.968). When all band samples were grouped together, PIA-MiraMon again showed better agreement (0.922), followed by ATCOR3 (0.918), 6S-LaSRC (0.892) and SAC-QGIS (0.862) (Table 3).

The Landsat-7 imagery acquired on 22 April 2017 had 54% cloud cover, but all of the corrections showed optimum fitting with in-situ data because the sky was clear over the measurement area. All of the methods yielded similar r^2 values for each band individually. When all of the bands were grouped together, 6S-LEDAPS showed the best agreement (0.919), followed by PIA-MiraMon (0.918), ATCOR3 (0.908), and SAC-QGIS (0.871) (Table 3).

In Landsat-8 imagery that was acquired on 1 June 2017 all of the corrections showed a good fit with in-situ data. 6S-LaSRC yielded the highest r^2 for the blue, green, and red bands (0.939, 0.939, 0.919), while PIA-MiraMon obtained better results for the NIR, SWIR1, and SWIR2 bands (0.990, 0.962, 0.931). When all of the bands were grouped together, PIA-MiraMon showed the best r^2 (0.954), followed by ATCOR3 (0.948), 6S-LaSRC (0.941), and SAC-QGIS (0.907) (Table 3).

The p-value of all the bands and methods is <0.01. Figure 8 shows the correlations between field data and its corresponding pixels of Landsat imagery, corrected with each method and each month, grouping all bands.

0.962, 0.931). When all of the bands were grouped together, PIA-MiraMon showed the best r^2 (0.954), followed by ATCOR3 (0.948), 6S-LaSRC (0.941), and SAC-QGIS (0.907) (Table 3).

The *p*-value of all the bands and methods is <0.01. Figure 8 shows the correlations between field data and its corresponding pixels of Landsat imagery, corrected with each method and each month, grouping all bands.

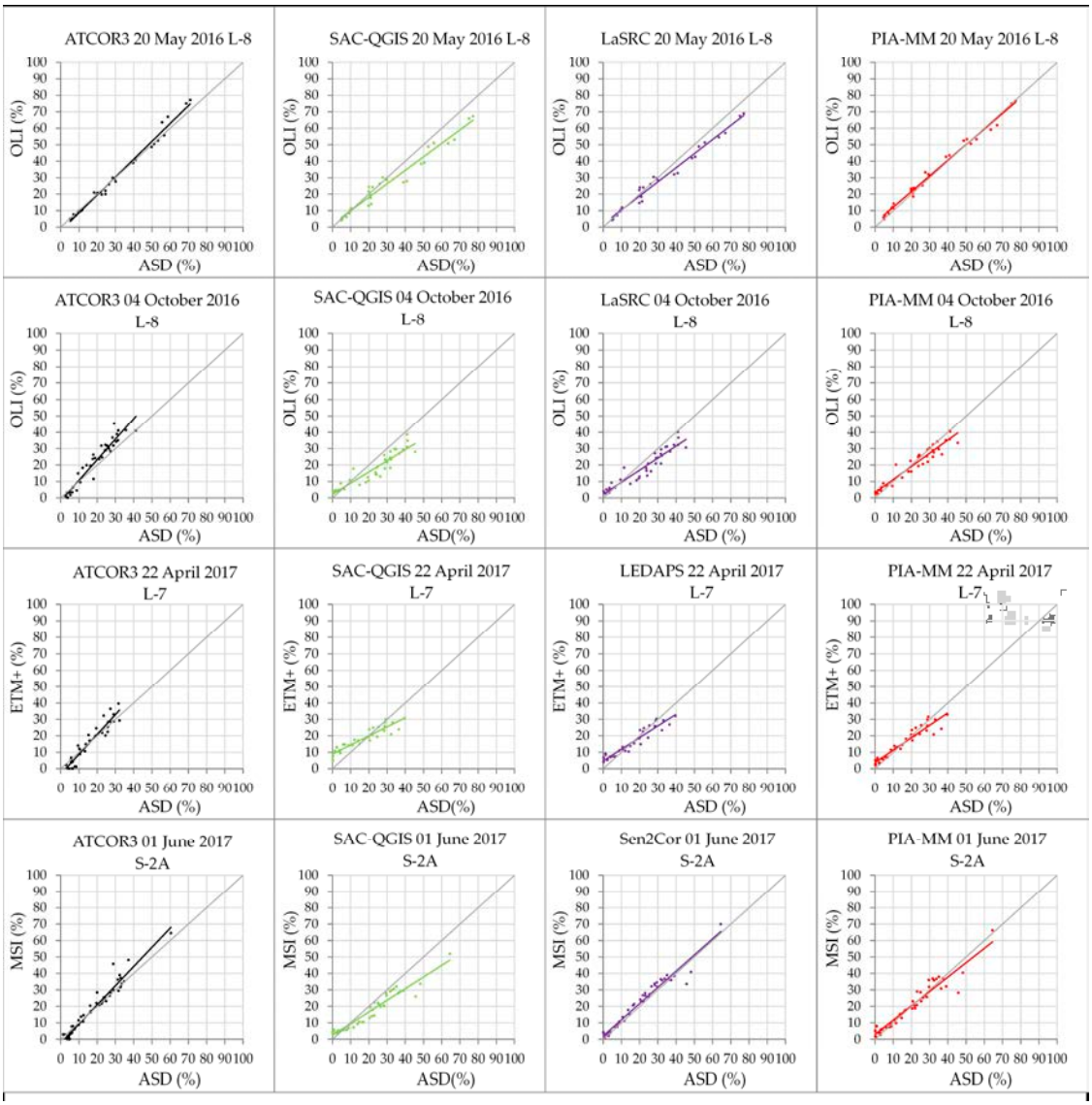

Figure 8. Scatterplots of the correlation between field measurements (*X* axis) and the values of its corresponding pixel in each each Landsat atmospheric correction method (*Y* axis) accounting for all bands (last column in Table 3).

Figure 8. Scatterplots of the correlation between field measurements (*X* axis) and the values of its corresponding pixel in each each Landsat atmospheric correction method (*Y* axis) accounting for all bands (last column in Table 3).

In terms of the differences in reflectance values of all the methods used for Landsat scenes, the PIA-MiraMon radiometric correction had the lowest RMSE values in five out of six bands (visible bands (1.588, 2.645, 3.384), SWIR1 (3.988), SWIR2 (5.350)), while ATCOR3 provided the best result in NIR (3.745). PIA-MiraMon had the best result for all band averages (3.468) (Table 4 and Figure 9).

In terms of the differences in reflectance values of all the methods used for Landsat scenes, the PIA-MiraMon radiometric correction had the lowest RMSE values in five out of six bands (visible bands (1.588, 2.645, 3.384), SWIR1 (3.988), SWIR2 (5.350)), while ATCOR3 provided the best result in NIR (3.745). PIA-MiraMon had the best result for all band averages (3.468) (Table 4 and Figure 9).

Table 4. Overall band-by-band RMSE between field spectroradiometry values and atmospheric corrections for Landsat (OLI and ETM+) imagery (% reflectance units) grouping all dates. Best values in bold.

Field vs. Landsat	Blue RMSE	Green RMSE	Red RMSE	NIR RMSE	SWIR1 RMSE	SWIR2 RMSE	Mean RMSE
ATCOR3	2.392	2.956	3.588	**3.745**	4.764	6.019	3.911
SAC-QGIS	5.871	5.987	5.755	5.083	5.710	7.199	5.934
6S	3.768	4.150	4.490	4.484	4.987	6.037	4.653
PIA-MM	**1.588**	**2.645**	**3.384**	3.948	**3.988**	**5.350**	**3.484**

in bold.

Field vs. Landsat	Blue RMSE	Green RMSE	Red RMSE	NIR RMSE	SWIR1 RMSE	SWIR2 RMSE	Mean RMSE
ATCOR3	2.392	2.956	3.588	**3.745**	4.764	6.019	3.911
SAC-QGIS	5.871	5.987	5.755	5.083	5.710	7.199	5.934
6S	3.768	4.150	4.490	4.484	4.987	6.037	4.653
PIA-MM	**1.588**	**2.645**	**3.384**	3.948	**3.988**	**5.350**	**3.484**

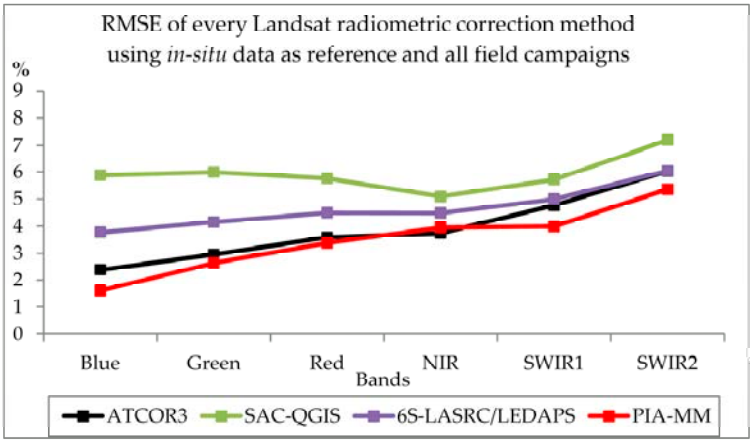

Figure 9. Band-by-band Root Mean Square Error of each radiometric correction method analyzed for Landsat images, grouping all dates.

Figure 9. Band-by-band Root Mean Square Error of each radiometric correction method analyzed for Landsat images, grouping all dates.

The band-by-band behavior of the PIA-MiraMon method for Landsat imagery (Table 3) shows good agreement, and October is the month with the lowest agreement results. PIA-MiraMon does not fail in any band when Landsat imagery is corrected. Moreover, when the RMSE is considered (Table 4), PIA-MiraMon obtains the lowest differences with respect to the in-situ data in all of the bands, except NIR.

The band-by-band behavior of the PIA-MiraMon method for Landsat imagery (Table 3) shows good agreement, and October is the month with the lowest agreement results. PIA-MiraMon does not fail in any band when Landsat imagery is corrected. Moreover, when the RMSE is considered (Table 4), PIA-MiraMon obtains the lowest differences with respect to the in-situ data in all of the bands, except NIR.

3.2. Results for the Sentinel Platform

3.2. Results for the Sentinel Platform

The Sentinel-2A imagery acquired on 20 May 2016 showed an excellent fit, with in-situ measurements for all of the methods. Sen2cor-SNAP yielded the highest r^2 for the blue, green, and red bands (0.999, 0.998, 0.999), SAC-QGIS for the NIR band (0.988), ATCOR3 for the SWIR2 band (0.945), and ATCOR3 and PIA-MiraMon showed the same r^2 for the SWIR1 band (0.969). When all of the bands were grouped together, PIA-MiraMon yielded the best r^2 (0.966), followed by Sen2cor-SNAP (0.961). ATCOR3 (0.960) agreement was very close to the Sen2cor-SNAP results, and finally SAC-QGIS (0.939) yielded the lowest agreement with in-situ data (Table 5).

Sentinel-2A imagery that was acquired on 4 October 2016 showed a good fit, with in-situ measurements for all of the bands and for all the methodologies. ATCOR3 yielded the highest r^2 for the blue, green, red, NIR, and SWIR1 bands (0.995, 0.994, 0.996, 0.955, 0.975), while for the SWIR2 band, PIA-MiraMon had the highest (0.983). When all of the bands were grouped together, Sen2Cor-SNAP had the best r^2 (0.963), followed by PIA-MiraMon (0.958), ATCOR3 (0.952), and SAC-QGIS (0.886) obtained the lowest fit to in-situ data (Table 5).

Sentinel-2A imagery acquired on 22 April 2017 showed a good fit with in-situ measurements for all of the bands and for all methodologies. ATCOR3 showed the highest r^2 for the green and SWIR1 bands (0.920, 0.991), Sen2Cor-SNAP for the NIR and SWIR2 bands (0.984, 0.986), followed by the PIA-MiraMon method for the blue band (0.922) and SAC-QGIS for the red band (0.915). When all of the bands were grouped together, Sen2Cor-SNAP had the best r^2 (0.948), followed by ATCOR (0.942), SAC-QGIS (0.907), and PIA-MiraMon (0.897) (Table 5).

Sentinel-2A imagery that was acquired on 1 June 2016 showed a good fit to in-situ measurements for all the bands and for all of the methodologies. Sen2Cor-SNAP yielded the highest r^2 for the blue, green and red bands (0.992, 0.991, 0.995), tying with ATCOR3 and PIA-MiraMon in the NIR and SWIR2 bands (0.992, 0.953). When all the bands were grouped together, Sen2Cor-SNAP again showed the best r^2 (0.961), followed by ATCOR3 (0.953), SAC-QGIS (0.939), and PIA-MiraMon (0.932) (Table 5).

The p-value of all the bands and methods is <0.01. Figure 10 shows the correlations between field data and its corresponding pixels of Sentinel-2 imagery corrected with each method and each month, grouping all of the bands.

Remote Sens. **2017**, *9*, 1319 17 of 26

Table 5. Band-by-band coefficient of determination (r^2) between field spectroradiometry values and atmospheric corrections for Sentinel-2A (MSI) imagery. Best values in bold.

Field vs. Sentinel-2A	Blue r^2	Green r^2	Red r^2	NIR r^2	SWIR1 r^2	SWIR2 r^2	All Bands r^2
ATCOR3	0.987	0.981	0.978	0.987	**0.969**	**0.945**	0.960
SAC-QGIS	0.994	0.997	0.998	0.986	0.968	0.942	0.961
Sen2Cor-SNAP	**0.999**	**0.998**	**0.999**	0.986	0.968	0.942	0.961
PIA-MM	0.994	0.997	0.997	0.987	**0.969**	0.944	**0.966**
ATCOR3	**0.995**	**0.994**	**0.996**	**0.955**	**0.975**	0.982	0.952
SAC-QGIS	0.989	0.975	0.986	0.952	0.971	0.982	0.886
Sen2Cor-SNAP	0.986	0.970	0.988	0.951	0.971	0.981	**0.963**
PIA-MM	0.986	0.972	0.984	0.950	0.972	**0.983**	0.958
ATCOR3	0.911	**0.920**	0.902	0.982	**0.991**	0.907	0.942
SAC-QGIS	**0.922**	0.917	**0.915**	0.983	0.988	0.985	0.907
Sen2Cor-SNAP	0.916	0.913	**0.915**	**0.984**	0.989	**0.986**	**0.948**
PIA-MM	**0.922**	0.917	0.914	0.982	0.985	0.983	0.897
ATCOR3	0.925	0.931	0.929	**0.992**	**0.970**	**0.953**	0.953
SAC-QGIS	0.979	0.982	0.991	0.991	0.967	0.952	0.939
Sen2Cor-SNAP	**0.992**	**0.991**	**0.995**	**0.992**	0.968	**0.953**	**0.961**
PIA-MM	0.979	0.982	0.992	**0.992**	0.968	0.952	0.951

Table 6. Overall band-by-band RMSE between field spectroradiometry values and atmospheric corrections for Sentinel-2A (MSI) imagery (% reflectance units) grouping all dates. Best values in bold.

Field vs. Sentinel-2A	Blue RMSE	Green RMSE	Red RMSE	NIR RMSE	SWIR1 RMSE	SWIR2 RMSE	Mean RMSE
ATCOR3	1.991	2.339	3.381	3.569	5.772	7.393	4.074
SAC-QGIS	1.262	2.217	5.068	5.129	6.621	7.726	6.006
Sen2Cor-SNAP	2.317	2.881	3.190	**3.519**	4.764	**5.353**	3.671
PIA-MM	**1.727**	**2.284**	**3.070**	3.973	**4.383**	5.370	**3.468**

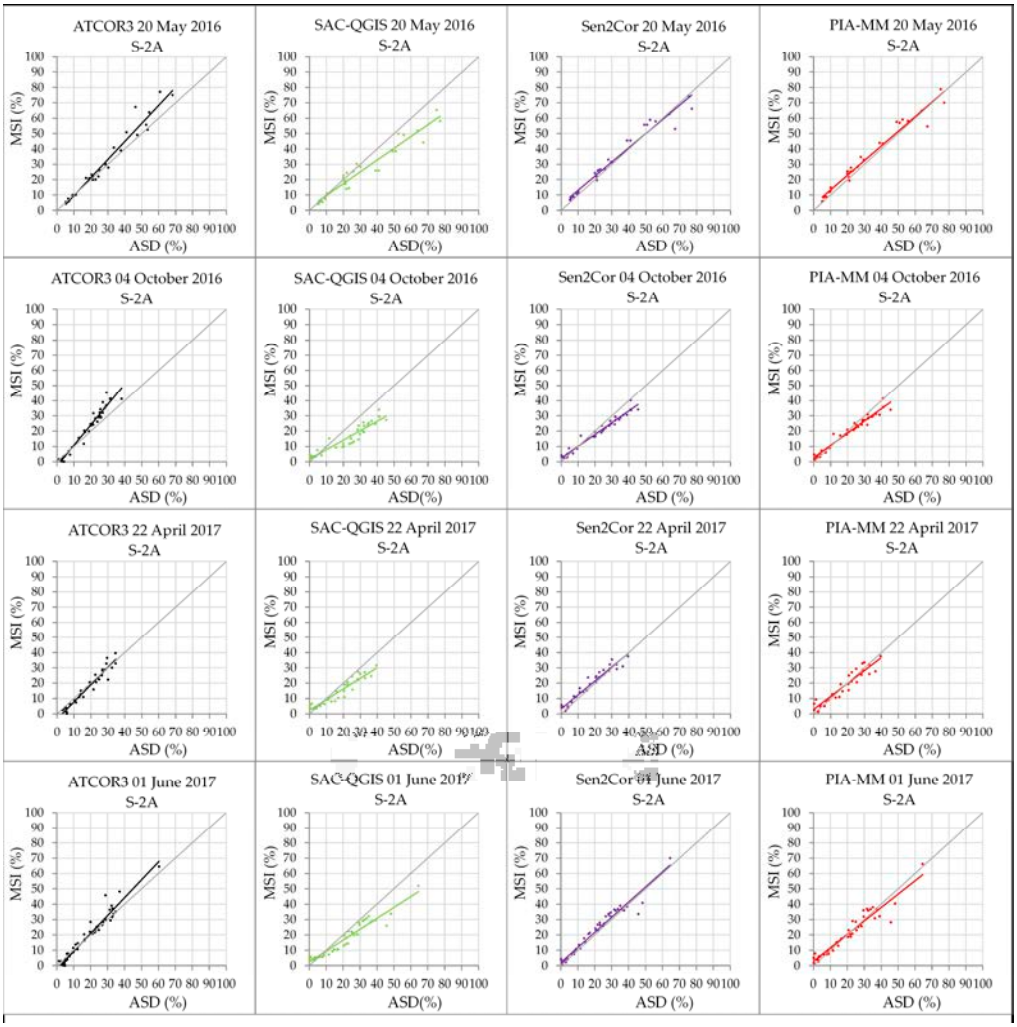

Figure 10. Scatterplots of the correlation between field measurements (*X* axis) and the values of its corresponding pixel in each Sentinel-2 atmospheric correction method (*Y* axis) accounting for all the bands (last column in Table 5).

Figure 10. Scatterplots of the correlation between field measurements (*X* axis) and the values of its corresponding pixel in each Sentinel-2 atmospheric correction method (*Y* axis) accounting for all the bands (last column in Table 5).

The analysis of the band-by-band behaviour of the PIA-MiraMon method for Sentinel-2A imagery (Table 5) shows that r^2 also yields a good agreement. There is no band where PIA-MiraMon fails when Sentinel-2A imagery is corrected. Moreover, when the RMSE is considered (Table 6), PIA-MiraMon obtains the lowest differences with respect to the in-situ data in all of the bands, except for NIR and SWIR2.

In terms of the differences in reflectance values of all methods used for Sentinel-2A images, the PIA-MiraMon radiometric correction had the lowest RMSE values in four out of six bands (visible bands (1.727, 2.284, 3.070) and SWIR1 (4.383)), the Sen2Cor-SNAP official product provided the best result in NIR and SWIR2 (3.519, 5.352), and ATCOR3 obtained better results in NIR (3.569) then PIA-MiraMon. PIA-MiraMon had the best result for all of the band averages (3.468) (Table 6 and Figure 11).

Table 6. Overall, band-by-band RMSE between field spectroradiometry values and atmospheric corrections for Sentinel-2A (MSI) imagery (% reflectance units) grouping all dates. Best values in bold.

Field vs. Sentinel-2A	Blue RMSE	Green RMSE	Red RMSE	NIR RMSE	SWIR1 RMSE	SWIR2 RMSE	Mean RMSE
ATCOR3	1.991	2.339	3.381	3.569	5.772	7.393	4.074
SAC-QGIS	4.262	7.217	5.068	5.129	6.621	7.736	6.006
Sen2Cor-SNAP	2.317	2.881	3.190	**3.519**	4.764	**5.352**	3.671
PIA-MM	**1.727**	**2.284**	**3.070**	3.973	**4.383**	5.370	**3.468**

Remote Sens. **2017**, *9*, 1319 18 of 26

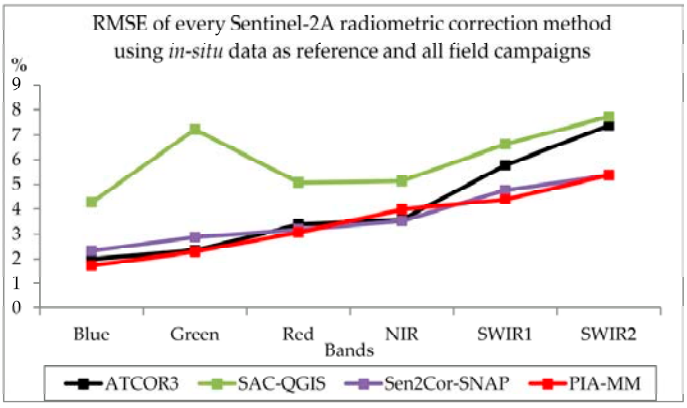

Figure 11. Band-by-band Root Mean Square Error of each radiometric correction method analyzed for Sentinel-2A images, grouping all dates.

Figure 11. Band-by-band Root Mean Square Error of each radiometric correction method analyzed for Sentinel-2A images, grouping all dates.

3.3. Inter-Sensor Coherence

The analysis of the band-by-band behaviour of the PIA-MiraMon method for Sentinel-2A imagery (Table 5) shows that r^2 also yields a good agreement. There is no band where PIA-MiraMon fails when Sentinel-2A imagery is corrected. Moreover, when the RMSE is considered (Table 6), PIA-MiraMon obtains the lowest differences with respect to the in-situ data in all of the bands, except for NIR and SWIR2.

3.3. Inter-Sensor Coherence

Correlation of Landsat and Sentinel-2A images that were acquired almost at the same time, and corrected with the same method (except for the official products (6S-LEDAPS/6S-LaSRC and Sen2Cor-SNAP)), showed the best coefficient of determination (r^2) for PIA-MiraMon in the blue, green, and red bands (0.916, 0.961, 0.966), for SAC-QGIS in the SWIR1 and SWIR2 bands (0.982, 0.972), and for ATCOR3 in NIR band (0.986) (Table 7). When all of the bands were grouped together, the best r^2 was found when the PIA-MiraMon method (0.964) was used, followed by ATCOR3 (0.960), SAC-QGIS (0.955), and the official products (0.929), as seen in Figure 12.

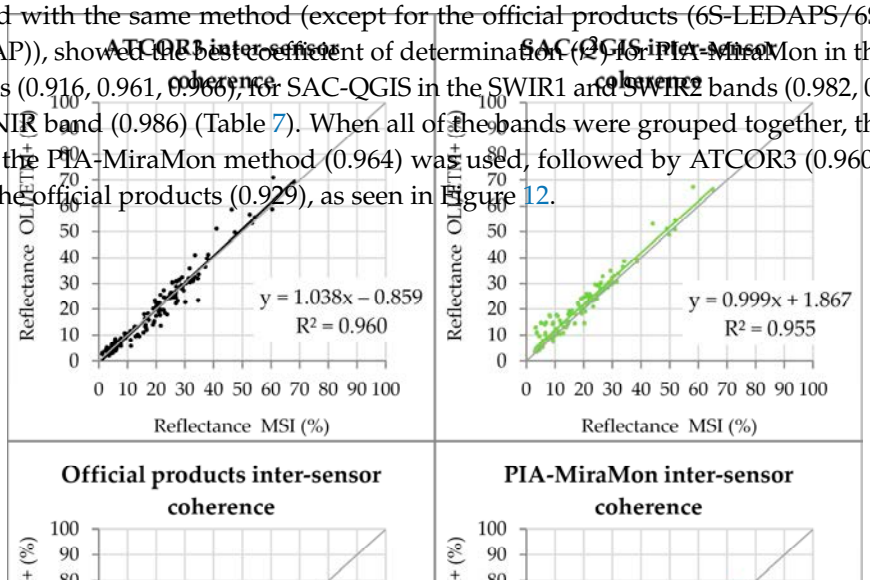

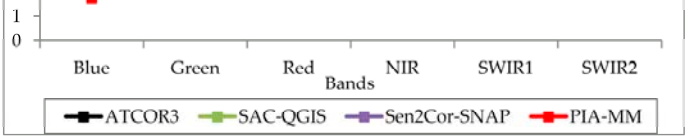

Figure 11. Band-by-band Root Mean Square Error of each radiometric correction method analyzed for Sentinel-2A images, grouping all dates.

Table 7. Band-by-band coefficient of determination (r^2) between simultaneous Landsat (ETM+ and OLI) and Sentinel-2A (MSI) radiometrically corrected images. Correlated values are sampled pixels. Best values in bold.

Sentinel-2A vs. Landsat	Blue r^2	Green r^2	Red r^2	NIR r^2	SWIR1 r^2	SWIR2 r^2	All Bands r^2
ALL DATES	ATCOR3	0.908	0.916	0.927	**0.986**	0.979	0.927	0.960
	SAC-QGIS	0.298	0.799	0.928	0.981	**0.982**	**0.972**	0.955
	Official products	0.901	0.939	0.931	0.976	0.976	0.967	0.929
	PIA-MM	**0.916**	**0.961**	**0.966**	0.972	0.975	0.970	**0.964**

3.3. Inter-Sensor Coherence

Correlation of Landsat and Sentinel-2A images that were acquired almost at the same time, and corrected with the same method (except for the official products (6S-LEDAPS/6S-LaSRC and Sen2Cor-SNAP)), showed the best coefficient of determination (r^2) for PIA-MiraMon in the blue, green, and red bands (0.916, 0.961, 0.966), for SAC-QGIS in the SWIR1 and SWIR2 bands (0.982, 0.972), and for ATCOR3 in NIR band (0.986) (Table 7). When all of the bands were grouped together, the best r^2 was found when the PIA-MiraMon method (0.964) was used, followed by ATCOR3 (0.960), SAC-QGIS (0.955), and the official products (0.929), as seen in Figure 12.

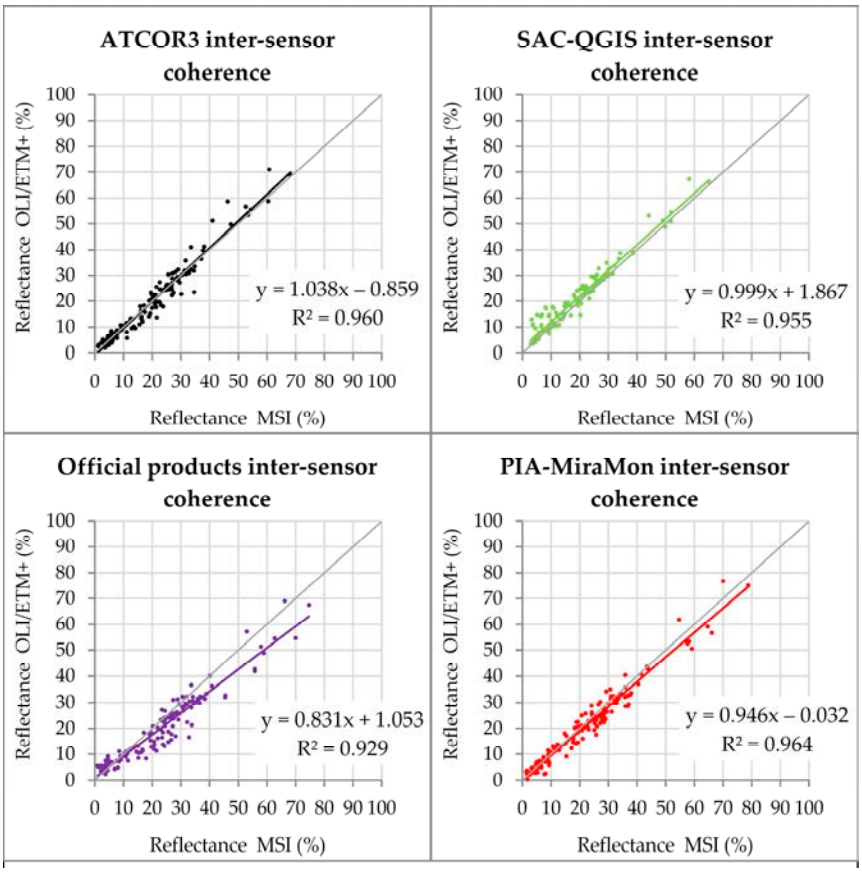

Figure 12. Correlation of Landsat and Sentinel-2A images corrected with the same method (except for official products) evaluating the pixels sampled with field measurements (n = 156).

4. Discussion

Analyzing the coeffecient of determination (r^2) results that are described above, we find that the PIA-MiraMon radiometric correction method showed a very good fit with field data for all of the bands. Only in seven out of the 48 analyses (6 bands × 4 dates × 2 platforms) did PIA-MiraMon yield the lowest r^2 value, but it is worth noting that, in these cases, the difference with the next worst method is only around 0.007 points. In 15 out of the 48 analyses PIA-MiraMon yielded the highest agreement (in some cases tying with other methods), and in the remaining 26 analyses the performance of PIA-MiraMon is comparable to the other methods.

When r^2 was calculated using all of the samples for all bands, and for a given sensor and date (last column in Tables 3 and 5), PIA-MiraMon obtained the highest value in four of the eight cases. The other four best results were obtained when official tools were used (6S-LEDAPS for ETM+, 6S-LaSRC for OLI, and Sen2Cor-SNAP for MSI). Moreover, PIA-MiraMon was the method that

performed best in three of the four cases of OLI imagery, and 6S-LEDAPS was the best in the remaining case. Sen2Cor-SNAP was the method that performed best in three of the four cases of MSI imagery, and PIA-MiraMon was the best in the remaining case.

Although the methods that we compared use different approaches and models, the results are not dramatically different, a similar situation also noticed by Song [47] when comparing different atmospheric correction methods for Landsat-5 TM imagery (DOS (4 variants), DDV, Modified DDV (MDDV), path radiance lineal regression (PARA), and linear relationship using PIF), showing very good and similar results for the DOS and PIF approaches. Now, our results over ETM+, OLI, and MSI show that the PIA-based method clearly offers better accuracies than the DOS method. Note that the PIF-based method uses a linear relationship between radiometric references and the image to be corrected, while the PIA-based method uses the radiometric references to fit the best combination of TOD and path radiance values. In consonance with our findings, where physical approaches do not significantly improve the results of radiometric reference approaches, Song concluded that a huge difference in model complexity does not necessary imply the same difference in accuracy.

The difference in the results cannot be explained by the use or not of a DEM because the selected area is absolutely plain, but can be explained by the influence of the atmospheric parameters (atmospheric spectral radiance ($Latm_\lambda$) and Total Optical Depth) that are used in each method. That the SAC-QGIS method does not use the TOD seems to be the major source of discrepancy for this method; SAC-QGIS obtains good coefficients of determination, but the RMSE (in reflectance values (%)) is not as good as other methods. ATCOR-based and 6S-based methods use OLI and MSI bands that are located at specific wavelengths to obtain the distribution of aerosol and water-vapor content in the atmosphere, yielding very good results, but it is worth noting that these bands do not exist in ETM+, TM, and MSS sensors, and the same exact method cannot be used for this imagery. The PIA-MiraMon method obtains similar results as the official products by adjusting the atmospheric parameters to a radiometric surface reflectance reference databank. The PIA-MiraMon method obtains good results because it can exclude the PIA that would not keep the reference value in the case of being corrected (due to cloud presence, land cover changes, etc.), while it can adjust the best combination of $Latm_\lambda$ and TOD in the PIAs that keep the reference value. Moreover, this capability makes it possible to correct images from the present and the past using the same PIA databank. The accurate selection of the most stable pixels of all the MODIS series to obtain the PIA databank is crucial for dealing with trustable radiometric surface reflectance references.

Besides showing a good adjustment to and low differences with field data, PIA-MiraMon obtained the best results in inter-sensor coherence. SAC-QGIS showed a good inter-sensor correlation in infrared bands, but in the reflectance differences (RMSE) to field data, the results were not as reliable as the other methods (PIA-MiraMon, ATCOR3 or official products). The results of the inter-comparison of official products were not unexpected, as the use of different radiometric correction codes, which are specifically adapted to each sensor, provided good outcomes for their corrected imagery, but not the best correlations between inter-sensor data. Vuolo et al. [90] evaluated the Sen2Cor-SNAP and 6S-LaSRC coherence at six european test sites, obtaining an $r^2 = 0.9$, similar to the $r^2 = 0.92$ obtained in the present study. On the other hand, PIA-MiraMon showed a good inter-sensor correlation ($r^2 = 0.96$), providing robustly corrected data, because it is based on common radiometric areas. Note that the SAC-QGIS inter-sensor coherence in the blue and green bands is notably lower than the other methods, a result that can be explained by the assumption of TOD = 1 of SAC-QGIS and to an inaccurate estimation of atmospheric radiance by the DOS method that is specially affecting the spectral regions where atmospheric scattering is more important. Finally, the effects of the different MSI, OLI, and ETM+ RSRF can explain the lower inter-sensor correlations in the blue band for all of the methods (Table 7), since MSI of Sentinel-2A has a significantly lower sensitivity between 460 nm and 520 nm [59] than OLI [58], ETM+ [57], or even the MSI instrument of Sentinel-2B [59] (Figure 5).

5. Conclusions

Field spectroradiometry measurements for different land cover types for four different dates were used to evaluate the performance of the PIA-MiraMon radiometric correction method applied to pairs of Landsat and Sentinel imagery acquired almost simultaneously. The results were also compared with three other radiometric correction methods.

The comparison of field spectroradiometric measurements with simultaneous acquisitions of Landsat-7 (ETM+), Landsat-8 (OLI), and Sentinel-2A (MSI) imagery that was radiometrically corrected using the PIA-MiraMon method yielded good agreement results ($r^2 > 0.9$) for the different dates. The results were similar, when not better, to the same field measurements with the imagery radiometrically corrected with other standard products (6S-LaSRC, 6S-LEDAPS, Sen2Cor-SNAP) and widely used methods (ATCOR3, SAC-QGIS).

Specifically, four pairs of images acquired almost simultaneously from two platforms, three pairs of Landsat-8 and Sentinel-2A, and another pair of Landsat-7 and Sentinel-2A were processed. When the RMSE was computed between radiometrically corrected satellite data and field spectroradiometric data for the whole set of Landsat images, PIA-MiraMon yielded superior results for five out of six bands (mean value: 3.484%), while ATCOR3 provided the best results for the NIR band (mean value of all bands: 3.911%). Similarly, the results for Sentinel-2A images also showed that PIA-MiraMon yielded the best results for four out of the six bands (mean value of all bands: 3.468%), while the official Sen2Cor-SNAP provided the best results for the other 2 (NIR and SWIR2) (mean value of all bands: 3.671%).

In general, the results of the methods from the official agencies (6S-LEDAPS, 6S-LaSRC, Sen2Cor-SNAP) showed very good agreement for their own sensors, but general products, especially ATCOR3, also showed very good results for MSI. On average, SAC-QGIS was the method showing least agreement, although it was not far from the other products analyzed.

The inter-sensor comparison has proven the consistency of the PIA-MiraMon method, showing that it provides a coherent correction of images that were acquired almost simultaneously ($r^2 > 0.964$); this confirms the robustness of this method when time series involving different sensors are corrected.

In accordance with previous demonstrations of the PIA approach that was used to radiometrically correct long time series [43], it has now been proven that this is a sound method for contributing to the Landsat time series legacy by coherently correcting imagery from the current Landsat continuity instrument (OLI) and a Landsat-like instrument, such as MSI.

In addition to being a reasonably robust and automatic radiometric correction procedure, it is important to highlight that the PIA-based radiometric correction method is capable of correcting pre-MODIS images and/or when no detailed atmospheric data is available, and it provides similar accuracies than other reference solutions. PIA-MiraMon is the Radiometric Correction module that is available in the Professional MiraMon GIS & RS software, running either from command line (CorRad.exe) or from a dialog box in the Tools main menu.

Acknowledgments: A special acknowledgment is given to Ruhtz for his advice given to C.P. during the 2016 EUFAR/ESA Expert Workshop on Atmospheric Correction of Remote Sensing Data. This work is supported by the European Union through the ECOPOTENTIAL Project (H2020 641762-2 EC) and by the Spanish Ministry of Science and Innovation through the ACAPI project (CGL2015-69888-P (MINECO/FEDER)). GRUMETS Research Group is partially supported by the Catalan Government under Grant (SGR2014-1491). Cristian Padró is the recipient of a FI-DGR scholarship grant (2016B_00410). Xavier Pons is the recipient of an ICREA Academia Excellence in Research Grant (2016–2020). We would like to acknowledge ESA-Copernicus and USGS-NASA for the availability of satellite data.

Author Contributions: Ricardo Díaz-Delgado, Javier Bustamante, Xavier Pons, David Aragonés and Cristina Domingo-Marimon conceived and designed the experiments. David Aragonés and Ricardo Díaz-Delgado performed the field data experiments. Lluís Pesquer and Xavier Pons wrote the needed software. Daniel Doktor and Maximilian Lange contributed to ATCOR3 corrections. Lluís Pesquer, Òscar González-Guerrero and Jordi Cristóbal contributed to the radiometric correction design and validation. Joan-Cristian Padró, David Aragonés, Diego García and Cristina Domingo-Marimon analyzed the data. Joan-Cristian Padró and Xavier Pons wrote the paper.

Conflicts of Interest: The authors declare no conflict of interest.

References

1. National Aeronautics and Space Administration (NASA). Landsat Data Continuity Mission (LCDM). Available online: https://www.nasa.gov/mission_pages/landsat/main/index.html (accessed on 28 October 2017).
2. GEOSS. GEOSS Evolution. Available online: http://www.earthobservations.org/geoss.php (accessed on 28 October 2017).
3. European Space Agency (ESA). ESA Sentinel Online. Sentinel-2 Mission. Available online: http://www.esa.int/Our_Activities/Observing_the_Earth/Copernicus/Sentinel-2 (accessed on 28 October 2017).
4. European Space Agency (ESA). ESA Sentinel Online. Sentinel-2 Mission Objectives. Available online: https://sentinel.esa.int/web/sentinel/missions/sentinel-2/mission-objectives (accessed on 28 October 2017).
5. Drusch, M.; Del Bello, U.; Carlier, S.; Colin, O.; Fernandez, V.; Gascon, F.; Hoersch, B.; Isola, C.; Laberinti, P.; Martimort, P.; et al. Sentinel-2: ESA's Optical High-Resolution Mission for GMES Operational Services. *Remote Sens. Environ.* **2012**, *120*, 25–36. [CrossRef]
6. Chander, G.; Markham, B.L.; Helder, D.L. Summary of Current Radiometric Calibration Coefficients for Landsat MSS, TM, ETM+, and EO-1 ALI Sensors. *Remote Sens. Environ.* **2009**, *113*, 893–903. [CrossRef]
7. Barsi, J.A.; Kenton, L.; Kvaran, G.; Markham, B.L.; Pedelty, J.A. The Spectral Response of the Landsat-8 Operational Land Imager (OLI). *Remote Sens.* **2014**, *6*, 10232–10251. [CrossRef]
8. Mishra, N.; Helder, D.; Barsi, J.; Markham, B. Continuous calibration improvement in solar reflective bands: Landsat 5 through Landsat 8. *Remote Sens. Environ.* **2016**, *1185*, 7–15. [CrossRef]
9. Czapla-Myers, J.; McCorkel, J.; Anderson, N.; Thome, K.; Bigar, S.; Helder, D.; Aaron, D.; Leigh, L.; Mishra, N. The Ground-Based Absolute Radiometric Calibration of Landsat 8 OLI. *Remote Sens.* **2015**, *7*, 600–626. [CrossRef]
10. Saunier, S.; Northrop, A.; Lavender, S.; Galli, L.; Ferrara, R.; Mica, S.; Biasutti, R.; Gory, P.; Gascon, F.; Meloni, M.; et al. European Space Agency (ESA) Landsat MSS/TM/ETM+/OLI Archive: 42 Years of our history. In Proceedings of the IEEE 9th International Workshop on the Analysis of Multitemporal Remote Sensing Images (MultiTemp), Brugge, Belgium, 27–29 June 2017.
11. Gascon, F.; Bouzinac, C.; Thépaut, O.; Jung, M.; Francesconi, B.; Louis, J.; Lonjou, V.; Lafrance, B.; Massera, S.; Gaudel-Vacaresse, A.; Languille, F.; et al. Copernicus Sentinel-2A Calibration and Products Validation Status. *Remote Sens.* **2017**, *9*, 584. [CrossRef]
12. CEOS-WGCV. CEOSS Cal/Val Portal. Available online: http://calvalportal.ceos.org/ (accessed on 28 October 2017).
13. Zhang, Z.; He, G.; Wang, X. A practical DOS model-based atmospheric correction algorithm. *Int. J. Remote Sens.* **2010**, *31*, 2837–2852. [CrossRef]
14. Markham, B.; Barsi, J.; Kvaran, G.; Ong, L.; Kaita, E.; Biggar, S.; Czapla-Myers, J.; Mishra, N.; Helder, D. Landsat-8 Operational Land Imager Radiometric Calibration and Stability. *Remote Sens.* **2014**, *6*, 12275–12308. [CrossRef]
15. Claverie, M.; Masek, J. Harmonized Landsat-8 Sentinel-2 (HLS) Product's Guide. v.1.3. 2017. Available online: https://hls.gsfc.nasa.gov/documents/ (accessed on 28 October 2017).
16. Atmospheric Correction Inter-Comparison Exercise (ACIX). Available online: https://earth.esa.int/web/sppa/meetings-workshops/acix (accessed on 28 October 2017).
17. Holben, B.N.; Eck, T.F.; Slutsker, I.; Tanré, D.; Buis, J.P.; Setzer, A.; Vermote, E.; Reagan, J.A.; Kaufman, Y.J.; Nakajima, T.; et al. AERONET—A Federated Instrument Network and Data Archive for Aerosol Characterization. *Remote Sens. Environ.* **1998**, *66*, 1–16. [CrossRef]
18. Pons, X.; Solé-Sugrañes, L. A simple radiometric correction model to improve automatic mapping of vegetation from multispectral satellite data. *Remote Sens. Environ.* **1994**, *45*, 317–332. [CrossRef]
19. Kokhanovsky, A.A.; de Leeuw, G. *Satellite Aerosol Remote Sensing over Land*, 1st ed.; Springer: Berlin/Heidelberg, Germany, 2009; p. 388.
20. Liou, K.N. *An Introduction to Atmospheric Radiation*, 2nd ed.; Academic Press: San Diego, CA, USA, 2002; p. 583.

21. Hadjimitsis, D.G.; Clayton, C.R.I.; Retalis, A. The use of selected Pseudoinvariant targets for the application of atmospheric correction in multi-temporal studies using satellite remotely sensed imagery. *Int. J. Appl. Earth Obs. Geoinf.* **2009**, *11*, 192–200. [CrossRef]
22. Kaufman, Y.J.; Sendra, C. Algorithm for automatic atmospheric corrections to visible and near-IR satellite imagery. *Int. J. Remote Sens.* **1988**, *9*, 1357–1381. [CrossRef]
23. Chavez, P.S., Jr. An improved dark-object subtraction technique for atmospheric scattering correction of multispectral data. *Remote Sens. Environ.* **1988**, *24*, 459–479. [CrossRef]
24. Vermote, E.; Justice, C.; Claverie, M.; Franch, B. Preliminary analysis of the performance of the Landsat 8/OLI land surface reflectance product. *Remote Sens. Environ.* **2016**, *185*, 46–56. [CrossRef]
25. Turner, R.E.; Malila, W.A.; Nalepha, R.F. Importance of atmospheric scattering in remote sensing. In Proceedings of the Seventh International Symposium on Remote Sensing of Environment, Ann Arbor, MI, USA, 17–21 May 1971; Volume 3, pp. 1651–1697.
26. Rozanov, V.V.; Rozanov, A.V. *User's Guide for the Software Package SCIATRAN (Radiative Transfer Model and Retrieval Algorithm V.3.5)*; Institute of Remote Sensing, University of Bremen: Bremen, Germany, 2016; pp. 1–166. Available online: http://www.iup.uni-bremen.de/sciatran/free_downloads/users_guide_sciatran.pdf (accessed on 6 September 2017).
27. Rozanov, A.; Rozanov, V.; Buchwitz, M.; Kokhanovsky, A.A.; Burrows, J.P. SCIATRAN 2.0–A new radiative transfer model for geophysical applications in the 175–2400 nm spectral region. *Adv. Space Res.* **2005**, *36*, 1015–1019. [CrossRef]
28. Kotchenova, S.Y.; Vermote, E.F.; Matarrese, R.; Klemm, F.J., Jr. Validation of a vector version of the 6S radiative transfer code for atmospheric correction of satellite data. Part I: Path radiance. *Appl. Opt.* **2006**, *26*, 6762–6774. [CrossRef]
29. Kotchenova, S.Y.; Vermote, E.F. Validation of a vector version of the 6S radiative transfer code for atmospheric correction of satellite data. Part II: Homogeneous Lambertian and anisotropic surfaces. *Appl. Opt.* **2007**, *46*, 4455–4464. [CrossRef] [PubMed]
30. Stamnes, K.; Tsay, S.-C.; Wiscombe, W.; Jayaweera, K. Numerically stable algorithm for discrete-ordinate-method radiative transfer in multiple scattering and emitting layered media. *Appl. Opt.* **1988**, *27*, 2502–2509. [CrossRef] [PubMed]
31. Stamnes, K.; Tsay, S.-C.; Wiscombe, W.; Laszlo, I. *DISORT, a General-Purpose Fortran Program for Discrete-Ordinate-Method Radiative Transfer in Scattering and Emitting Layered Media: Documentation of Methodology (Version 1.1)*; Tech. Rep.; Department of Physics and Engineering Physics, Stevens Institute of Technology: Hoboken, NJ, USA, 2000; p. 112.
32. Eriksson, P.; Buehler, S.A.; Davis, C.P.; Emde, C.; Lemke, O. ARTS, the atmospheric radiative transfer Simulator, version 2. *J. Quant. Spectrosc. Radiat. Transf.* **2011**, *112*, 1551–1558. [CrossRef]
33. Scott, N.A.; Chedin, A. A fast line-by-line method for Atmospheric Absorption Computations: The Automatized Atmospheric Absorption Atlas. *J. Appl. Meteorol.* **1981**, *20*, 802–812. [CrossRef]
34. Berk, A.; Conforti, P.; Kennett, R.; Perkins, T.; Hawes, F.; van den Bosch, J. MODTRAN6: A major upgrade of the MODTRAN radiative transfer code. In Proceedings of the SPIE 9088, Algorithms and Technologies for Multispectral, Hyperspectral, and Ultraspectral Imagery XX, Baltimore, MD, USA, 13 June 2014.
35. Mayer, B.; Kylling, A. Technical note: The libRadtran software Package for radiative transfer calculations—Description and examples of use. *Atmos. Chem. Phys.* **2005**, *5*, 1855–1877. [CrossRef]
36. Kokhanovsky, A.A.; Breon, F.-M.; Cacciari, A.; Carboni, E.; Diner, D.; Di Nicolantonio, W.; Grainger, R.G.; Grey, W.M.F.; Höller, R.; Lee, K.H.; et al. Aerosol remote sensing over land: A comparison of satellite retrievals using different algorithms and instruments. *Atmos. Res.* **2007**, *85*, 372–394. [CrossRef]
37. Kokhanovsky, A.A. *Light Scattering Media Optics. Problems and Solutions*, 3rd ed.; Willey-Praxis: Chichester, UK, 2004; p. 320, ISBN 978-3-540-21184-6.
38. Kokhanovsky, A.A. *Polarization Optics of Random Media*, 1st ed.; Springer: Berlin/Heidelberg, Germany, 2003; p. 224, ISBN 978-3-540-42635-6.
39. European Space Agency (ESA). ESA Missions. ENVISAT Instruments. SCIAMACHY. Available online: https://earth.esa.int/web/guest/missions/esa-operational-eo-missions/envisat/instruments/sciamachy (accessed on 28 October 2017).
40. Aerosol Robotic Network (AERONET). Aeronet Data Download Tool. Version 3 Direct Sun Algorithm. Available online: https://aeronet.gsfc.nasa.gov/ (accessed on 28 October 2017).

41. Chavez, P.S., Jr. Image-Based Atmospheric Corrections—Revisited and Improved. *PE&RS* **1996**, *62*, 1025–1036. Available online: https://www.unc.edu/courses/2008spring/geog/577/001/www/Chavez96-PERS.pdf (accessed on 28 October 2017).
42. Hall, F.G.; Strebel, D.E.; Nickeson, J.E.; Goetz, S.J. Radiometric rectification: Toward a common radiometric response among multidate, multisensor images. *Remote Sens. Environ.* **1991**, *35*, 11–27. [CrossRef]
43. Pons, X.; Pesquer, L.; Cristóbal, J.; González-Guerrero, O. Automatic and improved radiometric correction of Landsat imagery using reference values from MODIS surface reflectance images. *Int. J. Appl. Earth Obs. Geoinf.* **2014**, *33*, 243–254. [CrossRef]
44. Vidal-Macua, J.J.; Zabala, A.; Ninyerola, M.; Pons, X. Developing spatially and thematically detailed backdated maps for land cover studies. *Int. J. Digit. Earth* **2016**, *10*, 175–206. [CrossRef]
45. Smith, G.M.; Milton, E.J. The use of the empirical line method to calibrate remotely sensed data to reflectance. *Int. J. Remote Sens.* **1999**, *20*, 2653–2662. [CrossRef]
46. Xu, J.-F.; Huang, J.-F. Empirical Line Method Using Spectrally Stable Targets to Calibrate IKONOS Imagery. *Pedosphere* **2007**, *18*, 124–130. [CrossRef]
47. Song, C.; Woodcock, C.E.; Seto, K.C.; Lenney, M.P.; Macomber, S.C. Classification and Change Detection Using Landsat TM Data: When and How to Correct Atmospheric Effects? *Remote Sens. Environ.* **2001**, *75*, 230–244. [CrossRef]
48. Richter, R.; Schläpfer, D. Atmospheric/Topographic Correction for Satellite Imagery (ATCOR-2/3 User Guide, Version 9.0.2, March 2016). 2016. Available online: http://www.rese.ch/pdf/atcor3_manual.pdf (accessed on 28 October 2017).
49. Congedo, L. Semi-Automatic Classification Plugin Documentation. Release 5.3.2.1. 2016, pp. 161–164. Available online: https://media.readthedocs.org/pdf/semiautomaticclassificationmanual-v4/latest/semiautomaticclassificationmanual-v4.pdf (accessed on 6 September 2017).
50. Masek, J.; Vermote, E.F.; Saleous, N.E.; Wolfe, R.; Hall, F.G.; Huemmrich, K.F.; Gao, F.; Kutler, J.; Lim, T.-K. LEDAPS Calibration, Reflectance, Atmospheric Correction Preprocessing Code, Version 2. Model Product. Available online: https://daac.ornl.gov/MODELS/guides/LEDAPS_V2.html (accessed on 28 October 2017).
51. United States Geological Survey (USGS). *Product Guide. Provisional Landsat 8 Surface Reflectance Code (LaSRC) Product. Version 4.0*; Department of the Interior: Reston, VA, USA, 2016; p. 36. Available online: https://landsat.usgs.gov/sites/default/files/documents/lasrc_product_guide.pdf (accessed on 28 October 2017).
52. Richter, R.; Louis, J.; Müller-Wilm, U. [L2A-ATBD] Sentinel-2 Level-2A Products Algorithm Theoretical Basis Document. Version 2.0. 2012, pp. 1–72. Available online: https://earth.esa.int/c/document_library/get_file?folderId=349490&name=DLFE-4518.pdf (accessed on 28 October 2017).
53. United States Geological Survey (USGS). WRS-2 Scene Boundaries (Worldwide). Available online: https://landsat.usgs.gov/sites/default/files/documents/WRS-2_bound_world.kml (accessed on 28 October 2017).
54. European Space Agency (ESA). SENTINEL-2 Relative Orbits. Available online: https://sentinel.esa.int/documents/247904/685211/S2A_rel_orbit_groundtrack_10Sec/57bcb79f-2696-4859-8292-07ac7166e884 (accessed on 28 October 2017).
55. United States Geological Survey (USGS). EarthExplorer Download Tool. Available online: https://earthexplorer.usgs.gov/ (accessed on 28 October 2017).
56. European Space Agency (ESA). Copernicus Open Access Hub. Available online: https://scihub.copernicus.eu/dhus/#/home (accessed on 28 October 2017).
57. United States Geological Survey (USGS). Using the USGS Spectral Viewer. Landsat 7 ETM+. Available online: https://landsat.usgs.gov/sites/default/files/documents/L7_RSR.xlsx (accessed on 28 October 2017).
58. National Aeronautics and Space Administration (NASA). Landsat Science, Spectral Response of the Operational Land Imager In-Band. Available online: http://landsat.gsfc.nasa.gov/preliminary-spectral-response-of-the-operational-land-imager-in-band-band-average-relative-spectral-response/ (accessed on 28 October 2017).
59. European Space Agency (ESA). Sentinel Online, Sentinel-2A Document Library, Sentinel-2AA (S2A-SRF). Available online: https://earth.esa.int/documents/247904/685211/Sentinel-2+MSI+Spectral+Responses/ (accessed on 28 October 2017).

60. United States Geological Survey (USGS). Landsat-8 Data User Handbook. Version 2.0. Available online: https://landsat.usgs.gov/landsat-8-l8-data-users-handbook (accessed on 28 October 2017).
61. European Space Agency (ESA). Sentinel-2A User Handbook. Released 24/07/2015. Rev. 2. Available online: https://sentinels.copernicus.eu/web/sentinel/user-guides/document-library/-/asset_publisher/xlslt4309D5h/content/sentinel-2-user-handbook (accessed on 28 October 2017).
62. National Aeronautics and Space (NASA). Landsat Science, Spectral Response of the Multispectral Scanner System In-Band. Available online: http://landsat.gsfc.nasa.gov/spectral-response-of-the-multispectral-scanner-system-in-band-band-average-relative-spectral-response/ (accessed on 28 October 2017).
63. United States Geological Survey (USGS). Using the USGS Spectral Viewer. Landsat 5 TM. Available online: https://landsat.usgs.gov/sites/default/files/documents/L5_TM_RSR.xlsx (accessed on 28 October 2017).
64. Jiménez, M.; Díaz-Delgado, R. Towards a Standard Plant Species Spectral Library Protocol for Vegetation Mapping: A Case Study in the Shrubland of Doñana National Park. *ISPRS Int. J. Geo-Inf.* **2015**, *4*, 2472–2495. [CrossRef]
65. De Miguel, E.; Fernández-Renau, A.; Prado, E.; Jiménez, M.; Gutiérrez de la Cámara, O.; Linés, C.; Gómez, J.A.; Martín, A.I.; Muñoz, F. A review of INTA AHS PAF. *EARSeL eProc.* **2014**, *13*, 20–29. [CrossRef]
66. Jiménez, M.; Díaz-Delgado, R.; Vaughan, P.; De Santis, A.; Fernández-Renau, A.; Prado, E.; Gutiérrez de la Cámara, O. Airborne hyperspectral scanner (AHS) mapping capacity simulation for the Doñana biological reserve scrublands. In Proceedings of the 10th International Symposium on Physical Measurements and Signatures in Remote Sensing, Davos, Switzerland, 12–14 March 2007; Schaepman, M., Liang, S., Groot, N., Kneubühler, M., Eds.; Available online: http://www.isprs.org/proceedings/XXXVI/7-C50/papers/P81.pdf (accessed on 28 October 2017).
67. Hatchell, D.C. (Ed.) *Analytical Spectral Devices, Inc. (ASD) Technical Guide*, 3rd ed.; Analytical Spectral Devices, Inc.: Boulder, CO, USA, 1999.
68. Peña-Martinez, R.; Domínguez Gómez, J.A.; Ruiz-Verdú, A. Mapping of Photosynthetic Pigments in Spanish Reservoirs. In Proceedings of the MERIS User Workshop (ESA SP-549), ESA-ESRIN, Frascati, Italy, 10–13 November 2003.
69. Mueller, J.L.; Brown, S.W.; Clark, D.K.; Johnson, B.C.; Yoon, H.; Lykke, K.R.; Flora, S.J.; Feinholz, M.E.; Souaidia, N.; Pietras, C.; et al. Ocean Optics Protocols for Satellite Ocean Color Sensor Validation. In *Revision 2 NASA*; Fargion, G.S., Mueller, J.L., Eds.; Goddard Space Flight Center: Greenbelt, MD, USA, 2000.
70. Milton, E.J.; Schaepmann, M.E.; Anderson, K.; Kneubühler, M.; Fox, N. Progress in field spectroscopy. *Remote Sens. Environ.* **2009**, *113*, S92–S109. [CrossRef]
71. Meroni, M.; Colombo, R. 3S: A novel program for field spectroscopy. *Comput. Geosci.* **2009**, *35*, 1491–1496. [CrossRef]
72. Mira, M.; Niclòs, R.; Valor, E.; Pons, X.; Cea, C.; García-Santos, V.; Caselles, D.; Caselles, V. Espectroradiometría de Campo del Visible al Infrarrojo Térmico de Muestras con Características Espectrales Singulares. In Proceedings of the XVI Congreso de la Asociación Española de Teledetección, Sevilla, Spain, 21–22 October 2015; pp. 213–219. Available online: http://www.aet.org.es/congresos/xvi/XVI_Congreso_AET_actas.pdf (accessed on 28 October 2017).
73. Zhu, X.; Liu, D.; Chen, J. A new geostatistical approach for filling gaps in Landsat ETM+ SLC-off images. *Remote Sens. Environ.* **2012**, *124*, 49–60. [CrossRef]
74. Chen, J.; Zhu, X.; Vogelmann, J.E.; Gao, F.; Jin, S. A simple and effective method for filling gaps in Landsat ETM+ SLC-off images. *Remote Sens. Environ.* **2011**, *115*, 1053–1064. [CrossRef]
75. Mueller-Wilm, U. *Sen2Cor Configuration and User Manual V2.4*; European Space Agency: Paris, Frence, 2017; pp. 1–53. Available online: http://step.esa.int/thirdparties/sen2cor/2.4.0/Sen2Cor_240_Documenation_PDF/S2-PDGS-MPC-L2A-SUM-V2.4.0.pdf (accessed on 28 October 2017).
76. Pflug, B. Sentinel-2 L2A Processor Sen2Cor. In Proceedings of the EUFAR/ESA Expert Workshop on Atmospheric Correction of Remote Sensing Data, Berlin, Germany, 26–28 October 2016.
77. Instituto Geográfico Nacional. Plan Nacional de Ortofotografía aérea. Modelos Digitales del Terreno Obtenidos a Partir de Nubes de Puntos LIDAR. Available online: http://centrodedescargas.cnig.es/CentroDescargas/index.jsp (accessed on 28 October 2017).
78. NASA Jet Propulsion Laboratory (JPL). *NASA Shuttle Radar Topography Mission United States 1 Arc Second*; Version 3; NASA EOSDIS Land Processes DAAC, USGS Earth Resources Observation and Science (EROS) Center: Sioux Falls, SD, USA, 2013. Available online: https://lpdaac.usgs.gov (accessed on 28 October 2017).

79. Moran, M.; Jackson, R.; Slater, P.; Teillet, P. Evaluation of simplified procedures for retrieval of land surface reflectance factors from satellite sensor output. *Remote Sens. Environ.* **1992**, *41*, 169–184. [CrossRef]
80. Hale, S.R.; Rock, B.N. Impact of topographic normalization on land-cover classification accuracy. *Photogram. Eng. Remote Sens.* **2003**, *69*, 785–791. [CrossRef]
81. Chance, C.M.; Hermosilla, T.; Coops, N.C.; Wulder, M.A.; White, J.C. Effect of topographic correction on forest change detection using spectral trend analysis of Landsat pixel-based composites. *Int. J. Appl. Earth Obs. Geoinf.* **2016**, *44*, 186–194. [CrossRef]
82. Vermote, E.F.; Tanre, D.; Deuzé, J.L.; Herman, M.; Morcrette, J.-J. Second Simulation of the Satellite Signal in the Solar Spectrum, 6S: An Overview. *IEEE Trans. Geosci. Remote Sens.* **1997**, *35*, 675–686. [CrossRef]
83. Feng, M.; Huang, C.; Channan, S.; Vermote, E.F.; Masek, J.G.; Townshend, J.R. Quality assessment of Landsat surface reflectance products using MODIS data. *Comp. Geosci.* **2012**, *38*, 9–22. [CrossRef]
84. Feng, M.; Sexton, J.; Huang, C.; Masek, J.; Vermote, E.F.; Gao, F.; Narasimhan, R.; Channan, S.; Wolfe, R.E.; Townshend, J.R. Global surface reflectance products from Landsat: Assessment using coincident MODIS observations. *Remote Sens. Environ.* **2013**, *134*, 276–293. [CrossRef]
85. Vermote, E.F.; Kotchenova, S. Atmospheric correction for the monitoring of land surfaces. *J. Geophys. Res. Atmos.* **2008**, *113*, 2156–2202. [CrossRef]
86. Pons, X. MiraMon. Geographical Information System and Remote Sensing Software, Version 8.01b; Centre for Ecological Research and Forestry Applications (CREAF). Bellaterra. 2004. Available online: http://www.creaf.uab.cat/miramon/Index_usa.htm (accessed on 28 October 2017).
87. Pesquer, L.; Domingo, C.; Pons, X. A Geostatistical Approach for Selecting the Highest Quality MODIS Daily Images. In Proceedings of the Pattern Recognition and Image Analysis: 6th Iberian Conference, IbPRIA 2013, Funchal, Madeira, Portugal, 5–7 June 2013; pp. 608–615.
88. Marcello, J.; Eugenio, F.; Perdomo, U.; Medina, A. Assessment of Atmospheric Algorithms to Retrieve Vegetation in Natural Protected Areas Using Multispectral High Resolution Imagery. *Sensors* **2016**, *60*, 1624. [CrossRef] [PubMed]
89. Feilhauer, H.; Thonfeld, F.; Faude, U.; He, K.S.; Rocchini, D.; Schmidtlein, S. Assessing floristic composition with multispectral sensors—A comparison based on monotemporal and multiseasonal field spectra. *Int. J. Appl. Earth Obs. Geoinf.* **2013**, *21*, 218–229. [CrossRef]
90. Vuolo, F.; Zółtak, M.; Pipitone, C.; Zappa, L.; Wenng, H.; Immitzer, M.; Weiss, M.; Baret, F.; Atzberger, C. Data Service Platform for Sentinel-2 Surface Reflectance and Value-Added Products: System Use and Examples. *Remote Sens.* **2017**, *8*, 938. [CrossRef]

2.2. Comparació de quatre mètodes de georeferenciació d'UAV per propòsits de monitoratge ambiental focalitzats en l'ús combinat amb plataformes aèries i satel·litàries

Padró J.C., Muñoz F.J., Planas J., Pons X. (2019). Comparison of four UAV georeferencing methods for environmental monitoring purposes focusing on the combined use with airborne and satellite remote sensing platforms. *International Journal of Applied Earth Observation and Geoinformation, 79, 130-140*. DOI: 10.1016/j.jag.2018.10.018. https://doi.org/10.1016/j.jag.2018.10.018. (IF: 4.003, Q1: 7/30 (2017) [Remote Sensing]).

Resum: Aquest treball està dirigit a la comunitat de teledetecció ambiental que utilitza imatges òptiques procedents d'UAV en combinació amb dades aèries i/o satel·litàries. Tenint en compte els costos econòmics implicats i la inversió en el temps, s'ha avaluat l'exactitud de quatre mètodes de posicionament d'imatges adquirides per UAV: 1) georeferenciació directa mitjançant dades en brut del GNSS de bord (GNSSNAV), 2) georeferenciació directa utilitzant un sistema GNSS de fase portadora amb freqüència simple i post-processat cinemàtic sense suport terrestre *in-situ* (PPK1), 3) georeferenciació directa utilitzant un sistema GNSS de fase portadora amb freqüència doble i post-processat cinemàtic amb suport terrestre *in-situ* (PPK2), i 4) georeferenciació indirecta utilitzant punts de control sobre el terreny (GCP). S'han realitzat les proves amb un sensor multiespectral i amb un sensor RGB, a bord de dos multicòpters. S'han generat ortofotomosaics a una resolució espacial <0.05 m amb programari fotogramètric. L'exactitud absoluta de la imatge UAV s'avalua d'acord amb els estàndards establerts per l'American Society for Photogrammetry and Remote Sensing (ASPRS), emprant un conjunt de GCP com a coordenades de referència, obtinguts amb un receptor GNSS diferencial estàtic. La solució GNSSNAV ha obtingut una exactitud horitzontal (radial) i vertical en l'ordre de magnitud mètric (RMSEr≤1.062 m i RMSEz≤4.209 m); la solució PPK1 ha obtingut una exactitud de l'ordre decimètric (RMSEr≤0.256 m i RMSEz≤0.238 m); la solució PPK2 ha proporcionat una exactitud de l'ordre centimètric (RMSEr≤0.036 m i RMSEz≤0.036 m). La solució GCP ha obtingut l'exactitud més elevada (RMSEr≤0.023 m i RMSEz≤0.030 m). La solució GNSSNAV és una opció ràpida i de baix cost, útil per combinar imatges d'UAV amb imatges del satèl·lit tipus Sentinel-2. La solució PPK1 pot corregistrar imatges d'UAV amb productes de teledetecció de fins a 0.25 m de píxel, com imatges satel·litàries de tipus WorldView, lidar o ortoimatges aèries, però té un cost econòmic més elevat que GNSSNAV. L'opció PPK2 permet corregistrar productes de teledetecció de fins a 0.05 m de píxel, com altres imatges d'UAV, però és molt més costosa que el PPK1 i requereix posicionar una base dins de l'àrea d'estudi. L'opció GCP obté la màxima exactitud, però consumeix molt de temps si s'han de col·locar molts punts de control sobre el terreny i també requereix suport *in-situ*.

Paraules clau: UAV; dron; georeferenciació directa; georeferenciació indirecta; estàndards ASPRS; Post-Processat Cinemàtic.

Int J Appl Earth Obs Geoinformation 75 (2019) 130–140

Contents lists available at ScienceDirect

Int J Appl Earth Obs Geoinformation

journal homepage: www.elsevier.com/locate/jag

Comparison of four UAV georeferencing methods for environmental monitoring purposes focusing on the combined use with airborne and satellite remote sensing platforms

Joan-Cristian Padró[a,*], Francisco-Javier Muñoz[b], Jordi Planas[c], Xavier Pons[d]

[a] Grumets Research Group, Departament de Geografia, Universitat Autònoma de Barcelona, Departament de Geografia Office B1092, Edifici B. Universitat Autònoma de Barcelona, 08193 Bellaterra, Catalonia, Spain
[b] HEMAV S.L. Edifici RDIT. Office 0007. C\Esteve Terrades, 1. Parc Mediterrani de la Tecnologia, 08860 Castelldefels, Catalonia, Spain
[c] Universitat Autònoma de Barcelona, Departament de Geografia Office B1092. Edifici B, Universitat Autònoma de Barcelona, 08193 Bellaterra, Catalonia, Spain
[d] Grumets Research Group, Departament de Geografia, Universitat Autònoma de Barcelona, Departament de Geografia Office B1094. Edifici B. Universitat Autònoma de Barcelona. 08193 Bellaterra, Catalonia, Spain

ARTICLE INFO

Keywords:
UAV
Drone
Direct georeferencing
Indirect georeferencing
ASPRS standards
Post-Processed Kinematic

ABSTRACT

This work is aimed at the environmental remote sensing community that uses UAV optical frame imagery in combination with airborne and satellite data. Taking into account the economic costs involved and the time investment, we evaluated the fit-for-purpose accuracy of four positioning methods of UAV-acquired imagery: 1) direct georeferencing using the onboard raw GNSS (GNSSNAV) data, 2) direct georeferencing using Post-Processed Kinematic single-frequency carrier-phase without in situ ground support (PPK1), 3) direct georeferencing using Post-Processed Kinematic double-frequency carrier-phase GNSS data with in situ ground support (PPK2), and 4) indirect georeferencing using Ground Control Points (GCP). We tested a multispectral sensor and an RGB sensor, onboard multicopter platforms. Orthophotomosaics at < 0.05 m spatial resolution were generated with photogrammetric software. The UAV image absolute accuracy was evaluated according to the ASPRS standards, wherein we used a set of GCPs as reference coordinates, which we surveyed with a differential GNSS static receiver. The raw onboard GNSSNAV solution yielded horizontal (radial) accuracies of RMSEr ≤ 1.062 m and vertical accuracies of RMSEz ≤ 4.209 m; PPK1 solution gave decimetric accuracies of RMSEr ≤ 0.256 m and RMSEz ≤ 0.238 m; PPK2 solution, gave centimetric accuracies of RMSEr ≤ 0.036 m and RMSEz ≤ 0.036 m. These results were further improved by using the GCP solution, which yielded accuracies of RMSEr ≤ 0.023 m and RMSEz ≤ 0.030 m. GNSSNAV solution is a fast and low-cost option that is useful for UAV imagery in combination with remote sensing products, such as Sentinel-2 satellite data. PPK1, which can register UAV imagery with remote sensing products up to 0.25 m pixel size, as WorldView-like satellite imagery, airborne lidar or orthoimagery, has a higher economic cost than the GNSSNAV solution. PPK2 is an acceptable option for registering remote sensing products of up to 0.05 m pixel size, as with other UAV images. Moreover, PPK2 can obtain accuracies that are approximate to the usual UAV pixel size (e.g. co-register in multitemporal studies), but it is more expensive than PPK1. Although indirect georeferencing can obtain the highest accuracy, it is nevertheless a time-consuming task, particularly if many GCPs have to be placed. The paper also provides the approximate cost of each solution.

Abbreviations: APC, Antenna Phase Centre; ASPRS, American Society for Photogrammetry and Remote Sensing; AT, Aerial-Triangulation; DG, Direct Georeferencing; DGNSS, Differential Global Navigation Satellite System; EOPs, Exterior Orientation Parameters; ETRS89, European Terrestrial Reference System 1989; DSLR, Digital Single-Lens Reflex; GCP, Ground Control Points; GLONASS, Global'naya Navigatsionnaya Sputnikovaya Sistema; GNSS, Global Navigation Satellite System; GNSSNAV, Navigation GNSS onboard the UAV; GPS, Navstar Global Positioning System; ICP, Independent Check Points; IG, Indirect Georeferencing; IMU, Inertial Measurement Unit; ISO, Integrated Sensor Orientation; NSSDA, National Standard for Spatial Data Accuracy; NVA, NonVegetated Area; PC, Perspective Centre; PP, PostProcessed; PPK, PostProcessed Kinematic; PRS, Permanent Reference Station; RMSE, Root Mean Square Error; RTK, RealTime Kinematic; SRS, patial resolution; SfM, Structure from Motion; UAV, Unmanned Aerial Vehicle; VBS, Virtual Base Station

* Corresponding author.
E-mail addresses: JoanCristian.Padro@uab.cat (J.-C. Padró), jmunoz@hemav.com (F.-J. Muñoz), j.planas@creaf.uab.cat (J. Planas), Xavier.Pons@uab.cat (X. Pons).

https://doi.org/10.1016/j.jag.2018.10.018
Received 4 July 2018; Received in revised form 2 October 2018; Accepted 25 October 2018

1. Introduction

Capturing images by means of optical sensors installed in < 25 kg Unmanned Aerial Vehicles (UAV) or drones is gaining importance in quantitative remote sensing (Aasen et al., 2018), environmental research (Manfreda et al., 2018), remote sensing applications for vegetated areas (Komárek et al., 2018), precision agriculture (Borgogno Mondino and Gajetti, 2017), highly detailed metrology (Daakir et al., 2017) and cartographic (Crommelinck et al., 2017) applications. Moreover, their use in combination with other environmental remote sensing products, such as high Spatial Resolution (SR) satellite imagery (Lin et al., 2011) or airborne orthophotomaps of official mapping agencies (Whitehead and Hugenholtz, 2014) has attracted growing interest. In many European countries, current legislation allows a UAV to fly at a certain maximum height (e.g., 120 m in Spain (BOE, 2017). Consequently, commercial sensors usually provide SR between 0.01 m (1 cm) in RGB sensors and 0.10 m (10 cm) in multispectral sensors. A problem of this ultra-high SR is that it usually exceeds the accuracy of direct Exterior Orientation Parameters (EOPs) determination of individual images at the sensor exposure time, i.e., the positional (X,Y,Z) accuracy directly obtained from the platform onboard Global Navigation Satellite System (GNSS) receiver, and the sensor orientation (ω,φ,κ) directly obtained from the Inertial Measurement Unit (IMU) device. This particular process of determining EOPs for individual images at the exposure time entails an inaccurate georeferencing of the resulting orthophotomosaic, or at least an error largely exceeding the pixel size. The receiver rate of position measurements per second (Hz) is crucial for sampling the position of a mobile object; for example, at a velocity of 5 m/s, a 10 Hz GNSS receiver samples a position every 0.5 m. On the other hand, a receiver can work in code or carrier-phase mode, the latter usually provides more range accuracy, since the receiver is capable of distinguishing the sinusoidal wave oscillation where the signal code is located. This solution can be obtained in an expedient manner by using a single-frequency receiver. Moreover, the final accuracy can be improved by using a dual-frequency differential GNSS (DGNSS) receiver. A DGNSS is capable of reading two carrier-phases at two wavelengths (typically L1/L2) as well as consider signal delays caused by atmospheric effects (differential measurement). As reported by Colomina and Molina (2014), the Direct Georeferencing (DG) accuracy of a conventional UAV depends on the quality of the GNSS receiver; for example, in precision code, the positioning error can reach 0.77 m, and in the L1/L2 carrier-phase, the error can reach 0.01 m (Colomina and Molina, 2014). The code-based moderate accuracy is acceptable in UAV campaigns that only require low metric quality (Remondino et al., 2012). However, this imagery can neither be used to generate detailed cartography at large scales, such as 1:200 (ASPRS, 2014), nor be assumed to have reasonable pixel co-registration in multitemporal studies using imagery with an SR < 0.1 m. A classic precise technique for accurate georeferencing of aerial imagery, known as Indirect Georeferencing (IG), consists of using Ground Control Points (GCPs) to support Aero-Triangulation (AT) and reaches accuracies of 0.02 m, which was evaluated by using Independent Check Points (ICPs) (Turner et al., 2014a, 2014b). IG was used in (Tian et al., 2017) to compare WorldView-2 imagery and UAV imagery. It provided pixel size accuracies of 1 cm RGB imagery and 7 cm multispectral (MicaSense RedEdge) imagery. Also (Zabala, 2017) used GCP to compare Sentinel-2 and MicaSense RedEdge data. The drawback is that taking data on the ground is not always feasible. When it is, it is very costly and entails a high volume of time and resources, which is ultimately not optimal or worth the overall investment of effort.

Post-Processing Kinematic (PPK) DG solution has been a widely used method in airborne platforms since 1990 (Skaloud et al., 1996). Recently, the market offers PPK solutions with devices light enough to be carried in < 25 kg UAV platforms. Consequently, PPK is an interesting option for remote sensing environmental users due to the accurate processing procedure after the flight (not in real-time, (Bisnath et al., 2004). In environmental and topographic mapping projects, usually there is no requirement for Real-Time Kinematic (RTK) georeferencing. Nevertheless, it is important to obtain an imagery positioning that is as accurate as possible. This can be realized by post-processing the sensor central coordinates at the image exposure time, which takes into account the UAV trajectory, sensor position at trigger time (Rehak and Skaloud, 2017), satellite geometries and atmospheric error sources. The UAV trajectory is determined by interpolating the onboard GNSS data, whereby the sensor position at trigger time requires synchronizing between the camera and the onboard GNSS, and the GNSS satellite constellation information can be provided by Permanent Reference Stations (PRS) or Virtual Base Stations (VBS). This solution was tested in UAV platforms combining a single-frequency low cost GNSS receiver and IMU data (Turner et al., 2014a,b; Rehak et al., 2013), achieving accuracies almost similar to those of the typical spatial resolution of optical sensors suitable in a low-weight UAV for remote sensing applications. Other studies (Bláha et al., 2012; Rehak and Skaloud, 2015) analyzed the capacity of post-processing GNSS and IMU sensor integration data in UAV to outperform DG providing results of centimetric accuracies. Chio (Chio, 2016) evaluated a VBS RTK GPS-assisted self-calibration bundle adjustment for aerial triangulation of UAV images for updating 1:5000 topographic maps; he collected the data by flying a fixed-wing UAS mounted with a 24-mm focal-length Canon EOS 5D Mark II camera at 550 m, with 0.27 m in planimetry and 0.24 m in height accuracies (RMSE). In a later study, Chio and Lin (2017) tested a thermal camera mounted on a UAV using a Trimble BD970GNSS and PPK data that gave good preliminary results. All these aforementioned precedents use GNSS and IMU post-processed data to directly determine EOPs (X,Y,Z; ω,φ,κ) before the bundle adjustment phase. The determination of the image position still depends greatly on the GNSS receiver. Furthermore, the Integrated Sensor Orientation (ISO), which is commonly referred to as the pose of the image (Aasen et al., 2018; Wouda et al., 2016), is not a trivial procedure for a non-specialized user.

In our study, we compare the geometric accuracy of four different georeferencing techniques: (1) onboard Navigation GNSS (GNSSNAV); (2) PPK single frequency and the corrections of a permanent reference station located 4 km away from the flight area (PPK1); (3) PPK dual frequency and the corrections of a base station located in the flight area; and (4) Ground Control Points and Independent Check Points (GCP–ICP). The evaluation of GNSSNAV and PPK methods consisted of a comparison of image-derived coordinates with well-determined surveyed coordinates on specifically materialized targets used as ICP (RMSEx, RMSEy, RMSEr and RMSEz), while cross-validation was performed for the GCP–ICP method.

2. Materials and methods

2.1. Study area

We used the test area of the Can Gelabert farm (municipality of Riner, Catalonia) located northeast of the Iberian Peninsula, in the Mediterranean basin between the Catalan Central Depression and the Pre-Pyrenees. The planned study area has an area of 60 000 m^2 (6 ha), forming a rectangle having a side of 300 m in the E–W direction and a side of 200 m in the N–S direction. The altitude of the terrain at the materialized points is between 719.01 m and 734.20 m. The terrain morphology is not absolutely flat, as there are some unevenness formed by abandoned vineyards (including plain benches ranging from a minimum slope of 0° to a maximum slope of near 90° when moving from one bench to another) as well as trees higher than 8 m. In the central zone, there is a field of cereal crops, and the woody vegetation of the area is formed mainly by *Quercus humilis*, *Quercus ilex*, *Ulmus minor* and *Pinus nigra* ssp. *salzmanii*. The man-made elements consist of an 18th century rural complex, which includes the house of Can Gelabert (floor plan of 325 m^2), two haystacks, a pond and a small well.

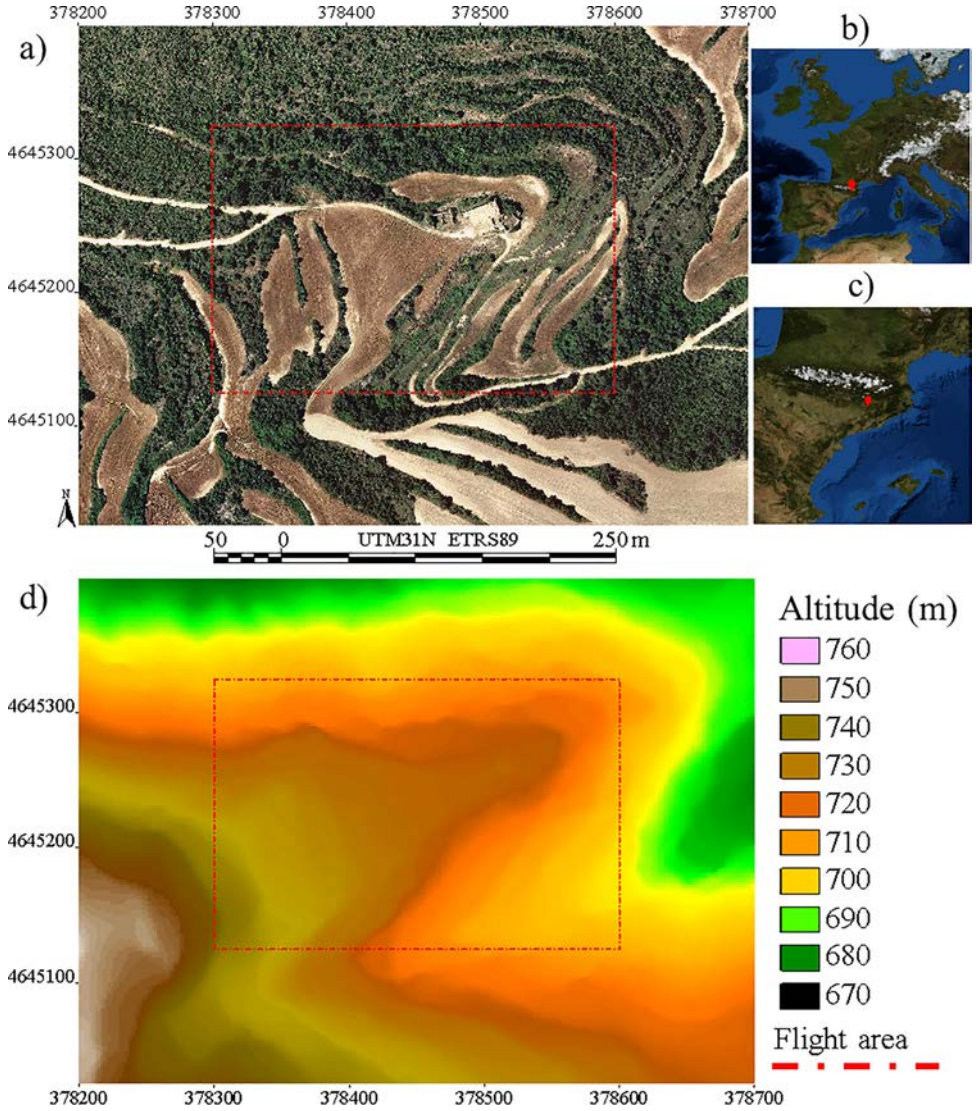

Fig. 1. a) Gelabert farm (Riner, Solsonès County). Red square shows the scope of the planned flight area. Background: Official cartography (SR = 0.25 m) (ICGC, 2018). b) Location of the area NE of the Iberian Peninsula. c) Location of the area in the European context. d) Digital Elevation Model of the planned flight area (Inverse Distance Weighted interpolation from official lidar cartography (SR = 2 m) (ICGC, 2018) (For interpretation of the references to colour in this figure legend, the reader is referred to the web version of this article).

A rural area, such as the one selected, proved to be an exemplary area for land cover mapping, environmental monitoring as well as for archeological purposes. Apart from this diversity, the test field followed the restrictions imposed by the Spanish aerial security agency (Agencia Estatal de Seguridad Aérea, AESA) (BOE, 2017), which prohibits flying UAVs in urban areas, in areas with large groups of people, or in the vicinity of aerodromes or airports (Fig. 1).

Eight flat concrete bases of 75 cm x 75 cm x 10 cm were purposely built within the study area in order to ensure the solidity and durability of these points. These bases, which were used as GCPs and ICPs, were distributed in the study area (Martínez-Carricondo et al., 2018) and covered the northing and easting ranges of the flight area. The location of the bases was planned to focus on the constructed complex and the main crop field surrounding the central flight area. The GCPs were all characterized by being located in plain areas not covered by vegetation. However, horizon visibility was not the same in all GCPs, as the sky view factor was > 89% in all GCPs, except in GCP Nr 7 (77%) (Table 1). These differences are important for the visibility of the satellites when measuring the GCP coordinates (Fig. 2).

A steel screw was placed at the center of each base to position the surveying rod used for determining the coordinate. A template was also created, wherein four quadrants of 25 cm could be easily painted on the base, thereby forming a checkered layout. This further ensured the necessary orthogonality for facilitating the location of the target center. A DGNSS static receiver, which was supported on a tripod with a clamp for high stability, was used to accurately determine the position of the GCPs (Fig. 3).

The DGNSS receiver (Leica Geosystems, 2017) can work with the information provided by a network of Permanent Reference Station (PRS), but this infrastructure has to be implemented in the region of the study area, as with the case of the European permanent reference station network (EUREF-EPN) (Ihde et al., 2014) or Continuously Operating Reference Stations (CORS) (Snay and Soler, 2008) in North America. For example, we used information from the PRS located in Solsona (SONA, http://catnet-ip.icc.cat/spiderweb/frmIndex.aspx), which is managed by the Institut Cartogràfic i Geològic de Catalunya (ICGC, 2017) and located about 4 km from our study area. The DGNSS measurements combined with the information of PRS allow the receiver's position to be determined more precisely than with RTK measurements. Nevertheless, these measurements require post-processing, and thus more time for obtaining the final positions. Continuous observation of the reference stations makes it possible to calculate

Table 1
Sky view factor (SVF) in the surveyed points used as reference coordinates.

Point-ID	Point-1	Point-2	Point-3	Point-4	Point-5	Point-6	Point-7	Point-8
SVF (%)	94.93	96.04	97.15	94.23	89.42	95.90	77.07	98.92

differential corrections to improve the accuracy of the broadcast orbits, the synchrony of the clocks of the satellites and receivers, and the modeling of ionospheric and tropospheric errors (Snay and Soler, 2008). PRS network data can be used in real time or in post-processing treatment.

2.2. Materials

The UAV platforms used were an octocopter (Fig. 4a) and a hexacopter (Fig. 4b). Both had a Pixhawk controller, which was assembled by the HEMAV Company to provide the team with more functionality and additional security measures (Table 2).

The octocopter was used to carry the SONY Alpha 7RII Digital Single-Lens Reflex (DSLR) camera (Table 3), which is sensitive in Red, Green and Blue (RGB) spectral regions, and included a 15-mm fixed lens (Voightländer, 2017). A memory card was located in the flash hotshoe, which recorded the GNSS time at the flash firing. The synchronization between the shooter rear curtain and flash firing is 1/250th of a second (Sony, 2017); the distance travelled by the UAV within this time at the programmed velocity (5 m/s) is 0.02 m.

The hexacopter was used to carry the multispectral and multilens MicaSense RedEdge camera (Table 4), which is sensitive to the RGB, red-edge and near-IR spectral regions (MicaSense, 2015). A port specifically intended for this purpose facilitated connection and synchronization between the camera and the GNSS device for recording the time in a memory card and geotagging the images.

The sensors were mounted on the gimbal of the corresponding platform. In the lab, the camera nodal point was aligned with the gimbal axis to prevent distortions in the lever-arm offsets when the gimbal compensates for the platform attitude angles. The lever-arm offset (X,Y,Z) between the Perspective Center (PC) camera position and the Antenna Phase Center (APC) was measured at a sub-centimetric level. The constant displacement vector (Skaloud et al., 1996) was further introduced in the post-processing software to compensate for the lever-arm offsets. Based on the corrected onboard GNSS signal and the time of image sensing, the PPK software interpolates the position of the camera PC camera position at the time of exposure, outputting the accurate estimation of every image PC position.

The photogrammetric software (Agisoft LLC, 2018) used in our study has been widely used in previous studies to process UAV images and generate orthophotomosaics (Lucieer et al., 2014; Turner et al., 2014a,b; Zabala, 2017; Martínez-Carricondo et al., 2018). The photogrammetric software makes it possible to use automatically geotagged image PC to locate the individual images (DG) or set GCP to aerotriangulate the block (IG). In the case of geotagged image PC (post-processed or not) and IMU data (if provided), the photogrammetric software locates the frames in the map space, following the provided external position coordinates (X,Y,Z), and finds the optimal orientation angles (ω,φ,κ) between overlapped images by rotating, translating and scaling the individual frames. We followed the photogrammetric software workflow proposal developed by the United States Geological Survey (USGS) National Unmanned Aircraft Systems (UAS) Project Office (NUPO) for DSLR imagery (USGS-NUPO(a) (United States Geological Survey - National Unmanned Aircraft Systems Project Office), 2017) and MicaSense RedEdge multispectral imagery (USGS-NUPO(b) (United States Geological Survey - National Unmanned Aircraft Systems Project Office), 2017) for the purpose of obtaining 3D reconstruction from UAV photogrammetric imagery using Structure from Motion (SfM) techniques. A 3D point cloud was created, from which a Digital Surface Model (DSM) was generated. When the optimal correlation of homologous tie points was found to account for the perspective, an automatic camera calibration was achieved with the current environmental conditions, which used more points (> 1k) than in classic lab calibrations (Harwin et al., 2015). Then, the final georeferenced (UTM31 N ETRS89) orthophotomosaic at 0.025 m SR in Sony RGB imagery and at 0.05 m SR in MicaSense RedEdge multispectral imagery (Table 5) was exported to a remote sensing and GIS software (Microstation v 8i (Bentley Systems, 2017) and MiraMon v 8.01b (Pons, 2016)) so as to compare the image-derived coordinates to surveyed points. We used a different camera for one of the experiments in order to carry out a more thorough exploration in spectral and spatial resolutions. We are aware that using two cameras could introduce asymmetry in the experiment design. Nevertheless, we consider the varying results to substantially enrich the comparison part of the paper.

2.3. Methods

The position of the GCPs was obtained by applying two

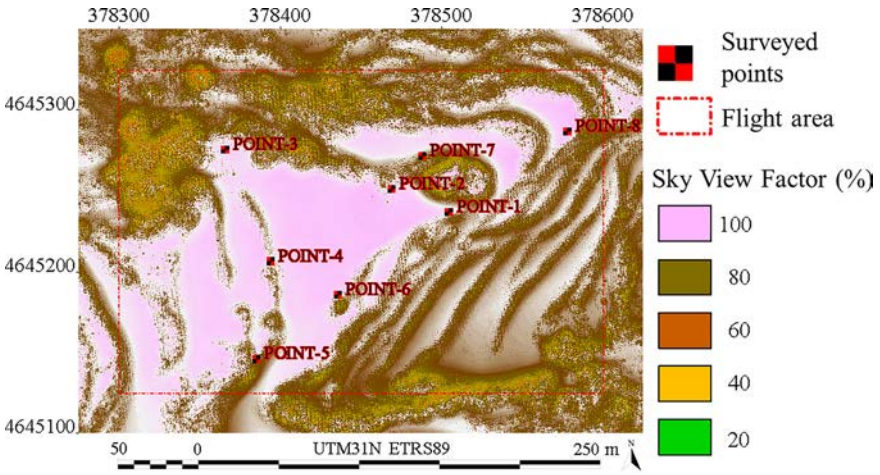

Fig. 2. Sky view factor map obtained from the Digital Surface Model (lidar official cartography (SR = 0.25 m) (ICGC, 2018) and the position of the Ground Control Points.

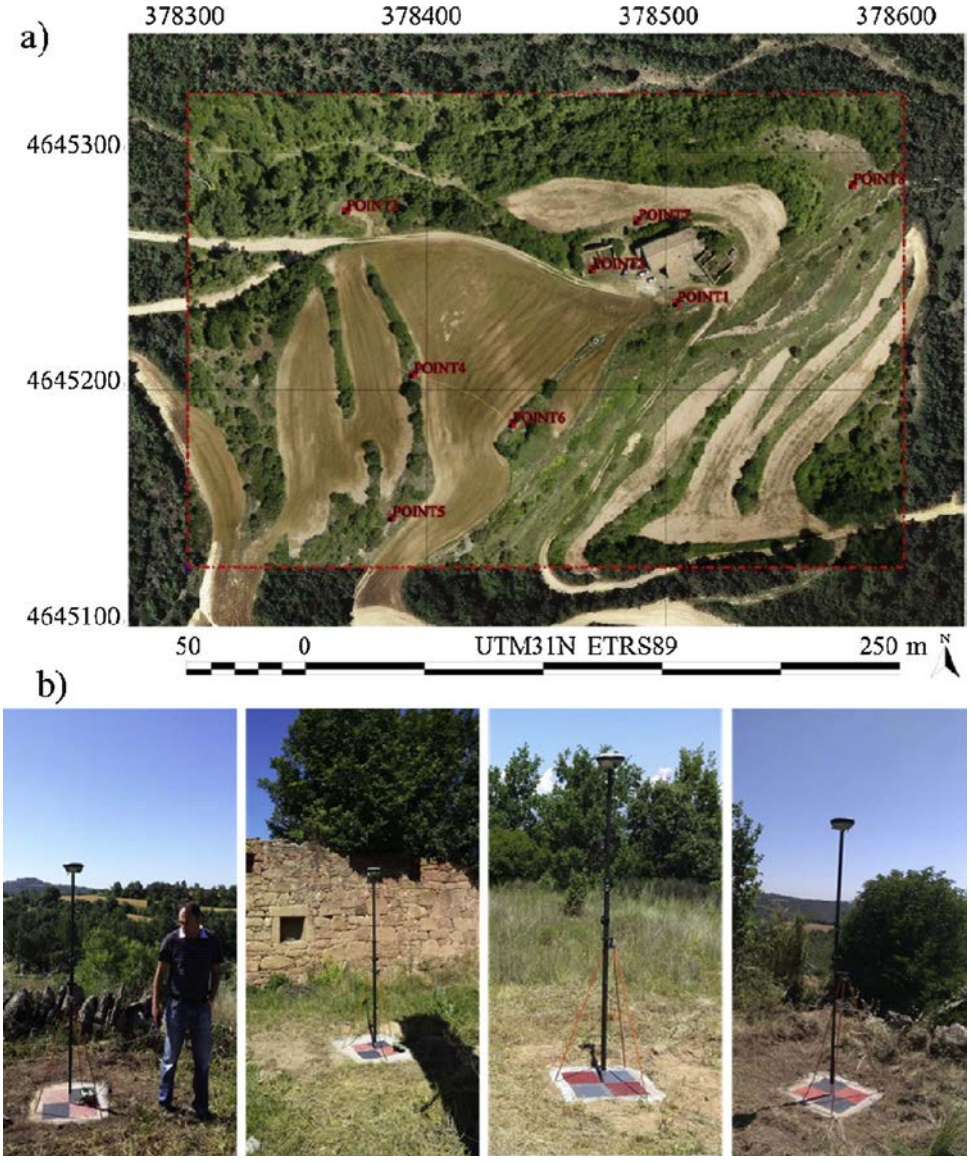

Fig. 3. a) The red rectangle indicates the distribution of surveyed GCPs on the orthophotomosaic generated with the PPK process (SR = 0.025 m). Background (outside the red rectangle): Official state-agency cartography (SR = 0.25 m) (ICGC, 2018). b) The DGNSS receiver, which was held on a tripod with a clamp, received measurements that were later analyzed in post-processing (For interpretation of the references to colour in this figure legend, the reader is referred to the web version of this article).

Fig. 4. a) Octocopter platform with the RGB sensor mounted on the gimbal; b) Hexacopter platform with the multispectral sensor mounted on the gimbal.

Table 2
UAV platforms and their main features.

Manufacturer-Model	Diameter Size (cm)	Flight autonomy (min)	MTOW (kg)	Optical sensor embedded type
DJI-S1000	105	15	11	RGB
DJI-S900	90	18	8.2	Multispectral

Table 3
SONY Alpha 7RII camera and its main features.

Manufacturer-Model	Size (mm)	Weight (g)	Raw radiometric resolution (bits) and expanded dynamic range (DN)	
SONY Alpha 7RII	127 × 96 × 60	625	12 (256 × 3 bands)	
Sensor type	Sensor size (pixels)	Pixel size (μm)	Focal Length (mm)	Bands
35 mm-CMOS	7952 × 5304	4.53	15	R-G-B

methodologies: firstly, all GCP measurements were made using static RTK, and secondly, the static DGNSS was set to collect data for a minimum of 20 min, which were post-processed (PP) to determine the most exact GCP position possible. Moreover, we opted to use RTK in order to expediently obtain coordinates that would be very similar to those calculated in the PP, thereby facilitating confirmation that the results obtained from the two methods are consistent because a priori PP measurements are much more reliable. In this study, we can see that the difference between the RTK and PP data is less than we expected, as it is horizontally almost always below 0.01 m, and vertically below 0.04 m (Table 6). However, for Point-7 there are larger variations between the two methods resulting in differences in X and Y of 0.06 m and 0.09 m, and 0.14 m in elevation.

Hence, the Point-7 position was considered not reliable enough to be taken as a reference. Thus, from the initial eight GCP we planned to use, we ultimately worked with the seven points that had well-known coordinates. Mean differences are 0.002 m in easting, 0.006 m in northing and −0.024 m in elevation (without considering Point-7).

The UAV georeferencing methods evaluation was carried out following the new ASPRS Positional Accuracy Standards for Digital Geospatial Data, which addresses recent innovations in digital imaging and non-imaging sensors, airborne GNSS, IMU and AT technologies (ASPRS, 2015). This standard defines accuracy classes based on RMSE thresholds for digital orthoimagery, digital planimetric data, and digital elevation data (ASPRS, 2015). Horizontal accuracy was assessed using $RMSE_X$ for the horizontal linear RMSE in the X direction (Easting), $RMSE_Y$ for the horizontal linear RMSE in the Y direction (Northing), and RMSEr for the horizontal linear RMSE in the radial direction, including both X- and Y-coordinate errors. Vertical accuracy was assessed using $RMSE_Z$ for the vertical linear RMSE in the Z direction (elevation). Note that vertical accuracy was evaluated as Non-Vegetated Area (NVA) RMSE statistics, since the GCPs were placed in vegetation-free locations. The threshold used to account for 95% of the error in the one-dimensional Z-axis over NVA was $\leq$1.96 x RMSE (ASPRS, 2015).

Horizontal and vertical thresholds (assuming normal distribution) established by ASPRS following the methodologies of the National Standard for Spatial Data Accuracy (NSSDA) FGDC, 1998) are shown in Table 7 (Table 7).

According to previous studies, in a simulation of populations, the high variability of NSSDA estimations is a result of the GCPs' sample size and population deviation (Ariza and Atkinson, 2008). In our case study, the relatively small sample size due to the limited extension of the study area led to a more conservative estimation, although the low population deviation seems to indicate otherwise. As our sample size is smaller than that of the Ariza and Atkinson (2008) simulations, we worked with NSSDA estimations. Indeed, for larger study areas and/or with more GCPs, those criteria proposed by Ariza and Atkinson could be applied.

The design basically consisted of checking the accuracy of the orthophotomosaics generated with the photogrammetric software using four different georeferencing methods, taking well-defined test points on the terrain as references, and comparing the results to the ASPRS standards. Finally, we proceeded to evaluate the differences between them, whereby we considered the estimated economic costs that can be amortized in several flight campaigns.

(1) GNSSNAV: The onboard navigation GNSS receiver used to determine the platform position works with the GPS/GLONASS constellations (using the European Geostationary Navigation Overlay System (EGNOS) augmentation system), L1/L2 frequencies with 20 channels, and a 10 Hz frequency rate (10 timestamps per second). The navigation GNSS method automatically geotags the central position (X,Y,Z) of the frames by recording the coordinates of the onboard GNSS APC at the closest trigger time (the offset between the APC and the PC was not accounted for), accordingly to the 10 Hz rate without differential correction. As previously introduced, at a velocity of 5 m/s, the positioning error due to this gap can range 0.5 m. In the photogrammetric software processing, we applied the workflow recommended by USGS for DSLR imagery (USGS-NUPO(a) (United States Geological Survey - National Unmanned Aircraft Systems Project Office), 2017). The derived orthophotomosaic absolute accuracy was validated with all the surveyed ICPs. The approximate economic cost of the GNSS device is less than 50 €. If direct positioning of images is applied, no time investment is necessary to process the onboard GNSS data. However, the photogrammetric software processing itself can take hours to determine the bundle block adjustment. Two PPK variants were used, which involved different hardware and fieldwork costs:

Table 4
MicaSense RedEdge sensor and its main features.

Manufacturer-Model	Size (mm)	Weight (g)	Raw radiometric resolution (bits) and expanded dynamic range (DN)	
MicaSense RedEdge	121 × 66 × 46	150	12 (0–65,535)	
Sensor type	Sensor size (pixels)	Pixel size (μm)	Focal Length (mm)	Number of bands
CCD	1280 × 960	3.75	5.5	5
#1 Blue FWHM (nm)	#2 Green FWHM (nm)	#3 Red FWHM (nm)	#4 Red-edge FWHM (nm)	#5 NIR FWHM (nm)
468–491	548–568	666–676	712–723	814–865

Table 5
Flight plan main features.

Platform and sensor	Side overlap (%)	Forward overlap (%)	Flight height (m)	Spatial resolution (m)	Georeferencing method
Octocopter -RGB	60	80	80	0.025	GNSSNAV; PPK2; GCP-ICP
Hexacopter Multispectral	60	80	80	0.050	PPK1

Table 6
Target coordinates (reference Ground Control Points) measured in the static Post-Processed (PP), and residuals with respect to Real-Time Kinematic (RTK) measurements.

TARGET COORDINATES UTM-31 N ETRS89 (m) POST-PROCESSED (PP)				RESIDUALS (m) PP *vs.* RTK		
Point-ID	X (Easting)	Y (Northing)	Z (Elevation)	Δ X (Easting)	Δ Y (Northing)	Δ Z (Elevation)
Point-1	378504.631	4645236.608	725.277	0.005	−0.001	−0.026
Point-2	378469.154	4645250.728	725.712	0.008	0.005	−0.012
Point-3	378366.020	4645275.324	726.314	0.008	0.006	−0.019
Point-4	378394.089	4645206.539	729.967	0.005	0.006	−0.014
Point-5	378385.341	4645145.964	734.201	−0.006	0.012	−0.037
Point-6	378435.762	4645185.649	728.625	−0.006	0.010	−0.036
Point-7	378488.194	4645271.260	723.034	−0.060	0.087	0.141
Point-8	378578.130	4645286.430	719.098	−0.004	0.005	−0.021

Table 7
Horizontal and Vertical (NVA) Accuracy Standards for Geospatial Data used to evaluate the four positioning methods.

Horizontal Accuracy at 95 % Confidence X, Y	Horizontal Accuracy at 95 % Confidence radial	Vertical Accuracy at 95 % Confidence Z (NVA)
≤ 2.4477 x *RMSE*	≤ 1.7308 x $RMSE_r$	≤ 1.9600 x *RMSE*

(2) PPK1: PPK1 method (Rokubun, 2018) consists of retrieving the PC camera position at the exposure time by calculating the flight path and interpolating the acquisition time of each image on the calculated trajectory. Argonaut 10 Hz single-frequency carrier-phase GNSS receiver with a 9-degree IMU embedded was used to obtain the position of the UAV. The triggering position was given by the onboard GNSS time sent to the camera MicroSD port, which was designed for this purpose. A Software as a Service (SaaS) (Rokubun, 2018) was used for data post-processing and determining the camera pose at exposure time, whereby we transferred the images and the MicroSD card data to the company by following online steps prescribed on their website (Rokubun, 2018). The PPK1 method, which requires the support of a PRS that continuously receives differential corrections and further corrects the onboard GNSS position, does not rely on any GCP or ground station in the study area. In the photogrammetric software processing, we applied the workflow recommended by USGS for multispectral imagery (USGS-NUPO(b) (United States Geological Survey - National Unmanned Aircraft Systems Project Office), 2017). The final orthophotomosaic absolute accuracy was validated with all surveyed GCPs. The approximate cost of the Argonaut receiver was 350 €, while the SaaS was 200 € (Rokubun, 2018).

(3) PPK2: PPK2 method (Drobit, 2017) proved to be the most sophisticated solution we tested and evaluated. The synchronization between the camera triggering and the GNSS time (Rehak and Skaloud, 2017) was carried out by a card device located in the flash support slit. Said card device collects the flash firing signal just before the rear curtain closes (flash is activated and synchronized with the rear curtain shutter). Drobit v1.6 software (Drobit, 2017), which was based on RTKlib open source libraries, was used for data processing in PPK2. During the post-processing stage, the lever-arm offsets were introduced in the software to obtain PC, instead of APC coordinates. Although PPK2 can work with a PRS, as PPK1 does, we nevertheless used a station located at known coordinates in the study area to improve the local characterization of ionospheric, tropospheric and geometric errors affecting the L1/L2 carrier-phase GNSS signals. Thus, we were able to minimize the distance-dependent errors affecting the accuracy. The function of this base, which was linked to the nearest PRS, was to receive differential corrections continuously to further correct the onboard GNSS position. In the photogrammetric software processing, we applied the workflow recommended by USGS for DSLR imagery (USGS-NUPO (a) (United States Geological Survey - National Unmanned Aircraft Systems Project Office), 2017). The final orthophotomosaic absolute accuracy was validated with seven surveyed GCPs. Although this method does not rely on any GCP, it is nevertheless dependent on the base station located in the study area. The approximate cost of the rover module itself was about 4000 € and the base module was about 4500 € (Drobit, 2017).

(4) GCP–ICP: This method is not supported by onboard GNSS data. IG, which is a well-known technique based on AT, provides a bundle block adjusted to the ground references, and can therefore determine the EOP of each image block in an indirect way. The image orientation with photogrammetric software was done without using the imagery geotagged information. Rather, we manually located the GCP markers in their corresponding individual image. We performed cross-validation to validate the final orthophotomosaic's absolute accuracy, thereby generating seven orthophotomaps georeferenced with six GCPs; the remaining point was the ICP evaluated in each orthophotomap. Cross-validation (leave-one-out) consists of estimating a model from a subset, leaving an isolated value (test point) to perform the validation process, which is then carried out iteratively with all the data of the set (Picard and Cook, 1984). Assuming an accessible region of interest, the economic costs of materializing GCPs, including renting a static DGNSS and the personnel costs approximately amounted to 500 € The time invested was about one hour per GCP for painting and materializing concrete platform points; obviously, the time duration would be reduced if tarps were used or stable ground locations were painted. In our study, we took one hour for each GCP static GNSS measurement, two hours for post-processing static measurements and two processing hours for accurately locating GCPs in individual images.

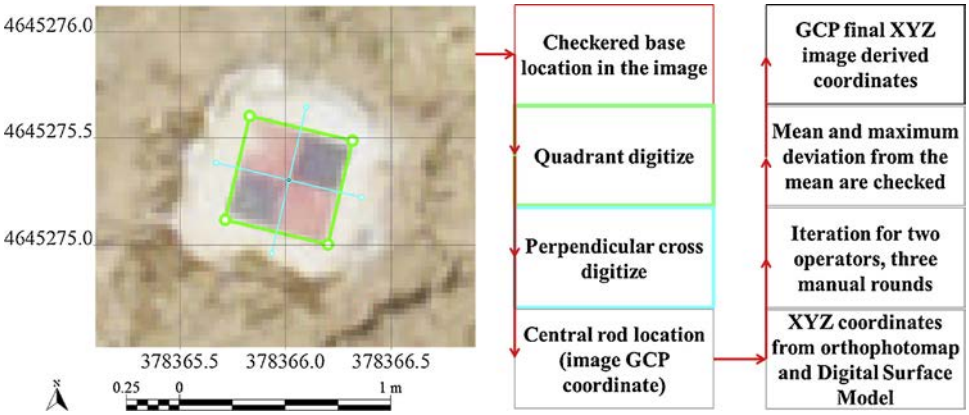

Fig. 5. Methodology for obtaining the image horizontal coordinates of GCPs (example for Point-3).

The coordinates in the resulting orthophotomosaics (image coordinates) were checked by two operators separately (Operator A and Operator B). In order to accurately determine the center of the target, i.e. the rod in the center of the concrete base, the procedure was based on digitizing the squared border (50 cm side) of the checkered area and drawing a centered cross. The coordinate of the crossing lines node was taken as the surveying rod coordinate in the image. Operator A performed this procedure twice, while operator B did a third round on the extraction of image coordinates. The mean value of the three manual rounds was the image value (see Table S1 Supplementary materials) compared with the reference surveyed coordinates. The image coordinates were considered valid if 90% of the coordinates have a difference from the mean value less than one-third of the pixel size and the remaining 10% do not exceed half of the pixel size; otherwise, measurements had to be repeated. In the GCP-ICP cross-validation procedure, seven orthophotomaps were made, whereby one GCP was left out in each map, and Operators A and B extracted the coordinates of this point with the same described procedure (Fig. 5).

3. Results

The well-known surveyed coordinates of the GCP points (static DGNSS with post-processing) were compared with their estimated image-derived position for each method (Table 8). Calculation of one-dimensional (Easting, Northing or elevation) differences between the reference and the estimated values shows that the GNSSNAV method has the highest inaccuracies at all points, whereby PPK1 reduces the order of the error magnitude at all points, while GCP–ICP and PPK2 have very similar levels of accuracy at Point-3, but has clearly higher differences in the remaining points (Table 8). It is worth noting that the PPK2 results show a mean bias (similar to the pixel dimension of 0.025 m), but these values are not large enough to invalidate applying the method in direct georeferencing of UAV imagery of very high resolution. In fact, in other studies using NSSDA accuracy standards FGDC, 1998), we found clearly larger values when scale and pixel dimension are compared.

The one-dimensional indicator of accuracy with respect to the reference points was positively checked for normality. As expected, the geometric errors in the univariate space (RMSE) were also of different orders of error magnitude between the different methods (Table 8). In the GNSSNAV option, the RMSE was under 1 m in X, 0.5 m in Y and over 4 m in Z, i.e. in the metric order; in the PPK1 option, the RMSE was up to 0.15 m in X, 0.20 m in Y and 0.24 m in Z, i.e. in the decimeter order; in the PPK2 option, the RMSE was up to 0.025 m in X or Y; and 0.036 m in Z; and in the GCP–ICP option the RMSE was up to 0.014 m in X, 0.018 m in Y and 0.030 m in Z, i.e. in the centimetric order (Table 9).

The synthetic indicator of planimetry precision, which assumed a normal distribution of the geometric errors in the XY bivariate space (combined in X and Y, or radial), showed a statistical error in 95% of the cases, i.e. 1.837 m in the GNSSNAV method, 0.443 m in the PPK1 method, 0.062 m in the PPK2 method, and 0.039 m in GCP-ICP method (Table 9). The radial indicator proved to be a robust method for determining the planimetric error, and thus for estimating the SR useful for each method, although the bivariate standard deviation of the errors was very valuable in obtaining the planimetric accuracy order of error magnitude of each method (Table 9).

4. Discussion

In this applied study, we used a lower number of GCPs than the number used in previous geometric accuracy evaluation studies (Ariza and Atkinson, 2008; Martínez-Carricondo et al., 2018). All the methods we tested have been proven to perform well in controlled situations. However, for this particular study, we used a realistic setting in UAV

Table 8
Residuals between reference coordinates (PP) and coordinates obtained using UAV positioning methods: (1) GNSSNAV, (2) PPK1, (3) PPK2, (4) GCP–ICP.

Positioning method	Point-ID	Point-1	Point-2	Point-3	Point-4	Point-5	Point-6	Point-8	μ	σ
1) Residuals (m) PP *vs.* GNSSNAV	Δ X	−0.946	−0.906	−0.845	−0.936	−1.001	−0.980	−0.938	−0.936	0.050
	Δ Y	0.436	0.476	0.604	0.528	0.511	0.511	0.398	0.495	0.067
	Δ Z	−4.257	−4.041	−3.591	−4.226	−4.652	−4.515	−4.095	−4.197	0.345
2) Residuals (m) PP *vs.* PPK1	Δ X	0.082	0.124	0.262	0.187	0.114	0.112	0.081	0.137	0.065
	Δ Y	−0.265	−0.272	−0.180	−0.116	−0.083	−0.219	−0.237	−0.196	0.074
	Δ Z	0.305	0.262	0.026	0.188	0.301	0.279	0.178	0.220	0.100
3) Residuals (m) PP *vs.* PPK2	Δ X	−0.030	−0.015	0.004	−0.016	−0.024	−0.034	−0.038	−0.022	0.014
	Δ Y	0.018	0.026	0.025	0.014	0.032	0.027	0.030	0.025	0.060
	Δ Z	−0.044	−0.010	−0.029	−0.032	0.028	−0.046	−0.045	−0.025	0.027
4) Residuals (m) PP *vs.* GCP-ICP cross-validation	Δ X	−0.012	0.008	0.013	0.007	0.007	−0.020	−0.023	−0.003	0.015
	Δ Y	−0.020	−0.002	−0.021	−0.008	−0.025	0.009	−0.025	−0.013	0.013
	Δ Z	0.017	0.023	−0.029	−0.030	0.022	−0.035	−0.046	−0.011	0.030

Table 9
RMSE in each of the univariate spatial components (X, Y and Z) and in the bivariate planimetric component (radial, combined XY) obtained using (1) GNSSNAV, (2) PPK1, (3) PPK2 and (4) GCP–ICP.

		RMSE	RMSE (95 % cases)
1) RMSE (m) GNSSNAV	X	0.937	1.837
	Y	0.499	0.977
	R (radial)	1.062	1.837
	Z	4.209	8.249
2) RMSE (m) PPK1	X	0.150	0.294
	Y	0.207	0.406
	R (radial)	0.256	0.443
	Z	0.238	0.467
3) RMSE (m) PPK2	X	0.025	0.050
	Y	0.025	0.050
	R (radial)	0.036	0.062
	Z	0.036	0.070
4) RMSE (m) GCP–ICP	X	0.014	0.028
	Y	0.018	0.035
	R (radial)	0.023	0.039
	Z	0.030	0.059

operational cases. Moreover, in our study, we learned that the field static measurements might result in proving the planned location of one GCP to be not reliable enough, such that this would have to be discarded, as in the case of Point-7.

Among the methods studied, the GCP-ICP method yielded the highest accuracy altogether. The PPK2 method, the PPK1 method and the GNSSNAV method yielded the second, the third and the fourth highest accuracies, respectively. Regarding the residuals (Table 8) and the image pixel size as a reference value, a clear bias is present in GNSSNAV and PPK1. These methods are not only less accurate in general terms, but they also provide a systematic displacement due to the combined error sources of the lever-arm offset, the lack of any ground reference point (GNSSNAV), or that this point was not close enough to our reference value (PPK1). Interestingly, the PPK2 and GCP–ICP methods, which had one or more ground reference points in the same study area, provided acceptable biases when compared with the reference value. Nevertheless, the economic cost, invested time and ground requirements of each method are different and can fit several remote sensing purposes. Note that even UAV imagery can be acquired at > 10 cm SR, and can thus be resampled to coarser pixel size to absorb geometric uncertainty, which is typically the radial error. Resampled imagery, which can be used to improve the processing of other remote sensing products, is not as detailed as drone-acquired imagery (Table 10).

The GNSSNAV method provided the poorer planimetric and altimetric accuracies, by overpassing 1 m. However, at an approximate cost of 50 €, GNSSNAV was the most affordable and the easiest-to-use option, and did not require ground or external support. Although this option is not useful for combining UAV imagery with satellite or airborne imagery < 2 m SR, it can nevertheless be useful for analyzing the intra-pixel features of airborne-acquired products of official mapping agency at 2.5 m (ICGC, 2018; PNOA, 2018) or satellite sensors with coarser SR, such as the 10-m bands of MSI onboard Sentinel-2 (ESA, 2015), or the 15-m panchromatic bands of ETM + onboard Landsat-7 and OLI onboard Landsat-8 (NASA, 2018).

The PPK1 method, which improved the raw GNSS data by one order of error magnitude without in situ ground support, approximately costs 600 € (amortizable). Using PRS increases the accuracy due to the correction of the GNSS satellite signal. However, a post-processing service has to be additionally contracted. This option was accurate enough to combine UAV resampled imagery with the airborne-acquired products of official mapping agency at 0.25 m or 0.50 m SR, lidar data at 2 points/m^2(ICGC, 2018; PNOA, 2018), or sub-metric satellite imagery as the panchromatic band of WorldView-4 (Nadir: 0.31 m SR, 56° Off-Nadir: 1.00 m SR) (DigitalGlobe, 2018). However, it did not reach the goal of registering UAV imagery with SR > 0.05 m. Moreover, this method is not useful if PRS is not accessible within a radius of 20 km.

The PPK2 method, which approximately costs 8500 € (amortizable) was consistent enough in generating large-scale mapping from UAV imagery with less effort than the GCP–ICP method. The use of a station in the study area and a double-frequency receiver allows a better correction of satellite signal, and the synchronization of camera acquisition with the GNSS receiver is almost optimal. The cartographic quality that can be generated will depend on the specific norms applied. Nevertheless, it is clear that highly detailed maps (ASPRS, 2015; FGDC, 1998) can be produced with the PPK2 method. According to ASPRS tables (see Table 2), the goal of mapping at 1:200 scale with 5-cm SR imagery can be achieved in planimetry and in altimetry. Moreover, it seems that the UAV products processed with the PPK2 method constitute a valid alternative to the GCP–ICP method. However, such accuracy depends on the logistics of mounting a base station and in situ ground support.

Among all four methods studied, the GCP-ICP method proved to be the most accurate method. As far as the time invested and the economic costs involved, we spent one hour for static GNSS measurements for each GCP (displacing and setting the DGNSS) with specialized equipment (renting a DGNSS) and hiring a skilled personnel (500 €), and about two hours for post-processing the data. If GCPs materialized in concrete bases prove useful in future campaigns, as was the case in our study, then the process of materializing and painting the targets should be carried out the day before the flight. In our experience, the markers had to be placed in the corresponding images, which proved to be a tedious task that required over one hour. Apart from setting the GCPs, it is fair to note that the region of interest is not always accessible and this method is not useful in every case.

5. Conclusions

The positioning of UAV-acquired frame imagery can be solved by applying different methods with corresponding accuracies (ASPRS), economic costs and time investments. Aside from the multiple combinations of optical sensors, GNSS receivers, platforms, gimbals, and

Table 10
Summary of the pros and cons of the evaluated georeferencing methods.

	1) GNSSNAV	2) PPK1	3) PPK2	4) GCP–ICP
$RMSE_r$ (m)	1.062	0.256	0.036	0.023
$RMSE_z$ (m)	4.209	0.238	0.036	0.030
Approximate initial investment cost (€)	50	600	8500	500
Time consuming (h)	≥1	≥24	≥24	≥48
Involved personnel	≥1	≥1	≥2	≥2
In situ ground support	NO	NO	YES	YES
Suggested SR of the corrected imagery (m)	≥2	≥0.25	≥0.05	≥0.025
Examples of RS products to be combined with UAV data	Sentinel-2, imagery and coarser	WorldView imagery, airborne AHS, CASI, lidar data, and coarser	UAV Sequoia, Cubert data and coarser	UAV reflex cameras data and coarser
ASPRS associated maximum map scale	1:12000	1:1500	1:400	1:200

software that can be tested, we compared four commonly used georeferencing solutions in a real operational case for environmental remote sensing purposes with commonly used materials. Although the raw GNSS receiver direct georeferencing solution is not suitable for registering UAV data in different flight acquisitions, it is easy to use, can be purchased at a low cost, and does not require ground support, which is useful for visual inspections of remote sensing products with a pixel size coarser than 2 m, such as Landsat-like imagery. The Post-Processed Kinematic solution using single-frequency carrier-phase GNSS receiver and correcting GNSS signal with information from a permanent reference station located up to 20 km away, is valid for registering drone imagery with airborne lidar data or orthoimagery with a ground sampling distance of up to 25 cm. The Post-Processed Kinematic solution using double-frequency carrier-phase GNSS receiver and correcting the GNSS signal with information from a base station located in the study area, reaches the goal of registering UAV imagery at its common spatial resolution ($\geq$5 cm). However, the logistics require the support of in situ materials and the cost is higher. The conventional indirect georeferencing using ground control points is the most accurate solution, as it is useful for registering UAV imagery with any other remote sensing coarser product. However, it also requires intense in situ ground support and is by far more time-consuming.

This study demonstrates that different UAV optical frame imagery georeferencing methods can be suitable and most effective when combined with conventional and freely available remote sensing products (e.g. Landsat, Sentinel-2, official mapping agencies lidar or orthoimagery). Obviously, the most accurate solutions are more expensive. Moreover, time and ground support are important factors to consider. Our paper is intended to be a quick and reliable guide for environmental scientists that provides a comparison of four known georeferencing methods to help them select the best option that suits their purpose, particularly in view of the accuracy required when combining UAV imagery with well-known airborne and satellite remote sensing platforms.

Author contributions

F.M., J.P. and C.P. conceived and designed the experiments. J.P and C.P performed the field data experiments. J.P and C.P. analyzed the data. J.P., C.P. and X.P. wrote the paper. F.M and X.P. supervised the paper and the overall experiments.

Conflicts of interest

The authors declare that there are no conflicts of interest. The sponsors had no role in the design of the study, the collection, analyses, or interpretation of data, the writing of the manuscript, or the decision to publish the results.

Acknowledgments

This work was supported by the European Union through the ECOPOTENTIAL Project (H2020 641762-2 EC) and by an Innovation grant from the Spanish Ministry of Science (ACAPI, CGL2015-69888-P). The GRUMETS Research Group is partially supported by the Catalan Government under Grant (SGR2017-1690). C.P. is a recipient of a FI-DGR scholarship grant (2016B_00410). X.P. is a recipient of an ICREA Academia Excellence in Research Grant (< GN542016-2020 < / GN4 >). We would like to acknowledge R.F., who collaborated on measuring the control points with the static GNSS and their post-processing, X.C., who collaborated on the materialization of points and logistics, and J.B., who also collaborated on the materialization of the points. The HEMAV Company collaborated on the flight campaign and made its technical team available. M.S.'s expertise in the UAV flight was of great help. This work was carried out as part of the Doctoral Program of the Geography Department of the Universitat Autònoma de Barcelona.

Appendix A. Supplementary data

Supplementary material related to this article can be found, in the online version, at doi:https://doi.org/10.1016/j.jag.2018.10.018.

References

Aasen, H., Honkavaara, E., Lucieer, A., Zarco-Tejada, P.J., 2018. Quantitative remote sensing at ultra-high resolution with UAV spectroscopy: a review of sensor technology, measurement procedures, and data correction workflows. Remote Sens. 10, 1091–1933. https://doi.org/10.3390/rs10071091.

Agisoft LLC, 2018. PhotoScan User Manual, Professional Edition, Version 1.4.1. URL: (Last date accessed: 1 Oct. 2018). http://www.agisoft.com/pdf/photoscan-pro_1_4_en.pdf.

Ariza, F.J., Atkinson, A.D., 2008. Variability of NSSDA estimations. J. Surv. Eng. 134, 39–44. https://doi.org/10.1061/(ASCE)0733-9453(2008)134:2(39).

ASPRS (American Society for Photogrammetry and Remote Sensing), 2014. ASPRS Positional Accuracy Standards for Digital Geospatial Data. Edition 1, Version 1.0.0. URL: (Last date accessed: 1 Oct. 2018).. https://www.asprs.org/wp-content/uploads/2015/01/ASPRS_Positional_Accuracy_Standards_Edition1_Version100_November2014.pdf.

ASPRS (American Society for Photogrammetry and Remote Sensing), 2015. New Standards for New Era: Overview of the 2015 ASPRS Positional Accuracy Standards for Digital Geospatial Data. URL: (Last date accessed: 1 Oct. 2018. https://www.asprs.org/wp-content/uploads/2015/01/PERS_March2015_Highlight.pdf.

Bentley Systems, 2017. MicroStation, Version 8.1. URL: (Last date accessed: 1 Oct. 2018). https://www.bentley.com.

Bisnath, S., Wells, D., Santos, M., Cove, K., 2004. Initial results from a Long baseline, kinematic, differential GPS carrier phase experiment in a Marine environment. PLANS 2004 Position Location and Navigation Symposium. IEEE, Monterey, USA, pp. 625–631. https://doi.org/10.1109/PLANS.2004.1309052. 2004 Apr 26–29, Cat. No. 04CH37556.

Bláha, M., Eisenbeiss, H., Grimm, D., Limpach, P., 2012. Direct georeferencing of UAVs. ISPRS - International Archives of the Photogrammetry, Remote Sensing and Spatial Information Sciences, Volume XXXVIII-1/C22, 2011 ISPRS Zurich 2011 Workshop; 2011 Sep 14–16; Zurich, Switzerland. p. 131–136. https://doi.org/10.5194/isprsarchives-XXXVIII-1-C22-131-2011.

BOE (Boletín Oficial del Estado), 2017. “Real Decreto 1036/2017, de 15 de diciembre, por el que se regula la utilización civil de las aeronaves pilotadas por control remoto” [Royal Decree RD 1036/2017, of December 15, for the regulation of the civil use of remotely piloted aircrafts], vol. 316. Ministerio de Fomento, Madrid, Spain, pp. 129609–129641. BOE n URL: (Last date accessed: 1 Oct. 2018). http://www.boe.es/boe/dias/2017/12/29/pdfs/BOE-A-2017-15721.pdf.

Borgogno Mondino, E., Gajetti, M., 2017. Preliminary considerations about costs and potential market of remote sensing from UAV in the Italian viticulture context. Eur. J. Remote Sens. 50, 310–319. https://doi.org/10.1080/22797254.2017.1328269.

Chio, S.-H., 2016. VBS RTK GPS-assisted self-calibration bundle adjustment for aerial triangulation of fixed-wing UAS images for updating topographic maps. Bol Cienc Geod. 22, 665–684. https://doi.org/10.1590/S1982-21702016000400038.

Chio, S.-H., Lin, C.-H., 2017. Preliminary study of UAS equipped with thermal camera for volcanic geothermal monitoring in Taiwan. Sensors 17, 1649–1666. https://doi.org/10.3390/s17071649.

Colomina, I., Molina, P., 2014. Unmanned aerial systems for photogrammetry and remote sensing: a review. ISPRS – J. Photogramm. 92, 79–97. https://doi.org/10.1016/j.isprsjprs.2014.02.013.

Crommelinck, S., Bennett, R., Gerke, M., Ying Yang, M., Vosselman, G., 2017. Contour detection for UAV-Based cadastral mapping. Remote Sens. 9, 171–184. https://doi.org/10.3390/rs9020171.

Daakir, M., Pierrot-Deseilligny, M., Bosser, P., Pichard, F., Thom, C., Rabot, Y., Martin, O., 2017. Lightweight UAV with on-board photogrammetry and single-frequency GPS positioning for metrology applications. ISPRS – J. Photogramm. 127, 115–126. https://doi.org/10.1016/j.isprsjprs.2016.12.007.

DigitalGlobe, 2018. DigitalGlobe Products and Services. URL: (Last date accessed: 25 Jan. 2018. https://www.digitalglobe.com/#products.

Drobit, 2017. The Onboard Surveyor. A PPK Solution for Drone-mapping. URL: (Last date accessed: 1 Oct. 2018). https://www.drobit.es/drobit-specs-sheet.pdf.

ESA (European Space Agency), 2015. Sentinel-2A User Handbook. Released 24/07/2015. Rev.2 https://sentinels.copernicus.eu/web/sentinel/user-guides/document-library/-/asset_publisher/xlslt4309D5h/content/sentinel-2-user-handbook URL: (Last date accessed: 1 Oct. 2018).

FGDC (Federal Geographic Data Committee), 1998. Geospatial Positioning Accuracy Standards. Part 3: National Standard for Spatial Data Accuracy (NSSDA). URL: (Last date accessed: 1 Oct. 2018). https://www.fgdc.gov/standards/projects/accuracy/part3/chapter3.

Harwin, S., Lucieer, A., Osborn, J., 2015. The impact of the calibration method on the accuracy of point clouds derived using unmanned aerial vehicle multi-view stereopsis. Remote Sens. (Basel) 7, 11933–11953. https://doi.org/10.3390/rs70911933.

ICGC (Institut Cartogràfic i Geològic de Catalunya), 2017. Fonaments Del Posicionament Diferencial I Introducció a NTRIP” [Fundamentals of Differential Positioning and Introduction to NTRIP]. URL: (Last date accessed: 1 Oct. 2018). http://www.icgc.

cat/content/download/48729/337223/version/5/file/NTRIP_a_ICGC_%20v8.pdf.
ICGC (Institut Cartogràfic i Geològic de Catalunya), 2018. Aerial Photos and Orthophotos. URL: (Last date accessed: 1 Oct. 2018. http://www.icgc.cat/en/Public-Administration-and-Enterprises/Downloads/Aerial-photos-and-orthophotos.
Ihde, J., Habrich, H., Sacher, M., Söhne, W., Altamimi, Z., Brockmann, E., Bruyninx, C., Caporali, A., Dousa, J., Fernandes, R., Hornik, H., Kenyeres, A., Lidberg, M., Mäkinen, J., Poutanen, M., Stangl, G., Torres, J.A., Völksen, C., 2014. EUREF's contribution to national, European and global geodetic infrastructures. Proceedings of the IAG General Assembly 139, 189–196. https://doi.org/10.1007/978-3-642-37222-3_24. 2011 Jun 28–Jul 2.
Komárek, J., Klouček, T., Prošek, J., 2018. The potential of Unmanned Aerial Systems: A tool towards precision classification of hard-to-distinguish vegetation types? Int J Appl Earth Obs. 71, 9–19. https://doi.org/10.1016/j.jag.2018.05.003.
Geosystems, Leica, 2017. Leica Viva GS14 Technical Specifications. URL: (Last date accessed: 1 Oct. 2018). http://www.leica-geosystems.es/downloads123/zz/gpsgis/VivaGS14/brochures-datasheet/Leica_Viva_GS14_DS_en.pdf.
Lin, A.Y.M., Novo, A., Har-Noy, S., Ricklin, N.D., Stamatiou, K., 2011. Combining GeoEye-1 satellite remote sensing, UAV aerial imaging, and geophysical surveys in anomaly detection applied to archaeology. IEEE – J. Sel. Top. Appl. 4, 870–876. https://doi.org/10.1109/JSTARS.2011.2143696.
Lucieer, A., Turner, D., King, D.H., Robinson, S.A., 2014. Using an Unmanned Aerial Vehicle (UAV) to capture micro-topography of Antarctic moss beds. Int J Appl Earth Obs. 27, 53–62. https://doi.org/10.1016/j.jag.2013.05.011.
Manfreda, S., McCabe, M., Miller, P., Lucas, R., Pajuelo Madrigal, V., Mallinis, G., Ben-Dor, E., Helman, D., Estes, L., Ciraolo, G., et al., 2018. On the use of unmanned aerial systems for environmental monitoring. Remote Sens. 10, 641–669. https://doi.org/10.3390/rs10040641.
Martínez-Carricondo, P., Agüera-Vega, F., Carvajal-Ramírez, F., Mesas-Carrascosa, F.J., García-Ferrer, A., Pérez-Porras, F.J., 2018. Assessment of UAV-photogrammetric mapping accuracy based on variation of ground control points. Int. J. Appl. Earth Obs. 72, 1–10. https://doi.org/10.1016/j.jag.2018.05.015.
MicaSense, 2015. MicaSense RedEdge™ 3 Multispectral Camera User Manual. MicaSense, Inc., Seattle, WA, pp. 33. URL: (Last date accessed: 1 Oct. 2018). https://support.micasense.com/hc/en-us/article_attachments/204648307/RedEdge_User_Manual_06.pdf.
NASA (National Aeronautics and Space Administration), 2018. Landsat Data Continuity Mission (LCDM). URL: (Last date accessed: 1 Oct. 2018). https://www.nasa.gov/mission_pages/landsat/main/index.html.
Picard, R., Cook, D., 1984. Cross-validation of regression models. J. Am. Stat. Assoc. 79, 575–583. https://doi.org/10.1080/01621459.1984.10478083.
PNOA (Plan Nacional de Ortofotografía Aérea), 2018. Productos generados" [Generated products]. URL: (Last date accessed: 1 Oct. 2018). http://pnoa.ign.es/productos.
Pons, X., 2016. "MiraMon. Sistema d'Informació Geogràfica i software de Teledetecció. Versió 8.01b" [MiraMon. Geographical Information System and Remote Sensing software. Version 8.01b]. Centre de Recerca Ecològica i Aplicacions Forestals, CREAF. Bellaterra. ISBN: 84-931323-4-9. URL: http://www.creaf.uab.cat/miramon/ (Last date accessed: 1 Oct. 2018).
Rehak, M., Skaloud, J., 2017. Time synchronization of consumer cameras on Micro aerial Vehicles. ISPRS – J. Photogramm. 123, 114–123. https://doi.org/10.1016/j.isprsjprs.2016.11.009.
Rehak, M., Mabillard, R., Skaloud, J., 2013. A Micro-UAV with the capability of direct georeferencing. ISPRS - International Archives of the Photogrammetry, Remote Sensing and Spatial Information Sciences, Volume XL-1/W2, 2013 UAV-g2013; 2013 Sep. 4–6; Rostock, Germany 317–323. https://doi.org/10.5194/isprsarchives-XL-1-W2-317-2013.
Rehak, M., Skaloud, J., 2015. Fixed-wing micro aerial vehicle for accurate corridor mapping. ISPRS - Annals of the Photogrammetry, Remote Sensing and Spatial Information Sciences, Volume II-1/W1, 2015 International Conference on Unmanned Aerial Vehicles in Geomatics; 2015 Aug 30–Sep 02 23–30. https://doi.org/10.5194/isprsannals-II-1-W1-23-2015.
Remondino, F., Barazzetti, L., Nex, F., Scaioni, M., Sarazzi, D., 2012. UAV Photogrammetry for Mapping and 3d Modeling -current Status and Future Perspectives-. ISPRS - International Archives of the Photogrammetry, Remote Sensing and Spatial Information Sciences, Volume XXXVIII-1/C22, 2011 ISPRS Zurich 2011 Workshop; 2011 Sep 14–16, Zurich, Switzerland, pp. 1–7. https://doi.org/10.5194/isprsarchives-XXXVIII-1-C22-25-2011.
Rokubun, 2018. Argonaut Datasheet. URL: (Last date accessed: 1 Oct. 2018). http://rokubun.cat/wp-content/uploads/2017/12/ARGONAUT_Brochure.pdf.
Skaloud, J., Cramer, M., Schwarz, K.P., 1996. Exterior orientation by direct measurement of camera position and attitude. ISPRS - International Archives of Photogrammetry and Remote Sensing Vol. XXXI, Part B3; 1996 Jul 9–19; Vienna, Austria. P. 125–130. URL: (Last date accessed: 1 Oct. 2018). http://www.ifp.uni-stuttgart.de/publications/1996/wien96_gpsins.pdf.
Snay, R.A., Soler, T., 2008. Continuously operating reference stations (CORS): history, applications, and future enhancements. J Surv Eng. 134, 95–104. https://doi.org/10.1061/(ASCE)0733-9453(2008)134:4(95).
Sony, 2017. α7R e-mount Camera With Full Frame Sensor. Full Specifications and Features. URL: (Last date accessed: 1 Oct. 2018). https://www.sony.com/electronics/interchangeable-lens-cameras/ilce-7r/specifications#specifications.
Tian, J., Wang, L., Li, X., Gong, H., Shi, C., Zhong, R., Liu, X., 2017. Comparison of UAV and WorldView-2 imagery for mapping leaf area index of mangrove forest. Int. J. Appl. Earth Obs. 61, 22–31. https://doi.org/10.1016/j.jag.2017.05.002.
Turner, D., Lucieer, A., Malenovský, Z., King, D.H., Robinson, S.H., 2014a. Spatial Co-registration of ultra-high resolution visible, multispectral and thermal images acquired with a Micro-UAV over antarctic moss beds. Remote Sens. 6, 4003–4024. https://doi.org/10.3390/rs6054003.
Turner, D., Lucieer, A., Wallace, L., 2014b. Direct georeferencing of ultrahigh-resolution UAV imagery. IEEE Trans. Geosci. Remote 52, 2738–2745. https://doi.org/10.1109/TGRS.2013.2265295.
USGS-NUPO(a) (United States Geological Survey - National Unmanned Aircraft Systems Project Office), 2017. Unmanned Aircraft Systems Data Post-processing. Structure From Motion Photogrammetry. Section – 1 Digital Single-lens Reflex (DSLR) Imagery. URL: (Last date Accessed: 1 Oct. 2018). https://uas.usgs.gov/pdf/PhotoScanProcessingDSLRMar2017.pdf.
USGS-NUPO(b) (United States Geological Survey - National Unmanned Aircraft Systems Project Office), 2017. Unmanned Aircraft Systems Data Post-processing. Structure From Motion Photogrammetry. Section – 2 MicaSense 5-band Multispectral Imagery. URL: (Last date Accessed: 1 Oct. 2018). https://uas.usgs.gov/pdf/PhotoScanProcessingMicaSenseMar2017.pdf17.pdf.
Voightländer, 2017. E-Mount 15 Mm / F 4.5 Super Wide Heliar Aspherical III. URL: (Last date Accessed: 1 Oct. 2018). https://www.voigtlaender.de/lenses/e-mount/15-mm-14-5-super-wide-heliar-aspherical-iii/?lang=en.
Whitehead, K., Hugenholtz, C., 2014. Remote sensing of the environment with small unmanned aircraft Systems (UASs), part 1: a review of progress and challenges. J. Unmanned Veh. Syst. 7, 69–85. https://doi.org/10.1139/juvs-2014-0007.
Wouda, F.J., Giuberti, M., Bellusci, G., Veltink, P.H., 2016. Estimation of full-body poses using only five inertial sensors: an eager or lazy learning approach? Sensors 16, 2138–2155. https://doi.org/10.3390/s16122138.
Zabala, S., 2017. Comparison of Multi-temporal and Multispectral Sentinel-2 and Unmanned Aerial Vehicle Imagery for Crop Type Mapping". Master of Science (MSc) Thesis in Geo-information Science and Earth Observation for Environmental Modelling and Management. June 2017. URL:. Lund University, Lund, Sweden. http://lup.lub.lu.se/luur/download?func=downloadFile&recordOId=8917610&fileOId=8917627.

2.3. Correcció radiomètrica d'escenes Landsat-8 i Sentinel-2A utilitzant imatges de dron en sinergia amb espectroradiometria de camp

Padró J.C., Muñoz F.J., Avila L.A., Pesquer L., Pons X. (2018). Radiometric Correction of Landsat-8 and Sentinel-2A Scenes Using Drone Imagery in Synergy with Field Spectroradiometry. *Remote Sensing, 10 (11), 1687-1713*. DOI: 10.3390/rs10111687. http://dx.doi.org/10.3390/rs10111687. (IF: 3.406, Q2: 8/30 (2017) [Remote Sensing]).

Resum: L'objectiu principal d'aquesta recerca és utilitzar dades captades amb un sensor multiespectral a bord d'UAV, en sinergia amb dades d'espectroradiometria de camp, per millorar la correcció radiomètrica d'imatges dels satèl·lits Landsat-8 (L8) i Sentinel-2 (S2). La hipòtesi central és que les imatges adquirides amb sensors multiespectrals en UAV i ben calibrades amb mesures de camp, poden omplir el buit d'escala entre imatges de satèl·lit i mesures *in-situ* convencionals. Això és possible mitjançant la captura de mostres en una àrea més gran, incloses les cobertes del sòl de difícil accés, i en menys temps, però alhora amb un acurat tractament radiomètric de les imatges d'UAV. Amb aquest objectiu i mitjançant imatges gairebé coincidents de L8 i S2, s'ha aplicat un flux de treball d'escalat ascendent, en el qual: (a) les dades multiespectrals adquirides per UAV s'han ajustat empíricament a les mesures de la reflectància *in-situ*, mitjançant un ampli conjunt de referències radiomètriques distribuïdes al llarg del domini espectral del sensor; (b) les dades de dron s'han adaptat a les malles de les imatges de satèl·lit i s'han comparat amb els productes oficials de correcció radiomètrica del L8 i del S2 (6S-LaSRC i Sen2Cor-SNAP, respectivament) i amb l'algorisme CorRad-MiraMon utilitzant PIA (PIA-MiraMon) per tal d'examinar la seva exactitud global; (c) a continuació, s'ha utilitzat un subconjunt de dades de dron com a referències de reflectància, en combinació amb l'algorisme CorRad-MiraMon (nou mètode anomenat UAS-MiraMon), per a corregir radiomètricament les bandes coincidents en els sensors de l'UAV, del L8 i del S2; i (d) per a avaluar la coherència entre sensors que ofereix el nou mètode, s'han comparat les escenes L8 i S2 corregides radiomètricament amb UAS-MiraMon. En el primer pas del flux de treball, els resultats han mostrat una bona correlació entre les mesures espectroradiomètriques de camp i les dades d'UAV en totes les bandes avaluades (R^2>0.946). En el segon pas, les dades d'UAV han indicat un bon ajust amb els productes oficials en bandes del visible ($RMSE_{VIS}$≤2.484 %), però s'han obtingut uns resultats deficients en el infraroig proper ($RMSE_{IRp}$≥6.688 %) a causa de les diferències de resposta espectral entre sensors. En el tercer pas, l'UAS-MiraMon ha tingut un millor ajust en el visible ($RMSE_{VIS}$≤2.018 %) que els altres mètodes de correcció radiomètrica (6S-LaSRC (RMSE≤2.680 %), Sen2Cor-SNAP (RMSE≤2.192 %) i PIA-MiraMon (RMSE≤3.130 %), però no ha aconseguit resultats suficients a la banda IRp ($RMSE_{IRp}$≤7.530 %), fet que també s'ha produït amb els altres mètodes. En la comparació entre sensors, el mètode UAS-MiraMon ha aconseguit un excel·lent ajust (L8-S2) ($RMSE_{VIS}$≤1 %). L'àrea mostrejada amb l'UAV inclou 51 píxels L8 (30 m), 143 píxels S2 (20 m) i 517 píxels S2 (10 m). El temps necessari per cobrir aquesta àrea ha estat de 10 minuts i ha inclòs àrees de difícil accés. El

mostreig obtingut ha estat sistemàtic en l'àrea d'estudi, de naturalesa ràster i amb una mida de píxel de 6 cm, cosa que ha permès una adaptació fàcil però rigorosa de les dades d'UAV a les diferents malles de satèl·lit. Aquests avenços milloren les capacitats humanes per al mostreig espectroradiomètric de camp convencional. Al mateix temps, l'estudi també mostra que l'espectroradiometria de camp és la columna vertebral que sustenta el flux de treball complet d'escalat ascendent. En conclusió, es demostra que la sinergia entre espectroradiometria de camp, sensors UAV i dades de satèl·lit tipus Landsat i Sentinel-2 pot ser una eina útil per a les correccions radiomètriques que s'utilitzen en estudis mediambientals de caràcter local o en zones protegides a tot el món.

Paraules clau: correcció radiomètrica; Landsat-8; OLI; Sentinel-2; MSI; UAS; UAV; MicaSense RedEdge; espectroradiometria de camp; escalat ascendent.

remote sensing

MDPI

Article

Radiometric Correction of Landsat-8 and Sentinel-2A Scenes Using Drone Imagery in Synergy with Field Spectroradiometry

Joan-Cristian Padró [1,*], Francisco-Javier Muñoz [2], Luis Ángel Ávila [3], Lluís Pesquer [4] and Xavier Pons [1]

1 Grumets Research Group, Dep. Geografia, Edifici B, Universitat Autònoma de Barcelona, 08193 Bellaterra, Catalonia, Spain; Xavier.Pons@uab.cat
2 HEMAV S.L. Edifici RDIT, 08860 Castelldefels, Catalonia, Spain; jmunoz@hemav.com
3 Instituto de Estudios de Régimen Seccional del Ecuador (IERSE), Universidad del Azuay, 010107 Cuenca, Azuay, Ecuador; luisavila@uazuay.edu.ec
4 Grumets Research Group, CREAF, Edifici C, Universitat Autònoma de Barcelona, 08193 Bellaterra, Catalonia, Spain; l.pesquer@creaf.uab.cat
* Correspondence: joancristian.padro@uab.cat; Tel.: +34-935-814-343

Received: 3 September 2018; Accepted: 24 October 2018; Published: 26 October 2018

Abstract: The main objective of this research is to apply unmanned aerial system (UAS) data in synergy with field spectroradiometry for the accurate radiometric correction of Landsat-8 (L8) and Sentinel-2 (S2) imagery. The central hypothesis is that imagery acquired with multispectral UAS sensors that are well calibrated with highly accurate field measurements can fill in the scale gap between satellite imagery and conventional in situ measurements; this can be possible by sampling a larger area, including difficult-to-access land covers, in less time while simultaneously providing good radiometric quality. With this aim and by using near-coincident L8 and S2 imagery, we applied an upscaling workflow, whereby: (a) UAS-acquired multispectral data was empirically fitted to the reflectance of field measurements, with an extensive set of radiometric references distributed across the spectral domain; (b) drone data was resampled to satellite grids for comparison with the radiometrically corrected L8 and S2 official products (6S-LaSRC and Sen2Cor-SNAP, respectively) and the CorRad-MiraMon algorithm using pseudo-invariant areas, such as reflectance references (PIA-MiraMon), to examine their overall accuracy; (c) then, a subset of UAS data was used as reflectance references, in combination with the CorRad-MiraMon algorithm (UAS-MiraMon), to radiometrically correct the matching bands of UAS, L8, and S2; and (d) radiometrically corrected L8 and S2 scenes obtained with UAS-MiraMon were intercompared (intersensor coherence). In the first upscaling step, the results showed a good correlation between the field spectroradiometric measurements and the drone data in all evaluated bands ($R^2 > 0.946$). In the second upscaling step, drone data indicated good agreement (estimated from root mean square error, RMSE) with the satellite official products in visible (VIS) bands ($RMSE_{VIS} < 2.484\%$), but yielded poor results in the near-infrared (NIR) band ($RMSE_{NIR} > 6.688\%$ was not very good due to spectral sensor response differences). In the third step, UAS-MiraMon indicated better agreement ($RMSE_{VIS} < 2.018\%$) than the other satellite radiometric correction methods in visible bands (6S-LaSRC (RMSE < 2.680%), Sen2Cor-SNAP (RMSE < 2.192%), and PIA-MiraMon (RMSE < 3.130%), but did not achieve sufficient results in the NIR band ($RMSE_{NIR} < 7.530\%$); this also occurred with all other methods. In the intercomparison step, the UAS-MiraMon method achieved an excellent intersensor (L8-S2) coherence ($RMSE_{VIS} > 1\%$). The UAS-sampled area involved 51 L8 (30 m) pixels, 143 S2 (20 m) pixels, and 517 S2 (10 m) pixels. The drone time needed to cover this area was only 10 min, including areas that were difficult to access. The systematic sampling of the study area was achieved with a pixel size of 6 cm, and the raster nature of the sampling allowed for an easy but rigorous resampling of UAS data to the different satellite grids. These advances improve human capacities for conventional

field spectroradiometry samplings. However, our study also shows that field spectroradiometry is the backbone that supports the full upscaling workflow. In conclusion, the synergy between field spectroradiometry, UAS sensors, and Landsat-like satellite data can be a useful tool for accurate radiometric corrections used in local environmental studies or the monitoring of protected areas around the world.

Keywords: radiometric correction; Landsat-8; OLI; Sentinel-2; MSI; UAS; MicaSense RedEdge; field spectroradiometry; upscaling

1. Introduction and Objectives

Knowledge of the Earth's surface is essential for properly planning and managing resources and making concrete progress in effective and durable sustainability, in which people and other living beings can develop in optimal ways with the necessary means [1]. Remote sensing (RS) plays a key role in this goal by contributing with a vast amount of data towards environmental monitoring [2], not only at global scales, but also regional and local scales [3]. International associations and governments have been creating an increasingly efficient Earth observation (EO) network in order to guarantee access to high-quality data systems [4]. For these purposes, an increasing temporal availability of EO resources is arising from political will and collaboration.

To maximize efforts in terms of scientific, social, and economic benefits, spatial agencies advance together through initiatives as the Global Earth Observation System of Systems (GEOSS) [5]. In GEOSS, the National Aeronautics and Space Administration (NASA) and the European Space Agency (ESA), among others, collaborate in the acquisition of high spatial resolution (SR) multispectral imagery, with the Landsat Data Continuity Mission (LDCM) [6] and the Copernicus Sentinel-2 (S2) [7] programs, respectively. The synergistic use of different satellite missions implies that images must have similar characteristics (spatial, spectral, radiometric, etc.). In fact, the design of several missions in recent years has gone in this direction, such as the aforementioned LCDM and Copernicus, currently with two Landsat (Landsat-7 (L7) and Landsat-8 (L8)) and two Sentinel-2 (Sentinel-2A (S2A) and Sentinel-2B (S2B)) satellites in orbit. The Sentinel constellation was designed to support the Landsat Program and provide continuity to the SPOT program [8] by embedding sensors with similar spatial and spectral resolution features. The temporal orbit cycle of Sentinel-2 platforms was specifically thought to maximize combined consecutive observations with Landsat [9], thereby increasing their joint monitoring possibilities.

Nevertheless, these efforts are still considered insufficient as long as the sensed raw data cannot be ensured to receive radiometric correction that allows the combined use of the different platforms and sensors intended to act in a coordinated way. The backbone of the radiometric correction of satellite data is the proper modeling of the atmospheric parameters affecting each captured image [10]. Perhaps the most interesting physical magnitude to be obtained after an atmospheric correction of remote sensing optical imagery is spectral surface reflectance ($\varrho_{s\lambda}$; dimensionless), which can be defined as the proportion of reflected radiant flux over the incident radiant flux in a given wavelength [11]. Indeed, surface reflectance is an essential variable for characterizing main land cover types with maximum accuracy. Besides atmospheric correction, topographic correction is also interesting for properly managing terrain incident angles, shadows, and so forth. [12]. Therefore, to this end, it is implemented in several radiometric correction processors (e.g., Sen2Cor-SNAP, CorRad-MiraMon) using a digital elevation model (DEM) as auxiliary data. The DEM can also be used for other purposes, such as modeling the transmittance as a function of the terrain height, assuming a higher atmospheric transmittance at higher altitudes (e.g., 6S-LaSRC).

Official agencies provide surface reflectance products of Landsat and Sentinel-2 data by using specifically designed radiometric correction processors. For L8, the United States Geological Survey

(USGS) uses an adaption of the Second Simulation of the Satellite Signal in the Solar Spectrum (6S) [13], namely Landsat Surface Reflectance Code (6S-LaSRC) [14]. For S2, ESA uses an adaption of the Atmospheric Correction (ATCOR3) [15] processor, also implemented in Sentinel's Application Platform (Sen2Cor-SNAP) [16,17]. Additionally, both official agencies work together towards harmonizing surface reflectance products to support the creation of time series combining L8 and S2 data (Harmonized Landsat and Sentinel (HLS)) [18]. Other works in this field have analyzed the geometric adaption of both grid origins and different spatial resolution grids [19] and the combined use of L8 and S2 data [20]. In recent years, international projects have been focusing on the radiometric coherence between sensors, and particularly between L8 and S2 products, developing and comparing atmospheric correction processors (Atmospheric Correction Intercomparison Exercise (ACIX) [21,22]). Thanks to these efforts, radiometric correction methods today provide an acceptable level of coherence, as can be validated by field spectroradiometric data captured almost simultaneously with satellite data [23]. Reaching a higher level of precision, a typical Landsat-like optical sensor measures spectral radiance ($L_{s\lambda}$; W m^{-2} sr^{-2} μm^{-1}), including both the land surface-reflected radiance, which is our main interest, and the atmospheric spectral radiance ($L_{atm\lambda}$), composed by the upwelling spectral radiance and the reflection of the downwelling spectral radiance of the atmosphere. Atmospheric spectral total optical depth ($\tau_{0\lambda}$; dimensionless) weakens the downwelling solar spectral irradiance ($E_{0\lambda}$; W m^{-2} μm^{-1}) and the upwelling surface-reflected radiance [24].

For years, satellite remote sensing has been attempting to relate the images with field spectroscopy data [25]. Field spectroradiometric measurement of surface reflectance at the satellite overpass is practically unaffected by atmospheric effects. Moreover, it is a valuable source of information for assessing and reinforcing the accuracy of radiometric correction [26,27]. Currently, in situ measurements are carried out by operators using portable field spectroradiometers, sometimes with elevator devices [28]. However, they face various challenges, such as trying to access high tree canopies or water surfaces, or the impossibility of measuring in dangerous or restricted areas. Another important restriction of conventional field spectroradiometry is the specific covered area and the sampling method themselves, since during the acceptable time of 20 min before and after the satellite overpass, a skilled operator can scan up to a reasonable area equivalent to 20 pixels of OLI 30 m, 45 pixels of MSI 20 m, or 180 pixels of MSI 10 m. Moreover, it is advisable to adapt sampling strategies to a predetermined satellite pixel size and origin, followed by a resampling of the pointer field data to the different satellite pixel sizes, which is neither a trivial nor easy task by any means. For example, although ground-sampling data is usually georeferenced in an accurate way, in some situations, such as the forest understory, it can be difficult to achieve accurate georeferencing [29].

In this context, imagery acquired with hyperspectral or multispectral sensors onboard unmanned aerial systems (UAS) is expected to complement field data, as the UAS platform can access those hardly accessible areas in a faster way than human operators and systematically sample the surface with higher spatial accuracy. The use of ultrahigh spatial resolution data acquired with UAS for quantitative remote sensing spectroscopy purposes has evolved enormously over the years, as comprehensively reviewed in [30]. In 2014, an international initiative (OPTIMISE) [31] was engaged in exploring new opportunities that UAS platforms and sensors could potentially provide to near-ground Earth observations. MacArthur and Robinson [32] presented a review of field spectroscopy and advanced the impact of new technologies, such as UAS, particularly in supporting the empirical calibration and validation of satellite observations. At the same time, they emphasize the importance of accurately processing UAS imagery to ensure its reliability.

Other works propose the use of reference panels in synergy with field spectroscopy data and UAS-acquired imagery; for example, using a band-by-band linear relationship between in situ field measurements and UAS sensor data [33], or the use of downwelling light sensors [34]. Previous studies compared UAS, airborne, and satellite data [35], since commercial sensors are now light enough to be embedded in low-weight platforms [36,37]. Zabala [38] compared VIS and NIR (VNIR) S2 bands with a multispectral consumer grade 2D-imager multicamera, such as MicaSense RedEdge [39],

thereby concluding that a good correlation exists between derived vegetation indices on both sensors. MicaSense RedEdge was designed to be embedded in low-weight UAS platforms and provides acceptable geometric and radiometric data [40]. Parrot Sequoia [41] is a similar frame sensor, whose imagery radiometric performance was analyzed and compared with WorldView satellite data in [42] and was found to fit well between the corresponding bands. Apart from radiometric issues, the geometric benefit of accurate georeferencing of UAS data is expected to result in a better comparison of the ground-truth plotted area and the satellite pixel grid. In that sense, as drone data can systematically (raster, quasi-continuous) sample the ground at a distance below 10 cm and with a geometric error comparable to its pixel size [43,44], the drone data can be rigorously resampled to any satellite pixel size and grid.

The primary objective of this paper is to demonstrate that UAS data in synergy with field spectroradiometry can be useful for the accurate radiometric correction of L8 and S2 imagery. The underlying hypothesis is that with the appropriate upscaling methodology, radiometrically corrected UAS imagery through field spectroradiometric measurements [45] can be used as a reference to correct Landsat-like images in single dates with high accuracy (which we referred to as the UAS-MiraMon method), in a similar way as pseudoinvariant areas are used as references to correct Landsat-like time series in other approaches [23,46] (which we referred to as the PIA-MiraMon method). Additionally, a second objective is to show how the corrected drone data can be used to validate preexisting satellite surface reflectance methods, such as PIA-MiraMon, 6S-LaSRC, or Sen2Cor-SNAP. To realize this aim, we used near-coincident observations of L8 and S2 data, drone-acquired data, and field spectroscopy data.

These objectives were achieved by following a workflow consisting of the following steps (explained in detail in "Section 3 Material and methods"):

- Radiometrically correcting drone data by using calibration panels and field spectroradiometric measurements;
- Using drone corrected and upscaled data to validate different radiometric products (PIA-MiraMon, 6S-LaSRC and Sen2Cor-SNAP). This point fulfills the second main objective;
- Splitting the drone corrected and upscaled data into fitting pixels and test pixels. Fitting pixels are used to feed the UAS-MiraMon satellite radiometric correction approach based on field spectroradiometric data in synergy with drone data. Test pixels are used to validate the new method. This point fulfills the first main objective. Additionally, as a second validation we compare the results of UAS-MiraMon with the current 6S-LaSRC, Sen2Cor-SNAP and PIA-MiraMon methods. This complements the second main objective;
- By taking advantage of the almost simultaneous acquisitions of our experimental design, we evaluate the L8 and S2 inter-sensor fitting for the UAS-MiraMon method. This is done at different radial distances from the study area, as we hypothesized that the accuracy of the new UAS-MiraMon method could be better in the drone area. However, we also hypothesized that the accuracy could decrease with increasing distance (local overfitting). This point complements the first main objective.

2. Study Area

The data acquisition was carried out on April 21, 2018, at Can Gelabert farm (41°56′59.3″N–1°32′1.4″E) in the region of Catalonia, Spain, where the overpassing of L8 and S2A were scheduled at 10:35:37 Coordinated Universal Time (UTC) and at 10:56:29 UTC, respectively. The region of interest (ROI) covered 5.26 ha and included 51 OLI 30 m pixels, 143 MSI 20 m pixels, and 517 MSI 10 m pixels (Figure 1). The landscape is a Mediterranean mosaic dominated by a forest environment. The altitude of the terrain at the study area is between 683 m and 739 m. The topography is not absolutely flat, as there are some abandoned vineyard terraces and there are trees of less than 15 m in height. The terrain slope ranges from 0° to 56°, being especially high in the steps between terraces. In the central zone, there is a field of cereal crops that, at the time of the flight, was in the growing season. The woody vegetation of the area is mainly formed by *Quercus humilis*, *Quercus ilex* ssp. *ballota*,

Ulmus minor, and *Pinus nigra* ssp. *salzmanii*. The man-made elements in the area are the house of Can Gelabert (650 m^2), a pond, and a small well in the southeastern corner of the central cultivation field. We considered appropriately selecting a mixed natural and rural area to be representative for land cover mapping and monitoring purposes.

Remote Sens. **2018**, *10*, 1687 5 of 26

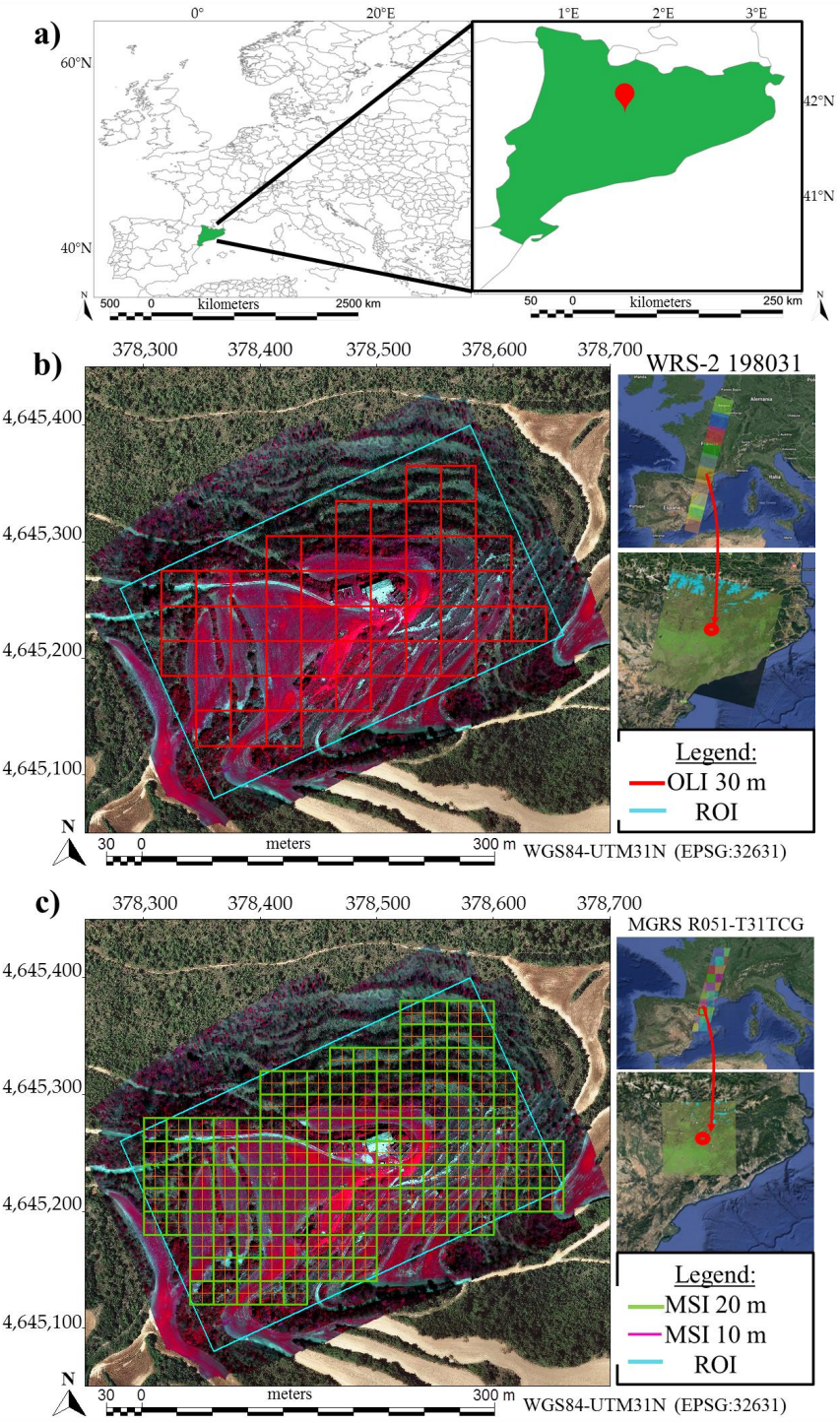

Figure 1. (**a**) Study area location map in Europe. (**b**) Unmanned aerial system (UAS) false color composite image (NIR, R, G) taken on 21 April 2018, and the corresponding Landsat-8 OLI pixel grid (WRS-2 198031 scene), with 51 pixels of 30 m; (**c**) UAS false color composite image (NIR, R, G) and the corresponding Sentinel-2A MSI pixel grid (MGRS R051-TCG tile), with 143 pixels of 20 m and 517 pixels of 10 m. ROI: region of interest; NIR: near-infrared; R: Red; G: Green; OLI: Operational Land Imager; MSI: MultiSpectral Imager.

3. Materials and Methods

The materials we used involved three geographical scales: (a) field spectroradiometric data (Section 3.1) covering surface reflectance measurements, (b) UAS data (Section 3.2) covering drone imagery, and (c) satellite data (Section 3.3) covering L8 and S2A imagery. The methodology applied and the overall upscaling workflow are both summarized in the final subsection (Section 3.4).

3.1. Field Spectroradiometric Data

Ground reflectance measurements were carried out with an OceanOptics USB2000+ spectroradiometer [47]. The spectral range covered the VIS and NIR regions (340 nm–1030 nm), with a sampling interval of 0.3 nm and a spectral resolution (full width at half maximum, FWHM) of 1.26 nm. The light was conducted on the portable instrument through a 50 µm diameter optical fiber of 25° field of view (FOV); the acquisitions were operated with the SpectraSuite software [48] (Table 1).

Table 1. Main characteristics of the OceanOptics USB2000+ field spectroradiometer instrument. FOV: Field of View; CCD: Charge-Coupled Device; FWHM: full width at half maximum.

Manufacturer-Model	**Size (mm)**	**Weight (g)**	**Design**	**Fiber Optic FOV (°)**
OceanOptics USB2000+	89.1 × 63.3 × 34.4	190	Czerny-Turner	25
Sensor manufacturer and type	**Sensor CCD samples**	**Sampling interval (nm)**	**Input Focal Length (mm)**	**Fiber optic diameter (µm)**
CCD Sony ILX511B	2048	0.3	42	50
Raw radiometric resolution (bits) and expanded dynamic range (DN)	**Grating #2 Spectral range (nm)**	**FWHM (nm)**	**Signal to Noise Ratio @ 50 ms**	**Minimum Integration time (ms)**
8 (0–65,535)	340–1030	1.26	250:1	1

The dark current of the instrument was measured before each measurement. The optical fiber head was located in the nadir position at 20 cm, projecting an 8.87 cm circular footprint over the sampled surfaces. A Spectralon reference panel was used to approximate the incoming irradiance. Once the reference was taken, the individual target reflectance of 17 rectangular ethylene–vinyl acetate (EVA) foam panels of different colors was measured, averaging 100 readings to obtain a robust measurement. The set of EVA panels was composed of two sizes, both covering at least 6 pixels of the drone imagery: a group of 50 cm × 50 cm × 2 cm included black, violet, blue, dark green, yellow, orange, and red colors (namely EVA in Figure 2), and another group of 40 cm × 60 cm × 0.2 cm included black, blue, sky blue, grey, brown, red, green, dark green, yellow, and pink colors (namely foam in Figure 2), to demonstrate the possible work with thinner plates and a larger set of colors. Targets were separated by 10 cm to minimize adjacency effects and they were located over a black matte carpet to minimize background contributions. The EVA foams present a highly Lambertian [49,50] behavior and a high horizontal homogeneity [51]; the panels are light, easy to transport, and easy to clean with compressed air, making them a good material to be used for reflectance reference when calibrating drone imagery in synergy with field spectroradiometric measurements. The mean, minimum, maximum, and standard deviation statistics of the 100 readings were calculated to analyze and detect possible procedural errors or spectral variabilities. The spectral signature of each panel was integrated within the drone sensor's relative spectral response function (RSRF) to be used in the empirical line correction [30]. The main motivation for using more than 15 EVA panels was to achieve a solid linear correlation between the ground-truth and the UAS sensor, with an extensive set of radiometric references distributed across the spectral domain (Figure 2).

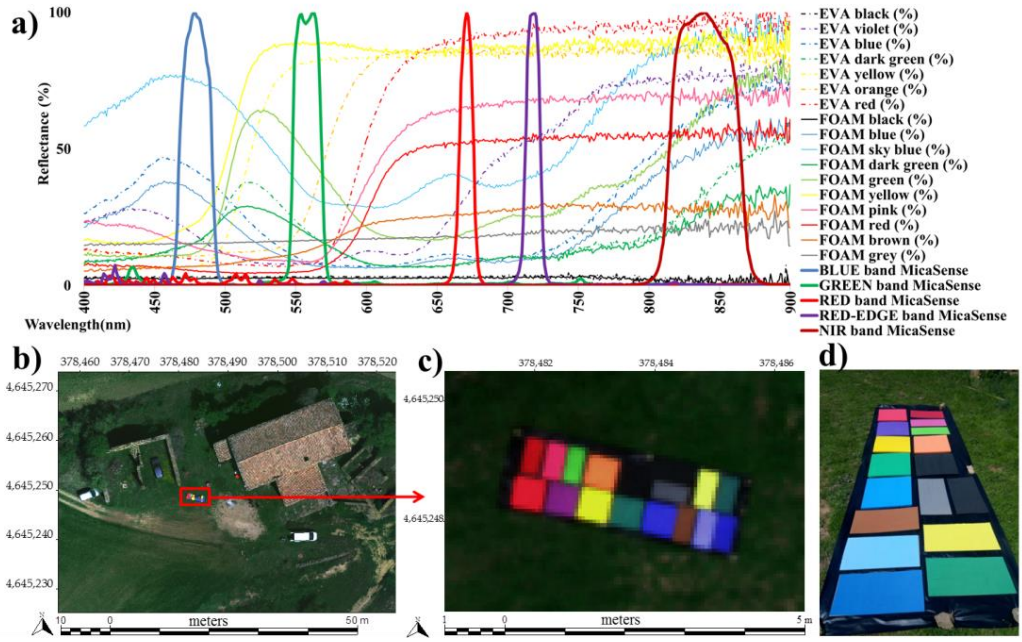

Figure 2. (a) Spectral signatures of targets and UAS sensor bands; (b) Target location in drone image; (c) Zoom in targets in the UAS image; (d) Field photograph of targets. Note coordinates in (b,c) are in WGS84 UTM Zone 30N (EPSG:32630). EVA: ethylene-vinyl acetate.

3.2. Unmanned Aerial System Data

Two drone flights were planned at 80 m above ground level (AGL) with a side overlap of 70% and a front overlap of 80%, resulting in a pixel size of 6 cm. The first flight time was between 10:31:52 UTC and 10:41:42 UTC, which corresponded to the L8 overpass. The second flight time was between 11:23:10 UTC and 11:32:18 UTC, which corresponded to the S2A overpass. Both acquisitions were performed under excellent illumination and meteorological conditions without cloud cover and with wind speed below 2 m/s.

The UAS platform was a DJI S900 vertical take-off and landing 6-rotor multicopter equipped by the MAVinci company to provide additional security measures. The drone was 90 cm wide and 82 cm tall and had a maximum weight of 9.7 kg (3.5 kg in flight mission configuration). The payload was 3 kg when carrying the MicaSense RedEdge camera sensor [39] with a focal length of 5.5 mm and a field of view of 47.2°. The complementary metal-oxide semiconductor (CMOS) is 1280 × 960 pixels per frame (Table 2). The MicaSense RedEdge is sensible in 5 broad spectral bands, which, following the typical RSR provided by the manufacturer [52], have a bandpass FWHM of 468 nm–491 nm (blue, #1), 548 nm–568 nm (green, #2), 666 nm–676 nm (red, #3), 712 nm–723 nm (red-edge, #5) and 814 nm–865 nm (near-infrared, #4) (Figure 3). The radiometric resolution is 12 bits, although the output is in the TIFF 16 bit format. The pixel size, which accounted for the focal length and the AGL distance, was rounded up to 6 cm.

Table 2. Main characteristics of the MicaSense RedEdge sensor. CMOS: Complementary Metal–Oxide–Semiconductor.

Manufacturer-MODEL	Size (mm)	Weight (g)	Raw Radiometric Resolution (Bits) and Expanded Dynamic Range (DN)
MicaSense RedEdge	121 × 66 × 46	150	12 (0–65,535)

Sensor type	Sensor size (pixels)	Pixel size (µm)	Focal Length (mm)	Field of View (°)
CMOS	1280 × 960	3.75 × 3.75	5.5	47.2

#1 Blue FWHM (nm)	#2 Green FWHM (nm)	#3 Red FWHM (nm)	#4 Red-edge FWHM (nm)	#5 NIR FWHM (nm)
468–491	548–568	666–676	712–723	814–865

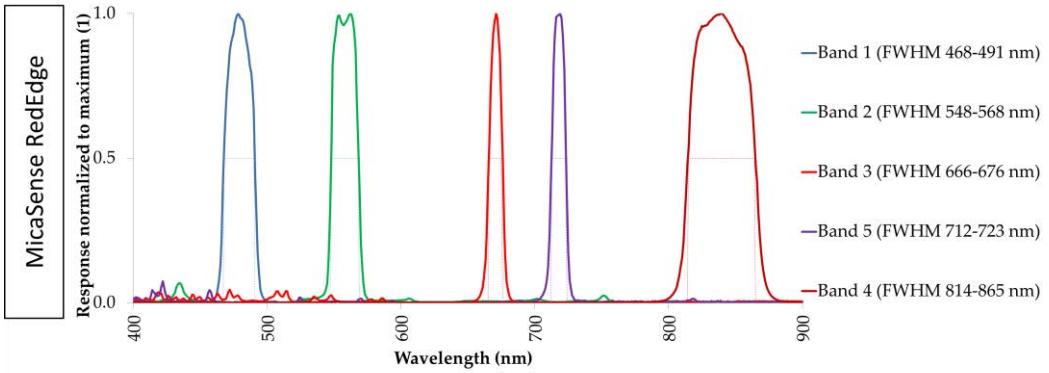

Figure 3. Relative spectral response function (RSRF) and full width at half maximum (FWHM) of the MicaSense RedEdge sensor embedded in the DJI S900 platform. Source: Micasense [52].

UAS data was geometrically and radiometrically processed using the photogrammetric software Agisoft PhotoScan V1.4.1 [53] and the remote sensing and geographic information system software (RS-GIS) MiraMon V8.1f [54]. Indirect georeferencing [43,44] was carried out using 7 ground control points (GCPs) measured with a post-processed Differential Global Positioning System (DGPS) Leica Viva GS14® GNSS [55] static receiver and distributed across the ROI. Although all the available GCPs were used in the orthomosaic georeferencing, a cross validation (leave-one-out) was carried out to assess an independent accuracy test. GCPs were materialized in concrete bases and painted with a checkered template to display a clear visualization of the central point (Figure 4) when locating the markers in the photograms. The RMSExy of the first flight was 0.053 m (cross validation), and the RMSExy of the second flight was 0.044 m (cross validation). The geometric accuracy of both orthomosaics (6 cm pixel size) met the requirements of the American Society for Photogrammetry and Remote Sensing (ASPRS) Standards for Digital Geospatial Data [56], which demand a minimum RMSExy of 0.071 m for a pixel size of 5 cm.

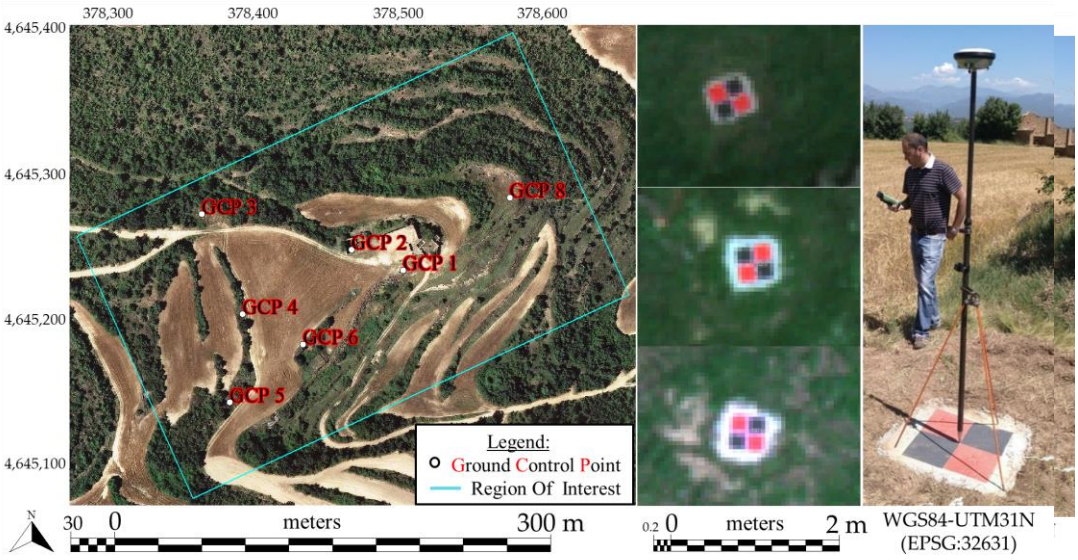

Figure 4. Ground control point (GCP) locations in the study area (**left**). Example of 3 GCPs in the UAS imagery (**center**). Static Differential Global Positioning System (DGPS) Leica taking data at GCP no. 6 (**right**).

Once the bundle block was adjusted and georeferenced, an orthomosaic of the surface reflectance values of each flight was generated. In this first radiometric correction processing step, we used the method based on the UAS camera manufacturer's method and implemented it in the

the downwelling solar spectral irradiance) [33] together with exchangeable image file format (EXIF) information that considers the camera features (e.g., vignette correction factor) and the acquisition parameters (e.g., dark current, ISO, exposure time) [40]. In a second radiometric correction processing step, we used the field spectroradiometric measurements to evaluate the radiometric accuracy of the orthomosaic generated with the photogrammetric software, and furthermore, to improve the results by using an empirical line correction and the RS-GIS software [46]. The spectroradiometer pointer, located at 20 cm over the center of each target, projected a circle of 8.87 cm in diameter. In the image, a buffer with the appropriate radius was traced from the center of each of the 17 radiometric EVA targets in order to calculate the area-weighted average value of the image pixels that corresponded to the field spectroradiometric measurements. The image average reflectance of the 17 reflectance targets was correlated band-by-band with the field spectroradiometric measurements (integrated in the UAS sensor band RSRF). The correlation gave a coefficient of determination (R^2) and a lineal function that, when applied to the UAS data, adjusted the UAS sensor reflectance values to the field spectroradiometric ground-truth reflectance, thus improving the surface reflectance reliability by applying an empirical line correction to the orthomosaic [45]. In empirical line calibration, several targets can be used. For example, when using two, the targets should be dark and bright, respectively. When several targets are used, they should cover the reflectance range well, but the reflectance spectra should not have intersections; otherwise, a large number of spectra is recommended to be used [15], and thus, we used a large number of targets.

3.3. Satellite Data

Two satellite multispectral push-broom sensors were used: The OLI onboard L8 platform and the MSI onboard S2A platform.

A. L8 OLI: The L8 satellite was launched on February 11, 2013, and tracks a sun-synchronous polar-orbit at an approximate altitude of 705 km, providing a temporal resolution of 16 days. L8 has two main instruments on board, the OLI and the Thermal Infrared Sensor (TIRS), both with an approximate swath of 180 km and a radiometric resolution of 12 bits. The OLI sensor captures images in the visible (VIS), near-infrared (NIR), and shortwave infrared (SWIR) spectral regions, through 9 spectral bands of 30 m spatial resolution (SR) and an additional panchromatic band of 15 m SR; band RSRFs are available in [58]. On the other hand, although it is not the focus of this study, the TIRS obtains data in the thermal infrared spectral region (8 µm–12 µm) with two spectral bands that have a 100 m SR (Table 3). Official products were obtained from the USGS website via the EarthExplorer tool [59], which are distributed in the World Reference System-2 tiling system (WRS-2). In our study, we used images from orbit 198, row 031 (Figure 5) and two processing levels. The L1T processing level product (Level 1 T: precision terrain-corrected to UTM31N, WGS84, top of atmosphere (TOA) radiances product, Tier 1) was downloaded so that we could perform radiometric correction on it with the CorRad module of MiraMon, using, on the one hand, pseudo-invariant areas (PIA-MiraMon) [46], and on the other, the UAS imagery as the reflectance reference (UAS-MiraMon). The L1T product was also converted to TOA reflectance using the metadata parameters and the center-of-scene sun elevation angle [60] for comparison with the radiometric correction results and the drone data. The L2A processing level product (Level 2 A: geometry as L1T and surface reflectance corrected for atmospheric effects with a cloud mask and a cloud shadow mask, as well as a water and snow mask), atmospherically corrected with the Landsat Surface Reflectance Code (6S-LaSRC) [14], was downloaded to have an independent reference of the results obtained with the MiraMon algorithm and for comparison with the official product of S2. On 21 April 2018, L8 overpassed the study area at 10:35:49 UTC (Table 3).

B. S2A MSI: The S2A satellite was launched on 23 June 2015 and is part of the European Space Agency (ESA) Copernicus space program. The S2A twin S2B satellite was put into orbit on March 7, 2017. Both track a sun-synchronous polar-orbit at an approximate altitude of 786 km,

Remote Sens. **2018**, *10*, x FOR PEER REVIEW 10 of 26

providing an individual temporal resolution of ten days and a combined temporal resolution of five days. S2A has a main instrument on board, the MSI, which has an approximate swath of 290 km and a radiometric resolution of 12 bits. The MSI sensor captures images in the visible (VIS), near-infrared (NIR), and shortwave infrared (SWIR) spectral regions through 4 spectral bands of 10 m SR, 7 bands of 20 m SR, and 3 bands of 60 m SR (Table 3); band RSRFs are available in [61] and are slightly different for the MSI onboard S2A and the MSI onboard S2B. Official products were obtained via the ESA—Copernicus Scientific Data Hub tool [62], which are distributed in the Military Grid Reference System tiling system (MGRS). In our study, we used images from the orbit R051 granule TCG and two processing levels: L1C (Level 1C: product results from using a digital elevation model to project the image in cartographic geometry (UTM31N, WGS84), where per-pixel radiometric measurements are provided in TOA reflectance); and L2A (Level 2A: Bottom of atmosphere (BOA reflectance in cartographic geometry (as for L1C)) (Figure 4). L1C was downloaded to be radiometrically corrected using PIA-MiraMon and UAS-MiraMon. The L2A product, radiometrically corrected with the Sen2Cor processor [17], was downloaded to have an independent reference of the results obtained with the MiraMon algorithm and be compared with the L8 official product. On April 21, 2018, the S2A overpassed the study area at 10:56:29 UTC.

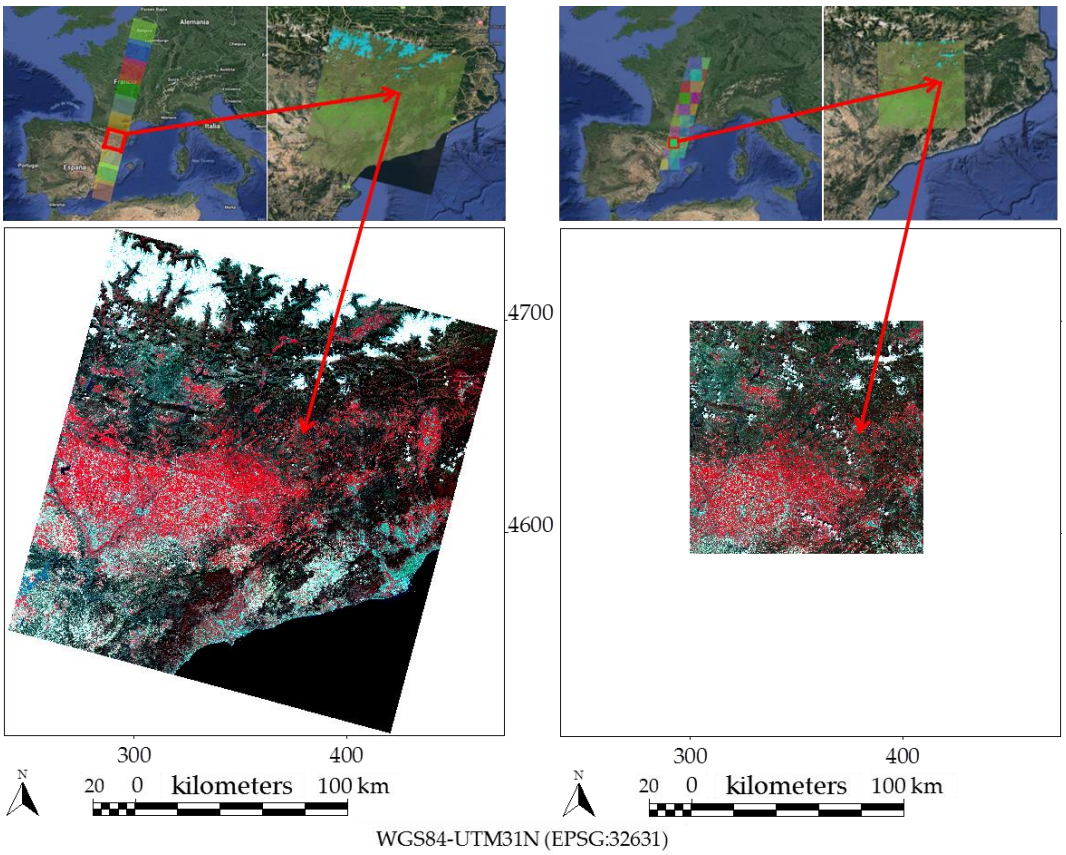

Figure 5. (**Left**) Landsat-8 L2A official product (6S-LaSRC) image used. False color composite image (L8-OLI 30 m RGB 543) on 21 April 2018, path 198, row 031. (**Right**) Sentinel-2A L2A official product (Sen2Cor-SNAP) image used. False color composite image (S2A-MSI 10 m RGB 843) on 21 April 2018, orbit R051, tile T31 TCG.

Table 3. Main characteristics of the Landsat-8 and Sentinel-2A imagery used.

Acquisition Date	**21 April 2018**	
Study Area	**1°32′1.4″E, 41°56′59.3″N**	
Platform	**Landsat-8**	**Sentinel-2A**
Sensor	Operational Land Imager (OLI)	Multi Spectral Imager (MSI)
Bands	10	13
Aerosols	B1: 435.0 nm–451.0 nm (30 m)	B1: 432.7 nm–452.4 nm (60 m)
Blue	B2: 452.0 nm–512.1 nm (30 m)	B2: 459.8 nm–524.0 nm (10 m)
Green	B3: 532.7 nm–590.1 nm (30 m)	B3: 542.8 nm–577.6 nm (10 m)
Red	B4: 653.9 nm–673.3 nm (30)	B4: 649.3 nm–679.9 nm (10 m)
NIR(RedEdge)		B5: 697.3 nm–711.3 nm (20 m)
NIR(RedEdge)		B6: 733.6 nm–747.3 nm (20 m)
NIR(RedEdge)		B7: 773.5 nm–792.5 nm (20 m)
NIR (wide)		B8: 782.5 nm–887.3 nm (10 m)
NIR	B5: 850.5 nm–878.8 nm (30 m)	B8A: 854.5 nm–875.0 nm (20 m)
Water Vapor		B9: 935.4 nm–954.9 nm (60 m)
Cirrus	B9: 1363.0 nm–1384.0 nm (30 m)	B10: 1359.0 nm–1388.1 nm (60 m)
SWIR1	B6: 1566.5 nm–1651.2 nm (30 m)	B11: 1568.7 nm–1658.3 nm (20 m)
SWIR2	B7: 2107.4 nm–2294.1 nm (30 m)	B12: 2112.9 nm–2286.5 nm (20 m)
Panchromatic	B8: 503.0 nm–676.0 nm (15 m)	
Thermal1	B10: 10.60 µm–11.19 µm (100 m)	
Thermal2	B11: 11.50 µm–12.51 µm (100 m)	
Acquisition time	10:35:49 (UTC)	10:56:29 (UTC)
Orbit-Scene	198-031	R051-TCG
Scene center	41°45′19.2″, 1°16′28.2″	41°56′41.6″, 1°14′58. 2″
Solar elevation	55.67° (Scene center) 56.14° (Study area)	57.73° (Scene center) 57.57° (Study area)
Solar Azimuth	144.75° (Scene center) 147.32° (Study area)	154.56° (Scene center) 153.80° (Study area)
View Zenith Angle	7.26° (Study area)	1.23° (Study area)

The radiometric performance requirements of the Landsat-8 [63] and Sentinel-2 [64] missions require producing data with a radiometric uncertainty below 3%. This is the threshold we used to discuss if the radiometric correction methods are compliant with the requirements, considering that a RMSE is good if it is below the 3% threshold and is bad if it overpasses this threshold. Other works use a 2% threshold [22,65], below which we could consider it to be an excellent result.

The satellite bands involved were OLI 452 nm–512 nm (blue, #2), 533 nm–590 nm (green, #3), 636 nm–673 nm (red, #4), and 851 nm–879 nm (near-infrared, #5); and MSI 460 nm–524 nm (blue, #2), 543 nm–578 nm (green, #3), 649 nm–680 nm (red, #4), and 855 nm–875 nm (near-infrared, #8a) (Figure 6). Note that all OLI bands are 30 m SR, MSI visible bands are 10 m SR, and the NIR band (#8a) is 20 m SR. The official RSRF was used to select the matching bands between both sensors and determined the bands to be compared with the UAS sensor. Also note that the OLI NIR band (#5) is very similar to the MSI NIR band #8a (designed to match the aforementioned OLI NIR band) (Figure 6), although the MSI NIR band has a wider NIR band (#8) in the same spectral region (which was designed to match the NIR band of the ETM+ of Landsat-7).

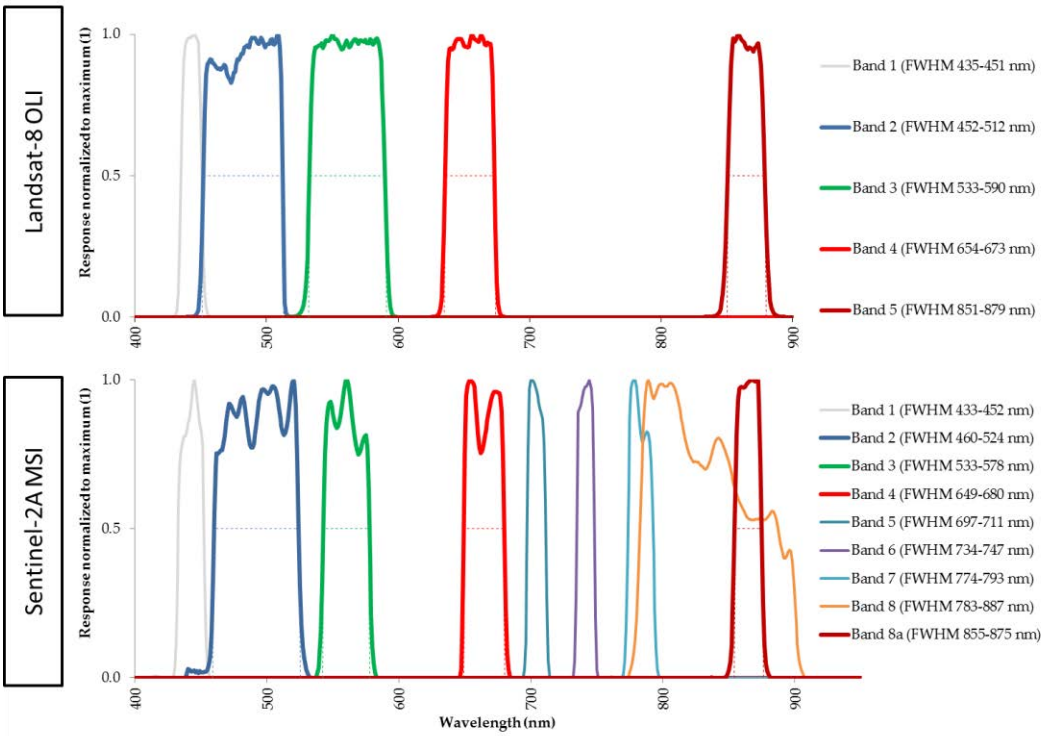

Figure 6. Relative spectral response function (RSRF) and full width at half maximum of VNIR bands of the OLI sensor onboard Landsat-8 (**top**) and the MSI sensor onboard Sentinel-2A (**bottom**).

The corresponding bands of the satellite sensors and UAS are located in the blue, green, red, and near-infrared regions of the electromagnetic spectrum, but have different spectral overlapping. In the blue band, the OLI and the MSI response are similarly wide, but the MSI band is displaced by about 20 nm to longer wavelengths. In the green band, the MSI band is narrower than the OLI band. In both the blue and green bands, the UAS sensor response is reasonably within the same spectral region and centered in the RSRF of the satellite sensors. In the red region, the MSI FWHM is narrower than the OLI and is displaced to lower frequencies, while the UAS sensor response matches the upper boundary of the satellites' RSRF, being decentered from the satellite RSRFs. The OLI NIR band is slightly wider than the MSI band; nevertheless, both reasonably match the same spectral region. At any rate, the UAS-NIR band peak is located at about 20 nm higher frequencies and only matches the satellite bands within a 10-nm spectral region where the response decreases such that, a priori, a weaker correlation is expected between the satellite and drone imagery along these bands (Figure 7).

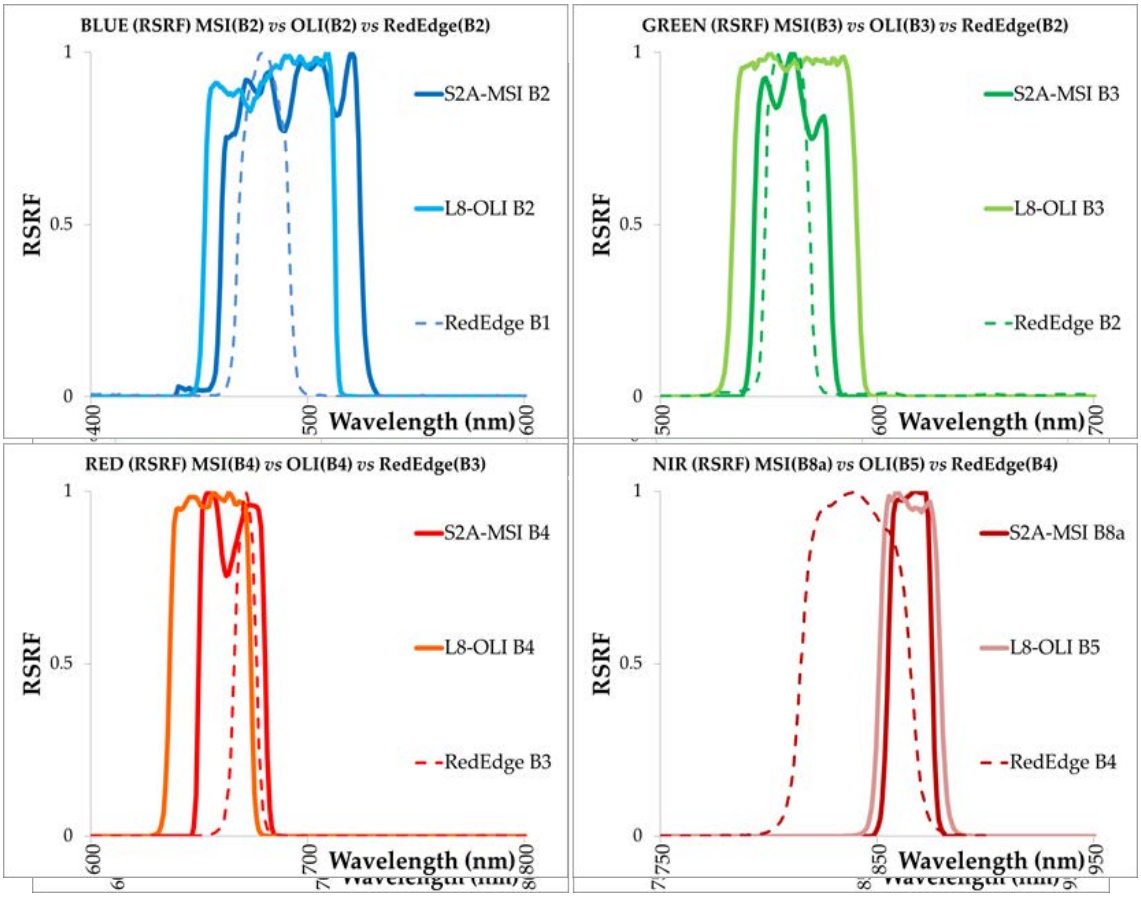

Figure 7. Relative spectral response function (RSRF) of matching bands in the OLI sensor, MSI sensor, and MicaSense RedEdge sensor.

Satellite imagery was masked by clouds and cloud shadows, accounting for both the clouds in the L8 image and the clouds in the S2A image, because cloud movement and growth was notable during the 20-min delay period between the overpass of both platforms, and as such, could cause a bad interpretation of the intercomparison correlations. The total matching area of the L8 198031 scene and the S2 R051 TCG tile was 1,204,945 ha, and the masked area was 111,562 ha (9.26% of the common area) (Figure 8).

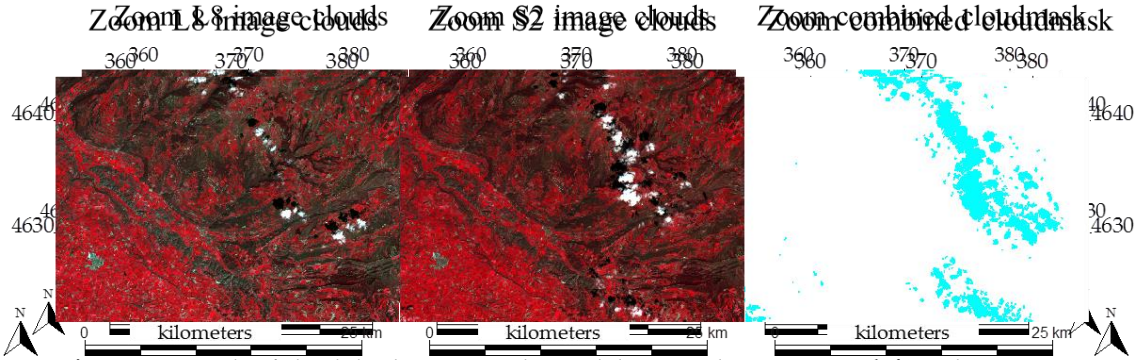

Figure 8. Example of cloud displacement and growth between the L8 sensing (**left**) and S2 sensing (**center**). The combined cloud and cloud-shadow mask includes both sources (**right**).

The CorRad algorithm was designed in 1994 to correct the topographic and atmospheric effects of Landsat-like imagery [24]. The topographic corrections followed a cosine-correction approach. The atmospheric correction followed a dark object subtraction (DOS) [66] approach to resolve the atmospheric path radiance, while the atmospheric total optical depth was assumed to be constant (wavelength-dependent). In 2014, Pons et al. [46] presented an automatic method designed to

(wavelength-dependent). In 2014, Pons et al. [46] presented an automatic method designed to massively correct Landsat-like imagery, thus solving the path radiance and the atmospheric total optical depth by fitting these unknowns to radiometric reflectance references obtained from Moderate-Resolution Imaging Spectroradiometer (MODIS) pixels that remained under a standard deviation threshold during the whole MODIS time series, namely pseudo-invariant areas (PIA). When a given Landsat-like image is processed with the PIA-MiraMon method, in each PIA, the CorRad algorithm resolves the optimal path radiance and the atmospheric total optical depth needed to obtain the reference value, and this process is carried out for all the PIA within the processed image extent. The PIA-MiraMon gets a band-by-band pairing of path radiance and atmospheric total optical depth values to correct the full scene.

However, the focus of this study was to use resampled UAS imagery as radiometric reflectance references to process a given Landsat-like image with the CorRad-MiraMon algorithm (UAS-MiraMon), thereby aiming to resolve the optimal path radiance and the atmospheric total optical depth in the study area in a still finer way by taking advantage of the current availability of drones and light multispectral sensors. The L1T L8 and S2 scenes were corrected with these atmospheric parameters, expecting to correct the satellite image with great accuracy near the UAS drone flight and also anticipating a possible worse-case adjustment in distant areas.

3.4. Summary of Upscaling Workflow and Validation from Field Measurements to Satellite Data

First Upscaling Step, from Ground-Truth to UAS:

The field spectroradiometric data at <1 nm spectral sampling was resampled to the drone sensor bandwidth, accounting for the RSRF provided by the manufacturer. Spectrally resampled ground-truth data was correlated band-by-band to the drone data (Figure 2).

Second Upscaling Step, from UAS to Satellite:

The weighted average value was calculated to resample drone data (6 cm) to the satellite pixel size (30 m in the case of L8, and 10 m or 20 m in the case of S2) using a 2D Gaussian procedure described in [67], similar to the one used in [68] to resample Landsat imagery to the MODIS pixel size. There were 250,000 drone pixels in a L8 30 m pixel, 111,111 drone pixels in a S2 20 m pixel, and 27,776 drone pixels in a S2 10 m pixel. We validated the overall consistency of the UAS data calculating the band-by-band RMSE between all the UAS resampled pixels and the corresponding satellite L1T product, the L2A official product (6S-LaSRC in the case of L8 and Sen2Cor-SNAP in the case of S2), and the PIA-MiraMon surface reflectance product.

Third Upscaling Step, Using UAS Data to Radiometrically Correct Satellite Data:

Of the total drone-resampled pixels, 40% were reserved for validation purposes as test areas, while 60% were used as radiometric references to perform the radiometric correction of satellite data using the CorRad algorithm (UAS-MiraMon). The RMSE between test areas and the L8 or S2 VNIR bands was calculated for the UAS-MiraMon, the PIA-MiraMon, and the two official products.

Fourth Upscaling Step, Radiometric Corrections Intersensor Comparison:

The availability of near-coincident observations of the L8 and the S2A, being less than 22 min apart, allowed us to correlate not only the UAS-MiraMon surface reflectance provided for the L8 and the S2A, but also the surface reflectance provided for the L8 official product and the S2 official product, and the PIA-MiraMon surface reflectance provided for the L8 and the S2A. To perform the correlation between these products with different pixel sizes and a misaligned grid, the MSI grid was adapted to the 30 m OLI grid by calculating the area-weighted pixel contribution of the 10 m or 20 m pixels to the 30 m resampled pixel, since the number of MSI pixels inside an OLI pixel does not exceed 16 units (Figure 9).

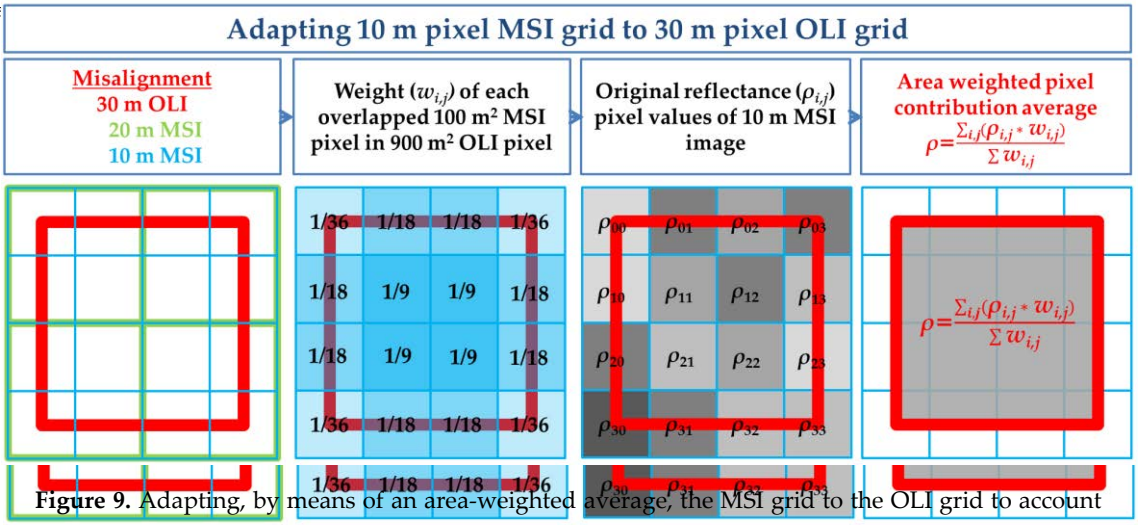

Figure 9. Adapting, by means of an area-weighted average, the MSI grid to the OLI grid to account for the misalignment and different pixel sizes (example of the 10 m MSI grid (blue squares) adapted to 30 m OLI grids (red squares)).

Figure 9. Adapting, by means of an area-weighted average, the MSI grid to the OLI grid to account for the misalignment and different pixel sizes (example of the 10 m MSI grid (blue squares) adapted to 30 m OLI grids (red squares)).

Once the S2 images were adapted to the L8 spatial grid (30 m pixel size), the band-by-band RMSE in reflectance values was calculated to intercompare the UAS-MiraMon radiometric correction method in near time-coincident acquisitions. The differences were calculated in concentric rings from the center of the study area in order to search for a possible degradation of L8–S2 correlation in the UAS-MiraMon method. The analyzed zones were from 0 km to 15 km (n = 681,950 pixels), 15 km to 30 km (n = 2,203,730), and additionally, the full TCG scene extent (n = 12,148,700) (Figure 10).

Once the S2 images were adapted to the L8 spatial grid (30 m pixel size), the band-by-band RMSE in reflectance values was calculated to intercompare the UAS-MiraMon radiometric correction method in near time-coincident acquisitions. The differences were calculated in concentric rings from the center of the study area in order to search for a possible degradation of L8–S2 correlation in the UAS-MiraMon method. The analyzed zones were from 0 km to 15 km (n = 681,950 pixels), 15 km to 30 km (n = 2,203,730), and additionally, the full TCG scene extent (n = 12,148,700) (Figure 10).

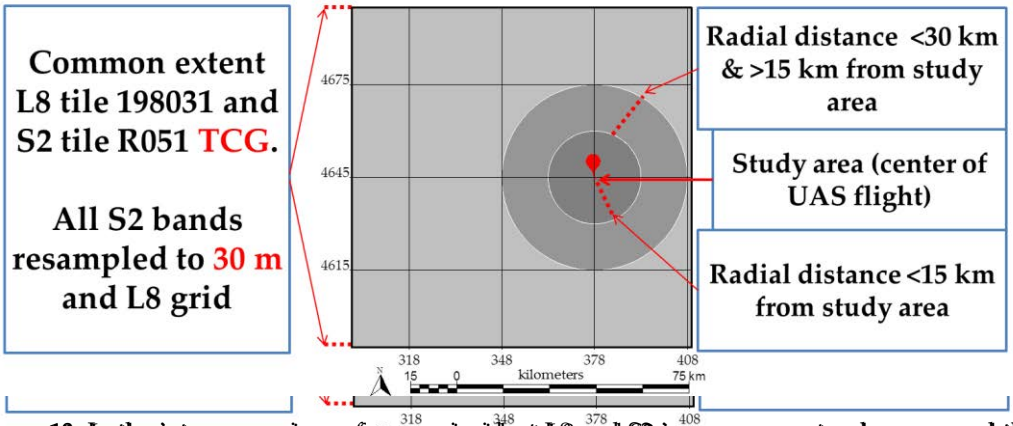

Figure 10. In the intercomparison of near-coincident L8 and S2 images, we not only compared the common extent of the L8 image and the S2 tile, but also the two concentric rings from the study area. This was done to test the hypothesis of whether the accuracy of the new UAS-MiraMon method could be better in the drone area. However, we hypothesized that the accuracy could decrease with increasing distance (though overfitting).

Figure 10. In the intercomparison of near-coincident L8 and S2 images, we not only compared the common extent of the L8 image and the S2 tile, but also the two concentric rings from the study area. This was done to test the hypothesis of whether the accuracy of the new UAS-MiraMon method could be better in the drone area. However, we hypothesized that the accuracy could decrease with increasing distance (though overfitting).

The overall methodology and the results can be summarized in (a) the fitting between the ground-truth and drone data, (b) the fitting between the drone data and satellite data, and (c) the fitting between the radiometric corrections of almost simultaneously acquired data with different satellite sensors. The full upscaling workflow from field measurements to satellite data can be seen in Figure 11.

The overall methodology and the results can be summarized in (a) the fitting between the ground-truth and drone data, (b) the fitting between the drone data and satellite data, and (c) the fitting between the radiometric corrections of almost simultaneously acquired data with different satellite sensors. The full upscaling workflow from field measurements to satellite data can be seen in Figure 11.

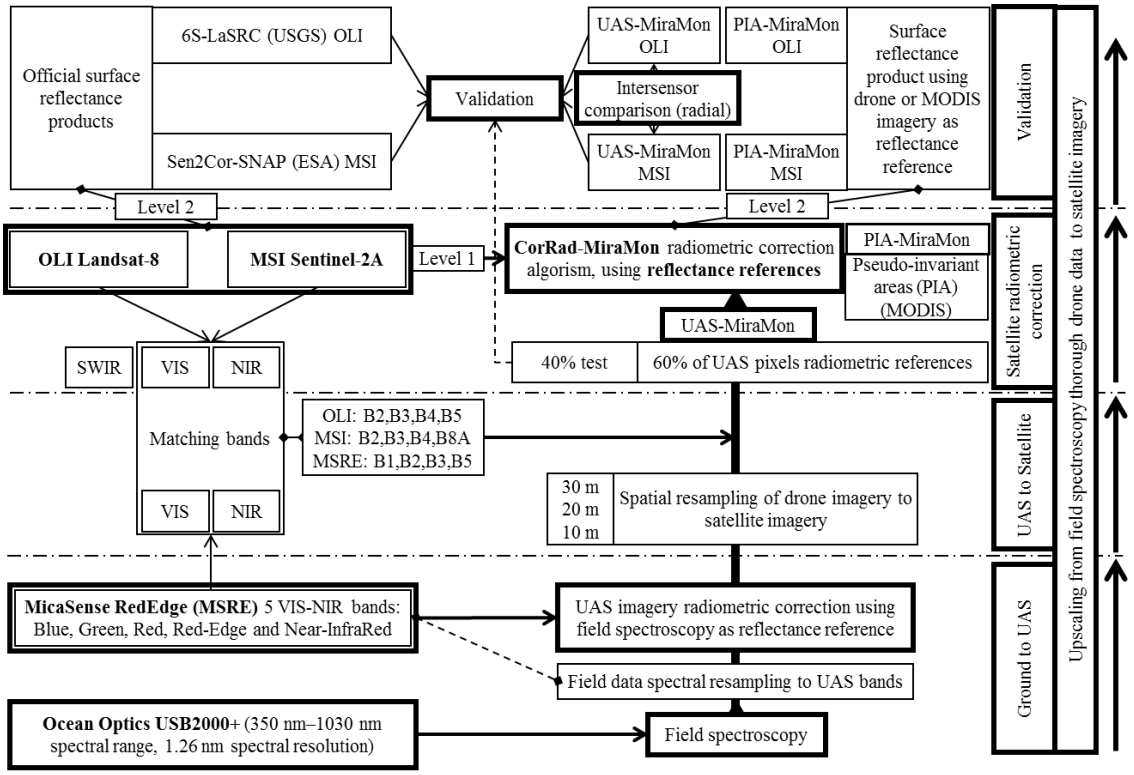

Figure 11. Graphical abstract of the upscaling and validation workflow from field measurements to satellite data. Note: please read the workflow from bottom to top. MODIS: Moderate Resolution Imaging Spectroradiometer; SWIR: Shortwave infrared.

4. Results

4.1. Fitting between Ground-Truth and Drone Data

The UAS imagery acquired by the overpass of L8 showed an excellent fitting to ground-truth measurements. VIS bands showed a high R^2 ($R^2_{BLUE} > 0.955$; $R^2_{GREEN} > 0.967$; $R^2_{RED} > 0.982$) and relatively low negative bias (−3.346%; −4.067%; −3.762%), meaning that the UAS reflectance values were slightly but systematically greater than those measured with the field spectroradiometric measurements. In the NIR band, this effect was relevant in dark targets, where the radiometer-measured surface reflectance was below 5%, while the UAS sensor-measured reflectance was between 15% and 20%, resulting in a relatively high negative bias (−16.956%), albeit also showing a high coefficient of determination ($R^2_{NIR} > 0.942$) (Figure 12a).

The UAS imagery acquired by the overpass of S2A obtained results that are very similar to the precedent L8. It also showed an excellent fitting to ground-truth measurements. VIS bands showed a high R^2 ($R^2_{BLUE} > 0.971$; $R^2_{GREEN} > 0.969$; $R^2_{RED} > 0.975$) and relatively low negative bias (−2.534%; −3.652%; −2.454%), also meaning that the UAS reflectance values were slightly but systematically greater than those measured with the field spectroradiometric measurements. In the NIR band, the effect was the same as those mentioned in the dark targets, where the radiometer-measured surface reflectance values were below 5%, while the UAS sensor-measured values were between 15% and 18% in this case, resulting in a relatively high negative bias (−17.921%), albeit also showing a high coefficient of determination ($R^2_{NIR} > 0.946$) (Figure 12b).

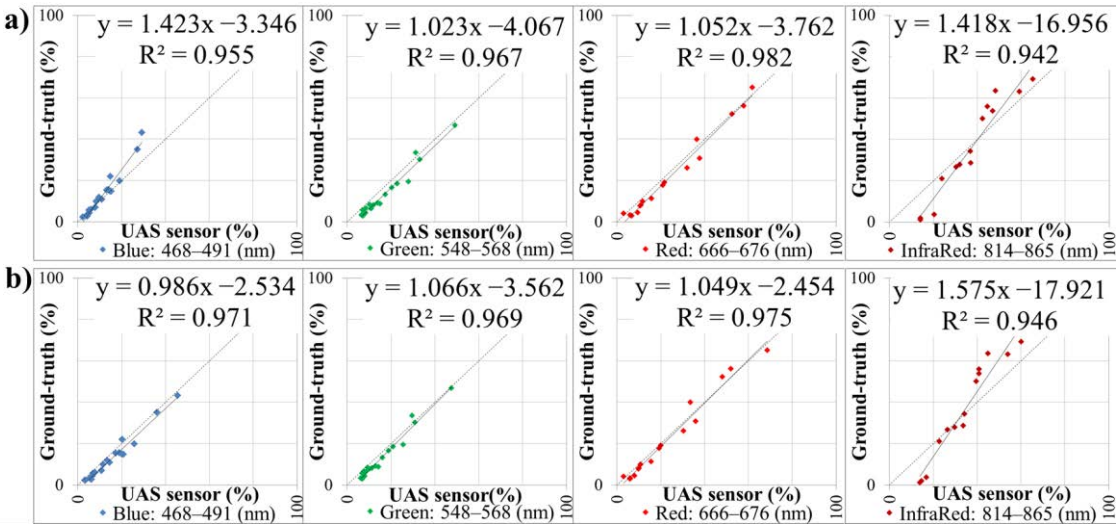

Figure 12. (a) Correlation of field spectroradiometric reflectance measurements and MicaSense RedEdge values on the drone flight by the overpass of L8 (b) Correlation of field spectroradiometric reflectance measurements and MicaSense RedEdge values on the drone flight by the overpass of S2A. Units are % of reflectance in all cases.

It is worth noting that the correlations in all the cases are significant, with p values of <0.05. When the linear function was applied, the bias was corrected and the coefficient of determination was maintained, thus accurately fitting the image values to the field spectroradiometric reflectance. The differences between both UAS images were in practice very low, since a delay of less than 22 min from one flight to the other only affected the sun position change, the small portion of atmosphere between the panels and the sensors, and the slight view difference.

4.2. Fitting between the Drone Data and the Satellite Data

Drone data (6 cm) resampled to 51 OLI grid pixels (30 m), 143 MSI grid pixels (20 m), and 517 MSI grid pixels (10 m) was compared band-by-band and pixel-by-pixel with official surface reflectance products (6S-LaSRC, Sen2Cor-SNAP) and with the PIA-MiraMon method. Results showed that the UAS data and satellite data follow the same trend, both for the OLI imagery (Figure 13a) and the MSI imagery (Figure 13b), although obviously the higher spatial resolution of the MSI increased the pixel variability over a smoother trend in the OLI sensor.

Focusing on the blue band, the PIA-MiraMon radiometric correction values were generally closer to the UAS data (RMSE$_{OLI} \leq 0.703\%$, RMSE$_{MSI} \leq 1.549\%$) than the 6S-LaSRC (RMSE$_{OLI} \leq 2.054\%$) or the Sen2Cor-SNAP (RMSE$_{MSI} \leq 2.192\%$) data (Table 4). The UAS surface reflectance data was always below that of the satellite, except in a bright pixel located over the house's roof. The MSI blue band showed the same trend as the OLI band, whereby it exhibited a good agreement between UAS and satellite surface reflectance data, despite the higher interpixel variability of the MSI blue band due to its higher spatial resolution (Figure 13).

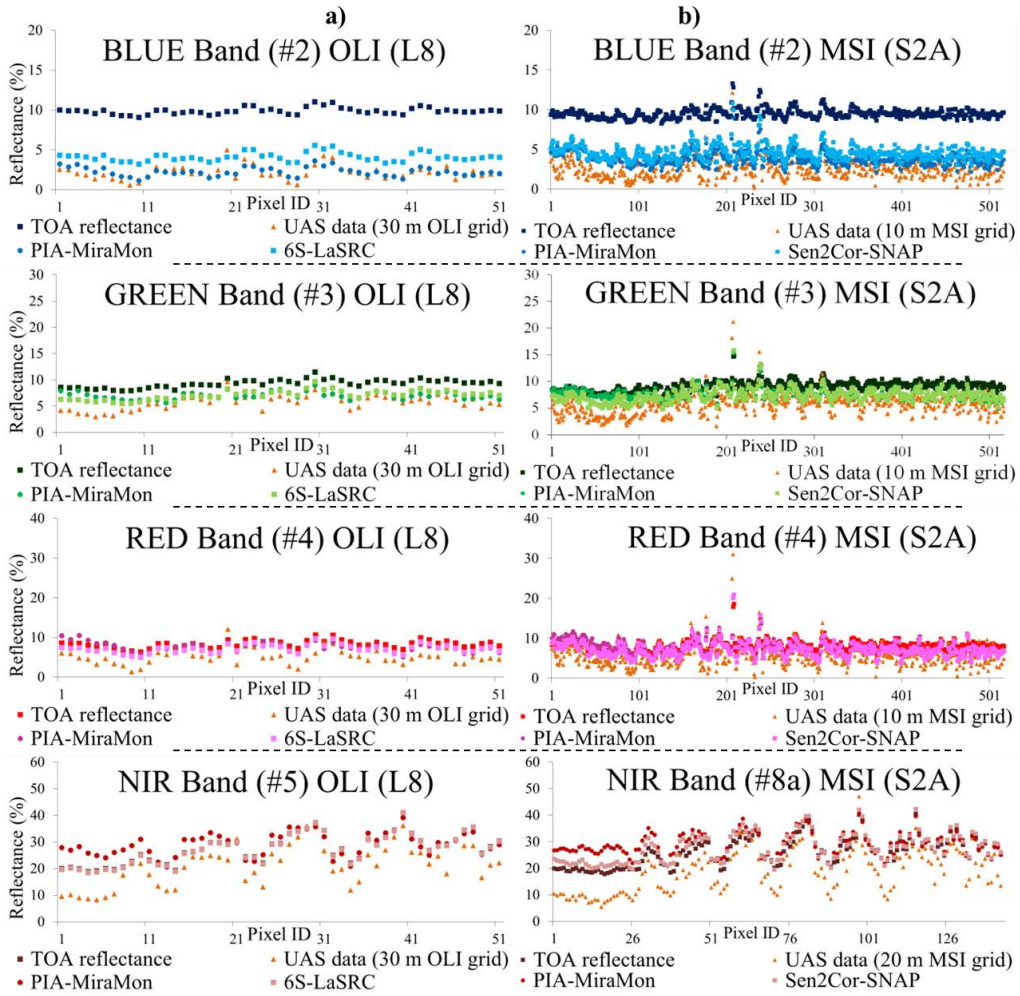

Figure 13. Pixel-by-pixel and band-by-band comparison of UAS surface reflectance data with: (a) OLI top of atmosphere (TOA) reflectance values and radiometrically corrected products (6S-LaSRC and PIA-MiraMon); (b) MSI TOA reflectance values and radiometrically corrected products (Sen2Cor-SNAP and PIA-MiraMon).

Focusing on the green band, the PIA-MiraMon and official products' surface reflectance values were both close to the UAS data, as the pixel-by-pixel plot indicates (Figure 13), but the 6S-LaSRC ($RMSE_{OLI} \leq 1.623\%$) and the Sen2Cor-SNAP ($RMSE_{MSI} \leq 2.058\%$) obtained slightly better adjustments than the PIA-MiraMon ($RMSE_{OLI} \leq 1.745\%$, $RMSE_{MSI} \leq 2.477\%$) in this spectral region (Table 4).

Focusing on the red band, the differences in radiometric corrections over the UAS data were slightly higher for the PIA-MiraMon ($RMSE_{OLI} \leq 3.017\%$, $RMSE_{MSI} \leq 2.802\%$), LaSRC ($RMSE_{OLI} \leq 2.484\%$), and Sen2Cor ($RMSE_{MSI} \leq 2.361\%$). The pixel-by-pixel comparison showed a high variability of the UAS red band, with a range of values wider than in the green and blue bands (Figure 13).

Focusing on the NIR band, the differences were dramatically high between the UAS data and the satellite data (Table 4) in both the PIA-MiraMon ($RMSE_{OLI} \leq 9.177\%$, $RMSE_{MSI} \leq 11.349\%$) and the official products ($RMSE_{OLI} \leq 6.688\%$, $RMSE_{MSI} \leq 8.783\%$). Although the overall trend was coherent, these differences were expected due to the RSRF drone sensor and the satellite sensors mismatching in this band (Figure 13).

With these results, we were concerned about the high differences between the UAS surface reflectance data and the satellite surface reflectance data in the NIR band. Thus, we compared the satellite surface reflectance products to investigate if there were higher differences than between the UAS data and satellite data. The differences between the PIA-MiraMon and official products (last row of Table 4) in the blue band ($RMSE_{OLI} \leq 1.882\%$, $RMSE_{MSI} \leq 0.818\%$), green band ($RMSE_{OLI} \leq 0.746\%$, $RMSE_{MSI} \leq 0.715\%$), and red band ($RMSE_{OLI} \leq 1.061\%$, $RMSE_{MSI} \leq 0.780\%$) indicated a general

of Table 4) in the blue band ($RMSE_{OLI} \leq 1.882\%$, $RMSE_{MSI} \leq 0.818\%$), green band ($RMSE_{OLI} \leq 0.746\%$, $RMSE_{MSI} \leq 0.715\%$), and red band ($RMSE_{OLI} \leq 1.061\%$, $RMSE_{MSI} \leq 0.780\%$) indicated a general agreement of both radiometric correction methods, thus either confirming the differences below, or that they are equal to 3.0% between the UAS data and the satellite data, which were radiometrically corrected using the other methods. In the NIR band, those differences were below 4% between the PIA-MiraMon and the 6S-LaSRC ($RMSE_{OLI} \leq 3.693\%$) and also between PIA-MiraMon and Sen2Cor-SNAP ($RMSE_{MSI} \leq 2.757\%$), which definitely points to a disagreement between the UAS data and the satellite data in this band (Figure 8).

Table 4. Band-by-band RMSE between the UAS resampled imagery, the satellite data corrected with the PIA-MiraMon method and the official surface reflectance products for the OLI (6S-LaSRC) and the MSI (Sen2Cor-SNAP). Bold values are the lowest difference in the corresponding band and sensor, being below the 3% accuracy requirement. Units: Reflectance (%).

	BLUE		GREEN		RED		NIR	
RMSE UAS Data vs. Data Source	**OLI #2 (n = 51)**	**MSI #2 (n = 517)**	**OLI #3 (n = 51)**	**MSI #3 (n = 517)**	**OLI #4 (n = 51)**	**MSI #4 (n = 517)**	**OLI #5 (n = 51)**	**MSI #8a (n = 143)**
TOA reflectance	7.743	6.981	3.684	3.674	3.533	3.101	6.847	8.050
PIA-MiraMon	**0.703**	**1.549**	1.745	2.477	3.017	2.802	9.177	11.349
Official products	2.054	2.192	**1.623**	**2.058**	**2.484**	**2.361**	6.688	8.783
RMSE PIA-MiraMon vs. Official products	1.882	0.818	0.746	0.715	1.061	0.780	3.693	2.757

4.3. Fitting of the UAS-Based Satellite Radiometric Corrections with the Test Areas

Comparing the test pixels (40% of 51) in the corrected L8 image (30 m) with the UAS-MiraMon method, for band-by-band reflectance, the RMSE was 0.712% in the blue band, 1.000% in the green band, 1.871% in the red band, and 7.530% in the NIR band, as expected based on the previous section's results. Comparing the test pixels (40% of 517) in the corrected S2 (10 m) image with the UAS-MiraMon method, for band-by-band reflectance, the RMSE was 0.745% in the blue band, 1.230% in the green band, and 2.018% in the red band; when comparing the test pixels (40% of 143) in the NIR band (20 m), the RMSE was 6.760%, also in consonance with previous results (Table 5).

When calculating the RMSE between test areas and the other radiometric correction methods, in the blue band, they were higher in the official products ($RMSE_{OLI} \leq 2.197\%$, $RMSE_{MSI} \leq 2.149\%$) than with the PIA-MiraMon correction method ($RMSE_{OLI} \leq 0.585\%$, $RMSE_{MSI} \leq 1.366\%$). In the green band, the official products ($RMSE_{OLI} \leq 1.653\%$, $RMSE_{MSI} \leq 1.806\%$) were slightly better than with the PIA-MiraMon method ($RMSE_{OLI} \leq 1.746\%$, $RMSE_{MSI} \leq 1.806\%$), as in the red band, where 6S-LaSRC and Sen2Cor-SNAP ($RMSE_{OLI} \leq 2.680\%$, $RMSE_{MSI} \leq 2.192\%$) obtained lower differences when compared to test areas than with the PIA-MiraMon method ($RMSE_{OLI} \leq 3.130\%$, $RMSE_{MSI} \leq 2.373\%$) (Table 5).

Table 5. Band-by-band RMSE between the test UAS areas and the satellite data radiometrically corrected by using: fitting UAS references (UAS-MiraMon), MODIS references (PIA-MiraMon) and the official products (6S-LaSRC for OLI and Sen2Cor-SNAP for MSI). Bold values are the lowest difference in the corresponding band and sensor, being below the 3% accuracy requirement. Units: Reflectance (%).

	BLUE		GREEN		RED		NIR	
RMSE Test Areas vs. Data Source	**OLI #2 (n = 20)**	**MSI #2 (n = 207)**	**OLI #3 (n = 20)**	**MSI #3 (n = 207)**	**OLI #4 (n = 20)**	**MSI #4 (n = 207)**	**OLI #5 (n = 20)**	**MSI #8a (n = 57)**
UAS-MiraMon	0.712	**0.745**	**1.000**	**1.230**	**1.871**	2.018	7.530	6.760
PIA-MiraMon	**0.585**	1.366	1.746	1.867	3.130	2.373	8.528	7.281
Official Products	2.197	2.149	1.653	1.806	2.680	2.192	5.841	7.690

4.4. Fitting between the Radiometric Correction of Almost Simultaneously Acquired L8 and S2 Data

The surface reflectance of the L8 and S2A images acquired at almost at the same time showed acceptable differences in the visible bands ($RMSE_{VIS}$ < 1.147%) and higher ones in the NIR band ($RMSE_{VIS}$ < 1.707%) (Table 6). The blue band had the lowest intersensor differences among all the performed comparisons, either when focusing 15 km around the study area (0.621%), in the ring between 15 km and 30 km (0.739%), or in the full TCG scene (0.852%). The green band presented a good fitting between both sensors, with differences lower than 1% in the three distances (0.741%, 0.815%, and 0.940%). In the red band, the fittings showed slightly higher differences (0.919%, 0.984%, and 1.147%) than in the blue and green bands. In the NIR band, the differences increased with respect to the visible bands (1.664%, 1.666%, 1.707%), but they followed the same distance pattern.

Table 6. Band-by-band correlation between almost simultaneous acquired images of L8 and S2 (resampled to 30 m pixels). Analysis performed in concentric radial distances from the center of the study area and in the R051 TCG tile extent. The radiometric correction was derived from data using UAS references (UAS-MiraMon).

RMSE (%) between Near Coincident L8 and S2 Images Corrected with the UAS-MiraMon Method				
Distance to UAS Central Scene (Number of Inter-Compared Pixels)	**BLUE**	**GREEN**	**RED**	**NIR**
0–15 km (n = 681,950)	0.621	0.741	0.919	1.664
15–30 km (n = 2,203,730)	0.739	0.815	0.984	1.666
TCG scene (n = 12,148,700)	0.852	0.940	1.147	1.707

5. Discussion

First of all, we would like to present that obtaining the field spectroradiometric measurement with the hand-held instrument and the reflectance reference EVA panels was operational and provided very useful data for this research. Analyzing the results of the fitting between the ground-truth and the 6-cm drone data described in the previous section, we found that the photogrammetric software reflectance calibration using the calibration target provided by the MicaSense RedEdge manufacturer and EXIF information obtains good fitting with in situ EVA panel measurements (R^2 > 0.942), resulting in a good performance of the MicaSense RedEge sensor and quite good radiometric treatment of the software. Although we found very low differences between the fitting of the in situ data and the two UAS flights carried out by the L8 overpass and by the S2A overpass, we should highlight a common negative bias, which means that the automatic UAS reflectance values are systematically higher than the field spectroradiometric reflectance values. In summary, in this first upscaling step, we were able to determine that using multiple reflectance targets distributed in the spectral domain, covering a wide range of intensities and characterized with field spectroradiometry measurements, facilitates the correction of drifts introduced by the simpler usage of the calibration target provided by the drone sensor manufacturer, all of which are consistent with very recent studies [30]. It is worth noting that two or three high-quality targets should be enough for calibration purposes, and the remaining targets could be used for the validation of results and accuracy analysis, but according to our experience, more panels could be used to guarantee an appropriate distribution of intensities and spectral references, and also to have some alternatives if some color is so intense that it saturates the UAS data. Nevertheless, as this research did not attempt to determine the minimum number of panels or the more appropriate colors, we have used a fairly large number of panels (17) and a wide set of colors in order to be sure that no problem occurred because of that. Further research will determine the appropriateness of the number of panels and the concrete colors we have suggested after more intensive tests focused on this objective.

Analyzing the results of the fitting between the drone data and the satellite data, the RMSE between the UAS and the satellite data was acceptable in visible bands (RMSE < 3.017%), as supported in the recent work of [38]. The spatial resampling of the drone data from 6 cm to 30 m, 20 m, and 10 m using a 2D Gaussian weighting function provided synthetic values coherent with the values

obtained from the satellite imagery that was radiometrically corrected using the official products and a well-proven method, such as the PIA-MiraMon. In this second upscaling step, we have to highlight three effects among the comparisons in all the bands, both in the OLI and the MSI. Firstly, the UAS surface reflectance values were systematically lower than satellite values (this effect was most visible in the blue and green bands). Secondly, the UAS data was more diverse than the satellite data; also, the 10 m and 20 m data were more diverse than the 30 m data; this is expected due to a larger pixel size (Figure 13). Third, and most importantly, the NIR band presented very high reflectance differences between the UAS data and the satellite data (RMSE > 6.688%), both in the OLI and the MSI and in all the radiometric correction methods, thus confirming that the band mismatch in the spectral configuration is too significant to be ignored. The spectral mismatching is the main source of this high difference, but in further works where the UAS band and the satellite NIR band have a good spectral matching, it will be necessary to consider if the signal-to-noise ratio (SNR) is the main significant source of error, because in OLI and MSI sensors, the SNR is poorer than in the VIS bands (due to the lower radiance signal in IR wavelengths), as stated in the Landsat-8 Data users handbook [63] and in the Sentinel-2 Technical Guide [64].

Analyzing the results of the fitting between the drone-based satellite radiometric corrections and test areas, we found that in the visible bands, the UAS-MiraMon radiometric correction achieves similar-quality results to the 6S-LaSRC, Sen2Cor-SNAP, or PIA-MiraMon alternatives (in the NIR band, the results are highly biased and cannot be compared), meeting the radiometric accuracy requirements. Indeed, in the visible bands of the OLI and MSI, the UAS-MiraMon achieves better fittings (RMSE < 2.018%) than the other tested methods (6S-LaSRC (RMSE < 2.680%), Sen2Cor-SNAP (RMSE < 2.192%), and PIA-MiraMon (RMSE < 3.130%)). This could be explained by the fact that the 6S-LaSRC, Sen2Cor-SNAP, and PIA-MiraMon use information for the whole scene, whereas in the UAS-MiraMon case, the atmospheric parameters of the CorRad-MiraMon model ($L_{atm\lambda}$, $\tau_{0\lambda}$) are fitted using the local drone references. Consequently, using the UAS references has improved local accuracy in radiometric correction, arising as a new methodology to radiometrically correct satellite imagery focusing in a special area of interest, rather than correcting a full scene with atmospheric parameters obtained from other sources, often out of the area of interest, as is done by the official products and other alternatives. Moreover, the presented method allows a much more robust usage of the point spectroradiometric measurements with regard to their direct comparison to satellite imagery. On the other hand, the UAS-MiraMon method should be used for correcting satellite images acquired almost simultaneously to UAS data.

Consistent with other findings [23], when analyzing the results of the surface reflectance differences between almost simultaneously acquired L8 and S2 data radiometrically corrected with UAS-MiraMon, we found that the method obtains good fittings (RMSE < 1.7%). As we hypothesized, the accuracy of the new UAS-MiraMon method is better in the drone area and decreases with increasing distance (local overfitting), since the solution for the atmospheric parameters is fitted to the study area surface reflectance references. However, the results for the coincident S2 and L8 tiles extent are also good ($RMSE_{VIS}$ < 1%), thus implying a good consistency of the UAS-MiraMon experimental approach. This high intersensor coherence, added to the improved radiometric correction accuracy in the area of interest, is an advantage of the UAS-MiraMon method for the generation of consistent temporal series using data from different sensors in specific areas of interest that need to be monitored in an accurate way.

6. Conclusions

In this research, we demonstrated the operational capabilities of unmanned aerial system (UAS) imagery in synergy with field spectroradiometric measurements to perform radiometric correction of satellite imagery. The use of UAS imagery as radiometric references in combination with the CorRad-MiraMon radiometric correction algorithm (UAS-MiraMon method) resulted in improved local accuracy of surface reflectance values of the satellite imagery. Radiometrically corrected official

products (6S-LaSRC and SNAP-Sen2Cor) and other alternatives (PIA-MiraMon) met the mission radiometric accuracy requirements as well (RMSE < 3%), but UAS-MiraMon obtains better accuracy because it focuses on the retrieval of atmospheric parameters in the area of interest, rather that correcting a full scene with atmospheric parameters obtained from other sources, often out of the area of interest. Also, the UAS imagery covers a larger area than conventional field spectroscopy measurements with reliable radiometric quality, and can be useful to support the validation of surface reflectance values of satellite imagery in specific areas of interest as well as their continuous monitoring with higher radiometric accuracy.

Correlating the drone data with the field spectroradiometric measurements was evaluated positively. However, a linear fitting using reference panels of different spectral response and intensity is required to improve the simpler correction based on the manufacturer's calibration panel. The UAS data provided an ultrahigh spatial resolution (6 cm) and sampled areas not accessible by human operators in previous field spectroradiometric campaigns; the results indicated consistent surface reflectance accuracy. One of the best methodological advantages of using the UAS instruments is the high sampling capacity over space, allowing an easy and efficient resampling to any satellite grid; in this study, we covered 517 MSI 10 m pixels in $\pm$5 min with the satellite overpass.

Altogether, the results showed that when the spectral response of the drone sensor reasonably matches the response of the satellite sensors, the results are good. However, a mismatch between them is a problematic issue, and we encourage the design of UAS sensors with spectral responses more similar to OLI or MSI sensors, especially in the NIR region. The UAS data resampled to satellite pixel sizes proved to be highly coherent with the official surface reflectance products in the visible bands of the L8 and the S2A. Nevertheless, use of the UAS data as a radiometric reference to fit the atmospheric parameters of the radiometric correction in combination with the CorRad-MiraMon algorithm revealed very good results in the study area. Moreover, although the surface reflectance accuracy slightly degrades with increasing distance from the study area, the comparison of near-coincident L8 and S2 images corrected with the UAS-MiraMon also provided an excellent intersensor fitting ($RMSE_{VIS}$ < 1%), thus suggesting a robust way for multisensor radiometric correction and the generation of more coherent time series focused on a specific study area that needs to be accurately monitored.

Field spectroradiometric measurement remains as the ground-truth reference source due to the proximity of the sensor to the surface, the intensity of scans, the control of the measurements, and the instrument features. Thus, the UAS-acquired data can benefit from conventional field spectroradiometry. Moreover, this type of synergy can provide valuable surface reflectance reference data.

Radiometric correction of Landsat-like images using drone imagery as reflectance references provides good results in the visible bands ($RMSE_{VIS}$ < 2.018%), meeting the mission radiometric requirements. This method is especially useful for the surrounding areas of the drone flight, such as in the studying and monitoring of protected areas. This contribution opens the door to the operational usage of spatially disperse drone flights campaigns, in synergy with ground-truth reflectance references, for radiometrically correcting satellite images or validating radiometric corrections results, especially when using remote sensors with a similar spectral configuration.

Author Contributions: X.P. and J.-C.P. conceived and designed the experiments. J.-C.P. and L.A.A. performed the field data experiments. X.P. and L.P. designed the algorithms and wrote the corresponding software. F.-J.M. contributed with the UAS materials, photogrammetric expertise, and the flight plan. J.-C.P., L.A.A., L.P., and X.P. analyzed the data. J.-C.P. and X.P. wrote the paper. L.P. revised the paper.

Funding: This research was funded by European Union through the grant H2020 641762-2 EC. This research was funded by the Spanish Ministry of Economy and Competitiveness (Ministerio de Economía y Competitividad) through the grant number CGL2015-69888-P (MINECO/FEDER, EU). This research was funded by Catalan Government (Departament d'Universitats, Recerca i Societat de la Informació) under grant number SGR2017-1690 and Catalan Government (Agència de Gestió d'Ajuts Universitaris i de Recerca) under grant number 2016B_00410. The APC was funded by Centre de Recerca Ecològica i Aplicacions Forestals (CREAF).

Acknowledgments: This work has been supported by the European Union through the ECOPOTENTIAL Project (H2020 641762-2 EC) and by the Spanish Ministry of Economy and Competitiveness through the ACAPI project (CGL2015-69888-P (MINECO/FEDER)). The GRUMETS Research Group is partially supported by the Catalan Government under Grant SGR2017-1690. Cristian Padró is the recipient of a FI-DGR scholarship grant (2016B_00410). Xavier Pons is the recipient of an ICREA Academia Excellence in Research Grant (2016–2020). We would like to acknowledge ESA-Copernicus and USGS-NASA for the availability of satellite data. We would like to acknowledge the HEMAV Company for supplying UAS material, the pilot (Xavier Jardí), and expertise. This work has been carried out in the framework of the Doctorate Program of the Geography Department at the Universitat Autònoma de Barcelona.

Conflicts of Interest: The authors declare no conflict of interest.

References

1. United Nations (UN). Transforming Our World: The 2030 Agenda for Sustainable Development. 21 October 2015. Available online: http://www.refworld.org/docid/57b6e3e44.html (accessed on 7 August 2018).
2. Emery, W.J.; Camps, A. *Introduction to Satellite Remote Sensing*, 1st ed.; Emery, W., Camps, A., Eds.; Elsevier: Amsterdam, The Netherlands, 2017; p. 860.
3. Diaz-Delgado, R.; Lucas, R.; Hurford, C. (Eds.) *The Roles of Remote Sensing in Nature Conservation: A Practical Guide and Case Studies*, 1st ed.; Springer: Cham, Switzerland, 2017; p. 318.
4. Group on Earth Observation (GEO). Earth Observations in support of the 2030 Agenda for Sustainable development. Japan Aerospace Exploration Agency (JAXA) and GEO (EO4SDG Initiative). 2017; p. 19. Available online: https://www.earthobservations.org/documents/publications/201703_geo_eo_for_2030_agenda.pdf (accessed on 7 August 2018).
5. GEOSS. GEOSS Evolution. Available online: http://www.earthobservations.org/geoss.php (accessed on 7 August 2018).
6. National Aeronautics and Space Administration (NASA). Landsat Data Continuity Mission (LDCM). Available online: https://www.nasa.gov/mission_pages/landsat/main/index.html (accessed on 7 August 2018).
7. European Space Agency (ESAa). ESA Sentinel Online. Sentinel-2 Mission. Available online: http://www.esa.int/Our_Activities/Observing_the_Earth/Copernicus/Sentinel-2 (accessed on 7 August 2018).
8. European Space Agency (ESAb). ESA Sentinel Online. Sentinel-2 Mission Objectives. Available online: https://sentinel.esa.int/web/sentinel/missions/sentinel-2/mission-objectives (accessed on 7 August 2018).
9. Li, J.; Roy, D.P. A Global Analysis of Sentinel-2A, Sentinel-2B and Landsat-8 Data Revisit Intervals and Implications for Terrestrial Monitoring. *Remote Sens.* **2017**, *9*, 902. [CrossRef]
10. Liou, K.N. *An Introduction to Atmospheric Radiation*, 2nd ed.; Liou, K.N., Ed.; Academic Press: San Diego, CA, USA, 2002; p. 583.
11. Nicodemus, F.E.; Richmond, J.C.; Hsia, J.J. *Geometrical Considerations and Nomenclature for Reflectance*; National Bureau of Standards, US Department of Commerce: Washington, DC, USA, 1977. Available online: http://physics.nist.gov/Divisions/Div844/facilities/specphoto/pdf/geoConsid.pdf (accessed on 7 August 2018).
12. Riano, D.; Chuvieco, E.; Salas, J.; Aguado, I. Assessment of different topographic corrections in Landsat-TM data for mapping vegetation types. *IEEE Trans. Geosci. Remote Sens.* **2003**, *41*, 1056–1061. [CrossRef]
13. Vermote, E.F.; Tanre, D.; Deuzé, J.L.; Herman, M.; Morcrette, J.-J. Second Simulation of the Satellite Signal in the Solar Spectrum, 6S: An Overview. *IEEE Trans. Geosci. Remote Sens.* **1997**, *35*, 675–686. [CrossRef]
14. Vermote, E.; Justice, C.; Claverie, M.; Franch, B. Preliminary analysis of the performance of the Landsat 8/OLI land surface reflectance product. *Remote Sens. Environ.* **2016**, *185*, 46–56. [CrossRef]
15. Richter, R.; Schläpfer, D. Atmospheric/Topographic Correction for Satellite Imagery (ATCOR-2/3 User Guide, Version 9.0.2, March 2016). 2016. Available online: http://www.rese.ch/pdf/atcor3_manual.pdf (accessed on 7 August 2018).
16. Richter, R.; Louis, J.; Müller-Wilm, U. [L2A-ATBD] Sentinel-2 Level-2A Products Algorithm Theoretical Basis Document. Version 2.0. 2012; pp. 1–72. Available online: https://earth.esa.int/c/document_library/get_file?folderId=349490&name=DLFE-4518.pdf (accessed on 7 August 2018).
17. Mueller-Wilm, U. *Sen2Cor Configuration and User Manual V2.4*; European Space Agency, 2017; pp. 1–53. Available online: http://step.esa.int/thirdparties/sen2cor/2.4.0/Sen2Cor_240_Documenation_PDF/S2-PDGS-MPC-L2A-SUM-V2.4.0.pdf (accessed on 7 August 2018).

18. Claverie, M.; Masek, J. Harmonized Landsat-8 Sentinel-2 (HLS) Product's Guide. v.1.3, 2017; Available online: https://hls.gsfc.nasa.gov/documents/ (accessed on 7 August 2018). [CrossRef]
19. Skakun, S.V.; Roger, J.-C.; Vermote, E.; Masek, J.; Justice, C. Automatic sub-pixel co-registration of Landsat-8 Operational Land Imager and Sentinel-2A Multi-Spectral Instrument images using phase correlation and machine learning based mapping. *Int. J. Digit. Earth* **2017**, *10*, 1253–1269. [CrossRef]
20. Mandanici, E.; Bitelli, G. Preliminary Comparison of Sentinel-2 and Landsat 8 Imagery for a Combined Use. *Remote Sens.* **2016**, *8*, 1014. [CrossRef]
21. CEOS-WGCV. CEOSS Cal/Val Portal. Available online: http://calvalportal.ceos.org/ (accessed on 7 August 2018).
22. Doxani, G.; Vermote, E.; Roger, J.-C.; Gascon, F.; Adriaensen, S.; Frantz, D.; Hagolle, O.; Hollstein, A.; Kirches, G.; Li, F.; et al. Atmospheric Correction Inter-Comparison Exercise. *Remote Sens.* **2018**, *10*, 352. [CrossRef]
23. Padró, J.C.; Pons, X.; Aragonés, D.; Díaz-Delgado, R.; García, D.; Bustamante, J.; Pesquer, L.; Domingo-Marimon, C.; González-Guerrero, O.; Cristóbal, J.; et al. Radiometric Correction of Simultaneously Acquired Landsat-7/Landsat-8 and Sentinel-2A Imagery Using Pseudoinvariant Areas (PIA): Contributing to the Landsat Time Series Legacy. *Remote Sens.* **2017**, *9*, 1319. [CrossRef]
24. Pons, X.; Solé-Sugrañes, L. A simple radiometric correction model to improve automatic mapping of vegetation from multispectral satellite data. *Remote Sens. Environ.* **1994**, *45*, 317–332. [CrossRef]
25. McCoy, R.M. *Field Methods in Remote Sensing*, 1st ed.; McCoy, R.M., Ed.; The Guilford Press: New York, NY, USA, 2005; p. 159, ISBN 1-59385-080-8.
26. Milton, E.J.; Schaepmann, M.E.; Anderson, K.; Kneubühler, M.; Fox, N. Progress in field spectroscopy. *Remote Sens. Environ.* **2009**, *113*, S92–S109. [CrossRef]
27. Smith, G.M.; Milton, E.J. The use of the empirical line method to calibrate remotely sensed data to reflectance. *Int. J. Remote Sens.* **1999**, *20*, 2653–2662. [CrossRef]
28. Colwell, R.N.; Ulaby, F.T.; Simonett, D.S.; Estes, J.E.; Thorley, G.A. *Manual of Remote Sensing*, 2nd ed.; Colwell, R.N., Ed.; American Society of Photogrammetry: Falls Church, VA, USA, 1983; Volume 2, p. 2440, ISBN 093729442X.
29. Sánchez Alberola, J.; Oliver, P.; Estornell, J.; Dopazo, C. Estimación de variables forestales de Pinus Sylvestris L. en el contexto de un inventario forestal aplicando tecnología LiDAR aeroportada [Estimation of forest variables of Pinus Sylvestris L. in the context of a forestry inventory applying airborne LiDAR technology]. *GeoFocus* **2018**, *21*, 79–99. [CrossRef]
30. Aasen, H.; Honkavaara, E.; Lucieer, A.; Zarco-Tejada, P.J. Quantitative Remote Sensing at Ultra-High Resolution with UAV Spectroscopy: A Review of Sensor Technology, Measurement Procedures, and Data Correction Workflows. *Remote Sens.* **2018**, *10*, 1091. [CrossRef]
31. OPTIMISE. Innovative Optical Tools for Proximal Sensing of Ecophysiological Processes (ESSEM COST Action ES1309). Available online: https://optimise.dcs.aber.ac.uk/ (accessed on 7 August 2018).
32. Mac Arthur, A.; Robinson, I. A critique of field spectroscopy and the challenges and opportunities it presents for remote sensing for agriculture, ecosystems, and hydrology. In Proceedings of the SPIE Remote Sensing for Agriculture, Ecosystems, and Hydrology, Toulouse, France, 14 October 2015.
33. Iqbal, F.; Lucieer, A.; Barry, K. Simplified radiometric calibration for UAS-mounted multispectral sensor. *European J. Rem. Sens.* **2018**, *51*, 301–313. [CrossRef]
34. Honkavaara, E.; Kaivosoja, J.; Mäkynen, J.; Pellikka, I.; Pesonen, L.; Saari, H.; Salo, H.; Hakala, T.; Marklelin, L.; Rosnell, T. Hyperspectral Reflectance Signatures and Point Clouds for Precision Agriculture by Light Weight UAV Imaging System. In Proceedings of the XII ISPRS Annals of Photogrammetry, Remote Sensing and Spatial Information Sciences, Melbourne, VIC, Australia, 25 August–1 September 2012; Volume I-7, pp. 353–358. [CrossRef]
35. Matese, A.; Toscano, P.; Di Gennaro, S.F.; Genesio, L.; Vaccari, F.P.; Primicerio, J.; Belli, C.; Zaldei, A.; Bianconi, R.; Gioli, B. Intercomparison of UAV, Aircraft and Satellite Remote Sensing Platforms for Precision Viticulture. *Remote Sens.* **2015**, *7*, 2971–2990. [CrossRef]
36. Adão, T.; Hruška, J.; Pádua, L.; Bessa, J.; Peres, E.; Morais, R.; Sousa, J.J. Hyperspectral Imaging: A Review on UAV-Based Sensors, Data Processing and Applications for Agriculture and Forestry. *Remote Sens.* **2017**, *9*, 1110. [CrossRef]

37. Manfreda, S.; McCabe, M.; Miller, P.; Lucas, R.; Pajuelo Madrigal, V.; Mallinis, G.; Ben-Dor, E.; Helman, D.; Estes, L.; Ciraolo, G.; et al. On the Use of Unmanned Aerial Systems for Environmental Monitoring. *Remote Sens.* **2018**, *10*, 641. [CrossRef]
38. Zabala, S. Comparison of Multi-Temporal and Multispectral Sentinel-2 and Unmanned Aerial Vehicle Imagery for Crop Type Mapping. Master of Science (MSc) Thesis, Lund University, Lund, Sweden, June 2017.
39. MicaSense. *MicaSense RedEdge™ 3 Multispectral Camera User Manual*; MicaSense, Inc.: Seattle, WA, USA, 2015; p. 33. Available online: https://support.micasense.com/hc/en-us/article_attachments/204648307/RedEdge_User_Manual_06.pdf (accessed on 1 July 2018).
40. Jhan, J.P.; Rau, J.Y.; Haala, N.; Cramer, M. Investigation of Parallax Issues for Multi-Lens Multispectral Camera Band Co-Registration. *Int. Arch. Photogramm. Remote Sens. Spatial Inf. Sci.* **2017**, *XLII-2/W6*, 157–163. [CrossRef]
41. Parrot Drones. Parrot Sequoia Technical Specifications. 2018. Available online: https://www.parrot.com/global/parrot-professional/parrot-sequoia#technicals (accessed on 7 August 2018).
42. Fernández-Guisuraga, J.M.; Sanz-Ablanedo, E.; Suárez-Seoane, S.; Calvo, L. Using Unmanned Aerial Vehicles in Postfire Vegetation Survey Campaigns through Large and Heterogeneous Areas: Opportunities and Challenges. *Sensors* **2018**, *18*, 586. [CrossRef] [PubMed]
43. Rumpler, M.; Daftry, S.; Tscharf, A.; Prettenthaler, R.; Hoppe, C.; Mayer, G.; Bischof, H. Automated End-to-End Workflow for Precise and Geo-accurate Reconstructions using Fiducial Markers. In Proceedings of the ISPRS Technical Commission III Symposium, Zurich, Switzerland, 5–7 September 2014; pp. 135–142. [CrossRef]
44. Martínez-Carricondo, P.; Agüera-Vega, F.; Carvajal-Ramírez, F.; Mesas-Carrascosa, F.J.; García-Ferrer, A.; Pérez-Porras, F.J. Assessment of UAV-photogrammetric mapping accuracy based on variation of ground control points. *Int J Appl Earth Obs.* **2018**, *72*, 1–10. [CrossRef]
45. Wang, C.; Myint, S.W. A Simplified Empirical Line Method of Radiometric Calibration for Small Unmanned Aircraft Systems-Based Remote Sensing. *IEEE J. Sel. Top. Appl. Earth Obs. Remote Sens.* **2015**, *8*, 1876–1885. [CrossRef]
46. Pons, X.; Pesquer, L.; Cristóbal, J.; González-Guerrero, O. Automatic and improved radiometric correction of Landsat imagery using reference values from MODIS surface reflectance images. *Int. J. Appl. Earth Obs. Geoinf.* **2014**, *33*, 243–254. [CrossRef]
47. OceanOptics. *USB2000+ Fiber Optic Spectrometer Installation and Operation Manual*; Ocean Optics, Inc.: Dunedin, FL, USA, 2010.
48. OceanOptics. *USB200+ Data Sheet*; Ocean Optics, Inc.: Dunedin, FL, USA, 2006. Available online: https://oceanoptics.com/wp-content/uploads/OEM-Data-Sheet-USB2000-.pdf (accessed on 7 August 2018).
49. Rees, W.G. *Physical Principles of Remote Sensing*, 3rd ed.; Rees, W.G., Ed.; Cambridge University Press: New York, NY, USA, 2013; p. 441, ISBN 978-1-107-00473-3.
50. National Aeronautics and Space Administration (NASA). Landsat Science: A Lambertian Reflector. 2018. Available online: https://landsat.gsfc.nasa.gov/a-lambertian-reflector/ (accessed on 29 September 2018).
51. Ponce-Alcántara, S.; Arangú, A.V.; Plaza, G.S. The Importance of Optical Characterization of PV Backsheets in Improving Solar Module Power. Available online: https://www.ntc.upv.es/documentos/photovoltaics/PVI26_Paper_03_NTC-UPV-7.pdf (accessed on 29 September 2018).
52. Ciesielski, E.; MicaSense, Seattle, WA, USA. Personal communication, 2016.
53. Agisoft LLC. PhotoScan User Manual, Professional Edition, Version 1.4.1. 2018. Available online: http://www.agisoft.com/pdf/photoscan-pro_1_4_en.pdf (accessed on 1 July 2018).
54. Pons, X.; MiraMon. Sistema d'Informació Geogràfica i software de Teledetecció. Versió 8.1f [MiraMon. Geographical Information System and Remote Sensing Software. Version 8.1f]. Centre de Recerca Ecològica i Aplicacions Forestals, CREAF. Bellaterra. 2018. ISBN 84-931323-4-9. Available online: http://www.creaf.uab.cat/miramon/Index_usa.htm (accessed on 1 July 2018).
55. Leica Geosystems. Leica Viva GS14 Technical Specifications. 2017. Available online: http://www.leica-geosystems.es/downloads123/zz/gpsgis/VivaGS14/brochures-datasheet/Leica_Viva_GS14_DS_es.pdf (accessed on 1 July 2018).

56. ASPRS (American Society for Photogrammetry and Remote Sensing). ASPRS Positional Accuracy Standards for Digital Geospatial Data. Edition 1, Version 1.0.0. 2014. Available online: http://www.asprs.org/a/society/divisions/pad/Accuracy/ASPRS_Positional_Accuracy_Standards_for_Digital_Geospatial_Data_Edition1_V1_FinalDraftForPublication.docx (accessed on 1 July 2018).
57. MicaSense. RedEdge Camera Radiometric Calibration Model. 2018. Available online: https://support.micasense.com/hc/en-us/articles/115000351194-RedEdge-Camera-Radiometric-Calibration-Model (accessed on 7 August 2018).
58. National Aeronautics and Space Administration (NASA). Landsat Science, Spectral Response of the Operational Land Imager in-Band. 2018. Available online: http://landsat.gsfc.nasa.gov/preliminary-spectral-response-of-the-operational-land-imager-in-band-band-average-relative-spectral-response/ (accessed on 7 August 2018).
59. United States Geological Survey (USGS). EarthExplorer Download Tool. 2018. Available online: https://earthexplorer.usgs.gov/ (accessed on 7 August 2018).
60. United States Geological Survey (USGS). Landsat 8 Data Users Handbook–Section 5: Conversion of DNs to Physical Units. 2018. Available online: https://landsat.usgs.gov/landsat-8-l8-data-users-handbook-section-5 (accessed on 7 August 2018).
61. European Space Agency (ESA). Copernicus Open Access Hub. Available online: https://scihub.copernicus.eu/dhus/#/home (accessed on 28 October 2017).
62. European Space Agency (ESA) Sentinel Online, Sentinel-2A Document Library, Sentinel-2AA (S2A-SRF). 2017. Available online: https://earth.esa.int/web/sentinel/user-guides/sentinel-2-msi/document-library/-/asset_publisher/Wk0TKajiISaR/content/sentinel-2a-spectral-responses (accessed on 7 August 2018).
63. United States Geological Survey (USGS). Landsat-8 Data User Handbook. Version 2.0. 2016. Available online: https://landsat.usgs.gov/landsat-8-l8-data-users-handbook (accessed on 21 September 2018).
64. European Space Agency (ESA). Sentinel-2 Radiometric Performance. 2018. Available online: https://earth.esa.int/web/sentinel/technical-guides/sentinel-2-msi/performance (accessed on 21 September 2018).
65. Gascon, F.; Bouzinac, C.; Thépaut, O.; Jung, M.; Francesconi, B.; Louis, J.; Lonjou, V.; Lafrance, B.; Massera, S.; Gaudel-Vacaresse, A.; et al. Copernicus Sentinel-2A Calibration and Products Validation Status. *Remote Sens.* **2017**, *9*, 584. [CrossRef]
66. Chavez, P.S., Jr. An improved dark-object subtraction technique for atmospheric scattering correction of multispectral data. *Remote Sens. Environ.* **1988**, *24*, 459–479. [CrossRef]
67. Schowengerdt, R.A. *Remote Sensing, Models and Methods for Image Processing*, 3rd Ed.; Schowengerdt, R.A., Ed.; Elsevier: San Diego, CA, USA, 2007; p. 560. ISBN 978-0-12-369407-2.
68. Anniballe, R.; Bonafoni, S. A Stable Gaussian Fitting Procedure for the Parameterization of Remote Sensed Thermal Images. *Algorithms* **2015**, *8*, 82–91. [CrossRef]

2.4. Monitoratge de restauracions en mines a cel obert utilitzant Sistemes Aeris no Tripulats (UAS)

Padró J.C., Carabassa V., Balagué J., Brotons Ll., Alcañiz, J.M., Pons X. (2018). Monitoring opencast mine restorations using Unmanned Aerial System (UAS) imagery. *Science of the Total Environment, 657, 1602-1614*. DOI: 10.1016/j.scitotenv.2018.12.156. https://doi.org/10.1016/j.scitotenv.2018.12.156. (IF: 4.610, Q1: 27/242 (2017) [Environmental Sciences])

Resum: L'activitat extractiva a cel obert és econòmicament inevitable, però alhora és ecològicament insostenible sense la restauració dels espais ambientalment degradats. El control de la restauració després d'una activitat extractiva és un requisit legal per les empreses mineres i les administracions públiques de molts països, que implica el bloqueig de recursos financers per prevenir litigis mediambientals. L'objectiu d'aquesta contribució és presentar una aplicació rigorosa, de baix cost i fàcil d'usar per donar suport al control de la restauració d'explotacions mineres a cel obert mitjançant drons, complementant les inspeccions convencionals. Per assolir-lo, s'utilitzen imatges multiespectrals de molt alta resolució espacial (<10 cm), i es genera documentació cartogràfica de la restauració amb mapes detallats de la cobertes del sòl. El potencial dels UAV com a eina per controlar els treballs de restauració es presenta en una pedrera calcària que ha experimentat diferents accions de restauració post-minera en els darrers 20 anys, representativa de quatre etapes recuperades. S'ha utilitzat un dron de baix pes (<2 kg) equipat amb un sensor multiespectral, juntament amb mesures espectroradiomètriques de camp que s'han emprat per validar i corregir radiomètricament les dades del sensor del dron. Les imatges s'han processat amb programari fotogramètric i amb programari de teledetecció i SIG, resultant en informació espectral, índexs de vegetació, informació estructural i mapes de cobertes del sòl. Les dades espectrals i la classificació de la cobertes del sòl, que han estat validades a través d'àrees de mostreig *in-situ*, han ajudat a detectar i quantificar l'abocament de residus miners, sòl nu recuperat, l'extensió i el desenvolupament de formacions vegetals. També han permès una comparació quantitativa, però al mateix temps visual i intuïtiva, respecte els sistemes de referència no degradats dels voltants de l'explotació. El protocol resultant d'aquesta investigació constitueix un flux de treball que ofereix una solució econòmica, ràpida i de qualitat, destinada a la implementació de l'avaluació de la restauració per part de les administracions públiques i empreses privades. A més, la solució proposada evita les interpretacions subjectives proporcionant dades objectives, que integren les noves tecnologies al servei de científics, gestors ambientals i responsables de la presa de decisions.

Paraules clau: restauració minera; monitorització minera; dron; Sistemes Aeris no Tripulats; UAS; UAV; teledetecció; imatges multiespectrals.

Science of the Total Environment 657 (2019) 1602–1614

Contents lists available at ScienceDirect

Science of the Total Environment

journal homepage: www.elsevier.com/locate/scitotenv

Monitoring opencast mine restorations using Unmanned Aerial System (UAS) imagery

Joan-Cristian Padró [a,*], Vicenç Carabassa [b], Jaume Balagué [c], Lluís Brotons [d], Josep M. Alcañiz [e], Xavier Pons [f]

[a] Grumets Research Group, Departament de Geografia, Universitat Autònoma de Barcelona, Departament de Geografia Office B1092, Edifici B, Universitat Autònoma de Barcelona, 08193 Bellaterra, Catalonia, Spain
[b] Centre de Recerca Ecològica i Aplicacions Forestals (CREAF), Edifici C, Campus UAB, 08193 Bellaterra, Catalonia, Spain
[c] Centre Tecnològic Forestal de Catalunya (CTFC), Centre de Recerca Ecològica i Aplicacions Forestals (CREAF), Ctra Sant Llorenç km 2, 24280 Solsona, Catalonia, Spain
[d] Centre Tecnològic Forestal de Catalunya (CTFC), Centre de Recerca Ecològica i Aplicacions Forestals (CREAF), Consejo Superior de Investigaciones Científicas (CSIC), Ctra Sant Llorenç km 2, 24280 Solsona, Catalonia, Spain
[e] Universitat Autònoma de Barcelona, Centre de Recerca Ecològica i Aplicacions Forestals (CREAF), Edifici C, Universitat Autònoma de Barcelona, 08193 Bellaterra, Catalonia, Spain
[f] Grumets Research Group, Departament de Geografia, Universitat Autònoma de Barcelona, Departament de Geografia Office B1094, Edifici B, Universitat Autònoma de Barcelona, 08193 Bellaterra, Catalonia, Spain

HIGHLIGHTS

- Fast, repeatable and systematic monitoring at sub-decimeter spatial resolution
- R2 between drone imagery and field spectroradiometric measurements over 0.9
- Multispectral imagery allows monitoring mine wastes, restored soil and vegetation.
- A solution for easy detection of failing or successful restoration actions
- Affordable equipment and protocol for rigorous and non-conflictive mine monitoring

GRAPHICAL ABSTRACT

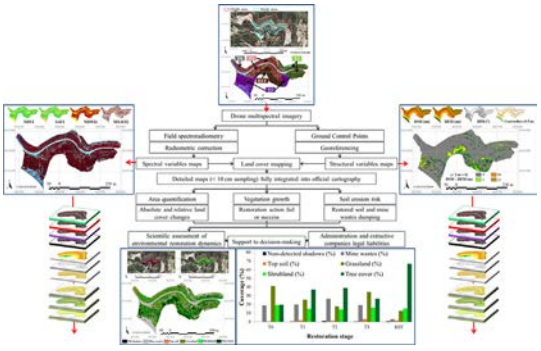

ARTICLE INFO

Article history:
Received 15 June 2018
Received in revised form 19 November 2018
Accepted 10 December 2018
Available online 13 December 2018

Keywords:
Mine restoration
Monitoring restoration

ABSTRACT

Open-pit mine is still an unavoidable activity but can become unsustainable without the restoration of degraded sites. Monitoring the restoration after extractive activities is a legal requirement for mine companies and public administrations in many countries, involving financial provisions for environmental liabilities. The objective of this contribution is to present a rigorous, low-cost and easy-to-use application of Unmanned Aerial Systems (UAS) for supporting opencast mining and restoration monitoring, complementing the inspections with very high (<10 cm) spatial resolution multispectral imagery, and improving any restoration documentation with detailed land cover maps. The potential of UAS as a tool to control restoration works is presented in a calcareous quarry that has undergone different post-mining restoration actions in the last 20 years, representing 4 reclaimed

Abbreviations: AGL, above ground level; ASPRS, American Society for Photogrammetry and Remote Sensing; DCSM, Digital Cast Shadow Model; DEM, Digital Elevation Model; DIM, Digital Illumination Model; DLS, Downwelling Light Sensor; DSM, Digital Surface Model; DTM, Digital Terrain Model; EVA, Ethylene-Vinyl Acetate; EXIF, Exchangeable Image File Format; FWHM, Full Width at Half Maximum; GCP, Ground Control Point; GIS, Geographical Information System; GNSS, Global Navigation Satellite System; GPS, Global Positioning System; GRE, green (spectral region); kNN, k-Nearest Neighbor; LDCM, Landsat Data Continuity Mission; lidar, Light Detection and Ranging; MSAVI, Modified Soil Adjusted Vegetation Index; NDVI, Normalized Difference Vegetation Index; NDWI, Normalized Difference Water Index; NIR, near-infrared (spectral region); RED, red (spectral region); REF, reference; REG, red edge (spectral region); ROI, Region Of Interest; RS, remote sensing; SAVI, Soil Adjusted Vegetation Index; TA, Training Area; TIN, Triangulated Irregular Network; TRA, Transit Area; UAS, Unmanned Aerial System; UAV, Unmanned Aerial Vehicle; VNIR, visible and near-infrared (spectral region); VA, Validation Area.

* Corresponding author.
E-mail addresses: JoanCristian.Padro@uab.cat (J.-C. Padró), V.Carabassa@creaf.uab.cat (V. Carabassa), Jaume.Balague@ctfc.cat (J. Balagué), Lluis.Brotons@ctfc.cat (L. Brotons), JoseMaria.Alcaniz@uab.cat (J.M. Alcañiz), Xavier.Pons@uab.cat (X. Pons).

https://doi.org/10.1016/j.scitotenv.2018.12.156

Drone
Unmanned Aerial System
UAS
UAV remote sensing
Multispectral imagery

stages. We used a small (<2 kg) drone equipped with a multispectral sensor, along with field spectroradiometer measurements that were used to radiometrically correct the UAS sensor data. Imagery was processed with photogrammetric and Remote Sensing and Geographical Information Systems software, resulting in spectral information, vegetation and soil indices, structural information and land cover maps. Spectral data and land cover classification, which were validated through ground-truth plots, aided in the detection and quantification of mine waste dumping, bare soil and other land cover extension. Moreover, plant formations and vegetation development were evaluated, allowing a quantitative, but at the same time visual and intuitive comparison with the surrounding reference systems. The protocol resulting from this research constitutes a pipeline solution intended for the implementation by public administrations and privates companies for precisely evaluating restoration dynamics in an expedient manner at a very affordable budget. Furthermore, the proposed solution prevents subjective interpretations by providing objective data, which integrate new technologies at the service of scientists, environmental managers and decision makers.

1. Introduction

Severe ecosystem changes are the result of opencast mining activities, which affect the soil, vegetation, fauna, hydrology and landforms (Drake et al., 2010). The restoration of degraded soils and human-disrupted landscapes involves a large number of priorities (Ockendon et al., 2018). Among them, post-mining restoration represents the specific challenge of creating ecological structures that become integrated into the surrounding environment, which starts from "point zero" (Hüttl and Weber, 2001). Mine wastes and rocky debris are common initial substrate conditions, being necessary artificially replacing soil (i.e. technosol) and introducing local vegetation by means of planting, sowing and encroaching the surrounding vegetation to drive the restoration process to pre-mining landscape conditions (Korjus et al., 2014). Ecological engineering scientists assume that after intensive opencast mining, the final soil conditions are usually extremely degraded thus leading the restoration process to either fail or simply not begin (Bradshaw, 1997). Consequently, the task of monitoring reclaimed areas becomes a fundamental feature in any restoration process, as it provides crucial information to environmental managers for those involved in assessing the success of adopted techniques (DITR, 2016). The objective of a restoration is to achieve a self-sustainable ecosystem at the overall affected landscape (Elmqvist et al., 2003). Restoration of opencast mines is regulated in most developed countries, and expected to be also in the remaining ones. For instance, in the European Union we can find different levels of legislation, the European (Directive 2006/21/EC), member states (e.g. Spanish RD975/2009, German Bundesberggesetz 1980) and regional governments (e.g. Catalan Law 12/1981), all of which require monitoring and periodically inspection of mine restorations. Moreover, extractive companies are required to provide a financial guarantee for environmental liabilities, which are blocked by the administration to assure that the companies comply with the regulations ensuring the proper restoration of the mined areas. Altogether, not only public administrations are interested in upholding legal measures for land restoration, also private companies want to recover the financial provision.

Environmental characterization, mapping and monitoring (Thenkabail, 2015) is one of the first and most productive applications of remote sensing (RS). The scientific use of environmental remote sensing data has been evolving since the 1970s, when the first Landsat satellite was put into orbit. The Landsat Data Continuity Mission (LDCM) (NASA, 2018), which has been the standard-bearer of Earth resources and environmental monitoring from space, uses sensors in the solar [0.450 μm to 2.500 μm] and thermal [8 μm to 13 μm] regions of the electromagnetic spectrum. The recent Sentinel-2 mission (ESA, 2015), which is represented by the Sentinel-2A and B platforms, is improving the spatial, spectral and temporal resolution of the free available satellite acquisitions. The joint synergy of those Earth observation programs is currently coordinated in the Global Earth Observation System of Systems (GEOSS). However, the Sentinel-2 spatial resolution (up to 10 m) is not detailed enough to monitor slight land cover changes in relatively small areas of interest, such as some opencast mine restorations, despite some studies have been done combining Landsat imagery and in-situ monitoring (e.g. Bonifazi et al., 2003). Alternatively, a much more detailed spatial and spectral resolution can be reached with airborne optical sensors, such as the Airborne Hyperspectral Scanner, which features 80 bands from visible to thermal regions, or the Compact Airborne Spectrographic Imager 1500, which features 288 bands between 0.35 μm and 1050 μm, allowing sub-metric pixels at a standard flight height of 3000 m above ground level (AGL). Light Detection and Ranging (lidar) sensors can be effectively used to reconstruct the vegetation structure (Listopad et al., 2015) and classify land cover surfaces in combination with optical imagery, but the cost of taking off a plane with this expensive payload solely for the purpose of monitoring a mine restoration is ultimately not cost-effective. Moreover, satellite and airborne optical imagery is often constrained by cloud cover conditions. On the other hand, such conditions do not pose a problem for lidar or optical sensors onboard Unmanned Aerial Systems (UAS or drones) when flying below the cloud cover thanks to their high sensitivity even when only diffuse irradiance exists. It is important to note that in such conditions, reflectance is much more Lambertian than under direct sunlight, and incoming diffuse irradiance can be measured in-situ at the time of the drone flight. A radiometric analysis of multispectral photogrammetric imagery acquired in different illumination conditions can be found in Markelin (2013). Then, the use of well-known remote sensing satellite and aerial techniques, which can be adapted to the imagery provided by multispectral optical sensors onboard low-weight drones (Sanders, 2017), can considerably facilitate the task of covering an area dimensioned to the platform, in that a much higher spatial resolution can be obtained with a low-cost revisit time and is not constricted to cloud cover. With all these advantages, such a solution can prove more suitable for the operative goal of acquiring RS data in monitoring mine exploitations and their restoration.

Although the regulation of <25 kg UAS may vary in each country, in most of them there are no major restrictions on their use in non-urban areas, such as in opencast mine undergoing restorations; nevertheless they comply with the regulations on flight height limitation and observing the security distance to airports, as recommended by the International Civil Aviation Organization (ICAO, 2011). Regulations aside, the proliferation of low-cost and low-weight UAS as data acquisition tools is rapidly promoting the transference of knowledge from the research sphere to the productive economy, and vice versa. Many studies make use of multispectral optical sensors onboard low-weight (<25 kg) drones and apply remote sensing techniques for wide-ranging applications, such as the 3D reconstruction of cultural heritage sites (Eisenbeiss and Zhang, 2006), identifying and evaluating climate-related diseases (Yoo et al., 2017), precision agriculture (Díaz-Varela et al., 2015), topography (Lucieer et al., 2014) or wildfire severity (Pla et al., 2017). Altogether these studies focus intensely on space and time due to the nature of the UAS platforms (fixed-wing or rotary-wing), which can

acquire images with ultra-high spatial resolution, usually from 1 cm to 10 cm depending on the flight height and the sensor instantaneous field of view. The extraction activities sector is also very interested in UAS remote sensing applications. When dealing with opencast mining cases, we find that extractive companies are interested in 3D quantification of mineral resource volumes (Xu et al., 2015) or the geomorphic characterization (Chen et al., 2015), while the environmental community is mainly focused on monitoring water and soil pollution (Capolupo et al., 2015). To the best known of the authors, there are no applications of UAS imagery specifically designed for the "standardized" monitoring of opencast mine restorations, a legal issue pointed out in much of the environmental legislations and that involves public administrations, companies, technicians and wastes time and economic resources (Minerals Council of Australia, 2015). The interaction of these actors is susceptible to involve subjective appreciations of a given restoration, so we propose a workflow for acquiring highly detailed imagery to produce thematic maps and complement on-field evaluation with objective cartographical evidences.

The current geometric theoretical basis of UAS remote sensing finds its roots in digital photogrammetry and computer vision background (Hartley and Zisserman, 2003; Granshaw and Fraser, 2015). Generally, multiple overlapped photograms are acquired and a bundle block adjustment is performed using aero-triangulation techniques. Homologous points between adjacent photograms are automatically detected by using computer vision techniques, which are further used as tie points to fit the whole model, by forming a mosaic of the photograms and reconstructing the surface with the stereo photogrammetric information. There are two georeferencing methods mostly used in UAS imagery: direct georeferencing and indirect georeferencing. Direct georeferencing is based on integrated navigation systems, which uses Global Navigation Satellite Systems (GNSS), e.g. GPS receiver as well as Inertial Measurement Unit (IMU) information to locate the camera perspective center and estimate its orientation parameters at the acquisition time (Skaloud et al., 2014; Rehak and Skaloud, 2017). In fact, the quality and accuracy of the onboard GNSS and IMU are key factors for proper direct georeferencing. In contrast, indirect georeferencing of UAS imagery is based on Ground Control Points (GCP), scene locations with well-known coordinates (Rumpler et al., 2014). GCP are commonly measured with static post-processed GNSS methods and surrounded with a chessboard target that is visible in the UAS imagery. Comparatively, indirect georeferencing is more time-consuming than direct georeferencing, and the accuracy depends on the correct measurement of GCP positions, the technician's skill in locating the references in the imagery, and the number of GCPs, reaching pixel size accuracies (Turner et al., 2014). A recent comparison of four UAS georeferencing methods for environmental monitoring purposes can be found in Padró et al. (2019).

The radiometric theoretical basis of optical multispectral remote sensing in the visible and near infrared regions (VNIR), i.e. between 400 nm and 900 nm, is attained by measuring the spectral surface reflectance (ρ_λ) in order to be comparable when imagery is acquired on different dates and/or by different sensors. Imagery is converted to ρ_λ at pixel level; ρ_λ is computed as the amount of spectral radiance (L_λ) ($W \cdot m^{-2} \cdot sr^{-1} \cdot \mu m^{-1}$) reflected by a surface located in a given pixel with respect to the total spectral irradiance (I_λ) ($W \cdot m^{-2} \cdot \mu m^{-1}$) received (Schaepmann-Strub et al., 2006). Satellite imagery is radiometrically corrected according to one of the different existing approaches (Kaufman and Sendra, 1988; Chavez, 1988; Pons et al., 2014; Vermote et al., 2016, as examples), and can be validated by using field spectroradiometric measurements as ground-truth (Padró et al., 2017). Moreover, as the incoming irradiance is difficult to approximate by modeling, it can be estimated empirically (Abdollahnejad et al., 2018), and as the UAS sensor is usually located in a very low AGL altitude (<120 m) the radiative transfer modeling has to be adapted or even substituted by other approaches (Aasen et al., 2015). A common approach for obtaining surface reflectance values from drone data (Honkavaara et al., 2012; Iqbal et al., 2018) is the numerical fitting (usually an empirical line through reference targets) of UAS-acquired radiometry and field spectroscopy data. Additionally, there are consumer grade cameras with a Downwelling Light Sensor (DLS) that measures the total incoming irradiance at-sensor level, which stores this information in the EXIF file of each photogram and obtaining direct information to calculate at-sensor reflectance. Nevertheless, as Hakala et al. (2018) point out, the challenge in this method is that the upwards looking sensor has to be horizontally stabilized, which is typically not the case when using low-cost instruments.

The main objective of this research is to provide a new tool using UAS that generates detailed, objective, exhaustive and rigorous cartography of opencast mine restorations. Introducing of UAS for acquiring imagery as a source to obtain data and produce digital maps is expected to improve the diligence and objectiveness of inspections, and as such could reduce disagreements between public administrations and private companies. As a secondary goal, this research focuses on how, besides the intrinsic interest in the detailed imagery for visual inspections, UAS imagery can provide quantitative spatial information about restoration failures or success in terms of monitoring the area covered by vegetation, mine waste dumping or bare soil at different restoration stages.

2. Materials

2.1. Study area and restoration stages

The implementation for monitoring mine restorations using UAS was carried out in Catalonia, Spain, where 483 mine exploitations were documented in 2018 (GENCAT, 2018). We have developed the presented workflow on an active calcareous sandstone quarry located in central Catalonia (lat. 41° 41′ 35″N lon. 1° 49′ 43″E), with representative landforms corresponding to different stages of restoration, namely from old restorations carried out >20 years ago to recent plantations. By accessing the historic orthophotographs of 1957, 1984, 2000 and 2016 (ICGC, 2018a, 2018b), we can report that the land use of this area before the mining activity was dominated by vineyards (1957), which were abandoned and spontaneously forested by the encroachment of autochthonous species (1984). This is a good example of the transition forest theory (Mather and Needle, 1998) in Mediterranean environments (Padró and Badia, 2017; Poyatos et al., 2003). In this area, mining began in the mid-1980's, and hit its activity peak on the 2000's decade. The restoration stages considered were, from the present to the past, T_0 (0–5 years), T_1 (5–10 years), T_2 (10–15 years) and T_3 (15–20 years); additionally, a non-disturbed area was taken as reference (REF), and a Transit Area (TRA) was masked to avoid a bias in the quantification (Fig. 1).

The material extracted was calcareous sandstone, exploited trough 10 m × 10 m banks. Bank-berm was the common landform model, resulting in steeped slopes. After a partial landform adaptation using mining debris, the surface was covered by new topsoil. The topsoil was a technosol, which was constructed using mine spoils and mineral sludge from the tailing process and was mixed with a small amount of previous topsoil stored for a long time. Organic amendments were added in order to increase soil fertility. Specifically, anaerobically digested sewage sludge was incorporated in a dose around 50 Mg/ha in order to increase soil organic matter, P and N contents, and improve soil aggregation. Revegetation measures consisted of sowing a mixture of herbaceous seeds (mainly grasses and leguminous) and planting local shrubs (mainly *Rosmarinus officinalis*) and trees (mainly *Pinus halepensis*), at a mean density of about 400 seedlings ha^{-1}. Vegetation in restored areas presented different grades of development according to the age of sowing and planting activities, which range from adult trees and dense shrub cover in T_3, to a dominant herbaceous cover in T_0. The reference system (REF, undisturbed area) is a *Pinus halepensis* forest, with a dense shrub layer and a low herbaceous cover.

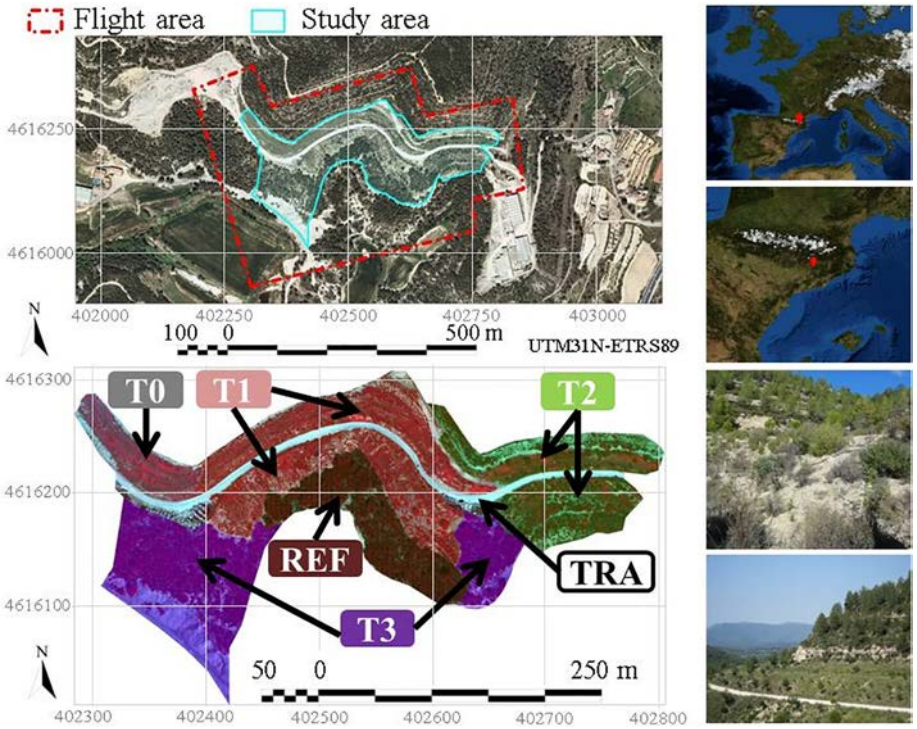

Fig. 1. Top left: Flight planned area and study area over the official local agency orthophotomap (ICGC, 2018a, 2018b). Bottom left: Restoration stages T_0 (0–5 years), T_1 (5–10 years), T_2 (10–15 years) and T_3 (15–20 years); non-altered area taken as reference (REF); Transit Area (TRA) masked to avoid bias in the quantification. Top right: Location maps. Bottom right: Restoration landscape.

The total dimension of the study area measured at 64,386 m^2, which comprised of T_0 4364 m^2, T_1 12,627 m^2, T_2 16,638 m^2, T_3 18,561 m^2, REF 8206 m^2 and TRA 3990 m^2. The planned flight (cf. Table S1 in the Supplementary materials) covered an additional area to assure the complete overlapping and preventing geometric distortions of the marginal photograms of the block. Previous flights were performed in mining activities to define a suitable flight altitude (90 m AGL) that balances the need for covering a typical opencast area and using a high spatial resolution product (<10 cm). These recommendations are in accordance with other experiences made in land cover classification of UAS imagery at different spatial resolutions (Ahmed et al., 2017).

It is worth noting that the season and the hour of the UAS data acquisition are crucial parameters to consider. After testing our method in all four seasons and at different hours of the day, we suggest that for acquiring imagery, in spring and summer are the best periods due to the leaf presence of deciduous vegetation, and during the hours of solar afternoon due to the high sun position, what minimizes shadows.

2.2. UAS sensor and platform

The optical sensor used on this study was a Parrot Sequoia (cf. Table S2 in the Supplementary materials), which is a multispectral sensor light enough to be embedded in <2 kg maximum take-off weight platforms. This sensor has four spectral bands (green (GRE), red (RED), red-edge (REG) and near infrared (NIR)), which are specifically disposed to improve the detection of vegetation and its features. The relative spectral response function (RSRF) is not provided by the manufacturer, and we assumed the Full Width Half Maximum (FWHM) provided in the specification sheet, by guessing the shape of the RSRF; other sensors providing detailed RSRF allow a more detailed integration (e.g. Padró et al., 2018). A detailed analysis of the Parrot Sequoia can be found in Fernández-Guisuraga et al. (2018). The Parrot Sequoia includes a DLS located at the top of the UAS, which registers the Sun total spectral irradiance at-sensor level and thus facilitates the automatic determination of the at-sensor reflectance. The performance of the DLS of the Parrot Sequoia was tested with in-situ reference targets, and finally at-sensor reflectance was numerically fitted to surface reflectance spectroradiometric measurements. The platform used was a DJI Phantom III Advanced (DJI, 2018) quadcopter (cf. Table S3 in the Supplementary materials) due to its compatibility with Android and iOS systems, fitness to the proposed procedures, low-cost, easy manageability, reduced dimensions, and capacity of embedding the multispectral sensor that we used therein. The default optical sensor was substituted by the Parrot Sequoia, which was mounted on the gimbal (Fig. 2).

2.3. Field spectroradiometer

The in-situ ground-truth reflectance was measured with an OceanOptics USB2000+ portable field spectroradiometer (OceanOptics, 2006) (Table S4 in the Supplementary materials). USB2000+ widely covers the VNIR spectral range of the multispectral UAS sensor commonly used. The physical magnitude measured with the spectroradiometer is the spectral surface reflectance ($\rho\lambda$), as explained in Pons et al. (2015) and Meroni and Colombo (2009). In order to account for the variability of measurements, 100 readings were obtained for each measurement and the overall data was statistically analyzed (mean, median, standard deviation, etc.) to evaluate its coherence, whereby we synthesized 1 nm of spectral resolution signature of every given surface.

We used a set of 24 matt Ethylene-Vinyl Acetate (EVA) rubber (foam) artificial targets of different colors (violet, blue, sky blue, green, yellow, orange, pink, red, brown, grey and black) in order to have several spectral reflectance references. A lower number of targets can be used for an empirical line correction (e.g. using two, the targets should be dark and bright). When more than two targets are used, they should properly cover the reflectance range, but avoiding reflectance spectra intersections; if it is the case, a large number of spectra is recommended to be used (Richter and Schläpfer, 2016), and thus, we used a large number of targets. The EVA foam material presented a highly Lambertian behavior and was useful in different campaigns. We worked with two

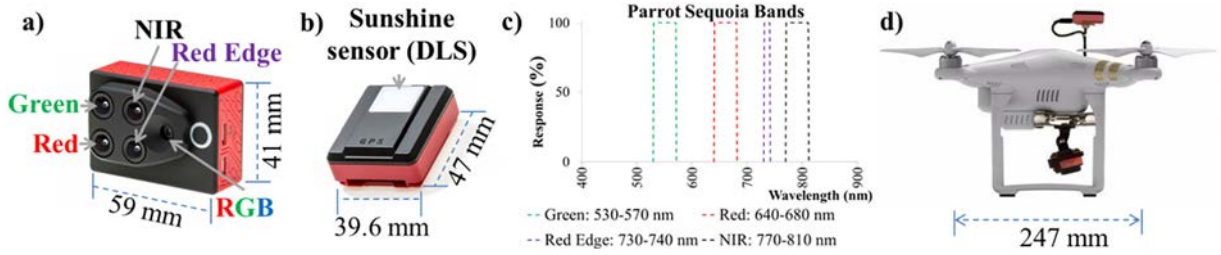

Fig. 2. UAS materials: (a) Parrot Sequoia multispectral sensor (b) Downwelling Light Sensor (DLS) (c) Nominal FWHM bandwidth (d) DJI Phantom III platform with the optical sensor equipment.

sizes of artificial targets, a group of 14 units of 50 cm × 50 cm × 2 cm (namely "EVA" in Fig. 3) and a group of 10 units of 40 cm × 60 cm × 0.2 cm (namely "foam" in Fig. 3). Those targets were big enough to be clearly seen in the UAS images (9 cm pixel size) with an equivalent surface of 30.9 pixels and 5.5 pixels × 5.5 pixels around the central pixel in the squared targets, and with an equivalent surface of 29.6 pixels and 4.4 pixels × 6.7 pixels in the rectangular targets. This always allowed one "pure" pixel (surrounded by 5 × 5 pixels) at the center in the squared targets, and, consequently, they were the preferred ones to relate the drone sensor values and the in-situ (spectroradiometer) values through fitting and testing. Rectangular targets were only used to complement the measurements since their pixels were not so symmetrically distributed around the central pixel.

Seven EVA targets were located in a shadow to experiment with diffuse irradiation conditions and support the de-shadowing process, while the remaining 17 targets were located under direct sunlight. To this end, the spectral signature of each target was integrated at the FWHM provided by the Parrot Sequoia manufacturer (Fig. 3).

3. Methods

3.1. Use of the photogrammetric software

We used Agisoft PhotoScan v.1.4.1 (Agisoft, 2018) photogrammetric software, which is widely used in current UAS projects (Kraaijenbrink et al., 2016). The software workflow initially locates the individual frames with the geotagged photocenters provided by the navigation GNSS, then uses automatic tie points to estimate more accurately the external coordinates (X,Y,Z) for every frame, and the orientation angles (ω,φ,κ). The Parrot Sequoia is a frame multilens sensor that generates four non-registered raw images in DN values, but the photogrammetric software uses the internal geometric information stored in the EXIF file of each image to register the multiple bands (Jhan et al., 2017). The orientation process was optimized by filtering out erroneous points and using GCPs that were obtained from the official reference points of this mining activity reported in the respective exploitation labor plan cartography, which were used for indirectly georeferencing the bundle block. The validation of the geometric accuracy was achieved using the cross-validation method and complying with the planimetry and altimetry standards of the American Society for Photogrammetry and Remote Sensing (ASPRS) for digital orthoimagery (ASPRS, 2014) (cf. Table S5 in the Supplementary materials). This process generated the bundle block adjustment with aero-triangulation, the individual images mosaicking and the photogrammetric construction of a dense point cloud with X, Y and Z coordinates. The 3D point cloud allowed the generation of a Triangulated Irregular Network (TIN), which was further rasterized in a Digital Surface Model (DSM), and finally outputting a georeferenced orthophotomosaic. Points classified as terrain were used to generate a Digital Elevation Model (DEM) and derive contour lines. DLS irradiance information stored in EXIF files was used to radiometrically correct each photogram, so as to obtain at-sensor reflectance values. The photogrammetric software output was composed by the orthophotomap, the DEM and the DSM, the elevation contour lines from the DEM, and the dense point cloud of each model.

3.2. Use of the RS&GIS software

We used MiraMon (Pons, 2016) RS&GIS software to radiometrically correct the at-sensor drone imagery, to generate the derived spectral and structural variables, to perform the digital classification to obtain land cover maps, and to integrate drone imagery with official mapping agencies cartography.

Shadow reduction is the first issue to be solved, processing separately those pixels irradiated with diffuse radiance (shadowed pixels)

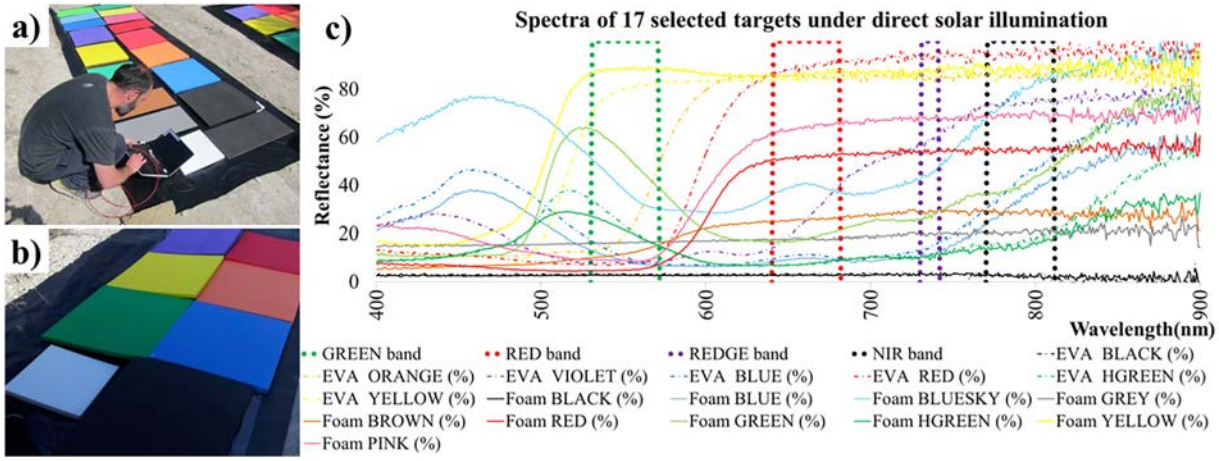

Fig. 3. Field spectroradiometric materials: (a) Field spectroradiometric measurements on targets (b) testing shadow effects (c) spectral signatures of targets, overlapped to Sequoia sensor bandwidth. The "foam" and the "EVA" panels differed in the size and, as seen in the spectral signature, in the color. (For interpretation of the references to color in this figure legend, the reader is referred to the web version of this article.)

from those pixels also illuminated by direct Sun irradiance (non-shadowed pixels) to recover information from as much shadowed pixels as possible (Movia et al., 2016). In our approach, the detailed shadow detection was obtained combining empirical and physical methods (Adeline et al., 2013). In order to limit the possible histogram commissions within the geometrically candidate pixels, the joint conditions for selecting shadowed pixels was: i) under the histogram threshold of the first quartile in the intensity image, in the REG band and in the NIR band; ii) under the shadow of the Digital Cast Shadow Model (DCSM) or Digital Illumination Model (DIM) [self-shadows]. Once masked, the reduction was achieved with the invariant color model method (Adeline et al., 2013) taking advantage of radiometric values taken in pairs of targets located in shadowed and non-shadowed conditions simultaneously. Non-shadowed pixels and de-shadowed pixels were tagged and, finally, a 5 pixels × 5 pixels mean filter was applied in the boundary belt of de-shadowed areas to smooth the transition (cf. Fig. S7 in Supplementary materials). Afterwards, at-sensor drone data obtained with DLS was radiometrically corrected by applying the empirical line technique supported in field spectroscopy measurements, so as to improve the fitting to target references and correcting possible biases.

When radiometrically corrected, imagery was used for calculating spectral variables to statistically discriminate land covers at pixel resolution. A large quantity of spectral indices using VNIR information are related in the specialized literature, which focused on detecting vegetation (Xue and Su, 2017) and soil (Viscarra Rossel et al., 2016) features. In order to distinguish and quantify the area occupied by mine spoil outcrops from replaced topsoil (technosol) and the considered vegetation strata (grassland, shrubland and tree cover), multiple referenced indices were tested according to the availability of UAS sensor bands. Calculating the correlation matrix between all the tested indices and the spectral bands showed that indices with less redundant information included:

i) Soil Adjusted Vegetation Index (SAVI) (Huete, 1988) [1] and Modified Soil Adjusted Vegetation Index 2 (MSAVI2) (Richardson and Weigand, 1977) [2], which minimize the effects of the soil background in the vegetation detection, and is widely used in soil erosion, drought and desertification analyses

[1] $SAVI = (NIR - RED)\ 1.5 / (NIR + RED + 0.5)$

[2] $MSAVI2 = 0.5\ [2\ NIR + 1 - \sqrt{((2\ NIR + 1)^2 - 8\ (NIR - RED))}]$

ii) Normalized Difference Water Index 1 (NDWI1) (McFeeters, 1996) [3] which was designed to delimit water bodies. However, in the study area context, it enhances the detection of vegetation and soil moisture

[3] $NDWI1 = (GRE - NIR) / (GRE + NIR)$

iii) Normalized Difference Vegetation Index (NDVI) (Rouse et al., 1974) [4], which is the most used index to discriminate vegetation and monitor its evolution in multi-temporal analysis

[4] $NDVI = (NIR - RED) / (NIR + RED)$.

Soil and vegetation structural features were important inputs to describe the categories we aimed to map. Thus Digital Terrain Models (DTM) provided information that was not in the spectral bands and indices. Note that DTM are digital models that represent any variable, a DEM is a DTM where the variable is the terrain elevation, and a DSM is a DTM where the variable is the surface elevation (including vegetation, buildings, etc.). To this end, the DSM was the base for calculating the DIM and the DCSM used in the shadow reduction process, while the DEM was the base to calculate the Digital Slope Model and the Digital Aspect Model used in the terrain morphology characterization and is capable of describing water runoff flows. A very valuable product is the height difference between the DSM and the DEM, which result in providing structural information ranging from the bare soil (~0 m of difference) up to the tree formations (>2 m of difference).

3.3. Classification methods and accuracy evaluation

The automatic land cover classification was carried out using k-Nearest Neighbor (kNN) classification algorithm (Cover and Hart, 1967) implemented as a parallelized 64-bit version in the MiraMon software. kNN is particularly robust when different spectral responses are associated to a unique informational class (Vidal-Macua et al., 2017).

Ground-truth plots with a known land cover played a key role at this step. Delimited areas were digitized over the orthophotomap, whereby and half of them were used to train the classifiers (Training Areas, TA) and the other half was set aside to validate the thematic accuracy (Validation Areas, VA) (Fig. 4).

Six land cover categories in the legend of thematic areas were considered:

Mine wastes: Outcrops of bare mineral substrates, very poor in organic matter (<0.5%), and without vegetation, formerly not restored soil (mine spoils dump). This category is well characterized spectrally in the restored area with a <1% standard deviation in in-situ measurements (Fig. 5).

Topsoil: Bare soil with any organic matter content (>0.5%) but without vegetation, replaced former soil coming from restoration activities (technosol). This category was well characterized spectrally in the restored area although a 2% standard deviation is observed throughout the measurements (Fig. 5).

Tree cover: Tree plant formations, typically forested zones of the latest stages in restored areas. Not only spectral features characterized this category, but structural information was used to consider that all vegetation pixels with a height AGL over 2 m corresponded to trees.

Shrublands: Plant formations of up to 2 m AGL, mainly bushes corresponding to medium successional stages. Several species and formations were included in this category, which also featured a wide spectral signature variety (Fig. 5).

Grasslands: Herbaceous plant formations with heights of up to 1 m, mainly consisting of grasses and forbs species that correspond to early successional stages in restored areas. Several grassland formations were included in this category, which featured a wide spectral signature variety (Fig. 5).

Remaining shadows: Shadows not corrected in the shadow reduction process can be considered as missing data. This category is scene-dependent (terrain morphology, solar zenith angle (θ) and solar azimuth angle (ϕ)).

4. Results

UAS-acquired spectral information in green, red, red-edge and near-infrared wavelength regions resulted in generating orthophotomaps of 9 cm pixel size that clearly showed mine wastes, topsoil, and vegetation structures. Locations that were inaccessible to technicians could also be observed and registered. A systematic multispectral measurement was done over the entire area of interest, complementing the traditional transecting operations.

Radiometric correction resulted in a good fitting to ground-truth radiometric measurements. Although the coefficient of determination between field data and at-sensor (Sequoia) reflectance data was over 0.9 in all bands, bias and gain were not good enough for highly accurate

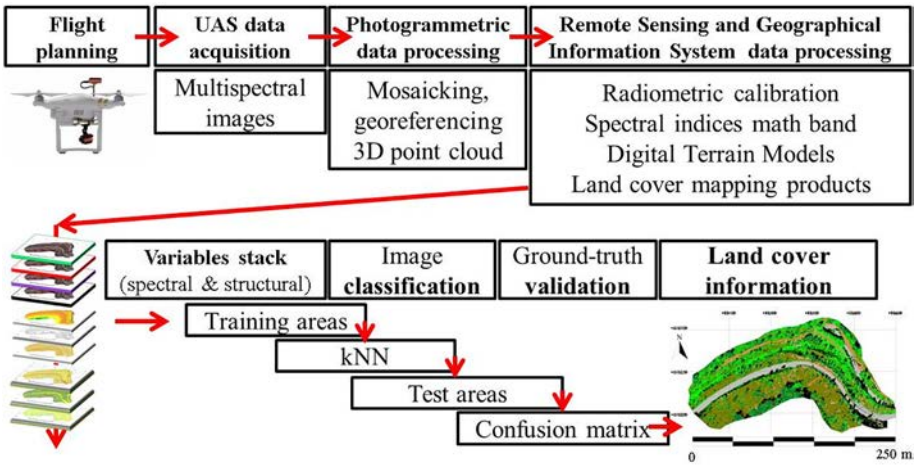

Fig. 4. General workflow for land cover mapping from UAS data using the kNN classifier.

applications. Establishing synergy between the conventional field spectroscopy measurements and novel UAS sensors, we finally applied the empirical line correction to at-sensor (DLS) reflectance values to fit the image data to in-situ observed values in the seven targets located in direct irradiance illumination conditions. However, we previously tested the accuracy of the results by performing the empirical line with three spectrally representative targets, including dark and bright ones, and evaluating the results with the remaining four. The obtained bias and gain clearly provided a better fitting to ground truth than fitting using the at-sensor Sequoia reflectance data. Once this was clarified, and given that the bias and gain values obtained using three or seven references provided similar model results, we finally applied the empirical line correction using all targets (seven) in order to minimize any error and obtain the more robust model. On the other hand, shadow reduction facilitated the process of classifying previously shadowed pixels, although the method was not perfect and some undetected shadows remained (Fig. 6).

Spectral information was combined to generate additional information and detect vegetation and soil properties (i.e. vegetation activity (NDVI), moisture content (NDWI1)). By visualizing false color combinations of drone images it was intuitive to find the presence of vegetation due to the high response of active vegetation in the NIR band. By mapping spectral indices, we could focus on the spatial distribution of the vegetation presence and activity (NDVI), the moisture content (NDWI1) and the soil effects on vegetated areas (SAVI and MSAVI2), which altogether facilitated in the process of quantifying vegetated areas and non-vegetated areas at 9 cm × 9 cm pixels (Fig. 7).

Additionally, structural information about the terrain morphology was constructed from the DEM and allowed simple topographic products as contour line vector maps, which, in combination with official topographic maps could complement the terrain morphology monitoring. Combining the information on sun position and the DSM, important landscape and ecological information was retrieved, as the vegetation projected shadows and sun illumination rates. Moreover, the differential map between the DSM and the DEM provided relevant information about the relative heights of structures, and thus, the vegetation height AGL. Firstly, in the classification step, the layer of the differential map between DSM and DEM (in combination with the spectral information layers) was used to statistically contribute to distinguishing high vegetation from low vegetation; in this respect it is important to note that a pixel with a spectral response different to vegetation can have a relative height but is note classified as vegetation. Secondly, in the interpretation of the results step, those pixels classified as vegetation can be crossed with the differential map between DSM and DEM to determine the vegetation height (Fig. 8).

Finally, selected digital information was used to generate a stack of nine statistical variables (spectral and structural) to characterize each land cover. Four variables represented the spectral bands of the Parrot Sequoia (GRE, RED, REG and NIR radiometrically corrected), three variables represented the vegetation indices (SAVI, NDWI1 and NDVI), one variable represented the intensity part of the color space transformation and the remaining variable represented the AGL difference between the DSM and the DEM.

A total of 60,402 pixels were used as Training Areas for the digital classification process, which were selected by photointerpretation on delimited plots visible in the drone image. The combination of training data, statistical remote sensing variables and the kNN classification method, produced a land cover map where the categories of interest

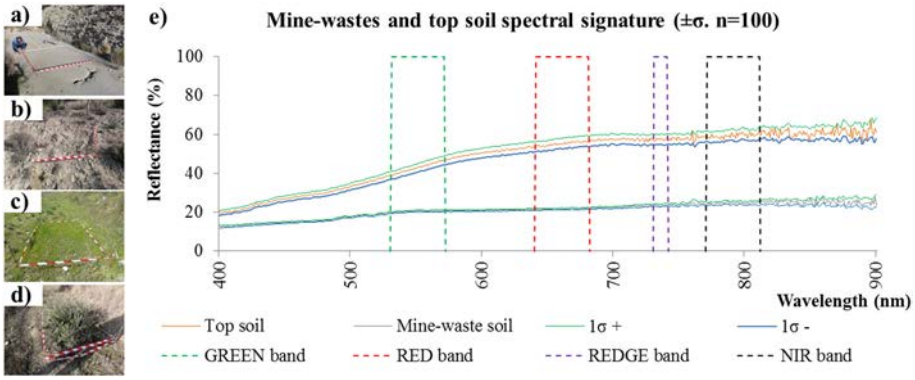

Fig. 5. Ground-truth data: Field plots of (a) mine-wastes soil (b) replaced topsoil (c) grasslands (d) shrublands (e) mine wastes and topsoil spectral signatures.

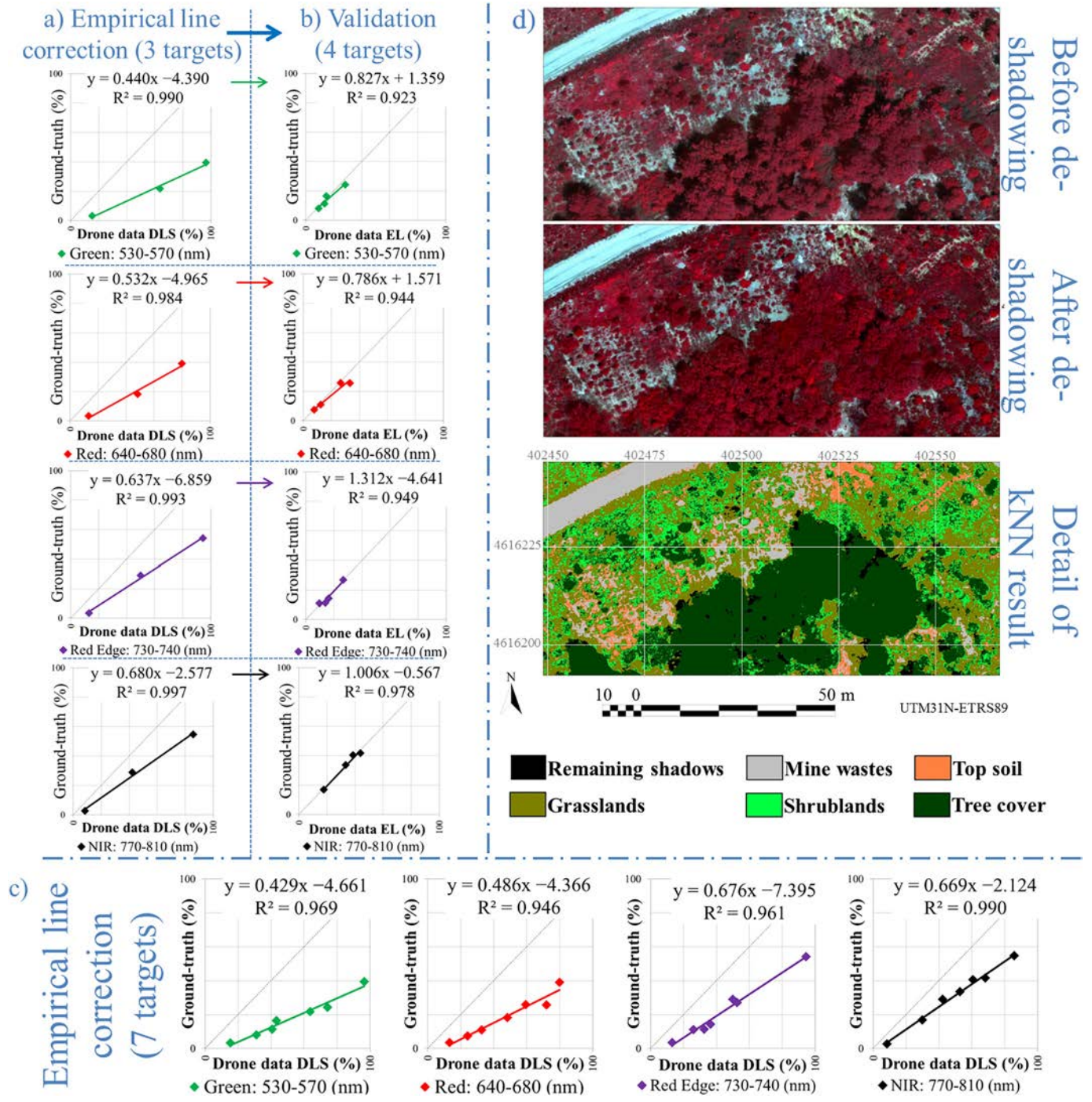

Fig. 6. Radiometric correction of drone data. (a) Regression resulting from the empirical line radiometric correction using three reference targets. (b) Validation, using four independent targets, of the empirical line correction performed from (a) results. (c) Regression resulting from the empirical line correction using seven targets (regression finally used for the empirical line correction). (d) Detail of the shadow reduction result in imagery and land cover classification (cf. Fig. S7 in Supplementary materials for more details).

were identified, and therefore individually monitored. A total of 11,872 pixels were used as test areas to evaluate the thematic accuracy. The overall accuracy was 94.71% and the kappa index was 0.92. The confusion matrix showed a good accuracy when splitting mine wastes and topsoil (>97%), tree cover was mapped with good results (>96%), and most of the confusion was found between grass and shrub vegetation, due principally to the intrinsic structural and spectral diversity of these categories (cf. Table S6 in the Supplementary materials).

The thematic land cover mapping was principally useful for quantifying diverse plant covered area and its spatial distribution trend, which was carried out by considering all the restoration stages together or at each individual stage scale (Table 1).

The land cover area occupied in each restoration zone was monitored not only in absolute units, but also comparing relative changes in the internal distribution of each stage. The analysis of the internal variation of land covers distribution was found as one of the most interesting results of the provided information. The study area presented different restoration stages and in all of them, the spatial particularities were mapped, which constitute a valuable product for environmental managers (Fig. 9).

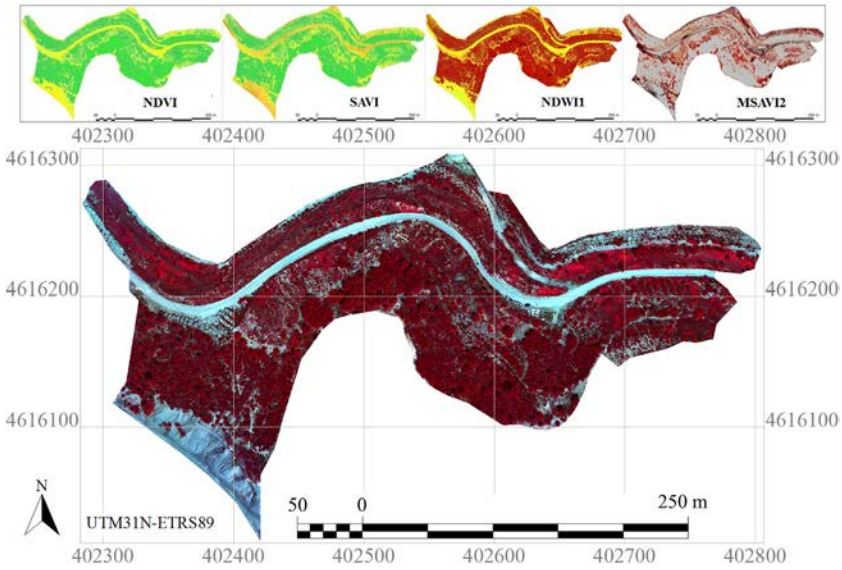

Fig. 7. Spectral information from UAS data: Top: Vegetation indices calculated with the RS&GIS software. Bottom: False color orthophoto generated from near-infrared, red and green bands. (For interpretation of the references to color in this figure legend, the reader is referred to the web version of this article.)

The mapping products obtained were fully integrated into the actual official cartography, which locally improves both the spatial resolution and the temporal resolution. Therefore, the visual inspection of restoration processes is greatly improved, as it provides crucial information in the event that a regularly updated official orthoimagery would not be feasible. If previous cartography is available, UAS products are useful in detecting anomalies in the restoration process, and thus make it possible to focus on zones where vegetation development remains low (Fig. 10).

5. Discussion

This medium-sizes opencast mine restoration (<10 ha) was easily covered by a low-weight rotary-wing UAS. Fast multispectral information acquired from the UAS sensor is particularly interesting due to the spatial resolution (9 cm) and coverage (64,386 m^2), which makes it possible to provide a very detailed visual inspection of the entire restored area, thus making it a highly valuable tool for controlling and monitoring restored mining areas. In addition to scientific interest, introducing UAS into the periodic inspections of mine restorations could be considered as an objective and effective solution for reducing disagreements between public administration and private companies, and at the same time, contributing to monitoring the sustainable development of extractive mining activities.

Validation issues regarding radiometric corrections were solved in synergy with in-situ spectroradiometric measurements, using inexpensive reference panels. In this study we used a large number of targets to test different spectral responses and for validation purposes. Nevertheless, a lower number of radiometric references can be used for this application (Richter and Schläpfer, 2016). Indeed, the empirical line regression using seven targets and using three targets is very similar (Fig. 6), but in this study we used seven references to perform a more robust regression. The use of the Parrot Sequoia DLS did not provide satisfactory reflectance values, as demonstrated in the regressions between image data and field spectroscopy data (Fig. 6). The coefficient of determination was good ($R^2 > 0.9$ in all bands) but the bias was higher

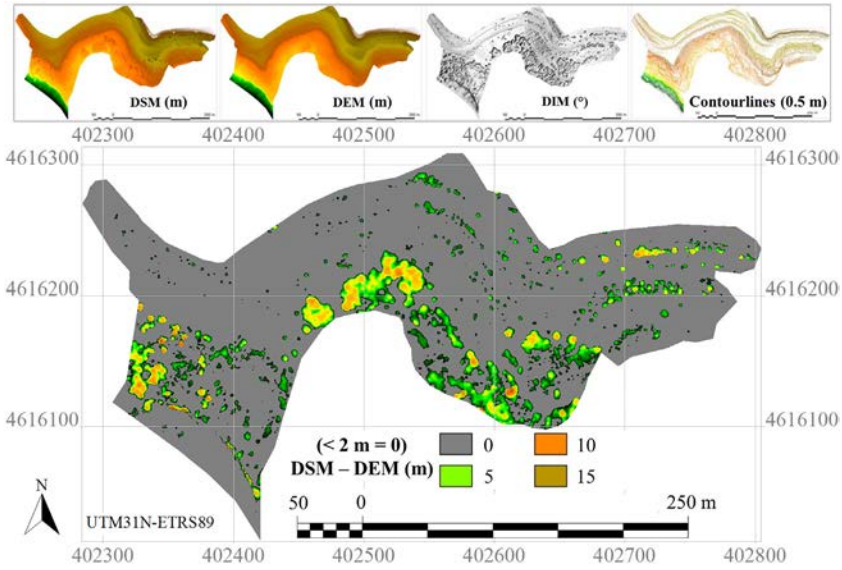

Fig. 8. Structural information from UAS data: Top: Digital Terrain Models accounting for vegetation, soil elevation, sun illumination and topographic contour line product. Bottom: Differential height between Digital Surface Model and Digital Elevation Model, representing vegetation height of over 2 m.

Table 1
Land cover area (m^2) mapped by soil and vegetation typologies and restoration stages. Abbreviations: T_0 = 0–5 years, T_1 = 5–10 years, T_2 = 10–15 years, T_3 = 15–20 years, REF = Reference area, TRA = Transit Area, ROI = Region Of Interest.

Surface cover/stage	T_0	T_1	T_2	T_3	REF	TRA	Total
Mine wastes	829	2536	4426	3608	233	3601	15,233
Topsoil	28	240	241	603	130	51	1293
Tree cover	862	4700	6470	4932	5480	42	22,485
Shrubland	833	1895	2363	2977	1273	28	9370
Grassland	1802	3206	2962	6387	1039	265	15,661
Remaining shadows	10	51	175	54	51	4	345
Total ROI	4364	12,627	16,638	18,561	8206	3990	64,386

than 4% in visible bands and reached 7% in the red-edge band. These biases have been corrected using the empirical line correction by fitting the image to the reflectance of reference targets (Padró et al., 2018). Nevertheless, previous works that used more accurate DLS instruments have demonstrated that the use of upwards looking irradiance sensors is a good system for converting images to at-sensor reflectance (Hakala et al., 2018; Markelin et al., 2018), but the challenge in the aforementioned method is ensuring that the upwards looking sensor are consistently horizontally leveled. Shadow reduction allowed the recovering of information from pixels that would be lost in the land cover mapping, although a relatively few number of pixels remained classified as shadows due to conservative masking decisions, as pointed out in previous studies (Movia et al., 2016; Adeline et al., 2013).

Band calculation using near infrared and visible information facilitates the quantification of vegetation activity in intensity maps, which point out areas with high vegetation development and areas with vegetation cover deficits. Using photogrammetric DSM and DEM provided the essential basis creating derived terrain models that contributed in obtaining valuable information by computing the sun illumination received in every pixel, the detailed terrain slope, or the vegetation height. It is worthy noting that spatial resolution of 9 cm is a fine systematic landscape sampling, which is enough to establish vegetation height classes reflecting the dynamics of the vegetation cover from the initial phases to the more advanced stages of the restoration. Airborne lidar data could typically offer spatial resolutions and samplings below 1 m, and rarely below 10 cm at low-cost. However, lidar sensors are currently being tested in combination with UAS platforms that could allow ultra-high spatial sampling. Perhaps in the future, the presented protocol could be complemented with lidar sensors. However, for many, the high expense of using and maintaining lidar sensors can prove ultimately non-cost effective (Manfreda et al., 2018). As a more viable alternative, photogrammetric solutions, such as those presented in this paper, offer more than reasonable answers to opencast mine restoration monitoring. Although the use of low-cost UAS imagery for monitoring purposes is plenty operative in developed countries, we point to developing countries, where often there are higher economically constrains. In this land cover degradation and restoration study, we found a solution that can effectively contribute towards integrating scientific methods and technologies, while working towards economically robust transitions in environmental management in accordance with the Sustainable Development Goals (United Nations, 2018).

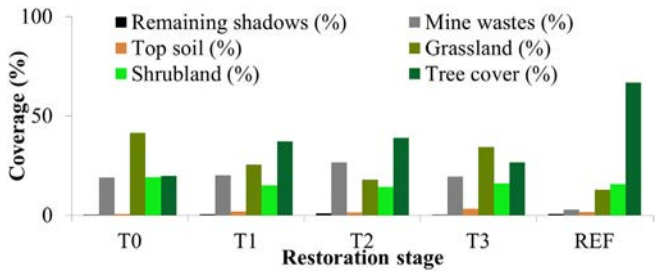

Fig. 9. Land cover relative distribution within each restoration stage.

The categorical treatment of land surfaces led to the quantification of the area covered by the different soil and vegetation types: not only within the overall restoration range, but also specifically within the different restoration stages. Detecting and distinguishing topsoil and mine waste cover was carried out and yielded good results. This is important when considering that topsoil and mine waste cover pose real concerns for identifying and interpreting restoration failures and risks (Espigares et al., 2011). Indeed, on the one hand, bare soil cover could be an indicator of sowings and planting failures, and/or of poor soil quality, which increase the risk of erosion (Van der Knijff et al., 2000; Espigares et al., 2011). On the other hand, mine waste dumping or mine waste used as soil substitute without a proper organic and/or mineral amendment, heavily limits vegetation establishment and encroachment, supposing an unacceptable situation in mine restoration (Ram et al., 2006; Jordán et al., 2008). Therefore, an expedient and precise quantification of these types of land cover is a useful tool for estimating erosion risks or soil quality limitations. Regarding monitoring vegetation and soil at stages, grasslands were the dominant cover in T_0 but some areas covered by mine wastes were still detected. Therefore, corrective measures are still imperative for improving vegetation encroachment (Jordán et al., 2008). In the restored areas from five and ten years ago (T_1) tree cover was relatively dominant in the landscape despite the same proportion of mine waste cover was detected. Restored areas from 10 and 15 years ago (T_2) occupied the most extensive tree cover area of the four restoration scenarios considered, but also mine waste outcrops were the second land cover in this stage, which could be attributed to failing restoration processes in problematic areas (steeped slopes, slope > 90%). The late stage restoration scenario (T_3), in which restoration measures were carried out >15 years ago, showed a land cover distribution far away from the reference landscape (REF) and the more recent stage considered, and thus demonstrating the need of revising the classical methodologies used for the restoration in this area. A plausible explanation of this result can be attributed to less exigent need for restoration regulations 20 years ago, whereby the usual practice at the time was the direct afforestation over the mine wastes with Aleppo pine (*P. halepensis*), without soil replacement, or over a very unfertile substrate.

A fixed-wing platform could be more suitable for much more extensive restorations and perhaps further improvements could be achieved using multispectral sensors with more bands (e.g. MicaSense RedEdge) or hyperspectral sensors with narrower bands to enhance the spectral information. Regarding image geometry, low-cost single-frequency GPS receivers do not allow direct georeferencing. As such, geometric accuracy relies on the accuracy of delimitation stacks used as GCPs, which mining companies are required to maintain by law, as well as the technician's skill to locate them in the imagery. A heavier multicopter typically offers more stability, while a fixed-wing platform typically offers much more autonomy and coverage, and a double-frequency carrier-phase GNSS provides much more direct georeferencing accuracy, and a lidar sensor could provide structural information (Listopad et al., 2015), but this material is much more expensive. Ultimately, our goal was to design a protocol that is low-cost and capable of offering acceptable results. The material is useful in different campaigns and costs altogether under 6000 €, which included the platform, the UAS sensor, the field spectroradiometer and the radiometric reference targets.

6. Conclusions

Monitoring opencast mining restoration with UAS imagery has been proven operational and useful, as it provides expedient and accurate spatial and thematic information. Resulting products can systematically and recurrently sample the restoration area of interest at sub-decimeter pixel size, which improves airborne imagery spatial resolution and allows monitoring in inaccessible, restricted or dangerous areas. In addition to the intrinsic

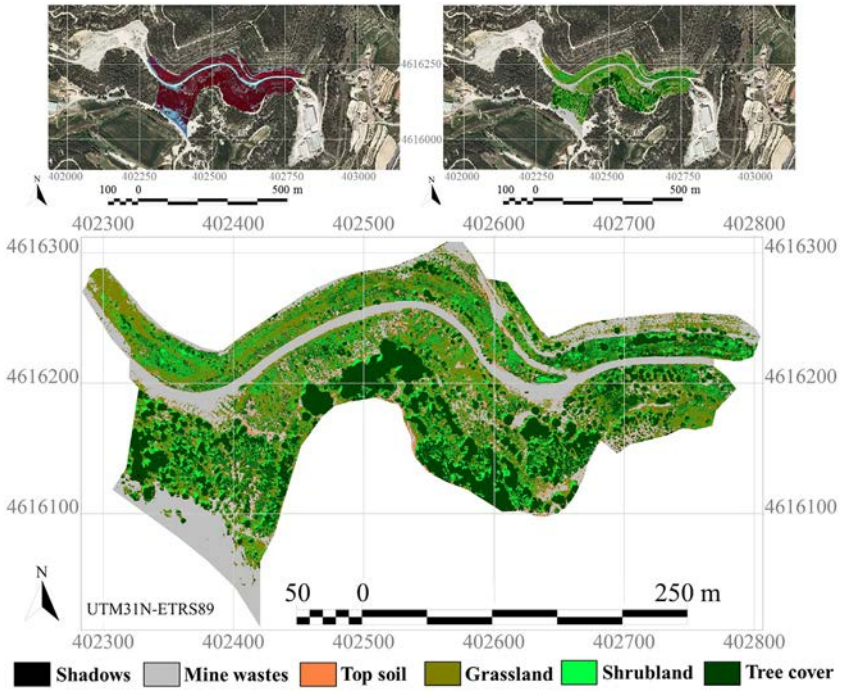

Fig. 10. Top: False color orthophotomap and land cover classification result integrated with official cartography. Bottom: Land cover classification of the study area.

interest of the imagery for visual inspections, photogrammetric and RS&GIS software treatment provided additional spatial information about vegetation development and restoration failure or success, plant cover and height, mine waste dumping, bare soil cover, and geomorphic terrain features.

With the relatively low-cost material used in this study i.e. low-weight platform, multispectral sensor, low-cost radiometric reference panels and field spectroradiometer, it is possible to generate rigorous cartographical documentation as orthophotomaps, Digital Elevation Models, Digital Surface Models, vegetation indices and thematic land cover maps fully integrated to previous cartography and official databases. The inclusion of new unmanned aerial technologies gives us a glimpse of new horizons for monitoring restoration with inexpensive materials and intensive samplings.

Not only did automatic land cover mapping allow us to dispense with the manual photointerpretation, it also provided accuracies of over 94%, although individual focusing on problematic areas could also be improved manually, if needed. The overall workflow was highly automatized with batch processes. Nevertheless, it is convenient for the specialized technician to verify the correct execution and help in important decisions, such as digitizing of the training and testing areas. Moreover, compared to what would have been carried out in a conventional inspection of the restored areas, the fieldwork time in our case study was reduced considerably, which altogether included geometric stacks maintenance, field spectroradiometric measurements, and UAS flight. To summarize, the time used for obtaining ground-truth data and the UAS flight, 2 h is sufficient for inspecting a restored area of 10 ha, while data processing can be fully done by one person in two working days. It is worth noting that while UAS can help and support the monitoring of restoration activities, it should not by any means replace in-situ inspections or technician supervision.

In addition to the interest of monitoring older restorations with an unprecedented detail, current UAS remote sensing products will certainly become a valuable precedent for future opencast mine monitoring studies all around the world, as it provides improved time-series information. Considering the potential, the obtained results and the objective information produced, the proposed protocol can be a suitable tool for administrations, mining and consulting companies as well as for environmental scientists.

Acknowledgments

This work was supported by the European Union as part of the ECOPOTENTIAL Project (H2020 641762-2 EC), by an Innovation grant from the Spanish Ministry of Science and Innovation (ACAPI, CGL2015-69888-P (MINECO/FEDER-ERDF, EU)), and by the Catalan Government (Department of Territory and Sustainability) under the project "Research and innovation in the monitoring and process of extractive activities restoration". GRUMETS Research Group is partially supported by the Catalan Government under Grant (SGR2017-1690). Joan-Cristian Padró is a recipient of the FI-DGR scholarship grant (2016B_00410). Xavier Pons is a recipient of the ICREA Academia Excellence in Research Grant (2016–2020).

Author contributions

C.P. and V.C. conceived and designed the experiments. J.B., V.C. and C.P., performed the field data experiments. C.P. and V.C. analyzed the data. C.P., V.C. and X.P. wrote the paper. L.B., J.A. and X.P. supervised the paper and the overall experiments.

Conflicts of interest

The authors declare that there are no conflicts of interest. The founding sponsors had no role in the design of the study; in the collection, analyses, or interpretation of data; in the writing of the manuscript, or in the decision to publish the results.

Appendix A. Supplementary data

Supplementary data to this article can be found online at https://doi.org/10.1016/j.scitotenv.2018.12.156.

References

Aasen, H., Burkart, A., Bolten, A., Bareth, G., 2015. Generating 3D hyperspectral information with lightweight UAV snapshot cameras for vegetation monitoring: from camera calibration to quality assurance. ISPRS J. Photogramm. Remote Sens. 108, 245–259. https://doi.org/10.1016/j.isprsjprs.2015.08.002.

Abdollahnejad, A., Panagiotidis, D., Surový, P., Ulbrichová, I., 2018. UAV capability to detect and interpret solar radiation as a potential replacement method to hemispherical photography. J. Remote Sens. 10 (3), 423–440. https://doi.org/10.3390/rs10030423.

Adeline, K.R.M., Chen, M., Briottet, X., Pang, S.K., Paparoditis, N., 2013. Shadow detection in very high spatial resolution aerial images: a comparative study. ISPRS J. Photogramm. Remote Sens. 80, 21–38. https://doi.org/10.1016/j.isprsjprs.2013.02.003.

Agisoft LLC, 2018. PhotoScan user manual, professional edition, version 1.4. http://www.agisoft.com/pdf/photoscan-pro_1_4_en.pdf, Accessed date: 1 November 2018.

Ahmed, O.S., Shemrock, A., Chabot, D., Dillon, C., Williams, G., Wasson, R., Franklin, S.E., 2017. Hierarchical land cover and vegetation classification using multispectral data acquired from an unmanned aerial vehicle. Int. J. Remote Sens. 38, 2037–2052. https://doi.org/10.1080/01431161.2017.1294781.

ASPRS (American Society for Photogrammetry and Remote Sensing), 2014. ASPRS Positional Accuracy Standards for Digital Geospatial Data. Edition 1, version 1.0.0. URL:. http://www.asprs.org/a/society/divisions/pad/Accuracy/ASPRS_Positional_Accuracy_Standards_for_Digital_Geospatial_Data_Edition1_V1_FinalDraftForPublication.docx, Accessed date: 1 November 2018.

Bonifazi, G., Cutaia, L., Massacci, P., Roselli, I., 2003. Monitoring of abandoned quarries by remote sensing and in situ surveying. Ecol. Model. 170, 213–218. https://doi.org/10.1016/S0304-3800(03)00228-X.

Bradshaw, A., 1997. Restoration of mined lands - using natural processes. Ecol. Eng. 8, 255–269. https://doi.org/10.1016/S0925-8574(97)00022-0.

Capolupo, A., Pindozzi, S., Okello, C., Fiorentino, N., Boccia, L., 2015. Photogrammetry for environmental monitoring: the use of drones and hydrological models for detection of soil contaminated by copper. Sci. Total Environ. 514, 298–306. https://doi.org/10.1016/j.scitotenv.2015.01.109.

Chavez Jr., P.S., 1988. An improved dark-object subtraction technique for atmospheric scattering correction of multispectral data. Remote Sens. Environ. 24, 459–479. https://doi.org/10.1016/0034-4257(88)90019-3.

Chen, J., Li, K., Chang, K.-J., Sofia, G., Tarolli, P., 2015. Open-pit mining geomorphic feature characterization. Int. J. Appl. Earth Obs. Geoinf. 42, 76–86. https://doi.org/10.1016/j.jag.2015.05.001.

Cover, T., Hart, P., 1967. Nearest neighbor pattern classification. IEEE Trans. Inf. Theory 13 (1), 21–27. https://doi.org/10.1109/TIT.1967.1053964.

Díaz-Varela, R.A., De La Rosa, R., León, L., Zarco-Tejada, P.J., 2015. High-resolution airborne UAV imagery to assess olive tree crown parameters using 3D photo reconstruction: application in breeding trials. Remote Sens. 7 (4), 4213–4232. https://doi.org/10.3390/rs70404213.

DITR (Department of Industry, Tourism and Resources), 2016. Mine Rehabilitation. Australian Government 0-642-72481-4, p. 77 URL:. https://archive.industry.gov.au/resource/Documents/LPSDP/LPSDP-MineRehabilitationHandbook.pdf, Accessed date: 1 November 2018.

DJI, 2018. Phantom 3 Professional. URL. https://www.dji.com/es/phantom-3-pro/info, Accessed date: 1 November 2018.

Drake, J.A., Greene, R.S.B., Macdonald, B.C.T., Field, J.B., Pearson, G.L., 2010. A review of landscape rehabilitation in ecosystem engineering for mine closure. In: Fourie, A., Tibett, M., Wiertz, J., Perth, W.A. (Eds.), Proceedings of International Conference on Mine Closure. Australian Center for Geomechanics, pp. 241–249.

Eisenbeiss, H., Zhang, L., 2006. Comparison of DSMs generated from mini UAV imagery and terrestrial laser scanner in a cultural heritage application. ISPRS Commission V Symposium 'Image Engineering and Vision Metrology', IAPRS Volume XXXVI, Part 5, Dresden 25–27 Sep. 2006, pp. 90–96.

Elmqvist, T., Folke, C., Nystrom, M., Peterson, G., Bengtsson, J., Walker, B., Norberg, J., 2003. Response diversity, ecosystem change and resilience. Front. Ecol. Environ. 1, 488–494. https://doi.org/10.1890/1540-9295(2003)001[0488:RDECAR]2.0.CO;2.

ESA (European Space Agency), 2015. Sentinel-2A user handbook. Rev. 2. URL:. https://sentinels.copernicus.eu/web/sentinel/user-guides/document-library/-/asset_publisher/xlslt4309D5h/content/sentinel-2-user-handbook, Accessed date: 1 November 2018.

Espigares, T., Moreno-de las Heras, M., Nicolau, J.M., 2011. Performance of vegetation in reclaimed slopes affected by soil erosion. Restor. Ecol. 19, 35–44. https://doi.org/10.1111/j.1526-100X.2009.00546.x.

Fernández-Guisuraga, J.M., Sanz-Ablanedo, E., Suárez-Seoane, S., Calvo, L., 2018. Using unmanned aerial vehicles in postfire vegetation survey campaigns through large and heterogeneous areas: opportunities and challenges. Sensors 18 (2), 586. https://doi.org/10.3390/s18020586.

GENCAT (Generalitat de Catalunya), 2018. Orígens i evolució de la mineria (Origins and evolution of mining). . Available online:. http://www.gencat.cat/icaen/recorregutenergia/unitat14/bloc3_unitat14_pag13.html, Accessed date: 1 November 2018.

Granshaw, S.I., Fraser, C.S., 2015. Editorial: computer vision and photogrammetry: interaction or introspection? Photogramm. Rec. 30, 3–7. https://doi.org/10.1111/phor.12092.

Hakala, T., Markelin, L., Honkavaara, E., Scott, B., Theocharous, T., Nevalainen, O., Näsi, R., Suomalainen, J., Viljanen, N., Greenwell, C., Fox, N., 2018. Direct reflectance measurements from drones: sensor absolute radiometric calibration and system tests for forest reflectance characterization. Sensors 18, 1417. https://doi.org/10.3390/s18051417.

Hartley, R., Zisserman, A., 2003. Multiple View Geometry in Computer Vision. Cambridge University Press 0521540518.

Honkavaara, E., Kaivosoja, J., Mäkynen, J., Pellikka, I., Pesonen, L., Saari, H., Salo, H., Hakala, T., Marklelin, L., Rosnell, T., 2012. Hyperspectral reflectance signatures and point clouds for precision agriculture by light weight UAV imaging system. ISPRS Annals of Photogrammetry, Remote Sensing and Spatial Information Sciences vol. I-7, pp. 353–358. https://doi.org/10.5194/isprsannals-I-7-353-2012.

Huete, A.R., 1988. A soil-adjusted vegetation index (SAVI). Remote Sens. Environ. 25 (3), 259–309. https://doi.org/10.1016/0034-4257(88)90106-X.

Hüttl, R.F., Weber, E., 2001. Forest ecosystem development in post-mining landscapes: a case study of the Lusatian lignite district. Naturwissenschaften 88 (8), 322–329. https://doi.org/10.1007/s001140100241.

ICAO (International Civil Aviation Organization), 2011. "Unmanned Aircraft Systems (UAS)". CIR328 AN/190.

ICGC (Institut Cartogràfic i Geològic de Catalunya), 2018a. Full 274–99 de l'Ortofoto de Catalunya 1:2500 (OF–25C) (1:2500 Catalonia orthophoto Tile 274–99). . URL. http://www.icc.cat/vissir3/, Accessed date: 1 November 2018.

ICGC (Institut Cartogràfic i Geològic de Catalunya), 2018b. VISSIR, Visor de avançat de geoinformació de Catalunya (VISSIR, Advanced geoinformation viewer of Catalonia). . URL. http://www.icc.cat/vissir3/, Accessed date: 1 November 2018.

Iqbal, F., Lucieer, A., Barry, K., 2018. Simplified radiometric calibration for UAS-mounted multispectral sensor. Eur. J. Remote Sens. 51 (1), 301–313. https://doi.org/10.1080/22797254.2018.1432293.

Jhan, J.P., Rau, J.Y., Haala, N., Cramer, M., 2017. Investigation of parallax issues for multi-lens multispectral camera band co-registration. Int. Arch. Photogramm. Remote. Sens. Spat. Inf. Sci. XLII-2/W6, 157–163. https://doi.org/10.5194/isprs-archives-XLII-2-W6-157-2017.

Jordán, M.M., Pina, S., García-Orenes, F., Almendro-Candel, M.B., García-Sánchez, E., 2008. Environmental risk evaluation of the use of mine spoils and treated sewage sludge in the ecological restoration of limestone quarries. Environ. Geol. 55, 453–462. https://doi.org/10.1007/s00254-007-0991-4.

Kaufman, Y.J., Sendra, C., 1988. Algorithm for automatic atmospheric corrections to visible and near-IR satellite imagery. Int. J. Remote Sens. 9, 1357–1381. https://doi.org/10.1080/01431168808954942.

Korjus, H., Laarmann, D., Sims, A., Paluots, T., Kangur, A., 2014. Assessment of novel forest ecosystems on post-mining restoration site in Aidu, Estonia. In: Polgár, A., Bazsó, T., Nagy, G., Gálos, B. (Eds.), Local and Regional Challenges of Climate Change Adaptation and Green Technologies. University of West Hungary Press, Sopron, pp. 35–44 https://doi.org/10.13140/2.1.4557.6640.

Kraaijenbrink, P., Meijer, S.W., Shea, J.M., Pellicciotti, F., De Jong, S.M., Immerzeel, W.W., 2016. Seasonal surface velocities of a Himalayan glacier derived by automated correlation of unmanned aerial vehicle imagery. Ann. Glaciol. 57 (71), 103–113. https://doi.org/10.3189/2016AoG71A072.

Listopad, C., Masters, R., Drake, J., Weishampel, J., Branquinho, C., 2015. Structural diversity indices based on airborne LiDAR as ecological indicators for managing highly dynamic landscapes. Ecol. Indic. 57, 268–279. https://doi.org/10.1016/j.ecolind.2015.04.017.

Lucieer, A., Turner, D., King, D.H., Robinson, S.A., 2014. Using an Unmanned Aerial Vehicle (UAV) to capture micro-topography of Antarctic moss beds. Int. J. Appl. Earth Obs. Geoinf. 27, 53–62. https://doi.org/10.1016/j.jag.2013.05.011.

Manfreda, S., McCabe, M., Miller, P., Lucas, R., Pajuelo Madrigal, V., Mallinis, G., Ben-Dor, E., Helman, D., Estes, L., Ciraolo, G., Müllerová, J., Tauro, F., de Lima, M.I., de Lima, J., Maltese, A., Francés, F., Caylor, K., Kohv, M., Perks, M., Tóth, B., 2018. On the use of Unmanned Aerial Systems for environmental monitoring. Remote Sens. 10, 641–669. https://doi.org/10.3390/rs10040641.

Markelin, L., 2013. Radiometric Calibration, Validation and Correction of Multispectral Photogrammetric Imagery. , pp. 1–86 URL:. https://aaltodoc.aalto.fi/bitstream/handle/123456789/10948/isbn9789517112956.pdf?sequence=1&isAllowed=y (Doctoral dissertation for the degree of Doctor of Science in Technology, Aalto University School of Engineering, Espoo, Finland, September 2013).

Markelin, L., Suomalainen, J., Hakala, T., Oliveira, R., Viljanen, N., Näsi, R., Scott, B., Theocharous, T., Greenwell, C., Fox, N., Honkavaara, E., 2018. Methodology for direct reflectance measurement from a drone: system description, radiometric calibration and latest results. ISPRS - International Archives of the Photogrammetry, Remote Sensing and Spatial Information Sciences vol. XLII-1, pp. 283–288. https://doi.org/10.5194/isprs-archives-XLII-1-283-2018.

Mather, A.S., Needle, C.L., 1998. The forest transition: a theoretical basis. Area 30, 117–124. https://doi.org/10.1111/j.1475-4762.1998.tb00055.x.

McFeeters, S.K., 1996. The use of the normalized difference water index (NDWI) in the delineation of open water features. Int. J. Remote Sens. 17, 1425–1432. https://doi.org/10.1080/01431169608948714.

Meroni, M., Colombo, R., 2009. 3S: a novel program for field spectroscopy. Comput. Geosci. 35, 1491–1496. https://doi.org/10.1016/j.cageo.2009.01.005 URL:. https://www.sciencedirect.com/science/article/pii/S0098300409000922, Accessed date: 1 November 2018.

Minerals Council of Australia, 2015. In: Minerals Council of Australia (Ed.), Mine Rehabilitation in the Australian Minerals Industry , p. 48 URL:. http://www.minerals.org.au/file_upload/files/reports/Mine_rehabilitation_in_the_Australian_minerals_industry_FINAL.pdf, Accessed date: 1 November 2018.

Movia, A., Beinat, A., Crosilla, F., 2016. Shadow detection and removal in RGB VHR images for land use unsupervised classification. ISPRS J. Photogramm. Remote Sens. 119, 485–495. https://doi.org/10.1016/j.isprsjprs.2016.05.004.

NASA (National Aeronautics and Space Administration), 2018. Landsat Science. URL:. https://landsat.gsfc.nasa.gov/about/history/, Accessed date: 1 November 2018.

OceanOptics, 2006. USB200+ Data Sheet. OceanOptics, Dunedin, FL, p. 38 URL:. https://oceanoptics.com/wp-content/uploads/OEM-Data-Sheet-USB2000-.pdf, Accessed date: 1 November 2018.

Ockendon, N., Thomas, D., Cortina, J., Adams, W., Aykroyd, T., Barov, B., Boitani, L., Bonn, A., Branquinho, C., Brombacher, M., Burrell, C., Carver, S., Crick, H., Duguy, B., Everett, S., Fokkens, B., Fuller, R.J., Gibbons, D.W., Gokhelashvili, R., Sutherland, W., 2018. One hundred priority questions for landscape restoration in Europe. Biol. Conserv. 221. https://doi.org/10.1016/j.biocon.2018.03.002.

Padró, J.-C., Badia, A., 2017. L'incendi de 1998 a la Catalunya Central. Anàlisi dels canvis en les cobertes del sòl (1956-2009) a diferents escales, d'incendi i de finca (The wildfire of 1998 in Central Catalonia. Analysis of land cover changes (1956–2009) at different scales: at the level of fire and property). Treballs de la Societat Catalana de Geografia 83, 79–108. https://doi.org/10.2436/20.3002.01.125.

Padró, J.-C., Pons, X., Aragonés, D., Díaz-Delgado, R., García, D., Bustamante, J., Pesquer, Ll., Domingo-Marimon, C., González-Guerrero, O., Cristóbal, J., Doktor, D., Lange, M., 2017. Radiometric correction of simultaneously acquired Landsat-7/Landsat-8 and Sentinel-2A imagery using pseudoinvariant areas (PIA): contributing to the Landsat time series legacy. Remote Sens. 9 (12), 1319. https://doi.org/10.3390/rs9121319.

Padró, J.-C., Muñoz, F.-J., Avila, L.-A., Pesquer, L., Pons, X., 2018. Radiometric correction of Landsat-8 and Sentinel-2A scenes using drone imagery in synergy with field spectroradiometry. Remote Sens. 10 (11), 1687. https://doi.org/10.3390/rs10111687.

Padró, J.-C., Muñoz, F.-J., Planas, J., Pons, X., 2019. Comparison of four UAV georeferencing methods for environmental monitoring purposes focusing on the combined use with airborne and satellite remote sensing platforms. Int. J. Appl. Earth Obs. Geoinf. 75, 130–140. https://doi.org/10.1016/j.jag.2018.10.018.

Pla, M., Duarte, A., Brotons, L., 2017. Potencial de las imágenes UAV como datos de verdad terreno para la clasificación de la severidad de quema de imágenes Landsat: aproximaciones a un producto útil para la gestión post incendio (Potential of UAV images as ground-truth data for the burning severity classification of Landsat imagery: approximations to a useful product for post-fire management). Revista de teledetección 49, 91–102. https://doi.org/10.4995/raet.2017.7140.

Pons, X., 2016. MiraMon. Sistema d'Informació Geogràfica i software de Teledetecció. Versió 8.01b. Centre de Recerca Ecològica i Aplicacions Forestals, CREAF, Bellaterra 84-931323-4-9 URL:. http://www.creaf.uab.cat/miramon/, Accessed date: 1 November 2018.

Pons, X., Pesquer, L., Cristóbal, J., González-Guerrero, O., 2014. Automatic and improved radiometric correction of Landsat imagery using reference values from MODIS surface reflectance images. Int. J. Appl. Earth Obs. Geoinf. 33, 243–254. https://doi.org/10.1016/j.jag.2014.06.002.

Pons, X., Moré, G., Cea, C., Serra, P., Mira, M., González, O., Zabala, A., Pérez, F., Tardà, A., Alamús, R., Palà, P., Lopez, A., 2015. A protocol for optimum usage of handheld spectroradiometers in airborne and satellite applications: the Ocean Optics USB2000+ case. Proceedings of the 9th EARSeL SIG Imaging Spectroscopy Workshop, Luxembourg (Luxembourg) , pp. 126–127 URL:. https://www.upf.edu/documents/3254890/0/program_short.pdf/bc40e341-f2a5-4b87-a89c-c8a84fe6fb8b, Accessed date: 1 November 2018.

Poyatos, R., Latron, J., Llorens, P., 2003. Land use and land cover change after agricultural abandonment. Mt. Res. Dev. 23, 362–368. https://doi.org/10.1659/0276-4741(2003)023[0362:LUALCC]2.0.CO;2.

Ram, L.C., Srivasta, N.K., Tripathi, R.C., Jha, S.K., Sinha, A.K., Singh, G., Manoharan, V., 2006. Management of mine spoils for crop productivity with lignite fly ash and biological amendments. J. Environ. Manag. 79, 173–187. https://doi.org/10.1016/j.jenvman.2005.06.008.

Rehak, M., Skaloud, J., 2017. Time synchronization of consumer cameras on Micro Aerial Vehicles. ISPRS J. Photogramm. Remote Sens. 123, 114–123. https://doi.org/10.1016/j.isprsjprs.2016.11.009.

Richardson, A.J., Weigand, C.L., 1977. Distinguishing vegetation from soil background information. PE&RS 43, 1541–1552 URL:. https://www.asprs.org/wp-content/uploads/pers/1977journal/dec/1977_dec_1541-1552.pdf, Accessed date: 1 November 2018.

Richter, R., Schläpfer, D., 2016. Atmospheric/Topographic Correction for Satellite Imagery (ATCOR-2/3 User Guide, Version 9.0.2, March 2016). URL:. http://www.rese.ch/pdf/atcor3_manual.pdf, Accessed date: 1 November 2018.

Rouse Jr., J.W., Haas, R., Schell, J., Deering, D., 1974. Monitoring vegetation systems in the Great Plains with ERTS. Third ERTS Symposium. NASA Special Publication 351 , pp. 309–317 URL:. https://ntrs.nasa.gov/archive/nasa/casi.ntrs.nasa.gov/19740022614.pdf, Accessed date: 1 November 2018.

Rumpler, M., Daftry, S., Tscharf, A., Prettenthaler, R., Hoppe, C., Mayer, G., Bischof, H., 2014. Automated end-to-end workflow for precise and geo-accurate reconstructions using fiducial markers. ISPRS Technical Commission III Symposium, 5–7 September 2014, Zurich, Switzerland, pp. 135–142 https://doi.org/10.5194/isprsannals-II-3-135-2014.

Sanders, A., 2017. Mapping the distribution of understorey *Rhododendron ponticum* using low-tech multispectral UAV derived Imagery. In: Díaz-Delgado, R., Lucas, R., Hurford, C. (Eds.), The Roles of Remote Sensing in Nature Conservation. A Practical Guide and Case Studies. Springer International Publishing AG2017, Springer, Cham, Switzerland. ISBN: 978-3-319-64332-8, pp. 167–181.

Schaepmann-Strub, G., Schaepmann, M.E., Painterd, T.H., Dangelb, S., Martonchik, J.V., 2006. Reflectance quantities in optical remote sensing – definitions and case studies. Remote Sens. Environ. 103, 27–42. https://doi.org/10.1016/j.rse.2006.03.002.

Skaloud, J., Rehak, M., Lichti, D., 2014. Mapping with MAV: experimental study on the contribution of absolute and relative aerial position control. ISPRS - International Archives of the Photogrammetry, Remote Sensing and Spatial Information Sciences, Volume XL-3/W1, 2014. EuroCOW 2014, the European Calibration and Orientation Workshop, 12–14 Feb. 2014, Castelldefels, Spain https://doi.org/10.5194/isprsarchives-XL-3-W1-123-2014.

Thenkabail, P.S., 2015. Land Resources Monitoring, Modeling, and Mapping With Remote Sensing. CRC Press, Boca Raton, FL, USA 9781482217957.

Turner, D., Lucieer, A., Malenovský, Z., King, D.H., Robinson, S.H., 2014. Spatial co-registration of ultra-high resolution visible, multispectral and thermal images acquired with a micro-UAV over Antarctic moss beds. Remote Sens. 6, 4003–4024. https://doi.org/10.3390/rs6054003.

United Nations, 2018. Sustainable development goals. URL. https://www.un.org/sustainabledevelopment/sustainable-development-goals/, Accessed date: 1 November 2018.

Van der Knijff, J.M., Jones, R.J.A., Montanarella, L., 2000. Soil Erosion Risk Assessment in Europe. European Soil Bureau, Joint Research Center, Ispra (34 pp.).

Vermote, E., Justice, C., Claverie, M., Franch, B., 2016. Preliminary analysis of the performance of the Landsat8/OLI land surface reflectance product. Remote Sens. Environ. 185, 46–56. https://doi.org/10.1016/j.rse.2016.04.008.

Vidal-Macua, J.J., Zabala, A., Ninyerola, M., Pons, X., 2017. Developing spatially and thematically detailed backdated maps for land cover studies. Int. J. Digital Earth 10 (2), 175–206. https://doi.org/10.1080/17538947.2016.1213320.

Viscarra Rossel, R.A., Behrens, T., Ben-Dor, E., Brown, D.J., Demattê, J.A.M., Shepherd, K.D., Shi, Z., Stenberg, B., Stevens, A., Adamchuk, V., Aïchi, H., Barthès, B.G., Bartholomeus, H.M., Bayer, A.D., Bernoux, M., Böttcher, K., Brodský, L., Du, C.W., Chappell, A., Fouad, Y., Genot, V., Gomez, C., Grunwald, S., Gubler, A., Guerrero, C., Hedley, C.B., Knadel, M., Morrás, H.J.M., Nocita, M., Ramirez-Lopez, L., Roudier, P., Rufasto Campos, E.M., Sanborn, P., Sellitto, V.M., Sudduth, K.A., Rawlins, B.G., Walter, C., Winowiecki, L.A., Hong, S.Y., Ji, W., 2016. A global spectral library to characterize the world's soil. Earth Sci. Rev. 155, 198–230. https://doi.org/10.1016/j.earscirev.2016.01.012.

Xu, Z.-H., Wu, L.-X., Chen, S.-J., Wang, Z., 2015. Method of engineering volume monitoring and calculation for open-pit mine from UAV images. J. Northeast. Univ. Nat. Sci. 37 (1), 84–88. https://doi.org/10.3969/j.issn.1005-3026.2016.01.018.

Xue, J., Su, B., 2017. Significant remote sensing vegetation indices: a review of developments and applications. J. Sens., 1353691 https://doi.org/10.1155/2017/1353691 (17).

Yoo, H.-T., Lee, H., Chi, S., Hwang, B.-G., Kim, J., 2017. A preliminary study on disaster waste detection and volume estimation based on 3D spatial information. Comput. Civ. Eng., 428–435 https://doi.org/10.1061/9780784480823.051.

Appendix A: Supplementary materials

Table S1: Programmed flight plan features and scene highlights.

Date	27/04/2018
First photogram capture time (UTC)	¶10:36:33
Last photogram capture time (UTC)	10:46:23
Total area covered (m^2)	193400
Flight height Above Ground Level (m)	90
Number of photograms (x4 = bands)	623 (2492)
Planned mean spatial resolution (cm)	8.48
Resampled spatial resolution (cm)	9
Planned along-track overlapping (%)	90
Planned across-track overlapping (%)	85
Center of scene latitude (°)	N 41° 41' 31.29''
Center of scene longitude (°)	E 1° 49' 43.18''
Sun azimuth at central time of flight (°)	146.50
Sun elevation at central time of flight (°)	58.37

Table S2: Parrot Sequoia sensor main characteristics (excluding panchromatic band).

Manufacturer-Model	**Size (mm)**	**Weight (g)**	**Sunshine sensor size (mm)**	**Sunshine sensor weight (g)**
Parrot Sequoia	59 x 41 x 28	72	47 x 39.6 x 18.5	35
Sensor type	**Sensor size (pixels)**	**Pixel size (μm)**	**Focal Length (mm)**	**Field of View (°)**
CCD	1280 x 960	3.75 x 3.75	3.98	47.5
Raw radiometric resolution (bits) and expanded dynamic range (DN)	**#1 Green FWHM (nm)**	**#2 Red FWHM (nm)**	**#3 Red-edge FWHM (nm)**	**#4 NIR FWHM (nm)**
10 (0-65535)	530–570	640–680	730–740	770–810

Table S3: DJI Phantom III Advanced platform main characteristics.

Manufacturer-Model	**Diagonal size without propellers (mm)**	**Weight with battery and camera (g)**	**Max. Take-off Weight (g)**	**Max. speed (m/s)**
DJI Phantom III Advanced	350	1216	1300	16
Number of rotors	**GNSS**	**GNSS accuracy (m)**	**Battery weight (g)**	**Max. flight time (min)**
4	Single-frequency GPS/GLONASS	± 0.5 vertical ± 1.5 horizontal	365	23

Table S4: OceanOptics USB2000+ field spectroradiometer sensor main characteristics.

Manufacturer-Model	Size (mm)	Weight (g)	Design	Fiber optic diameter (μm)
OceanOptics USB2000+	89.1 x 63.3 x 34.4	190	Czerny-Turner	400
Sensor manufacturer and type	**Sensor size (pixels)**	**Grating #2 Spectral range (nm)**	**Input Focal Length (mm)**	**Fiber optic FOV (°)**
CCD Sony ILX511B	2048	340–1030	42	25
Raw radiometric resolution (bits) and expanded dynamic range (DN)	**Sampling interval (nm)**	**FWHM (nm)**	**Signal to Noise Ratio @ 50 ms**	**Minimum Integration time (ms)**
8 (0-65535)	0.3	1.26	250:1	1

Table S5: Horizontal and Vertical (Non Vegetated Areas) Accuracy Standards for Geospatial Data used to evaluate the geometric accuracy (ASPRS, 2014).

RMSEr (radial) Combined XY	Horizontal Accuracy 95 % Confidence X, Y	Horizontal Accuracy at 95 % Confidence radial	Vertical Accuracy 95 % Confidence Z (NVA)
≤ 1.4142 * *RMSE*	≤ 2.4477 * *RMSE*	≤ 1.7308 * $RMSE_r$	≤ 1.9600 * *RMSE*
GSD (cm)	**Map scale**	**RMSEX or Y (cm)**	**RMSEr (cm)**
2.5 to 5.0	1:200	5.0	7.1
3.8 to 7.5	1:300	7.6	10.6
6.3 to12.5	1:500	12.5	17.7

Table S6: Confusion matrix of the kNN classification using ground truth plots (units = pixels).

	Remaining shadows	Mine wastes	Tree cover	Grassland	Shrubland	Top soil	TOTAL	Commis-sion error (%)	User's accuracy (%)
Remaining shadows	236	0	0	0	0	0	236	0	100
Mine wastes	0	1941	0	0	0	8	1949	0.41	99.59
Tree cover	0	0	6074	0	193	0	6267	3.08	96.92
Grassland	4	0	10	451	47	0	512	11.91	88.09
Shrubland	0	0	57	274	1021	0	1352	24.48	75.52
Top soil	0	35	0	0	0	1521	1556	2.25	97.75
TOTAL	240	1976	6141	725	1261	1529	11872		
Omission error (%)	1.67	1.77	1.09	37.79	19.03	0.52		Global accuracy = 94.71	
Producer's accuracy (%)	98.33	98.23	98.91	62.21	80.97	99.48		Kappa index = 0.92	

Figure S7: Workflow used in the shadow detection and shadow reduction process.

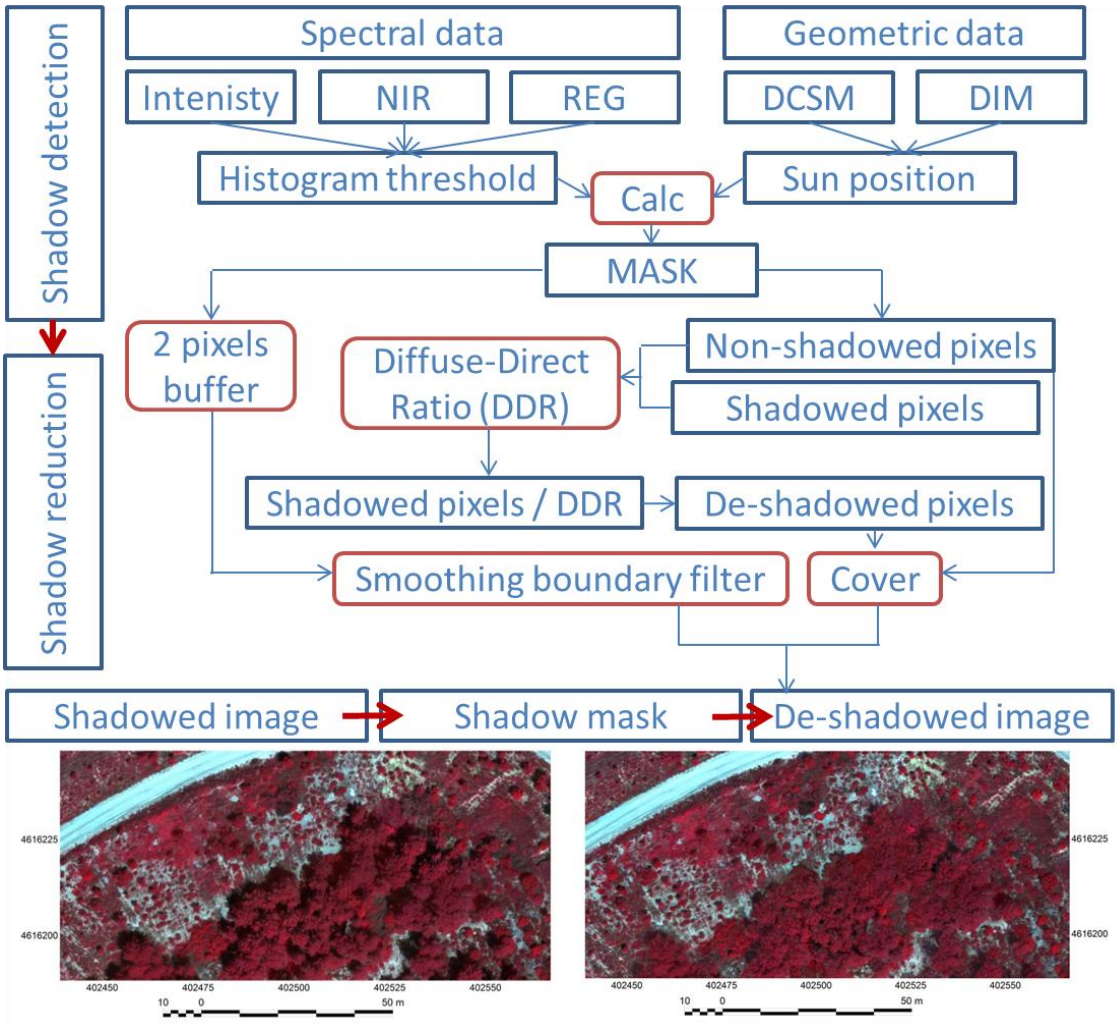

Capítol 3: Resum de resultats

3. Resum de resultats

El disseny experimental del capítol 2.1 ha permès analitzar l'ajust entre dades espectroradiomètriques de camp (aquí considerades com a veritat terreny) i els resultats del tractament radiomètric realitzat en imatges Landsat-7, Landast-8 i Sentinel-2A mitjançant mètodes de correcció radiomètrica contrastats (6S-LaSRC, 6S-LEDAPS, Sen2Cor-SNAP, ATCOR-3, SAC-QGIS, PIA-MiraMon). Les dades *in-situ* es van captar al pas dels satèl·lits, en quatre dates diferents, mostrejant un total de 26 píxels del Landsat en diferents tipus de cobertes com aigua, prat, matollar, dunes, sòl nu, herbassar o conreu de cereal. A part de l'avaluació, mitjançant dades *in-situ* (integrades amb la RSRF de l'ETM+, l'OLI i de l'MSI), de diferents mètodes de correccions radiomètriques realitzades a imatges Landsat i Sentinel, el fet de disposar d'imatges captades quasi-simultàniament amb dos sensors diferents ha permès analitzar la coherència dels mètodes de correcció radiomètrica assumint que els mètodes que ofereixen un ajust més gran són més idonis per la generació de sèries temporals d'imatges de teledetecció radiomètricament consistents.

L'ajust de la reflectància espectral banda a banda i data a data de cada mètode amb les dades *in-situ* s'ha avaluat calculant l'arrel de la mitjana del quadrat dels errors (RMSE), i ha mostrat, com era d'esperar, un bon ajust dels mètodes oficials per la seva respectiva plataforma, el 6S-LEDAPS per al Landat-7, el 6S-LaSRC per al Landsat-8 i el Sen2Cor-SNAP per al Sentinel-2.

No obstant, analitzant els resultats obtinguts en les plataformes Landsat, el mètode ATCOR-3 i el mètode PIA-MiraMon han superat els mètodes oficials de correcció d'imatges ETM+ i OLI (Taula 2), obtenint diferències mitjanes del 3.5 % (PIA-MiraMon), 3.9 % (ATCOR-3), 4.7 % (mètodes oficials), mentre que el mètode basat en la tècnica DOS ha obtingut el pitjor ajust amb un 5.9 % (SAC-QGIS).

Taula 2. Arrel de la mitjana del quadrat dels errors (RMSE) entre valors d'espectroradiometria de camp i valors de les correccions radiomètriques realitzades a imatges Landsat (ETM+ i OLI), agrupant totes les dates analitzades en el capítol 2.1 (% unitats de reflectància). Els millors ajustos s'han destacat en negreta.

***In-situ* vs. Landsat**	**Blau RMSE**	**Verd RMSE**	**Roig RMSE**	**IRp RMSE**	**IRoc1 RMSE**	**IRoc2 RMSE**	**Mitjana RMSE**
ATCOR3	2.392	2.956	3.588	**3.745**	4.764	6.019	3.911
SAC-QGIS	5.871	5.987	5.755	5.083	5.710	7.199	5.934
6S-LEDAPS i 6S-LaSRC	3.768	4.150	4.490	4.484	4.987	6.037	4.653
PIA-MM	**1.588**	**2.645**	**3.384**	3.948	**3.988**	**5.350**	**3.484**

En la comparació entre les dades de camp i les imatges Sentinel-2, s'ha constatat unes diferències mitjanes similars a les obtingues en les imatges Landsat. El mètode PIA-MiraMon ha obtingut l'RMSE més baix en quatre de les sis bandes analitzades, amb una diferència mitjana del 3.5 % i només és superat en les dues restants pel mètode oficial de correcció radiomètrica, amb una mitjana del 3.7 % (Sen2Cor-SNAP) (Taula 3).

Taula 3. Arrel de la mitjana del quadrat dels errors (RMSE) entre valors d'espectroradiometria de camp i valors de les correccions radiomètriques realitzades a imatges Sentinel-2 (MSI), agrupant totes les dates analitzades en el capítol 2.1 (% unitats de reflectància). Els millors ajustos s'han destacat en negreta.

***In-situ vs.* Sentinel-2**	**Blau RMSE**	**Verd RMSE**	**Roig RMSE**	**IRp RMSE**	**IRoc1 RMSE**	**IRoc2 RMSE**	**Mitjana RMSE**
ATCOR3	1.991	2.339	3.381	3.569	5.772	7.393	4.074
SAC-QGIS	4.262	7.217	5.068	5.129	6.621	7.736	6.006
Sen2Cor-SNAP	2.317	2.881	3.190	**3.519**	4.764	**5.352**	3.671
PIA-MM	**1.727**	**2.284**	**3.070**	3.973	**4.383**	5.370	**3.468**

La comparació de les dades procedents de diferents plataformes però captades quasi-simultàniament, i corregides radiomètricament amb el mateix mètode (excepte els productes oficials (6S-LEDAPS/6S-LaSRC i Sen2Cor-SNAP)), han mostrat el millor coeficient de determinació (R^2) per al mètode PIA-MiraMon a les bandes del visible, per SAC-QGIS a les bandes de l'infraroig d'ona curta, i per ATCOR3 a la banda de l'infraroig proper. Agrupant totes les bandes, el millor R^2 l'ha ofert el mètode PIA-MiraMon (0.964), seguit d'ATCOR3 (0.960), SAC-QGIS (0.955), i els productes oficials (0.929) (Taula 4).

Taula 4. Coeficient de determinació (R^2) entre les imatges Landsat (ETM+ o OLI) i Sentinel-2A (MSI) captades quasi-simultàniament, i corregides radiomètricament amb el mateix mètode (excepte en els mètodes oficials). La mostra correlacionada és la mateixa que píxels dels quals s'han fet mesures de camp. Els millors ajustos s'han destacat en negreta.

Sentinel-2A *vs.* Landsat	**Blau R^2**	**Verd R^2**	**Roig R^2**	**IRp R^2**	**IRoc1 R^2**	**IRoc2 R^2**	**Totes les bandes R^2**
ATCOR3	0.908	0.916	0.927	**0.986**	0.979	0.927	0.960
SAC-QGIS	0.298	0.799	0.928	0.981	**0.982**	**0.972**	0.955
Productes oficials (6S-LEDAPS i 6S-LaSRC *vs.* Sen2Cor-SNAP)	0.901	0.939	0.931	0.976	0.976	0.967	0.929
PIA-MM	**0.916**	**0.961**	**0.966**	0.972	0.975	0.970	**0.964**

El disseny experimental del capítol 2.2 ha permès analitzar l'ajust entre dades de posicionament *in-situ* (que es poden considerar com a veritat terreny) i els resultats de la georeferenciació d'imatges d'UAV a partir de mètodes de posicionament d'UAV àmpliament coneguts. Tres dels mètodes són de georeferenciació directa, que utilitzen les dades del sensor de posicionament de l'UAV (dades en brut del GNSS de bord (GNSSNAV), GNSS de fase portadora amb freqüència simple i post-processat cinemàtic sense suport terrestre *in-situ* (PPK1), GNSS de fase portadora amb freqüència doble i post-processat cinemàtic amb suport terrestre *in-situ* (PPK2)). El mètode de georeferenciació indirecta (GCP-ICP) utilitza de punts de control geomètric sobre el terreny (GCP) per realitzar l'ajust, però la validació es realitza mitjançant validació encreuada, és a dir, un dels punts s'exclou de l'ajust i és utilitzat com a punt de test independent (ICP), repetint aquest procés per tots els ICP disponibles i calculant l'RMSE amb els residuals. L'exactitud més elevada en la seva comparació amb les referències *in-situ* l'ha assolit el mètode GCP-ICP, seguit del mètode PPK2, el PPK1 i el GNSSNAV. No obstant, pel que fa al temps de processat i en l'aspecte operatiu, els mètodes de georeferenciació directa s'han mostrat més fàcils d'utilitzar que el mètode de georeferenciació indirecta (Taula 5).

Taula 5: Resum dels avantatge i inconvenients dels mètodes de georeferenciació avaluats.

	1) GNSSNAV	**2) PPK1**	**3) PPK2**	**4) GCP–ICP**
RMSEr (m)	1.062	0.256	0.036	0.023
RMSEz (m)	4.209	0.238	0.036	0.030
Inversió inicial aproximada (€)	50	600	8500	500
Temps dedicat (h)	≥1	≥24	≥24	≥48
Personal involucrat	≥1	≥1	≥2	≥2
Suport *in-situ*	NO	NO	SÍ	SÍ
Exemples de productes de teledetecció amb què es poden combinar les dades d'UAV posicionades amb aquest mètode	Imatges Sentinel-2, o de menor resolució espacial	Imatges WorldView, imatges aèries ICGC, dades lidar, o de menor resolució espacial	Imatges d'UAV multi o hiperespectrals, o de menor resolució espacial	Imatges d'UAV amb càmera rèflex, o de menor resolució espacial
Escala de més detall de la cartografia generada	1:12 000	1:1500	1:400	1:200

Abreviacions: GNSSNAV: dades en brut del GNSS de bord; PPK1: GPS de fase portadora amb freqüència simple i post-processat cinemàtic sense suport terrestre *in-situ*; PPK2: GPS de fase portadora amb freqüència doble i post-processat cinemàtic amb suport terrestre *in-situ*; GCP-ICP: punts de control geomètric sobre el terreny; RMSEr: Arrel de la mitjana del quadrat dels errors (RMSE) radial (combinat en X i Y); RMSEz: RMSE en altitud (Z); ICGC: Institut Cartogràfic i Geològic de Catalunya.

El disseny experimental del capítol 2.3 ha permès analitzar l'ajust entre dades espectroradiomètriques de camp sobre panells caracteritzats espectralment i imatges captades per un sensor multiespectral a bord d'un UAV. També ha permès analitzar l'ajust entre les dades de l'UAV i les dades dels satèl·lits Landast-8 i Sentinel-2A corregides amb diversos mètodes de correcció radiomètrica. Addicionalment, ha permès corregir imatges de satèl·lit utilitzant imatges d'UAV i comparar els resultats obtinguts en imatges del L8 i del S2. El lligam entre dades de camp i dades d'UAV ha permès considerar les dades d'UAV com a veritat terreny, ja que han estat corregides radiomètricament ajustant-les linealment a les dades *in-situ*. Així, aquestes dades d'UAV han servit per corregir les imatges de satèl·lit mitjançant el mètode de les referències radiomètriques (el nou mètode UAS-MiraMon).

Les dades d'UAV s'han captat al pas dels satèl·lits, fent un vol al moment de pas del Landsat-8 i un vol 20 minuts més tard al pas del Sentinel-2A. La possibilitat de fer dos mostrejos en tan poc temps ja és una millora respecte de l'espectroradiometria de camp convencional. Els dos vols, de 10 minuts de durada cadascun i programats amb el mateix pla fotogramètric, han obtingut l'àrea equivalent a 51 píxels de 30 m del Landsat-8, 143 píxels de 20 m del Sentinel-2 i 517 píxels de 10 m del Sentinel-2. L'ortomosaic generat amb imatges procedents d'UAV, de 6 cm de mida de píxel i georeferenciat mitjançant punts de control, ha tingut un error de posicionament menor a la mida de píxel i ha estat densificat a la mida de píxel del sensor satel·litari desitjat, esdevenint així una nova millora respecte de l'espectroradiometria de camp convencional. A més, el mostreig amb UAV ha inclòs tipologies de cobertes de difícil accés com capçades d'arbres, una bassa o una edificació, a part d'altres tipus de cobertes del sòl com conreus herbacis, matollars o herbassars.

Les imatges d'UAV adquirides al pas del L8 han mostrat un ajust excel·lent amb les mesures de veritat terreny, integrades amb la RSRF del sensor d'UAV ja que s'ha disposat de la funció de resposta d'aquest sensor concret (MicaSense RedEdge) [Ciesielski, 2016]. Les bandes del visible han obtingut un alt R^2 (R^2_{BLAU}>0.955; R^2_{VERD}>0.967; R^2_{ROIG}>0.982) i un biaix negatiu relativament baix (−3.346 %; −4.067 %; −3.762 %), el que significa que els valors de reflectància d'UAV han estat lleugerament però sistemàticament més grans que aquells mesurats amb espectroradiòmetre de camp. A la banda de l'IRp, aquest efecte ha estat rellevant en objectes foscos, on la reflectància mesurada amb el radiòmetre ha estat inferior al 5 %, mentre que la reflectància mesurada pel sensor UAV s'ha situat entre un 15 % i un 20 %, generant un biaix negatiu relativament elevat (−16.956 %), tot i que cal esmentar que també ha mostrat un elevat coeficient de determinació (R^2_{IRp}>0.942).

Les imatges d'UAV adquirides al pas superior de S2A han obtingut uns ajustos amb les dades de camp molt semblants als de L8. A les bandes del visible han obtingut un elevat R^2 (R^2_{BLAU}>0.971; R^2_{VERD}>0.969; R^2_{ROIG}>0.975) i un biaix negatiu relativament baix (−2.534 %; −3.652 %; −2.454 %), que també significa que els valors de reflectància de l'UAV han estat lleugera però sistemàticament més grans que els mesurats amb l'espectroradiòmetre de camp. A la banda de l'IRp, l'efecte ha estat el mateix en objectes foscos, on els valors de reflectància mesurats pel radiòmetre han estat menors al 5 %, mentre que els valors mesurats del sensor de l'UAV s'han trobat entre el 15 % i el 18 % en aquest cas, resultant en un biaix negatiu relativament elevat (−17.921 %), tot i que també cal esmentar que ha mostrat un alt coeficient de determinació (R^2_{IRp}>0.946).

Comparant la reflectància espectral en els píxels de test (40 % de 51) amb la imatge L8 (30 m) corregida amb el mètode UAS-MiraMon, l'RMSE ha estat de 0.712 % a la banda del blau, 1.000 % a la banda del verd, 1.871 % a la banda del roig i 7.530 % a la banda de l'IRp, en consonància amb els resultats anteriors. Comparant els píxels de test (40 % de 517) a la imatge S2 (10 m) corregida amb el mètode UAS-MiraMon, l'RMSE ha estat de 0.745 % a la banda del blau, 1.230 % a la banda del verd, i 2.018 % a la banda del roig. Quan s'han comparat els píxels de test (40 % de 143) a la banda IRp (20 m), l'RMSE és de 6.760 %, també en consonància amb resultats previs.

Comparant banda a banda l'RMSE entre els píxels de test i els altres mètodes de correcció radiomètrica, a la banda del blau els valors han estat més alts en els productes oficials ($RMSE_{OLI}$≤2.197 %, $RMSE_{MSI}$≤2.149 %) que en el mètode de correcció PIA-MiraMon ($RMSE_{OLI}$≤0.585 %, $RMSE_{MSI}$≤1.366 %). A la banda del verd, els productes oficials ($RMSE_{OLI}$≤1.653 %, $RMSE_{MSI}$≤1.806 %) han tingut unes diferències lleugerament inferiors que el mètode PIA-MiraMon ($RMSE_{OLI}$≤1.746 %, $RMSE_{MSI}$≤1.867 %), com a la banda roig, on el 6S-LaSRC i el Sen2Cor-SNAP ($RMSE_{OLI}$≤2.680 %, $RMSE_{MSI}$≤2.192 %) han obtingut diferències menors en comparació amb àrees de test que les obtingudes amb el mètode PIA-MiraMon ($RMSE_{OLI}$≤3.130 %, $RMSE_{MSI}$≤2.373 %) (Taula 6).

Taula 6: Arrel de la mitjana del quadrat dels errors (RMSE) banda a banda entre els àrees de test d'UAV i les dades de satèl·lit radiomètricament corregides utilitzant: L'ajust a referències radiomètriques obtingudes amb dron (nou mètode UAS-MiraMon); l'ajust a referències radiomètriques obtingudes amb imatges MODIS (PIA-MiraMon); els productes oficials (6S-LaSRC per a l'OLI i Sen2Cor-SNAP per a l'MSI). En negreta, els valors d'error més baixos i que estan per sota del 3 % (% unitats de reflectància).

	BLAU		**VERD**		**ROIG**		**IRp**	
RMSE àrees de test *vs*. Correcció radiomètrica	**OLI#2 (*n*=20)**	**MSI#2 (*n*=207)**	**OLI#3 (*n*=20)**	**MSI#3 (*n*=207)**	**OLI#4 (*n*=20)**	**MSI#4 (*n*=207)**	**OLI#5 (*n*=20)**	**MSI#8a (*n*=57)**
UAS-MiraMon	0.712	**0.745**	**1.000**	**1.230**	**1.871**	2.018	7.530	6.760
PIA-MiraMon	**0.585**	1.366	1.746	1.867	3.130	2.373	8.528	7.281
Productes oficials 6S-LaSRC i Sen2Cor-SNAP	2.197	2.149	1.653	1.806	2.680	2.192	5.841	7.690

Així, la comparació dels resultats obtinguts amb el nou mètode UAS-MiraMon i els resultats obtinguts per mètodes de correcció radiomètrica contrastats (6S-LaSRC, Sen2Cor-SNAP, PIA-MiraMon), ha demostrat que el mètode UAS-MiraMon és igual o millor en les bandes del visible, però també que ha obtingut uns resultats molt pitjors a l'infraroig proper.

La reflectància espectral de les imatges L8 i S2A adquirides gairebé simultàniament i corregides amb el mètode UAS-MiraMon, ha mostrat diferències acceptables a les bandes del visible ($RMSE_{VIS} \leq 1.147$ %) i superiors en la banda de l'IRp ($RMSE_{VIS} \leq 1.707$ %) (Taula 7). D'entre totes les comparacions realitzades, la banda del blau ha mostrat les diferències més baixes entre sensors OLI i MSI, tant en centrar-se a 15 km al voltant de l'àrea d'estudi ($RMSE_{BLAU} \leq 0.621$ %), com en l'anell entre 15 km i 30 km ($RMSE_{BLAU} \leq 0.739$ %) com a l'àmbit comú entre la imatge S2 i la L8 ($RMSE_{BLAU} \leq 0.852$ %). La banda del verd ha presentat un bon ajust entre els dos sensors, amb diferències inferiors a l'1 % en les tres distàncies ($RMSE_{VERD} \leq 0.741$ %, $RMSE_{VERD} \leq 0.815$ % i $RMSE_{VERD} \leq 0.940$ %). A la banda del roig, les diferències han estat lleugerament més elevades ($RMSE_{ROIG} \leq 0.919$ %, $RMSE_{ROIG} \leq 0.984$ % i $RMSE_{ROIG} \leq 1.147$ %) que en bandes del blau i el verd. A la banda de l'IRp, les diferències han estat més altes que a les bandes del visible ($RMSE_{IRp} \leq 1.664$ %, $RMSE_{IRp} \leq 1.666$ %, $RMSE_{IRp} \leq 1.707$ %), seguint el mateix patró d'increment en funció de la distància respecte a la zona d'adquisició de les dades d'UAV (Taula 7). Aquesta anàlisi ha estat rellevant per a contrastar la hipòtesi d'un possible pitjor ajust fora de l'àrea volada per l'UAV donat que ja som lluny d'on s'han ajustat els paràmetres atmosfèrics del model.

Taula 7. Arrel de la mitjana del quadrat dels errors (RMSE) banda a banda entre imatges L8 i S2 (adaptades a la malla de l'OLI) captades quasi-simultàniament i corregides radiomètricament mitjançant el mètode UAS-MiraMon. Anàlisi de l'evolució de l'ajust en funció de la distància radial al centre de l'àrea d'estudi, per tal d'avaluar l'hipotètic augment de l'error en funció de la distància a l'àrea de vol del dron (% unitats de reflectància).

RMSE (%) entre imatges L8 i S2 captades quasi-simultàniament i corregides amb dades de dron ajustades a dades espectroradiomètriques de camp (UAS-MiraMon)				
Distància a la zona de vol de l'UAV (Nombre de píxels comparats)	**BLAU**	**VERD**	**ROIG**	**IRp**
0-15 km (n = 681 950)	0.621	0.741	0.919	1.664
15-30 km (n = 2 203 730)	0.739	0.815	0.984	1.666
Escena TCG (n = 12 148 700)	0.852	0.940	1.147	1.707

El disseny experimental del capítol 2.4 ha permès generar cartografia temàtica a partir d'imatges procedents d'UAV. Les imatges multiespectrals de dron s'han corregit radiomètricament ajustant-les a dades espectroradiomètriques *in-situ*, obtingudes de panells de referència, i integrades amb l'ample de banda determinat per l'FWHM en comptes de la RSRF degut a la manca d'informació proveïda pel fabricant [Parrot, 2018]. Addicionalment, s'ha experimentat un mètode de detecció i reducció d'ombres en imatges de dron, obtenint uns resultats preliminars acceptables. La correcció geomètrica s'ha realitzat mitjançant punts de control sobre el terreny (GCP), que consistien en les estaques que totes les explotacions mineres tenen l'obligació legal de tenir i mantenir. La resolució espacial de les imatges i la cartografia generada ha estat de 9 cm per píxel.

La informació espectral s'ha combinat per generar informació addicional i detectar la vegetació i propietats del sòl. Mitjançant la visualització de combinacions en color fals de les imatges de drons, és intuïtiu trobar la presència de vegetació a causa de l'alta resposta de la vegetació activa a la banda de l'IRp. A més, mitjançant el càlcul d'índexs espectrals, s'ha pot identificar la distribució espacial de la presència de vegetació i la seva activitat vegetativa (NDVI), el contingut d'humitat (NDWI1) i separar els efectes del sòl en les àrees de vegetació (SAVI i MSAVI2), índexs que en general han facilitat el procés de quantificació d'àrees amb vegetació i àrees sense vegetació.

Addicionalment, la informació estructural sobre la morfologia del terreny s'ha derivat del Model Digital d'Elevacions (MDE) fotogramètric i ha permès obtenir productes topogràfics simples de corbes de nivell, que en combinació amb mapes topogràfics oficials, han complementat la monitorització de morfologia del terreny. Combinant la informació

de la posició solar i el Model Digital de Superfícies (MDS), també obtingut de les imatges del dron, s'ha obtingut informació important sobre les ombres projectades. A més, el mapa diferencial entre el MDS i el MDE ha proporcionat informació rellevant sobre les altures relatives d'estructures i, per tant, també respecte de l'altura de vegetació sobre el terreny.

En el procés de classificació de cobertes del sòl, realitzat amb el mètode kNN, s'han utilitzat les capes d'informació espectral en combinació amb les capes de l'estructura del terreny per classificar cada píxel en una categoria d'interès: residus miners, sòl nu orgànic, herbassar, matollar i arbrat. El mapa diferencial entre MDS i MDE ha contribuït estadísticament a distingir la vegetació alta (>2 m) de la baixa vegetació (≤2 m) així com a determinar l'alçada de la vegetació alta. En definitiva, els resultats del protocol proposat identifiquen clarament quines àrees estan essent ben restaurades, quines necessiten una atenció especial i quines no estan rebent cap mena de restauració. L'àrea ocupada en cada estadi de restauració i per cada tipus de coberta del sòl s'ha pogut controlar no només en unitats absolutes, sinó també en unitats relatives a la distribució interna de cada fase. L'anàlisi de la variació interna de les cobertes del sòl ha estat un dels resultats més interessants de la informació proporcionada.

Els productes cartogràfics obtinguts s'han pogut integrar plenament en la cartografia oficial, millorant tant la resolució espacial com la resolució temporal a nivell local de l'explotació. Per tant, la inspecció visual dels processos de restauració ha millorat considerablement ja que s'ha demostrat que es pot proporcionar informació crucial en casos on amb una ortoimatge aèria actualitzada amb regularitat no seria factible. Si es disposa de cartografia prèvia, com ha estat el cas, els productes UAV són útils per detectar anomalies en el procés de restauració i, per tant, permeten centrar la restauració en zones on el desenvolupament de la vegetació es manté baix.

Capítol 4: Discussió general

4. Discussió general

En el capítol 2.1 s'ha evidenciat que els mètodes de correcció radiomètrica habituals [Gascon et al., 2017; Vermote et al., 2016; Pons et al., 2014] tenen, en general, un bon ajust amb les dades radiomètriques de camp. No obstant, ni els mètodes oficials de cada sensor són els millors ni sempre tenen un bon ajust entre ells, fet que indica que es poden millorar. De fet, el mètode que utilitza referències radiomètriques (PIA-MiraMon), és el que obté un millor ajust respecte les dades de camp i un millor ajust entre diferents sensors, motiu pel qual ha estat l'algorisme de correcció radiomètrica utilitzat en la correcció d'imatges de satèl·lit mitjançant l'ús de dades procedents de dron en el capítol 2.3 i assolir els objectius principals de la Tesi.

D'altra banda, en aquest capítol també es posa de manifest que tot i que l'espectroradiometria de camp convencional permet el mostreig de diversos tipus de coberta, hi ha cobertes que no són fàcilment accessibles o requereixen molt temps de preparació (e.g. aigua), fet que fa perdre un valuós temps si es pretén fer mesures de camp just en el moment de pas del satèl·lit. El protocol geoestadístic amb què s'ha realitzat el mostreig *in-situ* amb espectroradiòmetre de camp s'ha demostrat vàlid per ser comparat amb les imatges de satèl·lit, però amb un esforç de càlcul i de processament elevat.

En el capítol 2.2 els resultats mostren que el mètode de georeferenciació indirecta mitjançant punts de control és el que dóna millor exactitud posicional i altimètrica, però també que és el més lent d'utilitzar. La georeferenciació directa mitjançant el post-processat de dades d'un GNSS de doble freqüència i fase portadora, amb suport de camp *in-situ*, dóna un nivell d'exactitud similar però a un cost econòmic molt superior. A un ordre de magnitud inferior, trobem el posicionament directe mitjançant dades post-processades d'un GPS de freqüència simple i fase portadora sense suport de camp *in-situ*. En canvi, utilitzar les dades del GNSS de bord permet fer treballs ràpids però amb un nivell d'exactitud baix. Conseqüentment, donada la disponibilitat de punts de control per aconseguir una molt exacta georeferenciació, el mètode de georeferenciació indirecta ha estat l'utilitzat, en el capítol 2.3, per combinar dades d'UAV amb dades de satèl·lit i, en el capítol 2.4, per tractar imatges d'UAV en una aplicació ambiental.

En el capítol central de la Tesi, el 2.3, en primer lloc s'ha posat de manifest la importància i utilitat de l'obtenció de mesures espectroradiomètriques de camp amb el radiòmetre portàtil i els panells de referència. Analitzant els resultats de l'ajust entre les dades *in-situ* i les dades d'UAV, el calibratge de reflectància del programari fotogramètric

en base al panell proporcionat pel fabricant de la càmera multiespectral ha obtingut un bon ajust (R^2>0.942). Tot i això, cal destacar un biaix negatiu comú, el que significa que els valors de reflectància en la imatge UAV obtinguts pel programari fotogramètric han estat sistemàticament més alts que els valors espectroradiomètrics de reflectància en superfície mesurats en el camp. En resum, en aquest primer pas ascendent, podem determinar que utilitzant múltiples referències de reflectància distribuïdes en el domini espectral i abastant una àmplia gamma d'intensitats, es facilita la correcció de les desviacions introduïdes en procediments de correcció radiomètrica més senzills com el proporcionat pel fabricant del sensor d'UAV, en consonància amb estudis molt recents [Aasen et al., 2018]. Cal assenyalar que alguns autors [Richter i Schläpfer, 2016] defensen que un mínim que dos o tres panells de referència d'alta qualitat poden ser suficients per a la correcció radiomètrica mitjançant l'ajust lineal empíric, i els panells restants es poden utilitzar per a la validació de resultats i l'anàlisi de precisió, tal com s'ha experimentat en el capítol 2.4, però segons l'experiència d'aquesta Tesi l'ús de més panells garanteix una adequada distribució d'intensitats i referències espectrals, a més de disposar d'alternatives si un color és tan intens que satura les dades del sensor de l'UAV. No obstant això, atès que aquesta investigació no intenta determinar el nombre mínim de panells o els colors més apropiats, s'ha utilitzat un ampli conjunt de colors per assegurar-se que no es produeix cap problema per aquesta causa. Futures investigacions addicionals determinaran la idoneïtat del nombre de panells i els colors concrets a suggerir després de proves més intenses focalitzades en aquest objectiu concret.

L'anàlisi dels resultats de l'ajust entre les dades de l'UAV i les dades de satèl·lit, ha ofert un RMSE acceptable a les bandes del visible ($RMSE_{VIS}$≤3.017 %), en consonància amb recents treballs d'altres autores [Zabala, 2017]. L'adaptació espacial de les dades de l'UAV de 6 cm a les malles de dades de satèl·lit de 30 m (OLI), 20 m i 10 m (MSI), ha proporcionat valors de reflectància espectral coherents amb els obtinguts mitjançant els mètodes de correcció radiomètrica oficials de les imatges de satèl·lit, és a dir, les dades de l'UAV són consistents amb les dels satèl·lits. En aquest segon pas d'escalat ascendent, cal destacar dos punts en les comparacions en totes les bandes, tant en l'OLI com en l'MSI. En primer lloc, els valors d'UAV han estat sistemàticament inferiors als valors de satèl·lit (aquest efecte és més visible a les bandes del blau i el verd). En segon lloc, i més important, la banda de l'IRp ha presentat diferències de reflectància molt elevades entre les dades de l'UAV i les dades de satèl·lit (RMSE≥6.688 %), tant en l'OLI com en l'MSI i en tots els mètodes de correcció radiomètrica, confirmant així que el desajust entre la configuració espectral (RSRF) del sensor de l'UAV emprat i els sensors satel·litaris amb què s'ha comparat és

massa important per ser ignorat. El desplaçament en ample de banda i posició espectral és la principal font d'aquesta alta diferència, però també cal tenir en consideració que la relació senyal-soroll (SNR) és una font d'error important en l'IRp a causa del menor senyal de radiancia en aquesta longitud d'ona, tal com s'indica en el manual dels usuaris del Landsat-8 [USGS, 2016] i en el guia tècnica Sentinel-2 [ESAd, 2018].

Analitzant els resultats de l'ajust entre les correccions radiomètriques d'imatges de satèl·lit i les àrees de test, a les bandes del visible la correcció radiomètrica UAS-MiraMon ha aconseguit resultats de qualitat similar als aconseguits amb els mètodes 6S-LaSRC, Sen2Cor-SNAP o PIA-MiraMon (a la banda NIR, els resultats són molt esbiaixats i no es poden comparar), acomplint els requisits oficials d'exactitud radiomètrica [USGS, 2016; ESAd, 2018]. De fet, a les bandes del visible de l'OLI i el MSI, el mètode UAS-MiraMon ha aconseguit millors ajustos ($RMSE_{VIS} \leq 2.018$ %) que els altres mètodes analitzats (6S-LaSRC ($RMSE_{VIS} \leq 2.680$ %), Sen2Cor-SNAP ($RMSE_{VIS} \leq 2.192$ %), i PIA-MiraMon ($RMSE_{VIS} \leq 3.130$ %). Això pot explicar-se pel fet que el 6S-LaSRC, Sen2Cor-SNAP i PIA-MiraMon utilitzen informació per a tota l'escena, mentre que en el cas UAS-MiraMon, els paràmetres atmosfèrics ($Latm_{\lambda}$, $\tau_{0\lambda}$) s'han obtingut utilitzant exclusivament referències locals.

En conseqüència, l'ús de les referències procedents d'UAV ha millorat l'exactitud local en la correcció radiomètrica, emergint com una nova metodologia per corregir radiomètricament les imatges de satèl·lit centrades en una àrea d'especial interès, en comptes de corregir una escena completa amb paràmetres atmosfèrics obtinguts d'altres fonts, sovint fora del àrea d'interès, tal com fan alguns productes oficials i altres alternatives. Malgrat que en l'anàlisi de correlació entre imatges captades quasi-simultàniament es confirma la hipòtesi que el nou mètode UAS-MiraMon disminueix la seva exactitud en funció de l'augment de la distància (pitjor ajust lluny del focus local) respecte l'àrea de vol de l'UAV, l'ajust en tota l'extensió coincident de les tessel·les L8 i S2 (més de 12 milions de píxels de 30 m de costat) ha estat manifestament bo ($RMSE_{VIS} \leq 1$ %), fet que implica una bona consistència de l'enfoc experimental UAS-MiraMon. Aquesta alta coherència entre sensors, sumada a l'exactitud de la correcció radiomètrica millorada, és un avantatge del mètode UAS-MiraMon per a la generació de sèries temporals, fent més coherents les dades captades amb diferents sensors en àrees d'especial interès en les quals és necessari efectuar el control d'una manera més acurada i regular.

A més, el mètode presentat permet un ús molt més robust de les mesures espectroradiomètriques puntuals quan s'apliquen a la seva comparació directa amb les imatges de satèl·lit. Per contra, un dels principals inconvenients del mètode UAS-MiraMon

és que només es pot utilitzar per corregir imatges de satèl·lit adquirides gairebé simultàniament a les dades de dron i *in-situ*.

El coneixement adquirit en tractament geomètric i radiomètric d'imatges de dron ha permès desenvolupar una aplicació específica per al monitoratge mediambiental, en concret per al seguiment de restauracions d'explotacions mineres a cel obert. Utilitzant imatges de generades amb un UAV de baix cost i un sensor multiespectral que no disposa d'una RSRF publicada, l'ajust amb la radiometria de camp s'ha resolt positivament i fins i tot s'ha investigat en la reducció d'ombres, obrint la porta a futures recerques en aquest àmbit. El protocol de seguiment d'activitats extractives és operatiu tant en països desenvolupats com en països en desenvolupament sense massa recursos econòmics, on sovint hi ha una major limitació pecuniària i un major conflicte entre la societat i les empreses extractives. En aquest estudi sobre la degradació i la restauració de les cobertes del sòl trobem una solució que contribueix efectivament a integrar mètodes i tecnologies amb forta base científica, alhora que col·labora en transicions econòmicament robustes de la gestió ambiental, d'acord amb els objectius de desenvolupament sostenible [Nacions Unides, 2018].

Conclusions generals / Conclusiones generales / Overall conclusions

Conclusions generals (català)

Aquesta Tesi doctoral aprofundeix en les creixents possibilitats que ofereixen els Vehicles Aeris no Tripulats (UAV), altrament anomenats Sistemes Aeris no tripulats (UAS) o drons, per recollir dades *in-situ* amb la finalitat de millorar la validació, el processament i/o la interpretació de les dades de satèl·lits que formen part de Sistema Global de Sistemes d'Observació de la Terra (GEOSS), fent especial èmfasi en les imatges captades pels sensors òptics a bord dels satèl·lits Landsat-8 i Sentinel-2 (A i B).

Entre les principals aportacions metodològiques, es presenta un innovador mètode de correcció radiomètrica de les imatges satel·litàries mitjançant dades captades amb dron, aquestes darreres calibrades amb dades *in-situ* adquirides amb espectroradiòmetres de camp. Les millores d'aquest nou mètode, anomenat UAS-MiraMon, consisteixen en:

1. Es millora l'ajust radiomètric entre dades adquirides amb dron i dades de reflectància espectral *in-situ* adquirides amb espectroradiòmetres de camp. S'utilitzen múltiples referències de reflectància distribuïdes en el domini espectral que abasten una àmplia gamma d'intensitats, caracteritzades amb espectroradiòmetre de camp, per ajustar les dades de dron. Aquestes dades de dron són altament fiables per ésser utilitzades com a referència radiomètrica *in-situ*, tant per corregir imatges de satèl·lit com per validar altres metodologies de correcció radiomètrica.
2. Es millora el mostreig, ja que la captura de dades mitjançant el dron és més ràpida i més extensa que l'obtinguda amb espectroradiometria de camp convencional. Addicionalment, permet un mostreig ràpid, sistemàtic i recursiu a cobertes del sòl difícilment accessibles en posició nadiral, com masses d'aigua o masses forestals.
3. Es millora la georeferenciació i el remostreig de les dades radiomètriques de referència. Les dades adquirides amb dron i ajustades a les dades *in-situ*, són georeferenciades acuradament i, donada la seva naturalesa ràster (<10 cm), adaptades a diferents malles de sensors satel·litaris com l'OLI del Landsat-8 (30 m de resolució espacial) o l'MSI del Sentinel-2 (20 m o 10 m) amb facilitat.
4. Es millora el resultat de la correcció radiomètrica. El mètode UAS-MiraMon proporciona un millor ajust, respecte dades espectroradiomètriques *in-situ*, que els mètodes de correcció radiomètrica oficials d'imatges del sensor OLI del Landsat-8 (6S-LaSRC) i del sensor MSI del Sentinel-2 (Sen2Cor-SNAP). Aquest millor ajust és degut al fet que els paràmetres atmosfèrics que nodreixen

l'algorisme de correcció radiomètrica s'obtenen d'un gran nombre de referències radiomètriques adquirides a la mateixa zona d'estudi, no amb una o poques dades ubicades en qualsevol punt de l'escena de satèl·lit a corregir.

5. Es millora l'ajust entre imatges corregides radiomètricament i procedents de diferents sensors. El mètode UAS-MiraMon proporciona un millor ajust entre imatges procedents dels sensors OLI i MSI captades quasi-simultàniament que els mètodes de correcció radiomètrica oficials 6S-LaSRC i Sen2Cor-SNAP entre ells. Aquest millor ajust és degut al fet que el nou mètode utilitza el mateix algorisme i uns paràmetres atmosfèrics molt similars, derivats de les dades del dron, per corregir les imatges procedents dels dos sensors satel·litaris. Aquest millor ajust demostra que el mètode UAS-MiraMon pot aportar una millora en la coherència de sèries temporals que utilitzin ambdues fonts d'imatges de satèl·lit, especialment el monitoratge de zones d'interès com àrees protegides.

La Tesi contribueix a la millora del tractament de les dades captades per satèl·lits d'observació de la Terra, introduint innovacions tecnològiques i metodològiques basades en l'ús d'UAV en sinergia amb dades espectroradiomètriques de camp, tal com s'havia plantejat en els objectius. Alhora, ha obert línies de recerca que encara no s'havien explorat ni nacional ni internacionalment, especialment pel que fa a l'ús de drons en la correcció i validació d'imatges de satèl·lit. Aquestes noves vies de treball s'albiren com a potencialment explorables per la comunitat científica a la llum de l'interès que han despertat, fins al moment, les publicacions resultants d'aquesta Tesi. Els resultats obtinguts són rellevants per a l'obtenció de dades mitjançant teledetecció i per a la generació de cartografia detallada i de qualitat, contribuint a la millora de l'estudi dels ecosistemes en tot el planeta. La vinculació entre imatges de satèl·lit de cobertura global i lliure accés, i imatges de dron captades amb plataformes de baix cost i de cobertura més local però alhora més detallada, fa que l'aplicabilitat dels resultats obtinguts amb aquesta Tesi sigui extrapolable a gairebé qualsevol societat i punt de la Terra.

Entre els punts destacables cal esmentar la component d'innovació tecnològica que representa la introducció d'UAV i l'acurat tractament espectroradiomètric de dades captades pels seus sensors òptics. Un dels reptes que s'ha superat satisfactòriament consisteix en l'elaboració d'un protocol per a l'adquisició de dades espectroradiomètriques de camp, útil per calibrar les imatges captades amb UAV, que són utilitzades per corregir radiomètricament imatges de satèl·lit captades quasi-simultàniament. La demostració de l'operativitat d'aquest protocol és un pas endavant en la validació d'imatges de satèl·lit,

esdevenint una contribució que considerem sincerament rellevant per una comunitat científica que encara té oberta la discussió sobre la validació de dades de teledetecció captades des de satèl·lits. Un altre punt destacable de la Tesi és que es nodreix dels sòlids coneixements i mètodes desenvolupats en els anys pretèrits, però alhora els ha aplicat en noves plataformes satel·litàries com Landsat-8 i Sentinel-2, i noves plataformes molt més properes a la superfície terrestre com els drons de baix pes. També és de destacar la recerca realitzada en el camp de la geometria de les imatges adquirides des dels drons, posant-la en el context de la seva aplicabilitat a diferents escales. A més, la recerca en el tractament geomètric i radiomètric d'imatges d'UAV ha contribuït a la aplicació de tècniques de processat en la generació de productes cartogràfics digitals per al seguiment restauracions de mines a cel obert, col·laborant així en la millora mediambiental de manera operativa, útil tant per l'administració pública com pel sector privat.

La recerca plantejada a la Tesi pot ser continuada en diversos aspectes, entre ells:

1. Els sensors òptics que actualment poden ser embarcats en UAV no tenen exactament la mateixa configuració de bandes espectrals que els sensors de satèl·lit, motiu pel qual s'ha detectat que algunes regions espectrals no poden ser corregides radiomètricament amb aquest mètode en la data de finalització d'aquesta Tesi. No obstant, ho podran ser quan una nova generació de sensors d'UAV repliqui més bandes dels sensors de satèl·lit, ja que la metodologia a seguir està sòlidament descrita i contrastada en els continguts que conformen aquesta Tesi i no hi ha motiu per pensar que no funcioni en altres regions espectrals de l'espectre solar.
2. L'ús de dades de dron en combinació amb espectroradiometria de camp millora la correcció radiomètrica d'imatges de satèl·lit, especialment en la zona d'interès, així que una futura recerca pot consistir a programar captacions simultànies de dades d'UAV en àrees distants i distribuïdes a través d'un escena de satèl·lit, per tal de tenir diverses referències que participin de la imatge de satèl·lit.
3. S'ha utilitzat referències radiomètriques que abasten tot el domini espectral de les imatges de dron i en diverses intensitats, per tal d'evitar tenir regions espectrals poc o mal mostrejades. No obstant, l'optimització del nombre de referències formarà part de futures investigacions.
4. El tractament geomètric i radiomètric d'imatges d'UAV s'ha mostrat eficaç, però encara hi ha marge de millora en la recuperació de píxels a l'ombra, una línia d'investigació que s'aborda amb èxit en aquesta Tesi però que pot ser millorada.

Conclusiones generales (castellano)

Esta Tesis doctoral profundiza en las crecientes posibilidades que ofrecen los Vehículos Aéreos no Tripulados (UAV), también llamados Sistemas Aéreos no tripulados (UAS) o drones, para recoger datos *in-situ* con el fin de mejorar la validación, el procesamiento y/o la interpretación de los datos de satélites que forman parte de Sistema Global de Sistemas de Observación de la Tierra (GEOSS), haciendo especial énfasis en las imágenes captadas por los sensores ópticos a bordo de los satélites Landsat-8 y Sentinel-2 (A y B).

Entre las principales aportaciones metodológicas, se presenta un innovador método de corrección radiométrica de las imágenes satelitales mediante datos captados con dron, estas últimas calibradas con datos *in-situ* adquiridos con espectrorradiómetros de campo. Las mejoras de este nuevo método, llamado UAS-MiraMon, consisten en:

1. Se mejora el ajuste radiométrico entre datos adquiridos con dron y datos de reflectancia espectral *in-situ* adquiridos con espectrorradiómetros de campo. Se utilizan múltiples referencias de reflectancia distribuidas en el dominio espectral que abarcan una amplia gama de intensidades, caracterizadas con espectrorradiómetro de campo, para ajustar los datos de dron. Estos datos de dron son altamente fiables para ser utilizados como referencia radiométrica *in-situ*, tanto para corregir imágenes de satélite como para validar otras metodologías de corrección radiométrica.
2. Se mejora el muestreo, ya que la captura de datos mediante el dron es más rápida y más extensa que la obtenida con espectrorradiometría de campo convencional. Adicionalmente, permite un muestreo rápido, sistemático y recursivo en cubiertas del suelo difícilmente accesibles en posición nadiral, como masas de agua o masas forestales.
3. Se mejora la georreferenciación y el remuestreo de los datos radiométricos de referencia. Los datos adquiridos con dron y ajustados a los datos *in-situ*, son georreferenciados cuidadosamente y, dada su naturaleza ráster (<10 cm), adaptadas a diferentes mallas de sensores satelitales como el OLI del Landsat-8 (30 m de resolución espacial) o el MSI del Sentinel-2 (20 m 10 m) con facilidad.
4. Se mejora el resultado de la corrección radiométrica. El método UAS-MiraMon proporciona un mejor ajuste, respecto datos espectrorradiométricos *in-situ*, que los métodos de corrección radiométrica oficiales de imágenes del sensor OLI del Landsat-8 (6S-LaSRC) y del sensor MSI del Sentinel-2 (Sen2Cor-SNAP). Este mejor

ajuste se debe al hecho de que los parámetros atmosféricos que nutren el algoritmo de corrección radiométrica se obtienen de referencias radiométricas adquiridas en la misma zona de estudio, no con uno o pocos datos ubicados en cualquier punto de la escena de satélite a corregir.

5. Se mejora el ajuste entre imágenes corregidas radiométricamente y procedentes de diferentes sensores. El método UAS-MiraMon proporciona un mejor ajuste, entre imágenes procedentes de los sensores OLI y MSI captadas casi-simultáneamente, que los métodos de corrección radiométrica oficiales 6S-LaSRC y Sen2Cor-SNAP entre ellos. Este mejor ajuste se debe al hecho de que el nuevo método utiliza el mismo algoritmo y unos parámetros atmosféricos muy similares, derivados de los datos del dron, para corregir las imágenes procedentes de los dos sensores satelitales. Este mejor ajuste demuestra que el método UAS-MiraMon puede aportar una mejora en la coherencia de series temporales que utilicen ambas fuentes de imágenes de satélite, especialmente en el monitoreo de zonas de interés como áreas protegidas.

La Tesis contribuye a la mejora del tratamiento de los datos captados por satélites de observación de la Tierra, introduciendo innovaciones tecnológicas y metodológicas basadas en el uso de UAVs en sinergia con datos espectrorradiométricos de campo, tal como se había planteado en los objetivos. Asimismo, ha abierto líneas de investigación que aún no se habían explorado ni nacional ni internacionalmente, especialmente en cuanto al uso de drones en la corrección y validación de imágenes de satélite. Estas nuevas vías de trabajo se vislumbran como potencialmente explorables por la comunidad científica a la luz del interés que han despertado, hasta el momento, las publicaciones resultantes de esta Tesis. Los resultados obtenidos son relevantes para la obtención de datos mediante teledetección y para la generación de cartografía detallada y de calidad, contribuyendo a la mejora del estudio de los ecosistemas en todo el planeta. La vinculación entre imágenes de satélite de cobertura global y libre acceso, e imágenes de dron captadas con plataformas de bajo coste y de cobertura más local pero a la vez más detallada, hace que la aplicabilidad de los resultados obtenidos con esta Tesis sea extrapolable a casi cualquier sociedad y punto de la Tierra.

Entre los puntos destacables, cabe mencionar la componente de innovación tecnológica que representa la introducción de UAVs y el cuidadoso tratamiento espectrorradiométrico de los datos captados por sus sensores ópticos. Uno de los retos que se ha superado satisfactoriamente consiste en la elaboración de un protocolo para la

adquisición de datos espectrorradiométricos de campo, útil para calibrar las imágenes captadas con UAV, que son utilizadas para corregir radiométricamente imágenes de satélite captadas casi-simultáneamente. La demostración de la operatividad de este protocolo es un paso adelante en la validación de imágenes de satélite, convirtiéndose en una contribución que consideramos sinceramente relevante para una comunidad científica que aún tiene abierta la discusión sobre la validación de datos de teledetección captadas desde satélites. Otro punto destacable de la Tesis es que se nutre de los sólidos conocimientos y métodos desarrollados en años pretéritos, pero a la vez los ha aplicado en nuevas plataformas satelitales como Landsat-8 y Sentinel-2, y nuevas plataformas mucho más cercanas en la superficie terrestre como los drones de bajo peso. También cabe destacar la investigación realizada en el campo de la geometría de las imágenes adquiridas desde los drones, poniéndola en el contexto de su aplicabilidad a diferentes escalas. Además, la investigación en el tratamiento geométrico y radiométrico de imágenes de UAV ha contribuido a la aplicación de técnicas de procesado en la generación de productos cartográficos digitales para el seguimiento restauraciones de minas a cielo abierto, colaborando así en la mejora medioambiental de manera operativa, útil tanto para la administración pública como por el sector privado.

La investigación planteada en la Tesis puede ser continuada en varios aspectos, entre ellos:

1. Los sensores ópticos que actualmente pueden ser embarcados en UAV no tienen exactamente la misma configuración de bandas espectrales que los sensores de satélite, por lo que algunas regiones espectrales no pueden ser corregidas radiométricamente con este método en a la fecha de finalización de esta Tesis. No obstante, lo podrán ser cuando una nueva generación de sensores de UAV replique más bandas de los sensores de satélite, ya que la metodología a seguir está sólidamente descrita y contrastada en los contenidos que conforman esta Tesis y no hay motivo para pensar que no funcione en otras regiones espectrales del espectro solar.
2. El uso de datos de dron en combinación con espectrorradiometría de campo mejora la corrección radiométrica de imágenes de satélite, especialmente en la zona de interés, así que una futura investigación puede consistir en programar captaciones simultáneas de datos de UAV en áreas distantes y distribuidas a través de un escena de satélite.

3. Se han utilizado referencias radiométricas que abarcan todo el dominio espectral de las imágenes de dron y en varias intensidades, para evitar tener regiones espectrales poco o mal muestreadas. Sin embargo, la optimización del número de referencias formará parte de futuras investigaciones.
4. El tratamiento geométrico y radiométrico de imágenes de UAV se ha mostrado eficaz, pero todavía hay margen de mejora en la recuperación de píxeles en la sombra, una línea de investigación que se aborda con éxito en esta Tesis pero que aún puede ser mejorada.

Overall conclusions (English)

This PhD thesis explores the increasing possibilities offered by Unmanned Aerial Vehicles (UAV), also called Unmanned Aerial Systems (UAS) or drones, to collect *in-situ* data in order to improve validation, processing and/or interpretation of satellite data that is part of the Global Earth Observation System of Systems (GEOSS), with particular emphasis on the images captured by the optical sensors on-board the Landsat-8 and Sentinel-2 satellites (A and B).

Among the main methodological contributions, we present an innovative method of satellite imagery radiometric correction based on the use of data collected with drones, the latter calibrated with *in-situ* data acquired with field spectroradiometers. The improvements to this new method, namely UAS-MiraMon, consist of:

1. The radiometric fitting between data acquired with drone and *in-situ* spectral reflectance data acquired with field spectroradiometers has been improved. Multiple reflectance references distributed in the spectral domain and covering a wide range of intensities, characterized by field spectroradiometric measurements, are used to fit the drone data. This drone data is highly reliable for use as *in-situ* radiometric reference, both for correcting satellite images and validating other radiometric correction methodologies.
2. The sampling method has been improved, since the capture of data using a drone is faster and more geographically extensive than that obtained with conventional field spectroradiometric measurements. Additionally, it allows a quick, systematic and recursive sampling of land covers that are difficult to access in a nadiral position, such as water bodies or forest masses.
3. Georeferencing and resampling of the radiometric reference data has been improved. The data acquired with drone and fitted to *in-situ* data is carefully georeferenced and, given their raster nature (<10 cm), easily adapted to different satellite sensors grids such as Landsat-8 OLI (30 m spatial resolution) or Sentinel-2 MSI (20 m or 10 m).
4. The result of radiometric correction has been improved. The UAS-MiraMon method provides a better fitting with *in-situ* spectroradiometric data than the official radiometric correction methods of Landsat-8 OLI sensor (6S-LaSRC) and Sentinel-2 MSI sensor (Sen2Cor-SNAP) imagery. This better fitting is due to the fact that the atmospheric parameters that feed the radiometric correction algorithm are obtained from a large number of radiometric references acquired inside the study area,

rather than one or a few located at any point across the satellite scene to be corrected.

5. The fitting between radiometrically corrected images sensed by different sensors has been improved. The UAS-MiraMon method provides a better correspondence between images from the OLI and MSI sensors captured almost simultaneously, than the 6S-LaSRC and Sen2Cor-SNAP official radiometric correction methods among them. This better fitting is due to the fact that the new method uses the same algorithm and very similar atmospheric parameters, which are derived from the drone data, to correct the images from the two satellite sensors. The adjustment shows that the UAS-MiraMon method can provide an improvement in the consistency of time series using both satellite image sources, especially the monitoring of areas of interest as protected areas.

This PhD thesis contributes to improving the treatment of data captured by Earth observation satellites, introducing technological and methodological innovations based on the use of UAVs in synergy with field spectroradiometric data, as set out in the objectives. At the same time, it has opened research lines that have not yet been explored either nationally or internationally, especially with regard to the use of drones in the correction and validation of satellite images. These new research lines could be potentially explored by the scientific community in light of the interest that have provided the publications resulting from this PhD thesis. The results are relevant to obtaining and processing remote sensing data and generating detailed and quality cartography, potentially contributing to the improvement of the study of ecosystems throughout the planet. The link between free access global coverage satellite imagery, and drone imagery captured with low-weight platforms with local coverage and more spatial detail, makes the applicability of the results obtained with this PhD thesis useful for most societies and places on Earth.

Among the strengths of this thesis include the technological innovation component representing the introduction of UAVs and the careful radiometric treatment of data captured by their optical sensors. One of the challenges that have been satisfactorily achieved is the development of a protocol for acquiring spectroradiometric field data useful for calibrating the images captured with UAV, which are applied to radiometrically correct satellite imagery captured almost simultaneously. The demonstration of the operability of this protocol is a step forward in the validation of satellite images, which, in our opinion, constitute a relevant contribution to a scientific community that still discussing the validation of remote sensing data captured from satellites. Another strong

point of the PhD thesis is that it is not only supported by solid knowledge and methods developed in recent years, but has also been able to apply them to new satellite platforms, such as Landsat-8 and Sentinel-2, as well as new platforms that are much closer on the ground surface, such as drones of low weight. Also worth mentioning is the research carried out in the field of the geometry of the images acquired from the drones, which focus on the combined use with airborne and satellite remote sensing platforms and their applicability to different scales. In addition, progress in the geometric and radiometric treatment of UAV images has contributed to the application of processing techniques in the generation of digital cartographic products for monitoring open-pit mine restorations, thus contributing to major environmental improvement in an operative and useful way for both the public administration and the private sector.

The research proposed in the PhD thesis can be developed in several aspects:

1. The optical sensors that can currently be embedded in UAV do not have exactly the same configuration of spectral bands as the satellite sensors, which cause that some spectral regions cannot be radiometrically corrected with this method at the date of completion of this PhD thesis. However, this may be conducted when a new generation of UAV sensors match more bands of satellite sensors, since the methodology to follow is solidly described and contrasted in the contents of this research. Nevertheless, this has been also conceived to work effectively in other spectral regions of the solar spectrum.
2. The use of drone data in combination with field spectroradiometry improves the radiometric correction of satellite images, especially in the area of interest; thus, a future research can consist of programming simultaneous captures of UAV data in distant areas and distributed through a satellite scene in order to provide several references that participate in the satellite image.
3. Radiometric references that cover the entire spectral domain of drone images and in various intensities have been used in order to avoid having sparse or poorly sampled spectral regions. Nevertheless, the optimization of the number of references will be part of future research.
4. Geometric and radiometric treatment of UAV images has been shown to be effective. At any rate, there is still space for improvement in shadow pixel recovery, which represents a line of research that is successfully addressed in this PhD thesis and can be further improved.

Referències

(Les referències dels apartats 2.1 a 2.4 estan al final dels corresponents apartats)

Referències

ACIX (Atmospheric Correction Inter-Comparison Exercise). (2018). URL: https://earth.esa.int/web/sppa/meetings-workshops/acix (Últim accés: 1 de desembre 2018).

Aasen, H.; Honkavaara, E.; Lucieer, A.; Zarco-Tejada, P.J. (2018). Quantitative Remote Sensing at Ultra-High Resolution with UAV Spectroscopy: A Review of Sensor Technology, Measurement Procedures, and Data Correction Workflows. ***Remote Sens.***, 10, 1091–1933, doi: 10.3390/rs10071091

Barsi, J.A.; Kenton, L.; Kvaran, G.; Markham, B.L.; Pedelty, J.A. (2014). The Spectral Response of the Landsat-8 Operational Land Imager (OLI). ***Remote Sens.***, 6, 10232–10251, doi: 10.3390/rs61010232.

Berk, A.; Conforti, P.; Kennett, R.; Perkins, T.; Hawes, F.; van den Bosch, J. (2014). MODTRAN6: A major upgrade of the MODTRAN radiative transfer code. *A: Proceedings of the SPIE 9088, Algorithms and Technologies for Multispectral, Hyperspectral, and Ultraspectral Imagery XX, Baltimore, MD, USA, 13 June 2014; Volume 90880H*, doi: 10.1117/12.2050433.

BOE (Boletín Oficial del Estado). (2017). "Real Decreto 1036/2017, de 15 de diciembre, por el que se regula la utilización civil de las aeronaves pilotadas por control remoto", vol. 316. Ministerio de Fomento, Madrid. pp. 129609–129641. URL: https://www.boe.es/buscar/doc.php?id=BOE-A-2017-15721 (Últim accés: 1 de desembre 2018).

CEOS-WGCV (Committee on Earth Observation Satellites—Working Group on Calibration and Validation) (2018). CEOSS Cal/Val Portal. URL: http://calvalportal.ceos.org/ (Últim accés: 1 de desembre 2018).

Chance, K.; Kurucz, R.L. (2010). An improved high resolution solar reference spectrum for Earth's atmosphere measurements in ultraviolete, visible and near infrared. ***Journal of Quantitative spectroscopy and Radiative Transfer***, 111, 1289–1295. URL: https://www.cfa.harvard.edu/atmosphere/publications/Chance-Kurucz-solar2010-JQSRT.pdf (Últim accés: 1 de desembre 2018).

Chander, G.; Markham, B.L.; Helder, D.L. (2009). Summary of Current Radiometric Calibration Coefficients for Landsat MSS, TM, ETM+, and EO-1 ALI Sensors. ***Remote Sens. Environ.***, 113, 893–903, doi:10.1016/j.rse.2009.01.007.

Chavez, P.S., Jr. (1988). An improved dark-object subtraction technique for atmospheric scattering correction of multispectral data. ***Remote Sens. Environ.***, 24, 459–479, doi: 10.1016/0034-425790019-3.

Chuvieco, E. (2008). Teledetección Ambiental. La observación de la Tierra desde el Espacio. 3a Ed.; Planeta: Barcelona; p. 594. ISBN 978-84-344-8073-3

Ciesielski, E. (2016). Comunicació personal amb MicaSense RedEdge Team support. (MicaSense, Seattle, WA, USA)

Claverie, M.; Masek, J. (2017). Harmonized Landsat-8 Sentinel-2 (HLS) Product's Guide. v.1.3. doi: 10.13140/RG.2.2.33017.26725. URL: https://hls.gsfc.nasa.gov/documents/ (Últim accés: 1 de desembre 2018).

Colomina, I. i Molina, P. (2014). Unmanned aerial systems for photogrammetry and remote sensing: a review. ***ISPRS – J. Photogramm***. 92, 79–97. doi: 10.1016/j.isprsjprs.2014.02.013.

Colwell, R.N.; Ulaby, F.T.; Simonett, D.S.; Estes, J.E.; Thorley, G.A. (1983). Manual of Remote Sensing, 2a Ed.; Colwell, R.N., Ed.; American Society of Photogrammetry: Falls Church, VA, USA; vol.2, p. 2440, ISBN 093729442X

Copernicus (2018). Copernicus. Europe's eyes on earth. URL: http://www.copernicus.eu/main/overview (Últim accés: 1 de desembre 2018).

Czapla-Myers, J.; McCorkel, J.; Anderson, N.; Thome, K.; Bigar, S.; Helder, D.; Aaron, D.; Leigh, L.; Mishra, N. (2015). The Ground-Based Absolute Radiometric Calibration of Landsat 8 OLI. ***Remote Sens.***, 7, 600–626, doi: 10.3390/rs70100600.

de Miguel, E.; Fernández-Renau, A.; Prado, E.; Jiménez, M.; Gutiérrez de la Cámara, O.; Linés, C.; Gómez, J.A.; Martín, A.I.; Muñoz, F. (2014). A review of INTA AHS PAF. ***EARSeL eProceedings***, 13, 20–29, doi: 10.12760/01-2014-1-03.

Diaz-Delgado, R.; Lucas, R.; Hurford, C. (Eds.) (2017). The Roles of Remote Sensing in Nature Conservation: A Practical Guide and Case Studies, 1a Ed; Springer: Cham, Switzerland; p.318. ISBN 978-3-319-64332-8.

Drusch, M.; Del Bello, U.; Carlier, S.; Colin, O.; Fernandez, V.; Gascon, F.; Hoersch, B.; Isola, C.; Laberinti, P.; Martimort, P.; et al. (2012). Sentinel-2: ESA's Optical High-Resolution Mission for GMES Operational Services. ***Remote Sens. Environ.***, 120, 25–36, doi: 10.1016/j.rse.2011.11.026.

EUMETSAT (European Organization for the Exploitation of Meteorological Satellites). (2018). METEOSAT. URL: https://www.eumetsat.int/website/home/Satellites/CurrentSatellites/Meteosat/index.html (Últim accés: 1 de desembre 2018).

ESAa (European Space Agency) (2018). Navigation. URL: http://www.esa.int/Our_Activities/Navigation/Galileo_and_EGNOS (Últim accés: 1 de desembre 2018).

ESAb (European Space Agency) (2018). ESA Sentinel Online. Sentinel-2 mission. URL: http://www.esa.int/Our_Activities/Observing_the_Earth/Copernicus/Sentinel-2 (Últim accés: 1 de desembre 2018).

ESAc (European Space Agency) (2018). ESA Sentinel Online. Sentinel-2 mission objectives. URL: https://sentinel.esa.int/web/sentinel/missions/sentinel-2/mission-objectives (Últim accés: 1 de desembre 2018).

ESAd (European Space Agency) (2018). Sentinel-2 Radiometric Performance. 2018. URL: https://earth.esa.int/web/sentinel/technical-guides/sentinel-2-msi/performance (Últim accés: 1 de desembre 2018).

Fernández-Guisuraga, J.M.; Sanz-Ablanedo, E.; Suárez-Seoane, S.; Calvo, L. (2018). Using Unmanned Aerial Vehicles in Postfire Vegetation Survey Campaigns through Large and Heterogeneous Areas: Opportunities and Challenges. ***Sensors***, 18 (2), 586. doi: 10.3390/s18020586

Gao, B.C.; Kaufman, Y.J. (1995). Selection of the 1.375 micrometer MODIS Channel for Remote Sensing of Cirrus Clouds and Stratospheric Aerosols from Space. ***Journal of the Atmospheric Sciences***, 52 (23), p.4231-4237.

Gascon, F.; Bouzinac, C.;Thépaut, O.; Jung, M.; Francesconi, B.; Louis, J.; Lonjou, V.; Lafrance, B.; Massera, S.; Gaudel-Vacaresse, A.; Languille, F.; et al. (2017). Copernicus Sentinel-2A Calibration and Products Validation Status. ***Remote Sens.***, 9, 584–665, doi: 10.3390/rs9060584

GEOSS (Global Earth Observation System of Systems) (2018). GEOSS Evolution. URL: http://www.earthobservations.org/geoss.php (Últim accés: 1 de desembre 2018).

GPS (Global Positioing System). (2018). GPS: The Global Positioning System A global public service brought to you by the U.S. government. URL: https://www.gps.gov/ (Últim accés: 1 de desembre 2018).

Hadjimitsis, D.G.; Clayton, C.R.I.; Retalis, A. (2009). The use of selected Pseudoinvariant targets for the application of atmospheric correction in multi-temporal studies using satellite remotely sensed imagery. ***Int. J. Appl. Earth Obs. Geoinf.***, 11, 192–200, doi: 10.1016/j.jag.2009.01.005.

Hall, F.G.; Strebel, D.E.; Nickeson, J.E.; Goetz, S.J. (1991). Radiometric rectification: Toward a common radiometric response among multidate, multisensor images. ***Remote Sens. Environ.***, 35, 11–27, doi:10.1016/0034-425790062-B.

Hakala, T., Markelin, L., Honkavaara, E., Scott, B., Theocharous, T., Nevalainen, O., Näsi, R., Suomalainen, J., Viljanen, N., Greenwell, C., Fox, N. (2018). Direct Reflectance Measurements from Drones: Sensor Absolute Radiometric Calibration and System Tests for Forest Reflectance Characterization. ***Sensors***, 18, 1417. doi: 10.3390/s18051417.

Hatchell, D.C. (Ed.). (1999). Analytical Spectral Devices, Inc. (ASD) Technical Guide, 3rd ed.; Analytical Spectral Devices, Inc.: Boulder, CO, USA, 1999.

Holben, B.N.; Eck, T.F.; Slutsker, I.; Tanré, D.; Buis, J.P.; Setzer, A.; Vermote, E.; Reagan, J.A.; Kaufman, Y.J.; Nakajima, T.; et al. (1998). AERONET—A Federated Instrument Network and Data Archive for Aerosol Characterization. ***Remote Sens. Environ.***, 66, 1–16, doi: 10.1016/S0034-425700031-5.

Honkavaara, E.; Kaivosoja, J.; Mäkynen, J.; Pellikka, I.; Pesonen, L.; Saari, H.; Salo, H.; Hakala, T.; Marklelin, L.; Rosnell T. (2012). Hyperspectral Reflectance Signatures and Point Clouds for Precision Agriculture by Light Weight UAV Imaging System. *A: Proceedings of the XII ISPRS Annals of Photogrammetry, Remote Sensing and Spatial Information Sciences, Melbourne, VIC, Australia, 25 August–1 September 2012, Volume I-7, 353–358*, doi: 10.5194/isprsannals-I-7-353-2012.

ICGCa (Institut Cartogràfic i Geològic de Catalunya). (2018). Imatges aèries i ortofotos. URL: http://www.icgc.cat/ca/Administracio-i-empresa/Descarregues/Imatges-aeries-i-de-satel-lit (Últim accés: 1 de desembre 2018).

ICGCa (Institut Cartogràfic i Geològic de Catalunya). (2018). Elevacions. URL: http://www.icgc.cat/ca/Administracio-i-empresa/Descarregues/Elevacions (Últim accés: 1 de desembre 2018).

Iqbal, F.; Lucieer, A.; Barry K. (2018). Simplified radiometric calibration for UAS-mounted multispectral sensor. ***European J. Rem. Sens.***, 51, 301–313, doi: 10.1080/22797254.2018.1432293.

Jiménez, M.; Díaz-Delgado, R.; Vaughan, P.; De Santis, A.; Fernández-Renau, A.; Prado, E.; Gutiérrez de la Cámara, O. (2007). Airborne hyperspectral scanner (AHS) mapping capacity simulation for the Doñana biological reserve scrublands. *A: Proceedings of the 10th Intl. Symposium on Physical Measurements and Signatures in Remote Sensing, Davos, Switzerland, 12–14 March 2007; Schaepman, M., Liang, S., Groot, N., Kneubühler, M., Eds.* URL: http://www.isprs.org/proceedings/XXXVI/7-C50/papers/P81.pdf (Últim accés: 1 de desembre 2018).

Jiménez, M.; Díaz-Delgado, R. (2015). Towards a Standard Plant Species Spectral Library Protocol for Vegetation Mapping: A Case Study in the Shrubland of Doñana National Park. ***ISPRS Int. J. Geo-Inf.***, 4, 2472–2495, doi: 10.3390/ijgi4042472.

Kaufman, Y.J.; Sendra, C. (1988). Algorithm for automatic atmospheric corrections to visible and near-IR satellite imagery. ***Int. J. Remote Sens.***, 9, 1357–1381, doi: 10.1080/01431168808954942.

Kotchenova, S.Y.; Vermote, E.F.; Matarrese, R.; Klemm, F.J., Jr. (2006). Validation of a vector version of the 6S radiative transfer code for atmospheric correction of satellite data. Part I: Path radiance. ***Appl. Opt.,*** 26, 6762–6774.

Kotchenova, S.Y.; Vermote, E.F. (2007). Validation of a vector version of the 6S radiative transfer code for atmospheric correction of satellite data. Part II: Homogeneous Lambertian and anisotropic surfaces. ***Appl. Opt.***, 46, 4455–4464.

Lillesand, T.M.; Kiefer, R.W.; Chipman, J. (2008). Remote Sensing and Image Interpretation, 7a Ed; John Wiley & Sons:, New York, NY, USA; p. 736. ISBN 978-1-118-34328-9

Liou, K.N. (2002). An Introduction to Atmospheric Radiation, 2a Ed.; Academic Press: San Diego, CA, USA; p. 583, ISBN 978-0-12-451451-5.

Mac Arthur, A.; Robinson, I. (2015). A critique of field spectroscopy and the challenges and opportunities it presents for remote sensing for agriculture, ecosystems, and hydrology. *A: Proceedings of the SPIE Remote Sensing for Agriculture, Ecosystems, and Hydrology, Toulouse, France, 14 October 2015.*

Manfreda, S.; McCabe, M.; Miller, P.; Lucas, R.; Pajuelo Madrigal, V.; Mallinis, G.; Ben-Dor, E.; Helman, D.; Estes, L.; Ciraolo, G. et. al. (2018). On the Use of Unmanned Aerial Systems for Environmental Monitoring. ***Remote Sens.***, 10, 641–669, doi: 10.3390/rs10040641.

Matese, A.; Toscano, P.; Di Gennaro, S.F.; Genesio, L.; Vaccari, F.P.; Primicerio, J.; Belli, C.; Zaldei, A.; Bianconi, R.; Gioli, B. (2015). Intercomparison of UAV, Aircraft and Satellite Remote Sensing Platforms for Precision Viticulture. ***Remote Sens.***, 7, 2971–2990, doi: 10.3390/rs70302971

Markelin, L. (2013). "Radiometric calibration, validation and correction of multispectral photogrammetric imagery." Doctoral dissertation for the degree of Doctor of Science in Technology, Aalto University School of Engineering, Espoo, Finland, September 2013. Pp. 1-86. URL: https://aaltodoc.aalto.fi/bitstream/handle/123456789/10948/isbn9789517112956.pdf?sequence=1&isAllowed=y (Últim accés: 1 de desembre 2018).

Markham, B.; Barsi, J.; Kvaran, G.; Ong, L.; Kaita, E.; Biggar, S.; Czapla-Myers, J.; Mishra, N.; Helder, D. (2014). Landsat-8 Operational Land Imager Radiometric Calibration and Stability. ***Remote Sens.***, 6, 12275–12308, doi: 10.3390/rs61212275

Martínez-Carricondo, P.; Agüera-Vega, F.; Carvajal-Ramírez, F.; Mesas-Carrascosa, FJ.; García-Ferrer, A.; Pérez-Porras, FJ. (2018). Assessment of UAV-photogrammetric mapping accuracy based on variation of ground control points. ***Int J Appl Earth Obs***., 72, 1–10, doi: 10.1016/j.jag.2018.05.015.

McCoy, R.M. (2005). Field Methods in Remote Sensing, 1a Ed.; McCoy, R.M., Ed.; The Guilford Press: New York, NY, USA, 2005; p. 159, ISBN 1-59385-080-8.

Meroni, M.; Colombo, R. (2009). 3S: A novel program for field spectroscopy. ***Comput. Geosci***., 35, 1491–1496, doi: 10.1016/j.cageo.2009.01.005.

MicaSense. (2015) MicaSense RedEdge™ 3 Multispectral Camera User Manual. MicaSense, Inc. Seattle, WA. URL: https://support.micasense.com/hc/en-us/article_attachments/204648307/RedEdge_User_Manual_06.pdf (accessed on 1 July 2018).

Milton, E.J.; Schaepmann, M.E.; Anderson, K.; Kneubühler, M.; Fox, N. (2009). Progress in field spectroscopy. ***Remote Sens. Environ***., 113, S92–S109, doi: 10.1016/j.rse.2007.08.001.

Mira, M.; Niclòs, R.; Valor, E.; Pons, X.; Cea, C.; García-Santos, V.; Caselles, D.; Caselles, V. (2015). Espectroradiometría de campo del visible al infrarrojo térmico de muestras con características espectrales singulares. *A: Proceedings of the XVI Congreso de la Asociación Española de Teledetección, Sevilla, Spain, 21–22 October 2015; Bustamante, J., Díaz-Delgado, R., Aragonés, D., Afán, I., García, D., Eds.; pp. 213-219.* URL: http://www.aet.org.es/congresos/xvi/XVI_Congreso_AET_actas.pdf (Últim accés: 1 de desembre 2018).

Mishra, N.; Helder, D.; Barsi, J.; Markham, B. (2016). Continuous calibration improvement in solar reflective bands: Landsat 5 through Landsat 8. ***Remote Sens. Environ.***, 1185, 7–15, doi: 10.1016/j.rse.2016.07.032.

Mueller, J.L.; Brown, S.W.; Clark, D.K.; Johnson, B.C.; Yoon, H.; Lykke, K.R.; Flora, S.J.; Feinholz, M.E.; Souaidia, N.; Pietras, C.; et al. (2000). Ocean Optics Protocols for Satellite Ocean Color Sensor Validation. *A: Revision 2 NASA; Eds. Fargion, G.S., Mueller, J.L., Eds.; Goddard Space Flight Center: Greenbelt, MD, USA, 2000.*

Mueller-Wilm, U. (2017). Sen2Cor Configuration and User Manual V2.4; European Space Agency, pp. 1–53. URL: http://step.esa.int/thirdparties/sen2cor/2.4.0/Sen2Cor_240_Documenation_PDF/S2-PDGS-MPC-L2A-SUM-V2.4.0.pdf (Últim accés: 1 de desembre 2018).

Nacions Unides. (2018). Sustainable Development Goals. URL: https://www.un.org/sustainabledevelopment/sustainable-development-goals/ (Últim accés: 1 de desembre 2018).

NASAa (National Aeronautics and Space Administration) (2018). Landsat Data Continuity Mission (LDCM). URL: https://www.nasa.gov/mission_pages/landsat/main/index.html (Últim accés: 1 de desembre 2018).

NASAb (National Aeronautics and Space Administration) (2018). Landsat Science – Landsat-7. URL: https://landsat.gsfc.nasa.gov/landsat-7/ (Últim accés: 1 de desembre 2018).

NASAc (National Aeronautics and Space Administration) (2018). Landsat Science – Landsat-8. URL: https://landsat.gsfc.nasa.gov/landsat-8/ (Últim accés: 1 de desembre 2018).

OceanOptics. (2006). USB200+ Data sheet. OceanOptics. Ocean Optics, Inc.: Dunedin, FL, USA. URL: https://oceanoptics.com/wp-content/uploads/OEM-Data-Sheet-USB2000-.pdf (Últim accés: 1 de desembre 2018).

OPTIMISE. (2018). Innovative optical Tools for proximal sensing of ecophysiological processes (ESSEM COST Action ES1309). URL: https://optimise.dcs.aber.ac.uk/ (Últim accés: 1 de desembre 2018).

Parrot. (2018). Parrot Sequoia+. Especificaciones técnicas. URL: https://www.parrot.com/soluciones-business/profesional/parrot-sequoia#parrot-sequoia-details (Últim accés: 1 de desembre 2018).

Peña-Martinez, R.; Domínguez Gómez, J.A.; Ruiz-Verdú, A. (2003). Mapping of Photosynthetic Pigments in Spanish Reservoirs. *A: Proceedings of the MERIS User Workshop (ESA SP-549), ESA-ESRIN, Frascati, Italy, 10–13 November 2003.*

Pflug, B. (2016). Sentinel-2 L2A Processor Sen2Cor. *A: Proceedings of the EUFAR/ ESA Expert Workshop on Atmospheric Correction of Remote Sensing Data, Berlin, Germany, 26–28 October 2016; Ruhtz, T., Ed.*

PNOAa (Plan Nacional de Ortofotografía Aérea). (2018). PNOA Imagen. URL: http://pnoa.ign.es/presentacion-y-objetivo (Últim accés: 1 de desembre 2018).

PNOAb (Plan Nacional de Ortofotografía Aérea). (2018). PNOA LIDAR. URL: http://pnoa.ign.es/presentacion (Últim accés: 1 de desembre 2018).

Pons, X.; Solé-Sugrañes, L. (1994). A simple radiometric correction model to improve automatic mapping of vegetation from multispectral satellite data. ***Rem. Sens. Environ.***, 45, 317–332, doi: 10.1016/0034-425790141-4.

Pons, X.; Pesquer, L.; Cristóbal, J.; González-Guerrero, O. (2014). Automatic and improved radiometric correction of Landsat imagery using reference values from MODIS surface reflectance images. ***Int. J. Appl. Earth Obs. Geoinf.***, 33, 243–254, doi: 10.1016/j.jag.2014.06.002.

Pons, X.; Arcalís, A. (2012). Diccionari terminològic de Teledetecció. Institut Cartogràfic i Geològic de Catalunya; p. 597. ISBN 978-84-393-9008-4.

Rehak, M.; Skaloud, J. (2017). Time synchronization of consumer cameras on Micro Aerial Vehicles. ***ISPRS Journal of Photogrammetry and Remote Sensing***, 123, 114–123. doi: 10.1016/j.isprsjprs.2016.11.009.

Rumpler, M.; Daftry, S.; Tscharf, A.; Prettenthaler, R.; Hoppe, C.; Mayer, G.; Bischof, H. (2014). Automated End-to-End Workflow for Precise and Geo-accurate Reconstructions using Fiducial Markers. *A: ISPRS Technical Commission III Symposium, 5–7 September 2014, Zurich, Switzerland, 135–142,* doi: 10.5194/isprsannals-II-3-135-2014.

Richter, R.; Schläpfer, D. (2016). Atmospheric/Topographic Correction for Satellite Imagery (ATCOR-2/3 User Guide, Version 9.0.2, March 2016). ReSe Appl. Schläpfer, 1–263.

Salamí, E.; Barrado, C.; Pastor, E. (2014). UAV Flight Experiments Applied to the Remote Sensing of Vegetated Areas. ***Remote Sens.***, 6, 11051–11081, doi: 10.3390/rs61111051

Sánchez Alberola, J.; Oliver, P.; Estornell, J.; Dopazo, C. (2018). Estimación de variables forestales de Pinus Sylvestris L. en el contexto de un inventario forestal aplicando tecnología LiDAR aeroportada. ***GeoFocus***, 21, 79–99, doi: 10.21138/GF.509

Saunier, S.; Northrop, A.; Lavender, S.; Galli, L.; Ferrara, R.; Mica, S.; Biasutti, R.; Gory, P.; Gascon, F.; Meloni, M.; et al. (2017). European Space Agency (ESA) Landsat MSS/TM/ETM+/OLI Archive: 42 Years of our history. *A: Proceedings of the 2017 IEEE 9th International Workshop on the Analysis of Multitemporal Remote Sensing Images (MultiTemp), Brugge, Belgium, 27–29 June 2017*.

Skaloud, J.; Rehak, M.; Lichti, D. (2014). Mapping with MAV: Experimental Study on the Contribution of Absolute and Relative Aerial Position Control. *A: ISPRS - International Archives of the Photogrammetry, Remote Sensing and Spatial Information Sciences, Volume XL-3/W1, 2014. EuroCOW 2014, the European Calibration and Orientation Workshop, 12–14 Feb. 2014, Castelldefels, Spain.* doi: 10.5194/isprsarchives-XL-3-W1-123-2014.

Smith, G.M.; Milton, E.J. (1999). The use of the empirical line method to calibrate remotely sensed data to reflectance. ***Int. J. Remote Sens.***, 20, 2653–2662, doi: 10.1080/014311699211994.

Song, C.; Woodcock, C.E.; Seto, K.C.; Lenney, M.P; Macomber, S.C. (2001). Classification and Change Detection Using Landsat TM Data: When and How to Correct Atmospheric Effects? ***Remote Sens. Environ.***, 75, 230–244, doi: 10.1016/S0034-425700169-3.

Turner, R.E.; Malila, W.A.; Nalepha, R.F. (1971). Importance of atmospheric scattering in remote sensing. *A: Proceedings of the Seventh International Symposium on Remote Sensing of Environment, Ann Arbor, MI, USA, 17–21 May 1971; Volume 3 (A72-11776 02-13), pp. 1651–1697.*

USGS (United States Geological Survey). (2016). Landsat-8 Data User Handbook. Version 2.0. URL: https://landsat.usgs.gov/landsat-8-l8-data-users-handbook (Últim accés: 1 de desembre 2018).

Vermote, E.F.; Tanre, D.; Deuzé, J.L.; Herman, M.; Morcrette, J-J. (1997). Second Simulation of the Satellite Signal in the Solar Spectrum, 6S: An Overview. ***IEEE Trans. Geosci. Remote Sens.***, 35, 675–686, doi: 10.1109/36.581987.

Vermote, E.; Justice, C.; Claverie, M.; Franch, B. (2016). Preliminary analysis of the performance of the Landsat 8 / OLI land surface reflectance product. ***Remote Sens. Environ.***, 185, 46–56, doi: 10.1016/j.rse.2016.04.008.

Vidal-Macua, J.J.; Zabala, A.; Ninyerola, M.; Pons, X. (2016). Developing spatially and thematically detailed backdated maps for land cover studies. ***Int. J. Digit. Earth***., 10, 175–206, doi: 10.1080/17538947.2016.1213320.

Xu, J.-F.; Huang, J.-F. (2007). Empirical Line Method Using Spectrally Stable Targets to Calibrate IKONOS Imagery. ***Pedosphere***, 18, 124–130, doi: 10.1016/S1002-016060110-6.

Zabala, S. (2017). Comparison of multi-temporal and multispectral Sentinel-2 and Unmanned Aerial Vehicle imagery for crop type mapping. Master of Science (MSc), Lund University, Lund, Sweden, June 2017.

Zhang, Z.; He, G.; Wang, X. (2010). A practical DOS model-based atmospheric correction algorithm. ***Int. J. Remote Sens.***, 31, 2837–2852, doi: 10.1080/01431160903124682.

Universitat Autònoma de Barcelona

Tesi Doctoral

Millora del tractament de les imatges captades pels satèl·lits Landsat-8 i Sentinel-2 mitjançant espectroradiometria de camp i sensors embarcats en Vehicles Aeris no Tripulats (UAV)

Autor: *Joan-Cristian Padró Garcia.* Director: *Xavier Pons Fernández*